

Synthesis and Functionalization of Silver Nanoparticles for the Preparation of High Permittivity Nanocomposites

THÈSE N° 6686 (2015)

PRÉSENTÉE LE 18 AOÛT 2015

À LA FACULTÉ DES SCIENCES ET TECHNIQUES DE L'INGÉNIEUR
LABORATOIRE DE TECHNOLOGIE DES POUDRES
PROGRAMME DOCTORAL EN SCIENCE ET GÉNIE DES MATÉRIAUX

ÉCOLE POLYTECHNIQUE FÉDÉRALE DE LAUSANNE

POUR L'OBTENTION DU GRADE DE DOCTEUR ÈS SCIENCES

PAR

Jose Enrico Quijano QUINSAAT

acceptée sur proposition du jury:

Prof. J. Brugger, président du jury
Prof. H. Hofmann, Dr D. M. Opris, directeurs de thèse
Dr A. Testino, rapporteur
Prof. M. Niederberger, rapporteur
Dr Y. Leterrier, rapporteur



ÉCOLE POLYTECHNIQUE
FÉDÉRALE DE LAUSANNE

Suisse
2015

“I know it seems hard sometimes but remember one thing. Through every dark night, there's a bright day after that. So no matter how hard it get, stick your chest out, keep ya head up.... and handle it.”

- 2Pac Shakur -

Acknowledgements

First of all, I would like to address my deepest gratitude to my two thesis directors, Prof. Dr. Heinrich Hofmann and Dr. Dorina Opris of the Laboratory of Powder Technology (LTP) of the Swiss Federal Institute of Technology Lausanne (EPFL) and of the Laboratory for Functional Polymers of the Swiss Federal Laboratories for Materials Science and Technology (Empa), respectively, for giving me the opportunity to conduct my thesis under their guidance and allow me to be part of their research activities.

My special thanks go out to Prof. Dr. Frank Nüesch, the head of the Laboratory for Functional Polymers at Empa, for giving me the chance to conduct my research in his laboratories. I would also like to extend my gratitude to Dr. Andrea Testino and his group at Paul Scherrer Institut (Chemical Processes and Materials) and Prof. Dr. Paul Bowen of the LTP at EPFL for their significant contributions to this project which includes providing experimental assistance up to fruitful discussions towards the successful outcome of this work.

Furthermore, I would like to thank the members of my groups from both EPFL and Empa, especially my group members from the Polymer Materials Division, Yee Song Ko, Simon Dünki, Dr. Monica Circu, Dr. Mihaela Alexandru, Dr. Elena Perju, for their kind assistance and support during my PhD thesis. It was a pleasure to have worked and learned from such talented people like you.

I also thank Mrs. Beatrice Fischer, Mr. Adrian Wichser, Mr. Michael Schneider, Mr. Daniel Schreier and Dr. Andreas Borgschulte for their respective contributions to this project, as well as Dr. Christian Scheller and Dr. Eduardo Cuervo-Reyes for the fruitful discussions involving experimental physics.

I would also like to acknowledge EPFL, Empa, Paul Scherrer Institut and the Swiss National Science Foundation (SNF project no. 132101) for enabling this work by providing the essential infrastructure and financial assistance.

Finally, I would like to thank my loved ones which are my family and friends for their love and never ending support which kept me going throughout this whole time. I am very lucky to have you all in my life and will always keep you in my heart forever, even when I will have to part from some of you. The times with you were unforgettable and I will always cherish these memories.

Thank you, Switzerland, for having been a great host country to me and giving me the opportunity of having a good education. I enjoyed the ten years that I've spent here very much. I hope to see you again in the future.

Zusammenfassung

Im Laufe des letzten Jahrzehnts ist das Interesse an der Nanochemie gewachsen, insbesondere aufgrund der interessanten Eigenschaften der Nanomaterialien, die von der Grösse, Form sowie der Oberflächenstruktur bestimmt werden. Dabei haben metallische Nanopartikel für grosses Aufsehen gesorgt, da ihre Eigenschaften es ihnen ermöglicht, in verschiedenen naturwissenschaftlichen Disziplinen eingesetzt zu werden. Trotz der Tatsache, dass sich die Eigenschaften von metallischen Nanopartikeln von der Masse unterscheiden, bleiben einige Eigenschaften weiterhin unverändert, darunter die unendlich grosse Dielektrizitätskonstante, die in Metallen vorgefunden werden. Aus diesem Grunde wurden metallische Nanopartikel benutzt, um Verbundwerkstoffe mit Polymere als Matrix herzustellen. Aus diesen Verbundwerkstoffen sollen dielektrische Materialien mit hohen Dielektrizitätskonstanten hervorgehen, die für die Energiespeicherung oder für die Energieumwandlung eingesetzt werden sollen.

Trotz der grossen Anzahl an Publikationen in den letzten Jahren, die sich mit der Herstellung von Verbundwerkstoffen mit hohen Dielektrizitätskonstanten befassen, gibt es weiterhin Verbesserungsmöglichkeiten für bestehende Materialien. Zum Beispiel werden in einigen Materialien weiterhin hohe dielektrische Verluste verzeichnet, und ausserdem führt die Nutzung von gewissen Füllmaterialien zu einer deutlichen Verschlechterung der mechanischen Eigenschaften, insbesondere mit zunehmendem Anteil des Füllmaterials. Dazu besitzen eine grosse Zahl von Verbundwerkstoffen keine gute Kontrolle über die Grösse und Form der Füllmaterialien sowie unzureichende Informationen bezüglich der Oberflächenbehandlung, die insgesamt zu weiteren Komplexitäten für das Verständnis der Materialeigenschaften beitragen.

Diese Arbeit versucht, sich mit den genannten Problemen von Verbundwerkstoffen zu befassen. Aus diesem Grunde wurden Silbernanopartikel (AgNPs) als Füllmaterial eingesetzt, während Polydimethylsiloxan (PDMS) als Polymermatrix auserwählt wurde. Die Vorteile von Silbernanopartikeln sind ihre relativ leichte Herstellungsmöglichkeiten sowie ihre Resistenz gegenüber Korrosion und Oxidation. Die Herstellung von grossen Mengen Silbernanopartikel wurde durch die Durchführung der Polyolsynthese in einem segmentierendem Rohrreaktor (SFTR) ermöglicht. Die Silbernanopartikel wurden mit einer Siliziumdioxidschicht umgeben, um der Entwicklung von leitfähigen Pfaden innerhalb des Verbundwerkstoffs vorzubeugen. Die dielektrischen Eigenschaften von diesen „Core-shell“-Partikeln wurden zudem in

Abhängigkeit von der Schalendicke untersucht. Die Siliziumdioxidschicht ermöglicht auch die Verbesserung der Kompatibilität zwischen den Partikeln und dem PDMS. Die Wahl von PDMS als Matrix erfolgte aufgrund ihrer guten elektromechanischen Eigenschaften wie etwa hohe Dehnbarkeit, niedrige Viskosität und elektrische Leitfähigkeit sowie tiefe Werte für den Verlustfaktor ($\tan \delta$).

Die hergestellten Verbundwerkstoffe haben im Vergleich zu PDMS höhere Dielektrizitätskonstanten. Ausserdem können die Materialien trotz des hohen Volumenanteils von Silber (20 vol%) weiterhin stark gedehnt werden (800 %). Andere Eigenschaften wie etwa die elektrische Leitfähigkeit oder der Verlustfaktor wurden niedrig gehalten, sodass die jeweiligen Materialien das Potential haben, als dielektrische Elastomere eingesetzt zu werden.

Stichwörter: Silbernanopartikel, Polyolsynthese, Rohrreaktor, Oberflächenbehandlung, Verbundwerkstoffe, dielektrische Elastomere.

Abstract

Over the last decade, a growing interest in nanochemistry has emerged due to the interesting features of nanomaterials that vary with size, shape and surface structure. In particular, metal nanoparticles have received much attention due to their properties that enable their use in various scientific disciplines. Although metal nanoparticles exhibit a number of properties that differ from bulk, some properties, such as their infinite permittivity, remain unchanged. As a result, metal nanoparticles have also been used to prepare nanocomposites with polymers in order to provide dielectric materials featuring high permittivities which can be used for applications such as energy storage (capacitors) or as materials for the conversion of electrical energy into mechanical motion (actuators).

Despite the large number of publications on the preparation of nanocomposites exhibiting high permittivities which have emerged over the years, there is still room for further improvement in the current materials properties. For instance, dielectric losses are still quite high in some materials, and the use of certain types of filler lead to a large deterioration in the mechanical properties of the nanocomposites, especially with increasing filler content. In addition, a large number of the fillers used for the preparation of the nanocomposites feature poor size and shape control as well as poorly defined surface properties thus adding to the complexity of understanding the resulting material properties.

This work tries to address some of the current issues concerning the preparation of dielectric materials. Therefore, silver nanoparticles (AgNPs) were used as filler, while polydimethylsiloxane (PDMS) was employed as the polymeric matrix. The advantages of using AgNPs as filler consist of their relative facile preparation, as well as the possibility of controlling their surface properties due to their resistance towards oxidation and corrosion. The possibility of preparing AgNPs in large amounts with control over the average size of the particles was realized by conducting the polyol synthesis of AgNPs in a Segmented Flow Tubular Reactor (SFTR). A SiO_2 layer was grown around the AgNPs to prevent the loss of the insulating nature of the composite due to the formation of conductive pathways, and the thickness dependency of the dielectric properties of the core-shell particles was also investigated in this work. Furthermore, the SiO_2 shell also provided the possibility of further surface functionalization, which was conducted in order to compatibilize the core-shell particles with the PDMS matrix. PDMS was chosen as the polymeric matrix due to its good

electromechanical properties, which include high elasticity, low viscosity as well as low conductivity and low tangent losses ($\tan \delta$).

The resulting nanocomposites featured enhanced permittivities compared to PDMS, while further optimization in the reaction conditions as well as in the processing procedure yielded nanocomposites with high flexibility that can undergo strains as high as 800 % at a silver content of 20 vol%. Other properties such as electric conductivity and the $\tan \delta$ were kept low which emphasizes the potential of the nanocomposites to being used as flexible dielectric materials.

Keywords: silver nanoparticles, polyol synthesis, segmented flow tubular reactor, surface functionalization, nanocomposites, dielectric elastomer.

Table of Contents

Chapter 1: Introduction	1
1.1 General Overview on Electroactive Polymers (EAPs).....	1
1.2 Basic Principle of Elastomers.....	6
1.3 Dielectric Properties of Materials.....	13
1.4. Polarization Mechanisms in Molecular Structures.....	16
1.5. Enhancing the Permittivity of Elastomers.....	20
1.5.1 Enhancing the Permittivity through Molecular Dipoles.....	21
1.5.2 Enhancing the Permittivity with the Introduction of High Permittivity Filler	24
1.6 Synthesis of Metal Nanoparticles	31
1.6.1 The Mechanisms Towards the Formation of Metal Nanoparticles	31
1.6.2 Preparation of Metal Nanoparticles: The Case of Silver.....	37
1.6.2.1 Preparation of Silver Nanoparticles with Inorganic Reducing Agents	39
1.6.2.2 Preparation of Silver Nanoparticles with Organic Reducing Agents.....	39
1.7 Surface Functionalization of Metal Nanoparticles	44
1.8 Current State of Functionalized Metals/Polymer Nanocomposites	48
1.9 Goals of the Thesis	51
1.10 Structure of the Thesis.....	51
1.11 References	53

Table of Contents

Chapter 2: Continuous Production of Tailored Silver Nanoparticles by Polyol Synthesis and Reaction Yield Measured by X-ray Absorption Spectroscopy: Towards a Growth Mechanism.	75
2.1. Introduction	76
2.2. Experimental Section	80
2.2.1. Continuous Segmented Flow Tubular Reactor (SFTR)	80
2.2.2 Polyol Synthesis of Silver Nanoparticles in the SFTR.....	81
2.2.3. Materials and Methods	82
2.3. Results	86
2.4. Discussion	98
2.5. Conclusions	101
2.6 Acknowledgements	101
2.7 References	102
2.8 Supporting information	110
Chapter 3: Dielectric Properties of Silver Nanoparticles Coated with Silica Shells of Different Thicknesses.....	113
3.1 Introduction	114
3.2 Experimental Section	117
3.2.1 Synthesis of Silver Nanoparticles (38 nm).....	117
3.2.2 Synthesis of Silica Coated Silver Nanoparticles Ag@SiO ₂ (x nm)	118
3.2.3 Synthesis of Hydrophobic Coating: (Ag@SiO ₂ (17 nm)@alkylsilane).....	119

Table of Contents

3.3 Materials and Methods	119
3.4 Results	120
3.4.1 Synthesis and Characterization of AgNPs Coated with SiO ₂	120
3.4.2 Dielectric Properties of Ag@SiO ₂ in Pressed Pellets	126
3.5 Conclusions	132
3.6 Acknowledgments	132
3.7 References	133
3.8 Supporting Information	140
Chapter 4: Highly Stretchable Dielectric Elastomer Composites Containing High Volume Fraction of Silver Nanoparticles (AgNPs)	143
4.1 Introduction	145
4.2 Experimental Section	148
4.2.1 Materials and Methods	148
4.2.2 Synthesis of AgNPs.....	150
4.2.3 Synthesis Ag@SiO ₂ Core-shell Particles	150
4.2.4 Synthesis of Ag@SiO ₂ @Si(CH ₃) ₃	151
4.2.5 Synthesis of Composites of Series A	151
4.2.6 Synthesis of Composites of Series B.....	151
4.2.7 Synthesis of Composite B ₃₁	151
4.3 Results and Discussion.....	152

Table of Contents

4.3.1 Synthesis and Characterization of the Filler Particles	152
4.3.2 Synthesis and Characterization of AgNP Composites	157
4.3.3 Dielectric Properties of the Filler and Composites	164
4.4 Conclusions and Outlook	170
4.5 Acknowledgements	170
4.6 References	171
4.7 Supporting Information	177
Chapter 5: Surface Hydrophobization of Silver Nanoparticles (AgNPs) through Surface-initiated Atom Transfer Radical Polymerization (SI-ATRP).....	185
5.1 Introduction	186
5.2 Experimental Section	188
5.2.1 Materials and Methods	188
5.2.2 Synthesis of AgNPs.....	189
5.2.3 Synthesis of Ag@SiO ₂ Core-shell Particles.....	189
5.2.4 Synthesis of APTES-Br.....	189
5.2.5 Synthesis of Initiator-coated Ag@SiO ₂ Core-shell Particles (Ag@SiO ₂ @Br).....	190
5.2.6 Surface-initiated (SI) ATRP on Initiator Coated Ag@SiO ₂ Core-shell Particles	190
5.3 Results and Discussion.....	191
5.3.1 Synthesis of AgNPs and Surface Functionalization with SiO ₂	191
5.3.2 Surface-initiated (SI) ATRP on the Ag@SiO ₂ Core-shell Particles	191

Table of Contents

5.4 Conclusion and Outlook.....	202
5.5 Acknowledgements	202
5.6 References	203
6. Conclusions	209
7. Outlook.....	211
8. Appendix	213
A1. Preparation of Silver Nanoparticles by Inverse Miniemulsions (Water-in-Oil System).	213
A2. The Preparation of Ag/PDMS Nanocomposites with Varying Particle Size and their Resulting Dielectric Properties.....	219
A3. References	231
9. Curriculum Vitae.....	233
 Fig. 1: Composition and working principle of DEA. Upon application of a voltage (right side) the film is compressed and elongated thus leading to the conversion of electrical energy into mechanical work.	3
Fig. 2: Typical stress-strain curve for an elastomer (PDMS).....	7
Fig. 3: Structure of hydroxyl-terminated PDMS.....	8
Fig. 4: Chemical structure of di- <i>n</i> -butyltin dilaureate DBTDL.....	9
Fig. 5: Chemical structure of Karstedt's catalyst.	9

Table of Contents

Fig. 6: Schematic illustration of a real polymer network. The present structural defects are encircled.	12
Fig. 7: Schematic illustration of randomly oriented dipole molecules (left) and their realignment towards the direction of the applied electric field (right) in a DEA.....	22
Fig. 8: Polymer network of PDMS with dipoles grafted onto the polymer backbone.	22
Fig. 9: Dipole molecule with vinyl functionality enabling the grafting onto PDMS.....	23
Fig. 10: Overview of typical dimension ranges of nanoparticles and colloids, together with some representative colloidal systems.	33
Fig. 11: LaMer model for the generation of nanocrystals involving the nucleation and growth stages.	34
Fig. 12: LaMer model for the generation of nanocrystals involving the nucleation and growth stages. The product quality depending on the nucleation time is also depicted in the image.	36
Fig. 13: Schematic illustration of surface plasmon resonance (SPR). The free conduction electrons in the metal nanoparticles undergo oscillation as a result of the strong interaction with the incident light.....	38
Fig. 14: Proposed reaction mechanism for the preparation of AgNPs with DMF.	40
Fig. 15: Proposed reaction mechanism for the preparation of AgNPs with the Tollens reaction.	40
Fig. 16: Proposed reaction mechanism for the preparation of AgNPs through the reduction with formaldehyde.....	41
Fig. 17: Proposed reaction mechanism for the preparation of AgNPs with the Turkevich method.....	42
Fig. 18: Proposed reaction mechanism for the preparation of AgNPs by the polyol process..	43

Table of Contents

Fig. 19: TEM micrographs of different silver nanostructures: (a) Silver nanocubes (AgNCs), (b) silver nanowires (AgNWs) and (c) silver nanoparticles (AgNPs).....	44
Fig. 20: Agglomeration of conductive particles within the polymeric matrix leading to percolation pathways (left) and insulated particles without agglomeration (right).....	44
Fig. 21: Silica nanoparticles prepared with the Stöber method.....	45
Fig. 22: Transformation of the PVP molecule to the enol conformation under basic conditions.	46
Fig. 23: Schematic illustration of the SFTR. The two reactants are introduced separately into the system and pass through various systems (micromixer, segmenter) in order to produce reaction microdroplets prior to going through the heated reactor where the formation of the particles occur.....	80
Fig. 24: AgNPs prepared with PVP 10k: (a) G0, (b) G1, (c) G2 and (d) G3.....	88
Fig. 25: AgNPs prepared with PVP 40k: (a) G4, (b) G5 and (c) G7.	89
Fig. 26: UV-vis spectra of the AgNPs prepared with the SFTR.	90
Fig. 27: Correlation of the mean particle diameter (measured with TEM) with the position of the absorption maxima in the UV-vis spectra.	91
Fig. 28: Particle size number distribution measured by DLS of the AgNPs prepared with the SFTR.....	91
Fig. 29: Particle size number distribution measured by DLS of the AgNPs prepared during the long term reaction (L1). Particles were analysed at different reaction times.	92
Fig. 30: Example of LC fit for (a) Sample G3 (Ag-L ₃) and (b) Sample G4 (Ag-K) edge XANES spectrum. Circles: experimental data; Red line: LC fit; Blue line: fraction of Ag ⁺ making up the fit; Pink line: fraction of Ag ⁰ making up the fit; Green line: Difference between experimental data and LC fit.....	95

Table of Contents

Fig. 31: TGA measurements conducted on the recovered powders from samples G3, G7 and L1.....	97
Fig. 32: Diffraction patterns collected on powder (G7) or on the as prepared suspension (G3, G4, G5) after background subtraction.....	98
Fig. 33: DLS spectra of the samples Ag_1, Ag_2 and Ag_3.	111
Fig. 34: UV-vis spectra of the samples Ag_1, Ag_2 and Ag_3.....	111
Fig. 35: TEM micrographs of the samples (a) Ag_1, (b) Ag_2 and (c) Ag_3 with corresponding particle size distribution (PSD).	112
Fig. 36: Insulator shell (light grey) on conductive Ag nanoparticles (dark grey) defining the minimum distance between the cores as twice the shell thickness.	116
Fig. 37: TEM images of AgNPs prepared by reduction of AgNO ₃ with ethylene glycol. The reaction was done starting with 6 g AgNO ₃	121
Fig. 38: TEM images of the AgNPs coated with a silica shell. The average diameters of AgNPs were 38 nm while the SiO ₂ shells were about 20 ± 2 nm (a); 17 ± 2 nm (b); 8 ± 1.5 nm (c); 6.6 ± 1.5 nm (d); 3.6 ± 1 nm (e).	123
Fig. 39: EDX of the naked AgNPs (a) and of the AgNPs coated with SiO ₂ (b).....	123
Fig. 40: UV-vis absorption spectra of AgNPs and of AgNPs coated with a silica shell recorded in MeOH. A small bathochromic shift is seen with increasing shell thickness.	125
Fig. 41: Hydrodynamic diameter D_H determined by DLS of AgNPs before and after coating with silica shell recorded in EtOH. An increase in particle size is observed with increasing shell thickness, except for Ag@SiO ₂ (3.6) the D_H -value of which does not match single particle size. For explanation, see text.	126
Fig. 42: Permittivity, dielectric loss, and conductivity of AgNPs coated with silica shells of different thickness as function of frequency.	127

Table of Contents

Fig. 43: The permittivity and conductivity of AgNPs coated with a 17 ± 2 nm silica shell and of a silica hydrophobized with a silane reagent.....	129
Fig. 44: Wettability test in water/toluene for the Ag@SiO ₂ (left) and that of hydrophobized with silane reagent (right). The hydrophobized particles are transferred in organic phase. ..	140
Fig. 45: Solid-state ²⁹ Si CP-MAS NMR spectrum of silver nanoparticles coated with silica shell and surface functionalized with octyl chains showing the chemical shift for the silicon nucleus of the surface- bound alkyl chains at $\delta = 13$ ppm.	140
Fig. 46: SEM image of Ag@SiO ₂ (6.6 nm) powder in pressed pellet. The sample was measured in high vacuum mode using 3 kV and a TLD detector.	141
Fig. 47: SEM image of Ag@SiO ₂ (6.6 nm) powder in pressed pellet. The sample was measured in low vacuum mode using 7 kV and a LVD detector.....	141
Fig. 48: SEM image of Ag@SiO ₂ (6.6 nm) powder in pressed pellet. The sample was measured in low vacuum mode using 7 kV and a LVD detector.....	142
Fig. 49a-b: TEM micrographs of AgNPs prepared by reduction of AgNO ₃ with ethylene glycol (left) and of their coating with a thin silica shell of about 3.3 nm (right).....	153
Fig. 50: UV-vis spectra of AgNPs (Δ) and silica-coated Ag@SiO ₂ core-shell particles (\square) recorded in ethanol.	155
Fig. 51: DLS spectra of AgNPs (Δ) and silica-coated Ag@SiO ₂ core-shell particles (\square) recorded in ethanol.....	155
Fig. 52: Wetting test of Ag@SiO ₂ core-shell particles conducted in toluene/water mixture before (left) and after (right) surface functionalization with HMDS.	157
Fig. 53a-g: SEM images of the freeze-broken Ag/PDMS nanocomposites of series A containing 5, 12, 18, 25 vol% and Ag (a-d) and of series B containing 9, 14, and 20	

Table of Contents

vol% Ag (e-g). Some present agglomerates are shown in the red circles. The scale bar is 50 μm	158
Fig. 54: Stress–strain curves of the composites of series A containing different vol% of Ag and of the neat matrix. The vol% of Ag was determined after the films were cross-linked by using ICP-OES.....	159
Fig. 55: Stress-strain curves of the matrix B_0 , B_{20}^{stiff} , B_{20} , B_{14} , and B_9 ; the enlargement for the low strains (insert); and photos of B_{20} in its relaxed and strained form (bottom) (the scale bar represents 1 cm).....	162
Fig. 56: Cyclic stress-strain relaxation curves of B_{14} at 50% strain (left) and dynamic mechanical analysis for B_{20} at different frequencies (right).	163
Fig. 57: TGA curves of composites B and of the matrix under helium.	164
Fig. 58: Permittivity, $\tan \delta$, and conductivity as function of frequency for series A (left) and series B and the filler (right).....	168
Fig. 59: Specific energy density per volume at a given electric field.	169
Fig. 60: Size distribution of AgNPs and Ag@SiO ₂ core-shell. The sizes were determined through TEM image analysis.	177
Fig. 61: XRD spectrum of the AgNPs prepared by polyol synthesis at 130 °C. The typical cubic silver diffraction was observed.	178
Fig. 62: TEM micrographs of the Ag@SiO ₂ produced via upscaling through the addition of 0.6 vol% ethanolic TEOS solution into the reaction mixture.....	178
Fig. 63: TEM micrographs of the AgNPs (left) and Ag@SiO ₂ core-shell particles (right) and their corresponding EDX spectrum below.	179
Fig. 64: Elemental analysis of the core-shell particles before and after surface treatment with HMDS recorded for both batches.....	179

Table of Contents

Fig. 65: XPS spectra of AgNPs prepared with the polyol synthesis at 130 °C. The peak indicative for the oxidized silver species is missing.	180
Fig. 66: The mechanical properties of B ₂₀ aged at room temperature for 10 days and at 150 °C for 5 days: the cyclic (left) and the stress-strain (right) tests.	180
Fig. 67: The strain reloading stress-strain curves after initial strain excursions of 50, 75, 100, all the way up to 450 % for B ₁₄	181
Fig. 68: Permittivity as function of filler content of the composite of series A and B.	181
Fig. 69: Breakdown field E_B as function of filler content of the composite of series A (red) and B (black). The averaged values are depicted with error bars and were obtained from the measurements using the electrodes with an area of 1 mm ²	182
Fig. 70: Electrodes used for breakdown strength measurements and the overall set-up of the system (from left to right).	182
Fig. 71: The setup used for measuring the dielectric properties.	183
Fig. 72: General scheme towards the preparation of PMMA-coated Ag@SiO ₂ core-shell particles.	187
Fig. 73: TEM micrographs of AgNPs (a), Ag@SiO ₂ (b), APTES-Br (c) and PMMA-coated Ag@SiO ₂ core-shell particles (d).	192
Fig. 74: UV-vis spectra of AgNPs, Ag@SiO ₂ and APTES-Br coated Ag@SiO ₂ core-shell particles. The spectra were recorded in EtOH.	193
Fig. 75: DLS spectra of AgNPs, Ag@SiO ₂ , APTES-Br and PMMA-coated Ag@SiO ₂ core-shell particles recorded in EtOH.	195
Fig. 76: Particle size distribution of AgNPs, Ag@SiO ₂ core-shell particles and PMMA-coated Ag@SiO ₂ core-shell particles obtained from the image analysis of TEM micrographs.	196

Table of Contents

Fig. 77: UV-vis spectra of APTES-Br coated Ag@SiO ₂ core-shell particles and PMMA-coated Ag@SiO ₂ core-shell obtained from the aliquots taken after a prescribed amount of time. The spectra were recorded in THF.	197
Fig. 78: Water/toluene extraction tests of AgNPs (a), Ag@SiO ₂ (b), APTES-Br -coated Ag@SiO ₂ (c) and PMMA-coated Ag@SiO ₂ core-shell particles (d). The organic phase is above the aqueous phase.	198
Fig. 79: Semi-logarithmic plot of the monomer conversion versus the polymerization reaction time.	199
Fig. 80: Molecular weight (M_n) of free, sacrificial PMMA obtained from GPC measurements of aliquots taken after a prescribed amount of reaction time.	200
Fig. 81: The development of the molecular weight M_n and the polymer dispersity index (PDI) with time.	201
Fig. 82: TGA curves of Ag@SiO ₂ , APTES-Br and PMMA-coated Ag@SiO ₂ core-shell particles.	201
Fig. 83: Structure of Span 85 (left) and D ₄ (right).	213
Fig. 84: TEM Micrographs of the samples 1-8 and the particle size distribution inserted in the images.	215
Fig. 85: TEM Micrographs of the samples 7 and 8 and the particle size distribution inserted in the images.	216
Fig. 86: DLS spectra of AgNPs (Tab. 16, samples 1-8) which were prepared by reverse miniemulsions measured in toluene.	216
Fig. 87: UV-vis spectra of AgNPs (Tab. 16, samples 1-8) which were prepared by the inverse miniemulsions technique measured in hexadecane.	217
Fig. 88a-d: TEM micrographs and size distribution (inserted) of the different AgNPs.	221

Table of Contents

Fig. 89: UV-vis spectra of AgNPs of different sizes recorded in EtOH.	222
Fig. 90: DLS spectra of AgNPs of different sizes recorded in EtOH.	222
Fig. 91a-d: TEM micrographs of the different Ag@SiO ₂ core-shell particles. The diameter of the AgNPs as well as the thickness of the SiO ₂ shell is mentioned in parenthesis.	223
Fig. 92: UV-vis spectra of Ag@SiO ₂ core-shell particles (~ 4 nm thick SiO ₂ shell) of different core sizes recorded in EtOH.	224
Fig. 93: DLS spectra of Ag@SiO ₂ core-shell particles (~ 4 nm thick SiO ₂ shell) of different core sizes recorded in EtOH.	224
Fig. 94: The permittivity of the Ag@SiO ₂ /PDMS nanocomposites with varying Ag core and filler content.	229
Fig. 95: The tan δ values of the Ag@SiO ₂ /PDMS nanocomposites with varying Ag core and filler content.	229
Tab. 1: Measured properties of few polymer dielectric materials.	4
Tab. 2: List of composites and their resulting dielectric properties.	30
Tab. 3: List of composites using Ag as filler and their corresponding dielectric properties.	50
Tab. 4: Summary of the <i>polyol synthesis</i> of AgNPs in the SFTR. In the parenthesis is reported the measured standard deviation of the particle population.	87
Tab. 5: Percentile Diameters measured with DLS for AgNPs (L1) prepared at 150 °C running over 4 hours.	93
Tab. 6: Mean diameter for AgNPs (L1) prepared at 150 °C running over 4 hours. In the parenthesis is reported the measured standard deviation of the particle population.	93

Table of Contents

Tab. 7: Summary of the amount of Ag^+ and Ag^0 of selected samples determined by XANES spectroscopy (L_3 -edge or K-edge). The yield is determined by Eq. 1.....	95
Tab. 8: Different batch reactions with constant AgNO_3/PVP ratio performed at 150°C . The reaction volume was varied for each reaction by a factor of 10.....	110
Tab. 9: Percentile and mean diameters of the samples Ag_1, Ag_2 and Ag_3.	112
Tab. 10: The amount of reagents used for the coating of AgNPs with different thickness silica shell.	119
Tab. 11: The calculated and measured ε' for different silica thicknesses.	131
Tab. 12: Size and λ_{max} data of AgNPs and $\text{Ag}@\text{SiO}_2$ obtained by TEM, DLS and UV-vis of the core-shell particles before and after the surface treatment with HMDS.	156
Tab. 13: The amount of components used for the synthesis of the matrix and of materials of series A and B.	161
Tab. 14: Summary of the densities, permittivity, loss factor, and breakdown field of the composites of series A and B.	167
Tab. 15: Determined size parameters of AgNPs, $\text{Ag}@\text{SiO}_2$ core-shell particles (before and after immobilization of APTES-Br) and PMMA-coated $\text{Ag}@\text{SiO}_2$ core-shell particles.....	197
Tab. 16: List of experiments conducted for the preparation of AgNPs via miniemulsions ...	218
Tab. 17: Summary of the size parameters of the different AgNPs and $\text{Ag}@\text{SiO}_2$ core-shell particles.	225
Tab. 18: Composition of the nanocomposites using functionalized $\text{Ag}@\text{SiO}_2@\text{Si}(\text{CH}_3)_3$ core-shell particles as high permittivity filler.....	226
Tab. 19: Summary of the dielectric properties of the different nanocomposites using different filler	230

Abbreviations

AC	Alternating Current
Ag	Silver
AgNCs	Silver nanocubes
AgNPs	Silver nanoparticles
AgNRs	Silver nanorods
AgNWs	Silver nanowires
Al	Aluminum
APTMS	3-(Aminopropyl)trimethoxysilane
APTES	3-(Aminopropyl)triethoxysilane
Ar	Argon
a.u.	Arbitrary units
AuNPs	Gold nanoparticles
BI-XDC	Brookhaven Instrument - X-ray disk centrifuge
BSED	Backscatter Electron Detector
CL	Cross-linker
Cu	Copper
DBTDL	Dibutyltindilaureate
DDA	Dodecanoic acid
DEA	Dielectric Elastomer Actuators
DEG	Dielectric Elastomer Generator
DET	Dielectric Elastomer Transducer
DLS	Dynamic Light Scattering
DMA	Dimethylamine or Dynamic mechanical analysis
DMF	Dimethylformamide
D ₄	Octamethylcyclotetrasiloxane
EAP	Electroactive polymer
EDX	Energy-dispersive X-ray spectroscopy
EG	Ethylene glycol
EtOH	Ethanol
eV	Electron volt
GNP	Graphene nanoplatelets
GPC	Gel permeation chromatography
GSAS	General Structure Analysis Software
h	Hours
hcp	Hexagonal close-packed
He	Helium
HMDS	Hexamethyldisilazane

Table of Contents

HPLC	High Performance Liquid Chromatography
Hz	Hertz
ICP-OES	Inductively Coupled Plasma-Optical Emission Spectroscopy
ICP-MS	Inductively Coupled Plasma-Mass Spectroscopy
J	Joules
(k)Da	(Kilo)Dalton
ICSD	Inorganic Crystal Structure Database
L	Litre
LCF	Linear Combination Fitting
LSPR	Localized surface plasmon resonance
MeOH	Methanol
(m)g	(Milli)gram(s)
MHA	16-Mercaptohexadecanoic acid
Min	Minute(s)
(m)M	(Milli)molar
MMA/PMMA	Methyl methacrylate/Poly(methyl methacrylate)
M_n	Number average molecular weight
MNP	Metal nanoparticle
MPa	Megapascal
MSA	Mercaptosuccinic acid
M_w	Weight average molecular weight
MWCNTs	Multiwalled carbon nanotubes
N	Newton
<i>n</i> -C ₁₂	Dodecane
Ni	Nickel
nm	nanometre
NMR	Nuclear Magnetic Resonance
PAA	Poly(acrylic acid)
Pa	Pascal
PANI	Polyaniline
PDI	Polymer (or particle) dispersity index
PDMS	Polydimethylsiloxane
PG	Propylene glycol
PMDETA	Pentamethyldiethylenetriamine
ppm	Parts per million
PTFE	Poly(tetrafluoroethylene)
PVDF	Poly(vinylidene difluoride)
PVP	Poly(vinyl pyrrolidinone)
PSD	Particles size distribution

Table of Contents

Ref.	References
rpm	Rounds per minute
RTV	Room temperature vulcanization
Sn	Tin
SEM	Scanning Electron Microscopy
SFTR	Segmented Flow Tubular Reactor
SI-ATRP	Surface-initiated atom transfer radical polymerization
Span 85	Sorbitane trioleate
Tan δ	Tangents of the loss angle δ
UV-vis	Ultraviolet-visible spectroscopy
TEA	Triethylamine
TEM	Transmission Electron Microscopy
TEOS	Tetraethoxysilane
TGA	Thermogravimetric analysis
THF	Tetrahydrofuran
TiO ₂	Titanium dioxide (titania)
TPU	Thermoplastic polyurethane
V	Volts
VHB (of 3 M)	Polyacrylate-based elastomer
vol	Volume
wt	Weight
XANES	X-ray Absorption Near End Spectroscopy
XAS	X-ray absorption spectroscopy
XPS	X-ray photoelectron spectroscopy
XRD	X-ray diffraction

Table of Contents

Chapter 1: Introduction

1.1 General Overview on Electroactive Polymers (EAPs)

The research community has shown a growing interest in the development of high dielectric permittivity (ϵ') materials due to their multiple application fields in the electrical industry. They are commonly used for electronic applications such as in capacitors, gate dielectrics, memories, pulse power energy storage and electroactive materials.¹⁻⁵ Non-electronic applications of high ϵ' materials include their use in biomedical imaging, non-destructive testing, active vibration control and aerospace.⁶

One of the fields where high ϵ' materials find potential application is in the preparation of Electroactive polymers (EAPs). EAPs are a class of smart materials that have the ability to change their size and shape through the influence of an electric field. The concept of EAPs can be traced back to 1880 when Roentgen observed that a film made of natural rubber could change its shape by applying an electric field across it.⁷ Since the mid-1990s, the research on EAPs has been intensified by the scientific community, and novel polymeric materials featuring large amounts of deformations (also known as actuation) through the application of external forces have emerged over the years. The high standing of the EAP research can also be attributed by the fact that, compared to inorganic materials, polymers are lightweight and can be produced in various shapes at relatively low costs.⁸ As for now, applications of EAPs are being considered for loudspeakers, tunable optical elements,⁹ cell and tissue engineering,¹⁰ robotics¹¹ and prosthetic devices.^{9,11-16} A more detailed list of applications for EAPs is reported elsewhere.^{5,17} The growing demand for EAPs and the need for interdisciplinary collaborations also led to the creation of the European Scientific Network for Artificial Muscles (ESNAM) in Europe, an organization consisting of both academic and industrial researchers.¹⁸ Global companies dealing with the development of EAPs are Artificial Muscle (USA), Danfoss PolyPower Eamex (Denmark/Japan),

1. Introduction

Environmental Robots (USA), Optotune (Switzerland), Creganna-Micromuscle (Ireland) and Strategic Polymer Sciences.¹⁹

In general, EAPs can be divided into the two subclasses: Ionic EAPs or electronic EAPs.^{19,20} Within the electronic EAPs, dielectric elastomers (DEs) have attracted significant interest due to their very large strains and high-power applications, which are properties of interest for the development of high performance actuators.^{5,8} Compared to the features of a mammalian skeletal muscle, DEs come close to mimicking their properties like strain and stress.²¹ With their proposal as actuators dating back to 1998, DEAs are electromechanical transducers which can transform electric energy into mechanical energy.²² The working principles of DEAs will be explained in this paragraph. A DEA consists of two electrodes separated by a dielectric elastomer film. The actuation in the electronic EAPs is induced by the application of a voltage difference between the electrodes (Fig. 1).¹⁷ This phenomenon leads to the buildup and accumulation of different charges on the opposing electrodes thus giving rise to Coulomb attraction between them. An electrostatic pressure p , also known as Maxwell stress, acts on the sandwiched film and causes it to be strained in thickness direction s_z and expand in-plane due to the incompressible nature of the elastomer. The electrostatic pressure p acting on the film for a given voltage U can be calculated using equations Eq. 1 and Eq. 2, where $\epsilon_0 = 8.85 \times 10^{-12} \text{ F}\cdot\text{m}^{-1}$ is the vacuum permittivity, ϵ_r is the permittivity or dielectric constant of the material, Y the Young's modulus and d is the initial thickness of the elastomer. After switching off the voltage, the DEA will return to its unstrained state.⁸

$$p = \epsilon_r \epsilon_0 \left(\frac{U}{d}\right)^2 \quad (\text{Eq. 1})$$

$$s_z = \frac{-p}{Y} \quad (\text{Eq. 2})$$

1. Introduction

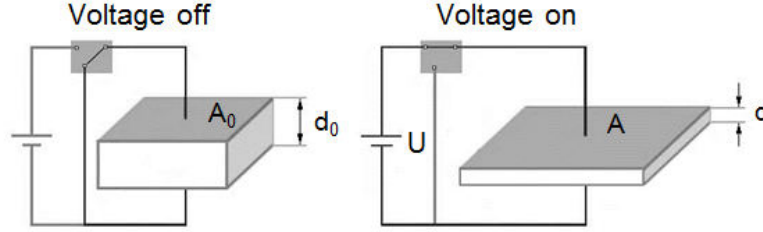


Fig. 1: Composition and working principle of DEA. Upon application of a voltage (right side) the film is compressed and elongated thus leading to the conversion of electrical energy into mechanical work.

Apart from generating mechanical motion from electrical energy, the reverse scenario can be exploited for energy storage. The latter can be produced through the charging of the DE in the stretched state followed by its gradual relaxation into the original state.²³ As a result, the tensile forces are reduced which leads to the thickening of the elastomer as it is released from the stretched state. This leads to the compression of like charges while opposite charges are brought further apart. This phenomenon leads to an increase in the voltage of the system. Overall, such dielectric elastomer generators (DEG) serve as capacitors, with some materials demonstrating energy densities as high as 400 mJ/g.^{24,25} The widely used materials in DEAs and DEGs are silicones (PDMS) and acrylic VHB (of 3 M) due to their ability to undergo large strains during deformation.²⁶ A list of elastomers that have been used in DEAs or DEGs is shown in Tab. 1.

Tab. 1: Measured properties of few polymer dielectric materials.

Polymer	Thickness Strain (%)	Actuation Pressure (MPa)	Young's modulus Y (MPa)	Relative permittivity ϵ_r (1 kHz)	Ref.
Acrylic VHB (3 M) ^a	79	7.2	3 ^b	4.8	[26]
Silicone Nusil CF19-2186	32	1.36	1.0	2.8	[27]
Silicone Dow Corning HS3*	41	0.13	0.125	2.8	[27]
Silicone Dow Corning Sylgard 186	32	0.51	0.7	2.8	[27]
Fluorosilicone (Dow Corning 730)	28	0.39	0.5	6.9	[27]
Fluoroelastomer (Lauren L143HC)	8	0.11	2.5	12.7	[27]
Polyurethane (Deerfield PT6100S)	11	1.6	17	7.0	[27]
Polyurethane (Estane TPU588)	8	0.14	-	6.0	[28]

^a With biaxial pre-stretching (300, 300); ^b Effective modulus.

1. Introduction

Despite the good attributes of current DEs, the biggest remaining challenge is the high driving (electric) field required for the actuation process (10 - 150 V/ μm) which hampers their applications within the proximity of human bodies due to safety issues.¹⁷

Eq. 1 illustrates that the film thickness as well as the other material properties such as the Young's modulus and the relative permittivity ϵ_r require optimization in order to enhance the electromechanical properties of the DEAs. As generally suggested,^{20,29} the reduction of d and Y as well as the enhancement of ϵ_r are necessary to lower the electric fields required for the actuation.

Conventional film formation techniques include dip coating and casting procedures, which also enable the formation of complex shapes. For thin films, spin coating is a commonly used method. Elastomeric films as thin as 1 μm with high uniformity have been prepared with this technique which effectively leads to the reduction of the driving voltage.²⁷ The typical film thickness of polymer membranes used for DEAs is around 50 μm .³⁰

The Young's modulus of elastomers can be reduced by reducing the amount of cross-linker in the system which leads to a lower cross-linking density.^{31,32} The lower cross-linking density allows the polymer chains to shear much easier as the chemical bonds between neighboring polymer chains is decreased. A detailed explanation on the relationship between the Y and the cross-linking density will be shown in the course of this chapter. Another solution is the use of plasticizers to soften the material.³³ The increase in the plasticizer content has led to a decrease in Y of the silicone elastomer, while ϵ_r remained quasi unaffected by the increasing content of the plasticizer. Further softening of the material properties to improve the electromechanical properties has been reported for tri-block copolymers using specific oil as the plasticizer.³⁴

Despite the feasibility of the mentioned strategies to improve the device performance, there are other obstacles that tend to occur along the way. For example, it is essential to lower the possibility of defects from occurring in the material.²⁷ Defects within the structure can propagate through the straining of the material (either during the assembly of the device or

1. Introduction

during the actual device performance) thus causing the premature destruction of the dielectric film.²⁹ This phenomenon manifests itself more strongly in thin films than in thicker materials and leads to a shorter life-time of the device. As for the reduction of Y , the method is limited by the fact that a very soft material becomes difficult to process. The mere increase in plasticizer leads to a reduction of the maximum absolute achievable strains and therefore the amount of plasticizer has to be adjusted to an optimal level.³³ The main motivation of this project is to enhance the dielectric properties of materials by exploiting the possibilities of increasing the permittivity ϵ_r of the material. Additionally, the materials should feature high degree of flexibility, which should manifest itself in the capability of the material to undergo large mechanical strains when subjected to external forces. The basic concepts and strategies towards the preparation of such high performance materials will be elucidated in the following chapters.

1.2 Basic Principle of Elastomers

Elastomers are amorphous polymers which exhibit a number of useful properties, including good electrical and thermal insulation as well as good mechanical properties.³⁵ The good mechanical properties of elastomers manifest itself in their low Young's modulus Y and their capability to undergo large mechanical strains through application of mechanical stress. The Young's modulus Y is mathematically described by Hooke's law which states that the deformation of an elastic material is proportional to the applied stress and hereby leads to

$$Y = \frac{d\sigma}{ds} \quad (\text{Eq. 3})$$

where σ is the stress that results in the corresponding strain s of the material. For small strains, the Young's modulus can also be calculated as $Y = \sigma/s$.³⁵

1. Introduction

Once released from the applied stress, the elastomer will return to its original configuration. A typical stress-strain curve is illustrated in Fig. 2. The stress-strain curve of an elastomer can be divided into three different regions *a*, *b* and *c*, which is typically observed for elastomers. The elastomer features a “hard” characteristic in the low strain region *a*, which manifests itself through the steep slope of the stress-strain curve. Thereafter, the material softens and the slope of the stress-strain curve decreases as it enters the region *b*. As the chains are stretched further, the slope of the curve increases again and the material undergoes strain-hardening.³⁰

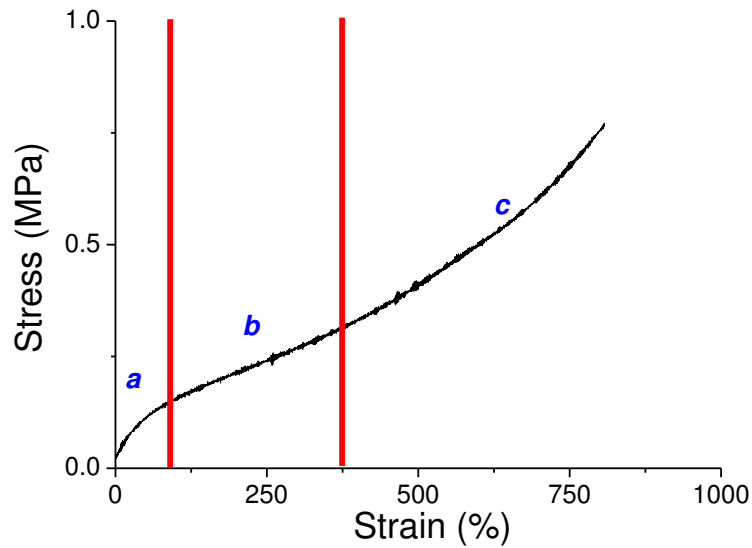


Fig. 2: Typical stress-strain curve for an elastomer (PDMS).

The elastomer is produced by cross-linking the polymer chains under the formation of a network. The cross-linking can occur through the physical interaction between segments in the polymer chains or through the chemical reaction of the polymer chains with cross-linker molecules which can be regarded as physical netpoints. Physical cross-linking is

1. Introduction

found in thermoplastic polymers (e.g. thermoplastic polyurethane (TPU)) while chemical cross-linking is observed for another group of elastomers which include synthetic and natural rubbers, polydimethylsiloxane (PDMS, Fig. 3) and polyacrylates.³⁶ For the cross-linking process, also known as curing or vulcanization, the addition of other ingredients, including curing agents, activators or accelerators is essential for obtaining the elastomeric film.³⁵

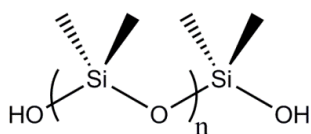


Fig. 3: Structure of hydroxyl-terminated PDMS.

In the case of PDMS, various methods have been applied to induce the chemical cross-linking reaction and eventually yield an elastomer. The cross-linking of PDMS has been achieved through condensation reactions between the hydroxy end-groups of the PDMS chain and the cross-linker (e.g. tetraethoxysilane (TEOS)) catalyzed by organotin or organotitanium catalysts e.g. di-*n*-butyltin dilaureate (DBTDL, Fig. 4).^{31,37} An alternative approach consists of the cross-linking via hydrosilylation. This method consists of an addition step involving the reaction of a hydrosilane group (Si-H) with the vinyl moiety in the presence of platinum catalyst (e.g. Karstedt's catalyst, Fig. 5). In this case, it is essential for the PDMS to be equipped with either hydrosilane- or vinyl functional groups. The advantage of the hydrosilylation is that no side-products are formed unlike the condensation-based cross-linking where alcohols are produced.³⁸ Additionally, only a very small material shrinkage is observed with this preparation method during the curing process.³⁹ The cross-linking by hydrosilylation can be accelerated by UV-activation. As a

1. Introduction

result, the cross-linking is accomplished after a few minutes.⁴⁰ The thiol-ene addition is another UV-initiated reaction which has been exploited for the cross-linking of PDMS as the reaction occurs at high yields in a matter of minutes.^{41–44}

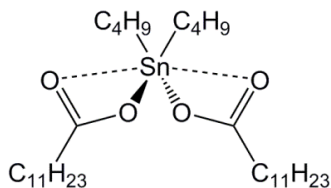


Fig. 4: Chemical structure of di-*n*-butyltin dilaureate DBTDL.³⁷

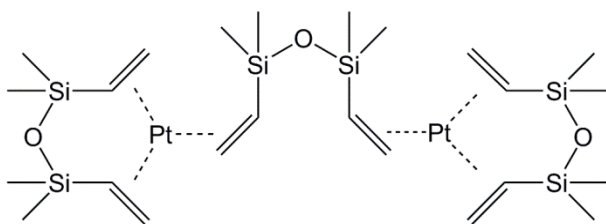


Fig. 5: Chemical structure of Karstedt's catalyst.³⁸

From a thermodynamic point of view, the cause of the elasticity in elastomers is the change in the Helmholtz free energy H of the system during deformation which is given by:

$$dH = dU - TdS \quad (\text{Eq. 4})$$

1. Introduction

Eq. 4 shows that H consists of two contributions: The internal energy U and the entropic term TdS . The force acting during the deformation is given by the derivative of H over the deformation length l .

$$F = \frac{\partial H}{\partial l} \quad (\text{Eq. 5})$$

The deformation of the elastomer leads to an ordering of the polymer chains by causing their alignment along the direction of the deformation. The elastomeric behavior is dominated by the entropic contribution in H as the change in entropy is larger than the change in the internal energy.⁴⁵ The return of the elastomer into its original state upon release from external forces is attributed to the system's objective to maximize its entropy. The calculation of the entropy change of the system ΔS has been conducted in previous works and will be briefly summarized in the following paragraph.^{46–49} The change of the entropy ΔS of the elastomer system is given as

$$\Delta S = -\frac{Nk_B}{2}(\lambda^2 + \frac{2}{\lambda^2} - 3) \quad (\text{Eq. 6})$$

where k_B is the Boltzmann constant, N the number of the polymer chains within the network and λ the relative change in the length of the elastomer as a result of the deformation. The deformation of the elastomer by applying an external force induces a mechanical stress. The mechanical stress σ is defined as the ratio between the applied force F over a cross sectional area A .

1. Introduction

$$\sigma = \frac{F}{A} \quad (\text{Eq. 7})$$

The combination of Eq. 6 and Eq. 7 leads to the following expression:

$$\sigma = \frac{nk_B T}{V} \left(\lambda - \frac{1}{\lambda} \right) = \gamma k_B T \left(\lambda - \frac{1}{\lambda} \right) \quad (\text{Eq. 8})$$

Here, the quantity n/V defines the network density γ . The correlation between γ and Y can be obtained by using the relationship of the shear modulus G with Y given as

$$Y = 2G(1 + \nu) \quad (\text{Eq. 9})$$

where $\nu = 0.5$ for incompressible materials thus giving rise to $Y = 3G$. With the expression $k_B T \gamma = G$, the expression for Y is given by

$$Y = 3k_B T \gamma \quad (\text{Eq. 10})$$

In an ideal elastomer, the polymer chains are interconnected by cross-linker molecules, and the mechanical properties can be tuned by the cross-linking density γ and the temperature T as depicted in Eq. 10. However, the real scenario is much more complex as structural defects are present within the entire network and are responsible for non-equilibrium mechanical properties of the network which manifests itself in the viscoelastic behavior of the elastomer.⁵⁰ Examples for such structural defects are the presence of dangling and

1. Introduction

unattached polymer chains as well as the entanglement of individual polymer chains thus giving rise to branched structures (Fig. 6). Both the dangling and branching of polymer chains are responsible for the extremely slow relaxation of the elastomer into its undeformed state. In the meanwhile, the effect of the unattached chains on the mechanical properties of the elastomer is more pronounced with increasing molecular weight.⁵⁰

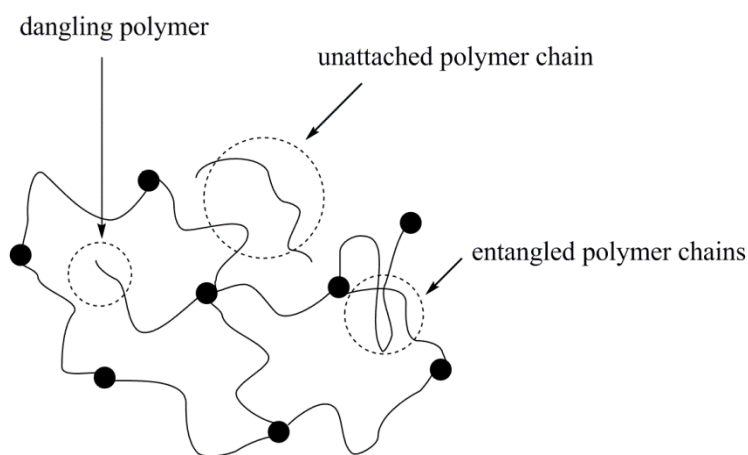


Fig. 6: Schematic illustration of a real polymer network. The present structural defects are encircled.

In conclusion, the prediction of the mechanical properties of elastomers is quite difficult as the presence of structural defects have the ability to influence the mechanical properties in a more or less pronounced way depending on their chemical structure. Therefore, knowledge on the chemical information of the system is essential in order to find arguments explaining the obtained mechanical parameters and their potential deviation from the predicted values observed in ideal elastomers which neglect the influence of structural defects.

1. Introduction

1.3 Dielectric Properties of Materials

Dielectric materials are electrical insulators which can be polarized by an external electric field. They are generally applied in capacitors which are devices used for energy storage. In the capacitor, the dielectric material is sandwiched by two opposing conductive plates. When a capacitor is subjected to an external field by the application of a voltage, opposite charges are built up in the area covered by the two opposing conductive plates due to the field-induced polarization and subsequent charge separation within the dielectric. This phenomenon gives rise to an internal electric field acting in the opposite direction. The resulting charge density φ which is found in the area A covered by the conductive plates with opposing charges Q is given by the expression

$$\varphi = \frac{Q}{A} \quad (\text{Eq. 11})$$

while the external electric field E induced by the applied voltage U is given by

$$E = \frac{U}{d} \quad (\text{Eq. 12})$$

where d is the distance between the plates. The amount of accumulated charges on the capacitor plates is proportional to the applied voltage and the capacitance C of the dielectric material. As a result, C is also detrimental for the total energy W_{el} stored in the capacitor device. This gives rise to the two following expressions:

$$Q = CU \quad (\text{Eq. 13})$$

1. Introduction

$$W_{el} = \frac{Q^2}{2C} = \frac{1}{2}CU^2 \quad (\text{Eq. 14})$$

The permittivity is a parameter which indicates the ability of a material to store electrical charge for a given volume.³⁵ The permittivity ε is a complex number and is given by

$$\varepsilon = \varepsilon' - i\varepsilon'' \quad (\text{Eq. 15})$$

where ε_r' and ε_r'' are the real and imaginary parts of the permittivity. In an alternating electric field, both ε' and ε'' depend on the angular frequency $\omega = 2\pi f$ (f being the ordinary frequency) of the oscillating electric field as the mobility of the charge carriers in the material responds to changes in the applied electric field.⁵¹ As a result, ε can also be written as

$$\varepsilon(\omega) = \varepsilon'(\omega) - i\varepsilon''(\omega) \quad (\text{Eq. 16})$$

The two parts of the complex permittivity i.e. ε' and ε'' can be used to define the dissipative energy losses of the dielectric system.⁵² For instance, the tangents of the loss angle ($\tan \delta$) can be calculated as

$$\tan \delta = \frac{\varepsilon''}{\varepsilon'} \quad (\text{Eq. 17})$$

1. Introduction

while the dielectric conductivity is given by

$$\sigma = \omega \varepsilon'' \quad (\text{Eq. 18})$$

Generally, it is a convention to use $\tan \delta$, ε'' and σ as parameters which describe the conductive and dissipative energy loss of a material. Therefore, they have to be kept as low as possible for DEs. The relative permittivity ε_r (or dielectric constant) describes the change of the electric field within the material compared to vacuum. This property is given as a dimensionless number and can be obtained from the permittivity ε by the expression below.⁵²

$$\varepsilon_r = \frac{\varepsilon}{\varepsilon_0} = \varepsilon_r' - i\varepsilon_r'' \quad (\text{Eq. 19})$$

The relative permittivity ε_r is an essential parameter to quantify the ability of materials to serve as a dielectric in capacitors for energy storage. From this point on, we will simply refer to ε_r as “permittivity” or dielectric constant.

The relationship between the permittivity and capacitance is given by

$$\varepsilon_r = \frac{C}{C_0} \quad (\text{Eq. 20})$$

1. Introduction

where C_0 is the capacitance of the capacitor in vacuum.³⁵ Besides ϵ_r , the geometry of the capacitor is important to determine the capacitance. Considering the geometry of a parallel plate capacitor, the capacitance of the material is given by:

$$C = \frac{\epsilon_r \epsilon_0 A}{d} \quad (\text{Eq. 21})$$

The performance of dielectric materials is limited by failure mechanisms which can be classified into the following categories: thermal, mechanical and electric breakdown.⁵³ The electrical breakdown is a failure mechanism in capacitors which leads to the destruction of the insulating capability of the material through the resulting formation of conducting pathways. Each dielectric material features an electrical breakdown strength which is normally given by the breakdown electric field E_B or by the corresponding voltage U_B . In DEAs, the electric breakdown causes the failure of the device prior to reaching the mechanical limits of the materials. In polymers, the electric breakdown is dependent on their initial physico-chemical properties as well as on inhomogeneities and defects within the material which can cause secondary breakdown mechanisms.⁵⁴ In order to increase the life-time of devices, the modification and improvement of current materials have been essential measures undertaken by various research groups. In DEAs, improvements in the breakdown strength of the devices include the pre-stretching of the actuator films,^{26,55,56} the use of self-clearing electrodes^{29,57} and by exploiting the effects of dielectric oil encapsulation.^{58–60}

1.4. Polarization Mechanisms in Molecular Structures

As stated earlier, the external electric field is responsible for the polarization of charges within the elastomer. The permittivity of a material is dependent on the polarization P of the material which can be described by the following equation (see next page):⁵¹

1. Introduction

$$P = (\varepsilon - 1)\varepsilon_0 E \quad (\text{Eq. 22})$$

Principally, there are four polarization mechanisms that can be induced within a material by the application of an electric field. They are known as (1) electronic, (2) atomic, (3) interfacial, and (4) orientation polarization.³⁵ The first two mechanisms are found in all materials and involve the displacement of electrons relative to the nucleus of the atoms and the separation of atomic nuclei from each other, respectively. The third mechanism has to be taken into account for inhomogenous materials (e.g. polymer blends) while the fourth mechanism occurs in polar molecules with a permanent dipole moment μ and lead to a net orientation of the dipole along with the field. Permanent dipoles are present if the gravitational centers of positive and negative charges do not overlap within a molecule. The net orientation vanishes again in the absence of the external electric field. The Polarization P can be given by summing up the dipole moments within a given volume V as shown by Eq. 23.

$$P = \frac{1}{V} \sum \mu_i \quad (\text{Eq. 23})$$

The polarizability α of an atom/molecule is the sum over all three polarization contributions.³⁵

The scalar quantity α of an atom/molecule is directly correlated to the permittivity and is defined by the Clausius-Mossotti equation as

$$\frac{N\alpha}{3\varepsilon_0} = \frac{(\varepsilon_r - 1)}{(\varepsilon_r + 2)} \quad \text{or} \quad \frac{N_A \alpha}{3\varepsilon_0} = \frac{(\varepsilon_r - 1)M_w}{(\varepsilon_r + 2)\rho} \quad (\text{Eq. 24})$$

1. Introduction

where N is the number of atoms or molecules *per* volume. The Clausius-Mossotti can also be written as a function of the molecular weight M_w and density ρ of the material to obtain the expression $N_A \alpha / 3\epsilon_0$ which is also known as molar polarization. However, this equation assumes the dielectric to be perfect, homogenous and isotropic and is only valid for nonpolar or weakly polar dielectric materials in the absence of permanent dipoles.^{35,61} In the case of polar molecules, the effect of orientation polarization has to be considered and the term becomes

$$\frac{N}{3\epsilon_0} \left(\alpha + \frac{\mu^2}{3k_B T} \right) = \frac{(\epsilon_r - 1)}{(\epsilon_r + 2)} \quad (\text{Eq. 25})$$

where μ is the permanent dipole moment, k_B the Boltzmann factor and T the temperature.⁵¹ The equation is also well-known as the Debye formula. It has to be noted that the Debye formula is generally accepted for the treatment of dielectric gases. However, it assumes that dipoles do not interact and influence each other thus neglecting those shielding effects also known as internal reaction fields, which is only an accurate approximation for very dilute systems. The Clausius-Mossotti and Debye formula are based on Lorentz's treatment of the problem where he considered a spherical cavity with polarization P in an infinitely extended media.⁶² In their theory, the orientation polarization is caused by a local electric field given as $E_{Loc} = E + \frac{1}{3} \left(\frac{P}{\epsilon_0} \right)$.⁵¹ Onsager took the interactions of the dipoles with each other into account and defined the theory of reaction field where the polarization of the environment contributes to the enhancement of the permanent dipole moment of a molecule.⁶³ Considering the same model used by Lorentz, the overall dipole moment m of the molecule can be described by $m = \mu + \alpha E_{Loc}$. The contribution of the orientation polarization to the dielectric function will be given by (see next page)

1. Introduction

$$\Delta\varepsilon = \varepsilon_S - \varepsilon_\infty = \frac{1}{3\varepsilon_0} F \frac{\mu^2}{k_B T} \frac{N}{V} \quad (\text{Eq. 26})$$

where

$$F = \frac{\varepsilon_S(\varepsilon_\infty + 2)^2}{3(2\varepsilon_S + \varepsilon_\infty)} \quad (\text{Eq. 27})$$

The quantity (N/V) defines the density volume of dipoles and $\Delta\varepsilon$ is the dielectric strength/intensity arising from the orientation polarization with $\varepsilon_S = \lim_{\omega \rightarrow 0} \varepsilon'(\omega)$ and $\varepsilon_\infty = \lim_{\omega \rightarrow \infty} \varepsilon'(\omega)$.⁵¹ The Onsager formula holds for the treatment of non-associating, polar liquids. However, it fails for associating liquids and a correlation factor g , also known as the Kirkwood-Fröhlich correlation factor, has to be introduced into the equation to give

$$\varepsilon_S - \varepsilon_\infty = \frac{1}{3\varepsilon_0} F g \frac{\mu^2}{k_B T} \frac{N}{V} \quad (\text{Eq. 28})$$

where

$$g = \frac{\langle \sum_i \mu_i \sum_j \mu_j \rangle}{N \mu^2} = \frac{\mu_{int}^2}{\mu^2} \quad (\text{Eq. 29})$$

and μ^2 gives the mean square dipole moment of non-interacting, isolated dipoles.^{64–66} Depending on the orientation of the molecules to each other, g can obtain values below or above 1. To further simplify the problem, Kirkwood and Fröhlich considered a region with N^* molecules and treated them while considering the remaining $N - N^*$ molecules as infinite continuum with ε_s characterizing their dielectric behavior.^{51,67}

1. Introduction

As a result, g can be written as

$$g = \frac{\langle \sum_{i=1}^{N^*} \sum_{i < j} \mu_i \mu_j \rangle}{N \mu^2} + 1 \quad (\text{Eq. 30})$$

A good statistical approximation requires N^* to be chosen as high as possible.

1.5. Enhancing the Permittivity of Elastomers

After mentioning potential difficulties and disadvantages associated with the strategies involving the reduction of the Young's modulus Y and the film thickness d (Fig. 1), the increase in the permittivity of the DE is the main guideline in this work in order to enhance their performance. Although existing elastomers exhibit good mechanical properties, their permittivity ϵ_r is rather low and offers room for further improvement (Tab. 1). The permittivity of the material can be enhanced by undertaking the following strategies:

- attaching permanent dipoles onto existing polymer structures

or

- dispersing high permittivity fillers into the polymeric matrix

1.5.1 Enhancing the Permittivity through Molecular Dipoles

As indicated by the Debye equation, an increase in the polarizability α and dipole moment of the compounds forming the DE consists is required in return for an enhancement in the permittivity. Eventually, this concept has defined the method of grafting polar substituents with permanent dipoles onto the backbone of existing, low permittivity polymers. Through the application of an external electric field, the randomly oriented dipoles on the polymer backbone will tend to align along the field direction. As a result, the polymers will experience strain and dimensional changes are produced Fig. 7. This feature makes “polar silicones” suitable materials as membranes for DEAs. Silicones, have been outstanding candidates for this approach due to their initial asset of having tunable mechanical properties through chemical modification steps and their ability to undergo chemical modification. The modifications of the silicone backbone generally requires the presence of vinyl groups in order to graft substituents which involves Pt-catalyzed hydrosilylation reactions.^{68–70} Other modification reactions were conducted with the thiol-ene⁴⁴ or click chemistry.⁷¹ As shown in Tab. 1, fluorosilicones exhibit higher permittivities than the unmodified PDMS. The observation of the higher permittivity for fluorosilicones has been attributed to the asymmetric charge distribution in the molecule due to the high electronegativity of the fluorine atom.²⁷ Kussmaul *et al.* reported the successful introduction of organic dipole molecules into the backbone of silicone (Fig. 8 and Fig. 9).^{72,73} Effectively, the variation of the dipole content to 13.4 wt% led to an increase in the permittivity of the elastomers from 3 to 5.98, while the Young’s modulus decreased from 1900 to 550 kPa as both the PDMS chain and the dipole molecule compete for the reaction with the cross-linker. This affected the network density and featured the decrease in the gel content of the compound.

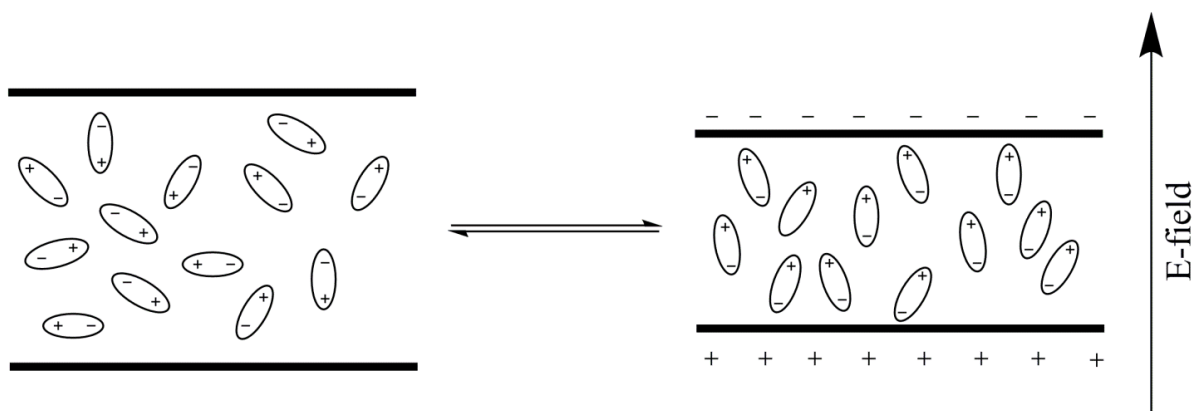


Fig. 7: Schematic illustration of randomly oriented dipole molecules (left) and their realignment towards the direction of the applied electric field (right) in a DEA.⁴⁴

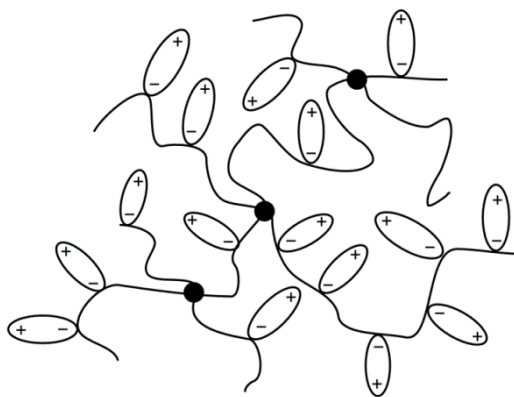


Fig. 8: Polymer network of PDMS with dipoles grafted onto the polymer backbone.

1. Introduction

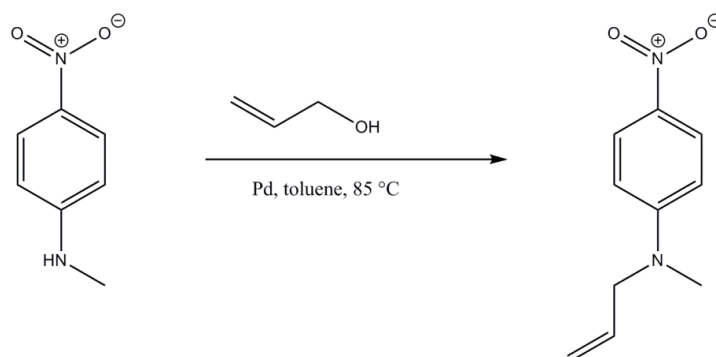


Fig. 9: Dipole molecule with vinyl functionality enabling the grafting onto PDMS.⁷³

Aside from grafting organic dipole molecules, functional groups such as chlorine and cyanopropyl groups can also serve as dipoles within the PDMS network. Madsen *et al.* reported the preparation of alkyl-chlorine siloxane copolymers which featured an increase in the permittivity compared to PDMS as well as low dielectric losses (< 0.001 at 100 Hz).⁷⁴ The alkyl-chlorine units are separated by dimethylsiloxane spacer units with different chain lengths. Despite the variation of the content of chloropropyl side-chains, the maximum permittivity observed just amounted to 4.7, which is still relatively low considering the permittivity of the reference PDMS in this study to be at 3.3. In comparison, the introduction of cyanopropyl groups has led to a larger increase in the permittivity of silicone. Racles *et al.* reported the preparation of silicones with tunable amounts of cyanopropyl side groups.³² This involves the preparation of the functionalized silicones through three (3) different methods involving cationic and anionic ring opening as well as copolymerization reactions. The grafting of the cyanopropyl groups onto the silicone was also conducted with the Pt-catalyzed hydrosilylation reaction as Si-H bonds are present in both the cycles and polymer backbone. The obtained copolymers with cyanopropyl functionalities featured an increase in the permittivity from 2.4 to 6.5 by tuning the number of repeating units equipped with cyanopropyl groups from 0 to 23 % in relation to the total polymer repeating units. Furthermore, the reduction of the amount of cross-linker led to the formation of materials with a lower Y compared to commercial PDMS although the strain at break was lower for the modified material. Further

1. Introduction

investigations in this subject provided PDMS modified up to 89 mol% with cyanopropyl groups exhibiting a permittivity of 15.9 at 10 kHz.⁶⁹ More recently, Dünki *et al.* have achieved the preparation of cyanopropyl-modified silicones by exploiting the thiol-ene addition reaction. The modified elastomers gave rise to good electromechanical properties by featuring a high permittivity (~ 10 at 10 kHz), a low Y (0.15 kPa) and a strain at failure amounting to 260 %.⁴⁴

1.5.2 Enhancing the Permittivity with the Introduction of High Permittivity Filler

The other approach is based on the blending of high permittivity materials into a relatively low permittivity polymeric matrix. The blending of fillers showed significant changes in the electromechanical properties of the resulting composites. Different theoretical approaches to calculate the resulting permittivity values of mixtures have been made, including the volume-fraction average, the Maxwell-Garnett as well as the Bruggemann model. Those theoretical approaches to estimate the permittivity assumed simplified geometry and structure within the material in order to obtain models which can predict the permittivity values for the resulting composites. The effective permittivity ε_{eff} of the composite can be calculated by the volume-fraction average approach as

$$\varepsilon_{\text{eff}} = \theta_1 \varepsilon_1 + \theta_2 \varepsilon_2 \quad (\text{Eq. 31})$$

where ε_1 and ε_2 are the permittivities of the matrix and filler and θ_1 and θ_2 are the respective volume fractions of the components. A linear increase in ε_{eff} with increasing filler content is described by this model which, however, is not supported by conducted

1. Introduction

experiments.^{75,76} However, the results from the volume-fraction average can still be used as an upper limit for ε_{eff} .

The mean-field theory gives rise to more realistic models to describe the resulting permittivity of a binary mixture. The Maxwell-Garnett equation was obtained from the Clausius-Mossotti formula where the macroscopic permittivity ε and the polarizability α are interconnected.⁷⁷ This model assumes the scenario of a spherical inclusions being surrounded by a continuous matrix consisting of polymer. The composite permittivity ε_{eff} can be calculated by:

$$\frac{\varepsilon_{\text{eff}} - \varepsilon_1}{\varepsilon_{\text{eff}} + 2\varepsilon_1} = \theta_2 \frac{\varepsilon_2 - \varepsilon_1}{\varepsilon_2 + 2\varepsilon_1} \quad (\text{Eq. 32})$$

However, the Maxwell-Garnett equation only finds validity if the filler fraction approaches the conditions of infinite dilution ($\theta_2 \rightarrow 0$) and multiple interactions between the spherical inclusions are neglected.^{78,79} Therefore the Maxwell-Garnett equation gives out values which could serve as lower limit of the composite permittivity. The Bruggeman model, which is also based on the mean field theory, describes the composition of the mixture as repeating unit cells consisting of spherical inclusions surrounded by the polymer matrix. In other words, the inclusions and their environment are treated symmetrically. The effective permittivity becomes

$$\theta_1 \left(\frac{\varepsilon_1 - \varepsilon_{\text{eff}}}{\varepsilon_1 + 2\varepsilon_{\text{eff}}} \right) + \theta_2 \left(\frac{\varepsilon_2 - \varepsilon_{\text{eff}}}{\varepsilon_2 + 2\varepsilon_{\text{eff}}} \right) = 0 \quad (\text{Eq. 33})$$

1. Introduction

The model predicts the sharp increase of ε_{eff} at a filler content of around 20 vol% and above which is the region of the percolation threshold which has been mentioned by various reports dealing with the dispersion of high permittivity filler into a polymeric matrix.^{80,81} There are also existing models for the prediction of the composite permittivity of complex structures.

For three-phase systems (e.g. core-shell type inclusions), Sihvola proposed the calculation of ε_{eff} by

$$\frac{\varepsilon_{\text{eff}} - \varepsilon_1}{\varepsilon_{\text{eff}} + 2\varepsilon_1} = (\theta_2 + \theta_3) \frac{\theta_2(\varepsilon_2 - \varepsilon_1) + \theta_2 t_{12}(\varepsilon_3 - \varepsilon_1)}{\theta_2(\varepsilon_2 + 2\varepsilon_1) + \theta_2 t_{12}(\varepsilon_3 + 2\varepsilon_1)} \quad (\text{Eq. 34})$$

where $t_{12} = \frac{3\varepsilon_2}{\varepsilon_3 + 2\varepsilon_2}$. The subscripts 1, 2 and 3 in this equation refer here to the matrix and the two different filler components, respectively. The formula is useful to treat composites using fillers with layered compositions such as core-shell particles.

So far, the models for the composite permittivity describe the behavior of spherical fillers. However, fillers which feature a deviation from the spherical shape lead to a different behavior in the resulting composite permittivity. Furthermore, their alignment within the material under the influence of an external electric field also has an impact on the composite permittivity.⁸² Overall, reports have shown that non-spherical filler with high aspect ratio lead to a higher increase in ε_{eff} compared to the use of spherical inclusions.⁶

The dispersion of filler into the polymeric matrix also influences the mechanical properties of the resulting nanocomposites. In most cases, the Young's modulus Y of the filler exceeds that of the matrix by orders of magnitude which leads to a deterioration of the mechanical properties with increasing filler content, although there are a few reports on the filler-induced increase of the composite permittivity without increasing Y as a result of

1. Introduction

using softeners as additives.^{83,84} The increase in Y is a major drawback of this approach compared to the chemical modification of polymers with dipole molecules. However, higher values for ϵ_{eff} are feasible, a fact which is the main asset of this method. The estimation of the resulting Y of a binary mixture can be calculated by adding the two different moduli according to their volume fraction assuming the arrangement of stacks between the two components and their equal subjection to the applied force acting in stack direction.^{85,86} The resulting composite modulus Y_{eff} can be calculated as

$$Y_{\text{eff}} = \theta_2 Y_2 + (1 - \theta_2) Y_1 \quad (\text{Eq. 35})$$

where Y_1 and Y_2 are the Young's moduli of the matrix and filler, respectively, and θ_2 is the volume content of the filler. This equation, however, gives values for Y_{eff} exceeding that of the actual composite at different filler content and can therefore be regarded as an upper limit for the calculation of Y_{eff} .^{86,87} In contrary, the orthogonal mixing rule assumes the perpendicular arrangement of the assumed stacking formation towards the applied force and Y_{eff} can be calculated by:

$$\frac{1}{Y_{\text{eff}}} = \frac{\theta_2}{Y_2} + \frac{(1-\theta_2)}{Y_1} \quad (\text{Eq. 36})$$

The orthogonal mixing rule gives out values corresponding to the lower limit of Y_{eff} with varying filler content. Further models that provide a more detailed and realistic estimation of the development of the composite modulus with varying filler content are featured in the report published by Bigg.⁸⁸ It was eventually determined that the polymer-filler interaction

1. Introduction

is decisive for the determination of the composite tensile strengths. The reinforcement of the materials through the use of filler is a direct result of a good adhesion of the polymer matrix to the inorganic filler which can be improved through the chemical modification of both the filler and the polymer.

Throughout the years, numerous reports on nanocomposites with high permittivities have emerged. A wide variety of composite materials have been prepared and investigated, including phthalocyanine/polymer composites,⁸⁹ ferroelectric ceramic/polymer composite,^{90–94} as well as conductive particle/polymer composites.^{80,95–98} Apart from PDMS, other polymeric matrices such as epoxy resin and poly(vinylidene difluoride)(PVDF) (Tab. 2) have been used for the preparation of high permittivity composites. Epoxy resin is commonly used in high voltage applications as insulating material and features good electrical and chemical properties as well as chemical stability.⁹⁹ PVDF belongs to the class of ferroelectric polymers which exhibit a permanent electric polarization as a result of their non-centrosymmetric structure. Upon application of an electric field, the dipoles of PVDF will align along the field direction and can be maintained even in the absence of the electric field.^{20,27} The main motivation for the use of PVDF as polymeric matrix lies in the ability of producing large ϵ_{eff} values as a result of the combination of the high permittivity of both the matrix and the filler.¹⁰⁰ However, PVDF is relatively stiff and is incapable of undergoing large strains as PDMS thus limiting its possibility of being used for the production of flexible composites.²⁰ Therefore, the use of PDMS as matrix is attributed to their tunable mechanical properties. Despite the ability to obtain high permittivity values, the use of certain fillers exhibited some drawbacks in their application. Phthalocyanines have been praised for their high permittivity values, but thorough investigations have proven that the large ϵ_{eff} values are not a direct result of their intrinsic features but due to observed proton conductivity in the presence of water.¹⁰¹ Ceramic powders such as BaTiO₃ and TiO₂ feature permittivity values of 1'700 and 80, respectively.¹⁰² As a result, BaTiO₃ is very attractive for the preparation of high permittivity composites. However, a large amount of ceramic filler is required to reach a substantial increase in the ϵ_{eff} , which eventually leads to a deterioration of the mechanical

1. Introduction

properties. By producing composites using ceramic BaTiO₃ as filler with a content $f \geq 0.5$, the material becomes increasingly brittle and breaks easily. For instance, a BaTiO₃/epoxy composite using 70 vol% of filler only led to an ϵ_{eff} of 60, not particularly high considering the very high filler loading.⁹⁰ Even the resulting composites with PVDF only gave moderate increases in the composite permittivity.¹⁰³ As a result, ceramics are unattractive as filler for the preparation of films where, apart from the increase of the permittivity, good mechanical properties such as a high degree of elasticity is desired.⁹² In particular, the use of conductive filler seems to have good perspectives. Having an infinite permittivity, they can lead to a significant enhancement of the resulting composite permittivity. Higher permittivity values were achieved with the use of conductive filler compared to the values obtained by using ceramic fillers (Tab. 2).

Tab. 2: List of composites and their resulting dielectric properties at 1 kHz.

Composite	ϵ_{eff}	ϵ_m	vol% filler	$\tan \delta$	Ref.
PANI ^a /PDMS	6-7	2.3	31.7	0.146	[96]
PANI/PVDF	385	7-13	50.0	0.85	[97]
Ni/PVDF	400	10	20.0	-	[104]
Al/epoxy	$\sim 50^b$	6.22^b	50.0	$\sim 0.07^b$	[105]
GNP ^c /PDMS	11	3	0.43	~ 0.03	[106]
MWCNTs/PDMS	4.6	3.1	1.0	~ 0.004	[107]
MWCNTs/PVDF	~ 300	10	2.0	-	[108]
TiO ₂ /PDMS	8.1	~ 3	30.0	-	[94]
BaTiO ₃ /epoxy	60	3.1	70.0	0.06-0.07	[90]
BaTiO ₃ /PDMS	~ 6	~ 4	10.0	-	[109]
BaTiO ₃ /PVDF	~ 45	11	50.0	0.009	[103]

^a Encapsulated in poly(divinyl benzene); ^b Values obtained at 10 kHz; ^c Graphene Nanoplatelets.

1. Introduction

When using conductive filler, ϵ_{eff} increases linearly with the filler content until reaching the vicinity of the percolation threshold where a dramatic increase of the permittivity is usually observed. This behavior can be described by the power law given as

$$\epsilon_{\text{eff}} = \frac{\epsilon_{\text{mr}}}{(f_c - f)^q} \quad (\text{Eq. 37})$$

whereby ϵ_{eff} and ϵ_{mr} are the permittivity of the composite and of the polymer matrix respectively, f_c is the percolation threshold fraction, f is the volume fraction of the filler, and q is a scaling constant.¹¹⁰ Metal particles,^{80,91,95,104,105,111–116} metal oxide particles,¹¹⁷ carbon nanotubes (CNTs),^{107,118} graphene,^{106,119} and conductive polymers^{89,96,97} have already been used as conductive fillers and confirmed their ability to enhance ϵ_{eff} significantly. In particular, metal nanoparticles are interesting due to the feasibility of preparing them with defined sizes and shapes. A large number of publications on the synthesis of metal nanoparticles currently exist, which provides us with a large variety of methods to obtain and use them as high permittivity filler. The preparation of metal nanoparticles, together with further necessary steps to compatibilize them with the corresponding matrix, will be illustrated in the following subchapters.

1.6 Synthesis of Metal Nanoparticles

1.6.1 The Mechanisms Towards the Formation of Metal Nanoparticles

In general, nanomaterials are objects that have, depending on their structure, at least one of their dimensions in the nanometer scale (1-100 nm, Fig. 10). They exhibit an array of interesting properties which differ from the corresponding bulk properties. While most of the bulk properties remain constant, the properties of nanomaterials vary with their size,

1. Introduction

shape and surface structure.¹²⁰ Particularly, metal nanoparticles have attracted significant interest from research groups around the world due to their wide range of application fields which include electronics,^{121–123} biomedicine,^{124–129} catalysis^{130–133} and photovoltaics.^{134,135} As a result, the research on the preparation of metal nanoparticles has been intensified over the last decades, and it has since become an ultimate goal to develop synthesis methods which feature a control over the size and shape of nanomaterials. The preparation of nanomaterials can be conducted in the vapor-, liquid and solid-phase.¹³⁶ The preparation of nanomaterials can generally be divided into two fundamental approaches: (a) top-down and (b) bottom-up approach (Fig. 10). While the top-down approach involves the formation of nanostructures by breaking down large structures, the bottom-up method deals with the formation of the nanostructures through the assembly of atoms or molecules.¹²⁰ Basically, it is very difficult to generate nanoparticles of very small sizes with controlled shapes with the top-down approach. In contrary, the bottom-up approach is much more suitable for the size-and shape-controlled preparation of nanoparticles.¹³⁷ However, there are reported cases where both approaches have been able to produce high quality particles. For instance, Wang *et al.* reported the preparation of bismuth colloids with a size range of 100-600 nm using both approaches. In both cases, the particles were relatively monodisperse.¹³⁸ For the bottom-up approach, the formation of nanoparticles involves the stages of nucleation and growth. The formation of metallic nanoparticles requires the generation of reduced metal species, which can be generated through the reduction of metal salts or precursors. The nucleation process is essential for the preparation of nanoparticles with defined shape. This process involves the initiation of a discontinuous phase transformation by a metastable system e.g. a supersaturated solution. The whole process of particle formation involving the nucleation and growth steps is illustrated in Fig. 11 which is the model described by LaMer.¹³⁹ In the case of the preparation of metal nanoparticles *via* liquid phase chemistry, the supersaturated solution is generated by the increase in the concentration of metal atoms through the continuous reduction of their corresponding ionic species (Phase I). Nucleation can occur as soon as a minimum concentration of metal atoms C_{\min} is present in the solution (Phase II). Once a critical concentration of metal atoms has been reached, the atoms will separate out from

1. Introduction

the solution through the formation of metal atom clusters thus leading to the establishment of a new phase caused by the unstable supersaturated solution.¹²⁰ As soon as the concentration of metal atoms decreases below the minimum critical supersaturation level, the nucleation process is terminated and further generation of metal atoms leads to the growth of the nanocrystals into larger particles (Phase III).

Nucleation can occur through two different processes, namely homogenous or heterogeneous. The homogenous nucleation requires the *in situ* formation of seed particles thus enabling nucleation and growth to occur with the same chemical process in a one-pot reaction. At the other hand, the heterogeneous nucleation requires the addition of previously formed seeds into the reaction mixture. This step separates nucleation and growth into two different processes as the growth of the nanocrystals occurs through the addition of atoms on the preformed seeds.¹⁴⁰

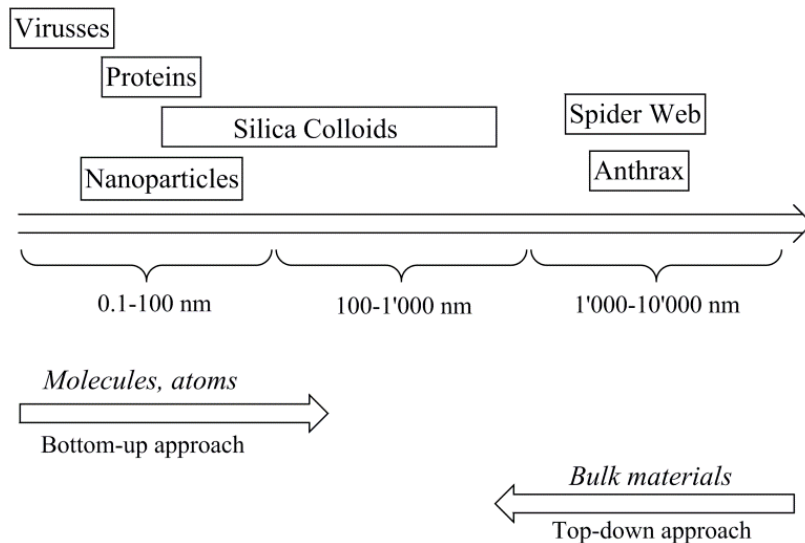


Fig. 10: Overview of typical dimension ranges of nanoparticles and colloids, together with some representative colloidal systems.¹⁴¹

1. Introduction

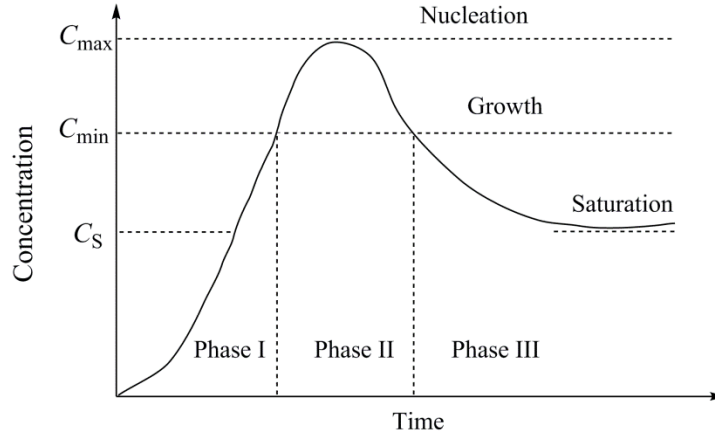


Fig. 11: LaMer model for the generation of nanocrystals involving the nucleation and growth stages.¹⁴⁰

The particle formation process involves changes in the free energy of the system which will be explained in this subchapter with detailed descriptions and corresponding equations.¹²⁰ The classical theory of nucleation states that the changes in the free energy of the system occurring in the homogenous nucleation process is given by

$$\Delta G_r = \Delta G_r^{Volume} + \Delta G_r^{Interface} \quad (\text{Eq. 38})$$

which can be written as

$$\begin{aligned} \Delta G_r &= \frac{4}{3}\pi r^3 \cdot \Delta G_v + 4\pi r^2 \gamma \\ &= -\frac{4}{3}\pi r^3 \cdot \frac{RT \ln S}{V_m} + 4\pi r^2 \gamma \end{aligned}$$

1. Introduction

where ΔG_r is the change in free energy per unit volume between atoms in solution and bulk crystal, γ is the surface free energy per unit area, R is the ideal gas constant, T the reaction temperature, r the radius of the spherical metal cluster, V_m is the molar volume of bulk crystal while S stands for the supersaturation ratio which gives the ratio between metal species in solution to that in the equilibrium saturation at the corresponding temperature. When $S > 1$, the solution is supersaturated and leads to negative values for ΔG_r . When plotting ΔG_r as a function of the radius r , a minimum within the curve is observed thus giving rise to two critical parameters, r_c and ΔG_c . Both parameters can be calculated by the following equations:

$$r_c = \frac{2\gamma V_m}{RT \ln S} \quad (\text{Eq. 39})$$

$$\Delta G_c = \frac{4\pi\gamma r_c^2}{3} \quad (\text{Eq. 40})$$

Metal clusters with a particle radius surpassing the critical radius r_c are thermodynamically stable and can undergo further growth through the continuous reduction of metal atoms. Basically, Eq. 38 and Eq. 39 show that the supersaturation level S directly influences r_c . A high value for S would lead to a decrease in r_c , which would facilitate the nucleation process as the reduction in r_c would enable small clusters to survive and experience further growth rather than undergoing dissolution. The surface energy γ can also be reduced through the attachment of surfactants or ligands in order to reduce r_c . A small r_c is essential for the preparation of monodisperse particles which also requires the clear separation of the nucleation and growth processes (Fig. 12). This requires the acceleration of the nucleation rate which can be conducted by reducing r_c , subsequently leading to a reduction in ΔG_c , and a high supersaturation ratio S .

1. Introduction

By upholding these conditions, the nucleation rate J is enhanced which is given by:

$$J = A \cdot \exp\left(-\frac{\Delta G_c}{RT}\right) \quad (\text{Eq. 41})$$

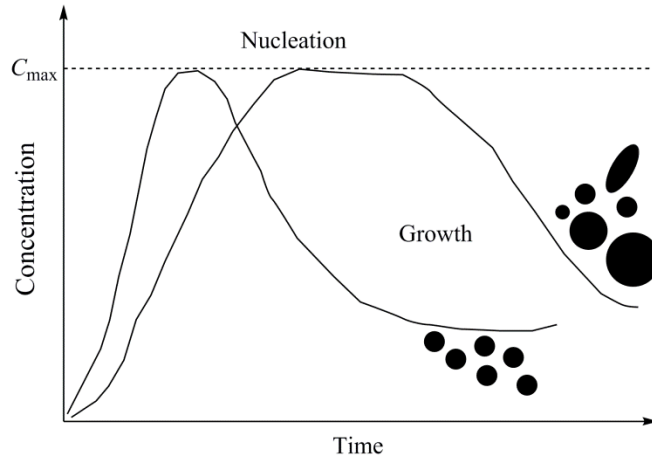


Fig. 12: LaMer model for the generation of nanocrystals involving the nucleation and growth stages. The product quality depending on the nucleation time is also depicted in the image.¹⁴⁰

Apart from ΔG_c , a high temperature T can also lead to an enhancement in the nucleation rate. Another method of initiating a rapid nucleation is through the application of the hot-injection method. The injection of the precursors into a hot solution induces a nucleation burst which leads to the growth of monodisperse nanocrystals. In comparison, the particles obtained from the slow addition of the precursor solution yielded a high polydispersity.¹⁴² This method is commonly used for the preparation of semiconductor quantum dots.^{143,144} To summarize, the particle quality depends on the ability to control the nucleation and growth phases. By reducing the nucleation time, both processes can be separated from each

1. Introduction

other. This can be achieved by manipulating reaction parameters and by the variation of the preparation method.

1.6.2 Preparation of Metal Nanoparticles: The Case of Silver

Metal nanoparticle dispersions consisting of gold, silver or copper feature intensive colors which vary with the corresponding size of the particles. As a matter of fact, these metal nanoparticles are known to undergo strong and specific interactions with the electromagnetic radiation when the particle size is much smaller than the wavelength of the incident light.^{145,146} This manifests itself in the observation of an intense and broad band absorption in the corresponding UV-vis spectra of the particle solution. The absorption band is referred to as surface plasmon resonance (SPR) which features the oscillation of the free conduction electrons under the generation of a dipole within the particle as a result of the interaction with the incident light (Fig. 13).¹⁴⁶ The discovery of SPR dates back to the 19th century which was documented by Michael Faraday.¹⁴⁷ When the frequency of the incident light corresponds to the frequency of the oscillation of the electrons, the resonance condition is satisfied and gives rise to the localized surface plasmon resonance (LSPR).

Plasmonics have attracted the attention of research groups working on photovoltaics due to their ability to improve the performance of photovoltaic devices which includes the enhancement in absorption and the potential of reducing the physical thickness of solar photovoltaic absorbers layers.¹³⁴ Quite recently, plasmonic polymer solar cells using metal nanoparticles achieved a power efficiency of 8.92 % and an external quantum efficiency of 81.5 %, which were the highest values obtained for such devices at that time.¹⁴⁸

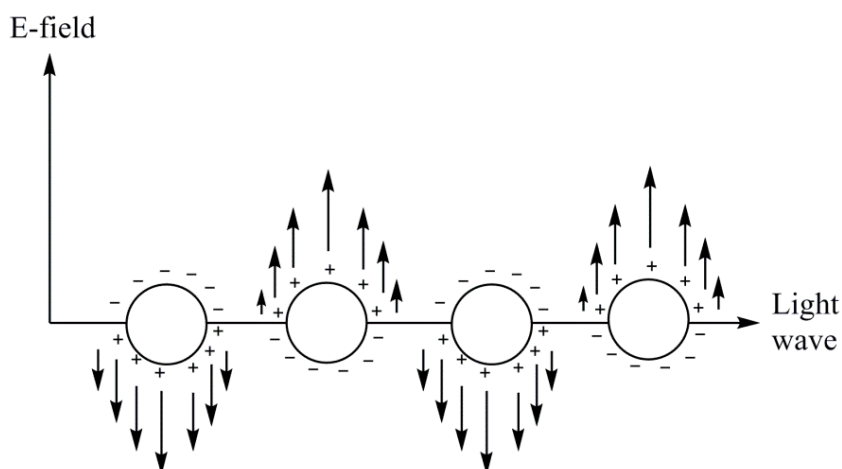


Fig. 13: Schematic illustration of surface plasmon resonance (SPR). The free conduction electrons in the metal nanoparticles undergo oscillation as a result of the strong interaction with the incident light.¹⁴⁶

There is no doubt that the potential of metal nanoparticles as an essential component in photovoltaics contributed immensely to the current research activity on metal nanoparticle preparation. In particular, silver exhibits the greatest band intensity.¹⁴⁵ Additionally, the cost of silver is cheaper than most of the other metals considered for plasmonic applications. The cost of silver amounts to ~ US\$ 472.6 per kilogram, which is much lower compared to the price of gold or platinum (US\$ 33'506 and US\$ 42'570 per kilogram, respectively). Although aluminum is a cheaper alternative to silver, it features certain drawbacks such as few feasible nanostructures as well as the susceptibility to surface oxidation thus requiring surface passivation for stabilization.¹⁴⁹ Apart from photovoltaics, silver nanostructures can also be used in other fields such as electronics,^{80,115,150} biomedicine¹²⁴⁻¹²⁶ and photocatalysis.^{133,151,152}

The preparation of silver nanostructures can be divided into the two following categories: (a) conventional and (b) unconventional methods.¹⁴⁵ The conventional method refers to the chemical synthesis of silver nanostructures, while the unconventional method is composed of a variety of preparation ways such as laser ablation, radiolysis, biosynthesis as well as vacuum evaporation. The following subchapter will only focus on a few methods involving

1. Introduction

the chemical synthesis of the silver nanostructures. The main route consists of the chemical reduction of silver salts such as AgNO_3 ,^{153–155} $\text{Ag}(\text{OAc})$,¹⁵⁶ AgClO_4 ^{157,158} or AgCO_2CF_3 ¹⁵⁹ into their metallic form.

1.6.2.1 Preparation of Silver Nanoparticles with Inorganic Reducing Agents

Favored by its high reactivity and low toxicity, sodium boron hydride (NaBH_4) is commonly used as reducing agent in Organic Chemistry. The first synthesis of AgNPs using sodium boron hydride was reported by Creighton and coworkers¹⁶⁰ which gave particles in the size range of 1-10 nm. Compared to other methods, this method can only give small particles as a result of the strong reducing power of the boron hydride.¹⁶¹

Hydrazine (N_2H_4) has also been used to generate AgNPs through the reduction of AgNO_3 . The reaction is conducted at room temperature using water as reaction medium. A basic pH (~ 11) is required for obtaining a stable solution. Particle sizes between 10-50 nm are feasible with this method, but it is difficult to control the size polydispersity.¹⁶² Another drawback is the toxic nature of hydrazine, making future industrial applications of this method very unlikely.

1.6.2.2 Preparation of Silver Nanoparticles with Organic Reducing Agents

N,N-dimethylformamide (DMF) is well known for its high synthetic value due to its wide liquid temperature range, chemical and thermal stability (boiling point at 153 °C), high polarity and wide solubility range for organic and inorganic compounds.¹⁶³ It has previously been reported that DMF can act as a powerful reductant to gold and silver salts.^{155,164} The first synthesis of AgNPs using DMF was pioneered by the group of Liz-Marzan in 1999.¹⁵⁵ It was shown that Ag^+ ions can be reduced at room temperature, with the possibility of increasing the reduction rate at higher temperature. Carbamic acid is formed during the course upon reduction of the silver ions to metallic silver, which can

1. Introduction

further decompose to carbon dioxide and dimethylamine at elevated temperatures (Fig. 14). The use of capping agents ought to ensure the long term stability of the silver dispersion. So far, stabilizers in form of 3-(aminopropyl)trimethoxysilane (APTMS), poly(vinyl pyrrolidinone), tetrabutoxytitanate and macrocyclic thiols have been employed.^{165–167} With this method, the synthesis of nanoparticles with a size range of 5-30 nm has been reported.

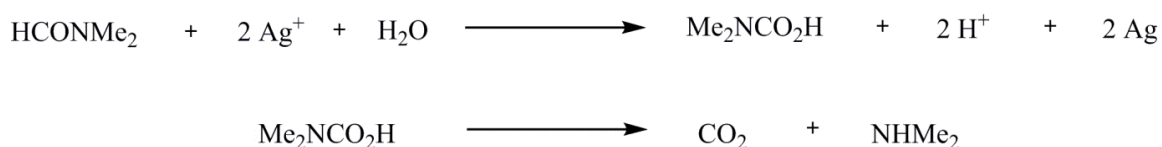


Fig. 14: Proposed reaction mechanism for the preparation of AgNPs with DMF.¹⁵⁵

The Tollens reaction, or silver mirror reaction, is famous for the chemical deposition of silver mirrors on various substrates as well as a suitable method to detect aldehydes.^{149,168} This method can also be applied for the synthesis of AgNPs.^{158,169} The advantage in this method lies in the mild preparative conditions as AgNPs are prepared at room temperature. Performed in aqueous medium, silver salts form the Tollens reagents, $\text{Ag}(\text{NH}_3)_2\text{OH}$, which is reduced by the sugar RCHO (Fig. 15).¹⁶⁹ With this method, nanoparticle sizes ranging from 20-100 nm have been prepared so far.^{158,170} Despite the limited shape control associated with this method,^{158,171} the use of triazole sugar ligands have featured improved control over the reaction with enhanced size and shape control.¹⁷²

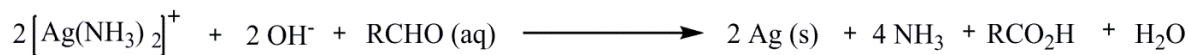


Fig. 15: Proposed reaction mechanism for the preparation of AgNPs with the Tollens reaction.¹⁴⁹

1. Introduction

In 2007, Hsu and coworkers reported the reduction of AgNO_3 with formaldehyde (CH_2O). In this method, organic bases such as triethylamine (TEA) and pyridine were used as reaction promoter.¹⁷³ The mechanism is shown in Fig. 16. While using TEA in the reaction afforded particle sizes between 20-30 nm, the particle sizes obtained with pyridine were smaller (10-20 nm) which can be explained by the weaker basicity of pyridine thus slowing down the reduction rate. High pH values favor the aggregation of primary particles which lead to the formation of larger particles. This effect was observed by Liu and coworkers as they succeeded in varying the particle size between 40-2'000 nm by adjusting the reaction conditions, including the pH, the reaction temperature as well as the amount of stabilizer.¹⁷⁴

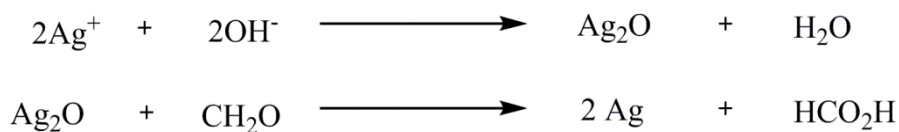


Fig. 16: Proposed reaction mechanism for the preparation of AgNPs through the reduction with formaldehyde.¹⁷⁵

The citrate synthesis, also known as Turkevich method, is a popular method to generate silver nanoparticles (AgNPs) and is still very commonly used due to its facile preparation manner. Back in 1951, Turkevich succeeded in preparing gold nanoparticles (AuNPs) through the reduction of chloroauric acid with sodium citrate in a boiling aqueous solution (Fig. 17).¹⁷⁶ The citrate ions simultaneously act as stabilizer and reducing agent. Since then, the method has also been extended to the preparation of AgNPs.¹⁷⁷ The outcome of the process mainly depends on the pH value of the solution since the reduction rate and the particle shape are influenced by this parameter. While high pH values favor the preparation of spherical and rod-like particles, low pH values lead to the formation of anisotropic shapes such as triangle and polygons.^{145,178} The formation of anisotropic nanowire

1. Introduction

structures has also been achieved with this method.¹⁷⁹ Overall, this method does not establish a defined control over the particle size and shape which effectively leads to the production of polydisperse particles (20-600 nm) with diverse shapes in a single batch reaction.¹⁴⁹ Another disadvantage of this method is the use of high amounts of water which makes the scale-up of the reaction a rather difficult task.¹⁸⁰



Fig. 17: Proposed reaction mechanism for the preparation of AgNPs with the Turkevich method.¹⁷⁹

Although a variety of methods for the preparation of AgNPs has been presented, most of the reactions suffer from drawbacks including toxicity, limited size and shape control and feasibility as well as high dilution conditions, with the latter causing problems for the upscaling of the synthesis. However, those limitations can be circumvented through the use of the polyol synthesis.

The polyol synthesis represents a very versatile way of generating silver nanostructures with varying sizes and morphologies.^{181,182} Extensive work on the polyol synthesis of silver nanostructures was conducted by the research group of Xia.^{181,182} The control over nucleation and growth process, which is crucial for the determination of quality and morphology of the resulting particles, can be achieved through varying reaction conditions such as temperature and concentration of reagents as well as the addition of additives and trace metal impurities.^{153,181–183} The type of seeds (formed from the growth of nuclei) present in the reaction mixture direct the future structure and morphology of the particles. The three different seeds structures which can grow into distinct morphologies of the silver nanostructures are classified as single crystal, singly- and multiply twinned seeds.¹⁸¹ In this process, a polyol (e.g. ethylene glycol (EG), propylene glycol (PG)) serves both as solvent and reductant while polymers such as poly(vinyl pyrrolidinone) (PVP),^{142,159,184,185} polyacrylamide¹⁸⁶ or polyacrylic acid (PAA)¹⁸⁷ act as stabilizing agent. The stabilizers can

1. Introduction

also direct the morphology of the nanostructures through preferential binding onto certain crystal facets. For instance, PVP is believed to undergo preferential binding to the {110} and {100} planes through the coordination of its carbonyl group onto the metal surface.¹⁴⁰ When the {111} planes are completely bounded by PVP, the deposition of metal atoms occurs on the {100} which leads to the formation of octahedrons. Considering the reverse scenario, the deposition will occur on the {111} site thus leading to the formation of nanocubes.¹⁸⁸ At elevated temperatures, glycoaldehyde, which is the actual reductant of the Ag^+ ions, is formed in the presence of oxygen (Fig. 18). The amount of glycoaldehyde is increased with increasing temperature thus affecting reduction kinetics.¹⁸⁹

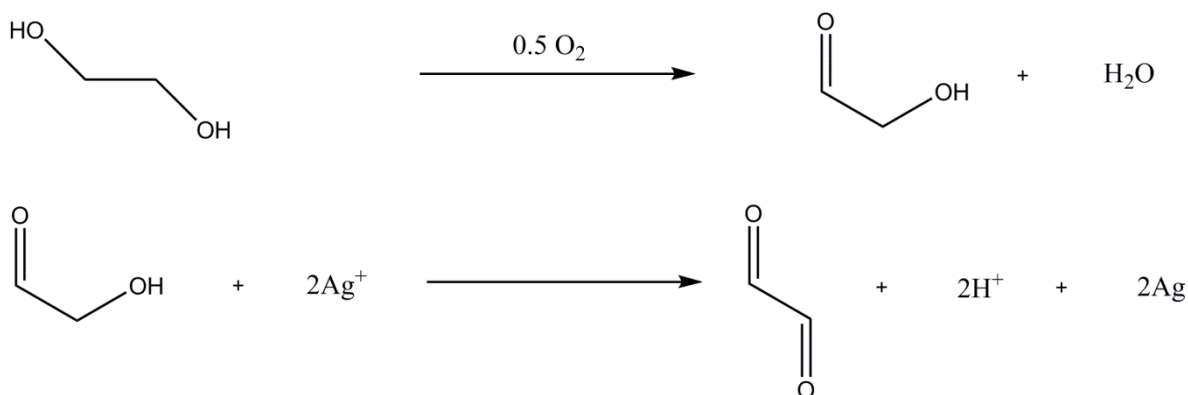


Fig. 18: Proposed reaction mechanism for the preparation of AgNPs by the polyol process.¹⁴⁹

So far, this method is regarded as the most convenient way of preparing different types of silver nanostructures. In summary, the polyol synthesis exhibits the possibility to control the size and shape of the particles through the careful variation of the reaction conditions (Fig. 19).^{142,182,190} Furthermore, it has also demonstrated the potential of upscaling the reaction by using continuous production methods.^{191,192} As a direct result, the polyol synthesis is quite attractive to prepare large amounts of silver nanostructures, a feature which makes this method stand out from the other methods.

1. Introduction

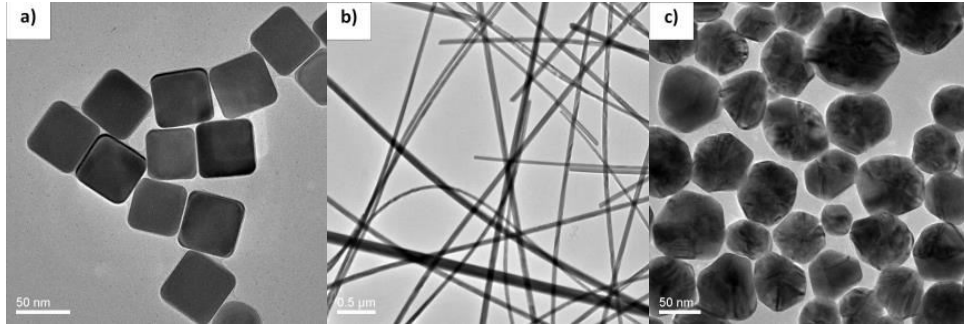


Fig. 19: TEM micrographs of different silver nanostructures: (a) Silver nanocubes (AgNCs), (b) silver nanowires (AgNWs) and (c) silver nanoparticles (AgNPs).

1.7 Surface Functionalization of Metal Nanoparticles

The surface functionalization of metal nanoparticles is often required to provide stability as well as compatibility of the resulting particles towards different media. In the case of the use of metal nanoparticles as conductive fillers for high permittivity materials, surface functionalization is essential due to the increasing dielectric loss and electrical conductivity at f_c where the insulator-conductor transition occurs thus diminishing the filler's prospect of being used for the preparation of high performance materials in spite of their high permittivities.^{80,81,104,193,194} At filler contents approaching f_c , the possibility of agglomerated particles forming a percolation pathways increases thus leading to electric shortcuts (Fig. 20).

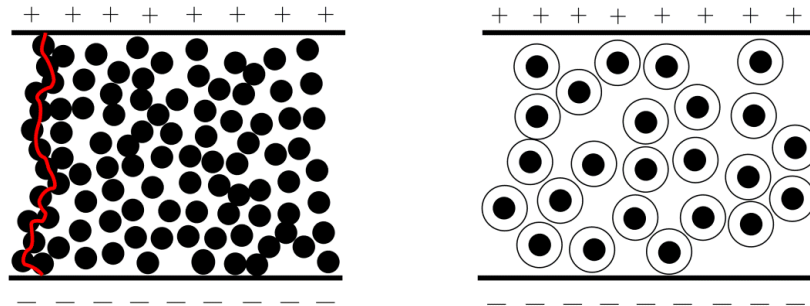


Fig. 20: Agglomeration of conductive particles within the polymeric matrix leading to percolation pathways (left) and insulated particles without agglomeration (right).⁹⁶

1. Introduction

In order to overcome these limitations and prevent electric shortcuts from occurring, the insulation of the particles prior to their dispersion into the matrix has become a common method to avoid electric breakdown due to agglomerated particles. For instance, Ni, Cu, and Al can undergo self-passivation in air which leads to the growth of an oxide shell on the surface.^{195–197} For noble metals, this process does not occur under ambient conditions due to their high reduction potential.¹⁹⁸ Therefore, additional materials need to serve as surface coating. In the case of AuNPs and AgNPs, it is possible to coat them with silica (SiO_2) with controllable shell thickness by using a modified Stöber method.^{170,199–203} Back in 1968, Stöber and coworkers reported the preparation of monodisperse SiO_2 colloids with varying sizes through the hydrolysis of tetraethoxysilane (TEOS) which was catalyzed by ammonia.²⁰⁴ Silica colloids prepared with this method are depicted in Fig. 21.

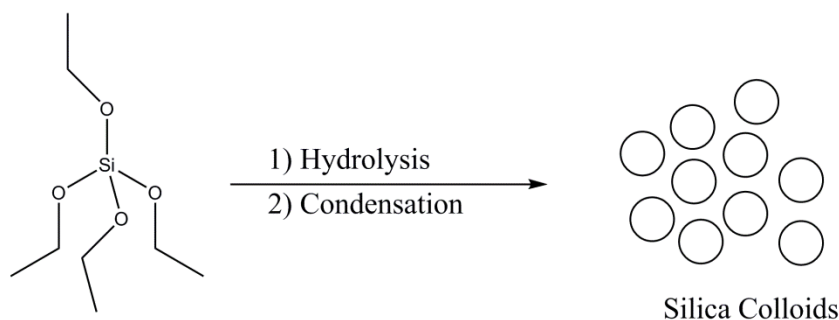


Fig. 21: Silica nanoparticles prepared with the Stöber method.²⁰⁴

Further research conducted over the years enabled this method to be extended to the coating of colloids and particles. For example, the main motivation to coat noble metal nanoparticles with SiO_2 , in particular Ag and Au, is the control over their plasmonic properties by stabilizing the dielectric environment of the metal core and by controlling the interparticle distance through the silica shell thickness.^{205–207} The SiO_2 shell also allows the deposition of other molecular structures such as quantum dots, dyes and

1. Introduction

biomolecules.^{208–211} The silica-coating of the metal nanoparticles has initially been conducted in the presence of surface coupling agents such as 3-(aminopropyl)trimethoxysilane (APTMS) or 16-mercaptohexadecanoic acid (MHA).^{212–214} However, the coating process could be performed directly on particles prepared via the polyol synthesis which was investigated by Graf *et al.*²¹⁵ Due to the alkaline conditions of the Stöber method, the enol tautomer of the PVP is predominant, and therefore the hydroxyl group serves as an anchoring group for the deposition of the hydrolyzed TEOS monomers which form the SiO₂ shell (Fig. 22).^{199,216} This coating-procedure has been demonstrated for various particle morphologies, including nanowires and nanoprisms.^{214,217} Metal colloids prepared by the Turkevich method could also be directly coated since the citrate ligand also serves as an interfacial layer essential for the growth of the SiO₂ shell.^{201,206,218} Various improvements in conducting the silica-coating have been reported throughout the years. The use of microwaves and the replacement of ammonia by other amine bases such as dimethylamine reduced the reaction time from hours to minutes and hindered the dissolution of Ag caused by the complexation with ammonia.²¹⁸ Furthermore, the one-pot synthesis of Ag@SiO₂ core-shell particles has been reported using micelle templates.^{213,219} The advantage of this method is the protection of the AgNPs from aggregation with the help of the micelles which provide stability, especially since particles below 50 nm are unstable and tend to agglomerate during the conventional Stöber method.^{204,220}

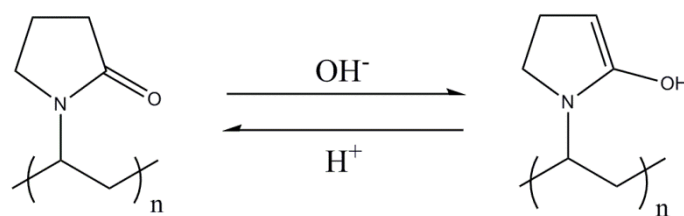


Fig. 22: Transformation of the PVP molecule to the enol conformation under basic conditions.²¹⁵

1. Introduction

Aside from silica, various other inorganic materials have also been used to coat metal colloids. The preparation of core-shell particles with titania (TiO_2) has also been a hot topic in the research community due to the possibility of combining the properties of the two moieties. TiO_2 is very attractive due to its chemical and thermal stability as well as its excellent electronic, optical and photocatalytic activity.^{221–223} Although numerous efforts on the preparation of Ag@TiO_2 core-shell particles exist,^{151,202,224–227} the obtained TiO_2 shells do not feature a well-defined uniformity and some of the reported synthesis routes are difficult to reproduce. While the Stöber method is used for the silica-coating, there are few existing reports on the preparation of TiO_2 shells using this method.²²⁸ In one of the few reports on the titania-coating with the Stöber method, the TiO_2 shells are produced through the hydrolysis and condensation of tetrabutyltitanate which was realized on the surface of Fe_2O_3 particles. In comparison to the silica-coating, the preparation of TiO_2 shells is quite difficult as the reaction kinetics of the hydrolysis/condensation of the titania precursor has to be controlled carefully in order to obtain core-shell structures with uniform TiO_2 shells.²²⁸

Other inorganic insulating shells which have also been demonstrated on metal cores include Al_2O_3 , Fe_3O_4 , $\text{Ni}(\text{OH})_2$, MnO , Eu_2O_3 , CdS , ZnS , ZnO and ZrO_2 .^{112,226,229–231}

While the insulation of metal nanoparticles has usually been achieved with inorganic materials, organic-based shell materials have also been successful in providing metal nanoparticles with an insulating layer. Shen and coworkers successfully insulated silver nanoparticles (AgNPs) with an organic shell and the produced Ag@C core-shell particles also featured a further advantage through the enhanced dispersibility in organic polymers. As a result, the organic shell facilitated the dispersion of the particles in order to form a homogenous composite. In direct comparison, surface treatment is generally required in order to enhance the compatibility of the core-shell particles with the matrix which is usually hydrophobic (e.g. PDMS). The shells could be tuned from 4-6 nm up to 8-10 nm. Qi and coworkers have used mercaptosuccinic acid (MSA) and dodecanoic acid (DDA) as a surfactant solution to prepare AgNPs which could be readily dispersed in epoxy in and

1. Introduction

form composites. Other routes to equip metal nanoparticles with a surrounding organic shell include the preparation of polymer-coated metal nanoparticles either through the grafting of the polymers onto the surface or by conducting a surface-initiated polymerization. The organic shell could be tuned from 2-50 nm although some of the reported polymer shells are hydrophilic in nature and therefore do not facilitate the dispersion in hydrophobic media.^{232–238} Further treatment such as the cross-linking of the polymer chains dangling around the particles can provide additional stability to the particles towards agglomeration, especially at high temperatures where polymer desorption from the surface can occur.²³⁹

1.8 Current State of Functionalized Metals/Polymer Nanocomposites

Metal fillers allowed a large increase in the permittivity ϵ_{eff} of the resulting composites with different polymer matrices (Tab. 2). As mentioned, metals such as Cu and Al obtain an insulating layer through self-passivation which disables the formation of a percolation pathway, even at high filler content. The passivating oxide layers are relatively thin and therefore the dispersion of the filler still leads to large permittivity values for the resulting composite.¹⁹⁷ However, the passivation does not seem to be a controlled reaction, and it is unclear whether further oxidation can occur with time which leads to the increase in the insulating layer. As a result, noble metal nanoparticles provide a better control which enables the precise control over the insulating shell surrounding them. In addition, noble metals offer the possibility of preparing different nanostructures, which can also be attractive for the investigation of the effects of the morphology on the composite properties. Silver nanostructures have already been used as filler for the preparation of high permittivity composites and gave high permittivity values upon reaching the percolation threshold. In the previous works involving the use of Ag as high permittivity filler, the main motivation for the preparation of the composites was their potential use as dielectrics/capacitors.^{1,80,114,240} The particles were insulated with various materials, including SiO₂, Al₂O₃ and carbonaceous shells as stated in the previous subchapter.

1. Introduction

Additional to the high permittivity values of the composites attributed to the use of Ag, the insulation of the particles also led to $\tan \delta$ values as low as 0.02 (Tab. 3). While thinner shells provided higher permittivities, the thicker shells led to an increase in the breakdown field E_B of the resulting composites.⁸¹ Ag was also used in the preparation of multiple-phase composites in order to yield a further increase in the permittivity ϵ_{eff} of the composite. This was observed by the addition of Ag@SiO₂ core-shell particles unto a BaTiO₃/PVDF composite as the permittivity increased by more than 20 times in the presence of 20 vol% of the core-shell particles.¹⁵⁰

The previous works involving the use of AgNPs as filler demonstrate the preparation of high permittivity composites and are an inspiration for further investigations on the potential of Ag particles as high permittivity filler.

Tab. 3: List of composites using Ag as filler and their corresponding dielectric properties at 1 kHz.

	ϵ_{eff}	ϵ_{m}	vol% Ag	$\tan \delta$	Ref.
AgNWs/TPU	16	~ 2	1.5	0.14	[240]
Ag@C/epoxy	300	$\sim 3^{90}$	20	0.04	[81]
Ag/epoxy	308	$\sim 3^{90}$	22	~ 0.03	[80]
Ag ^a @Al ₂ O ₃ /epoxy	410	$\sim 3^{90}$	30	~ 0.02	[112]
Ag@SiO ₂ /BaTiO ₃ /PVDF ^b	723	~ 30	20	~ 0.45	[150]
Ag ^a /epoxy	2'000	$\sim 3^{90}$	11.43	0.24	[1]
Ag/C/epoxy ^b	$\sim 2'400$	1600	4.2 ^c	0.98	[114]

^a Ag flakes; ^b Three-phase composite: The matrix permittivity ϵ_{m} refers to the value of the composite without Ag;

^c The amount of Ag is given in wt%

1.9 Goals of the Thesis

The goal of this project is to provide a model system for the preparation of silicone elastomer composites blended with functionalized AgNPs as fillers with potential use in actuators and generators. Tab. 3 shows a number of composites where Ag is used as filler, but a number of them do not feature a control over the particles size, morphology and surface properties. Furthermore, the reported nanocomposites generally neglect the corresponding mechanical properties. This work will try to address the mentioned issues, and therefore each step towards the preparation of the nanocomposites will be subjected to investigations. The initial part of this project consists of the preparation and functionalization of AgNPs. Since the preparation of nanocomposites requires substantial amounts of filler, a reliable method to prepare AgNPs in high amounts with control over size and shape will also be sought. The purpose of the surface functionalization of the AgNPs is to provide them with an insulating layer followed by the hydrophobization of the surface in order to enhance compatibility with PDMS, the latter being chosen as the polymeric matrix material due to the possibility of obtaining flexible materials with it. The insulating shell can be both of inorganic and organic nature. After the functionalization of the particles, they will be used as filler in order to prepare nanocomposites with enhanced dielectric and mechanical properties. The preparation of the nanocomposites and subsequent film-formation will be conducted with the doctor blade method to yield thin elastic films ($< 200\ \mu\text{m}$). Thereafter, the dielectric and mechanical properties of the resulting nanocomposites will be investigated by conducting mechanical tensile tests and by analyzing the dielectric properties via impedance spectroscopy in the range of $1\text{-}10^5\ \text{Hz}$.

1.10 Structure of the Thesis

Chapter 2 illustrates the attempts of preparing AgNPs of different sizes in a continuous fashion with the use of the Segmented Flow Tubular Reactor (SFTR) as an alternative

1. Introduction

route to the conventional preparation of AgNPs with batch reactions which has also been used in this work. The goal is to develop a reliable and reproducible method to prepare AgNPs in large amounts with a good control over the product quality (particle size, morphology, particle size distribution).

Chapter 3 deals with the investigation of the effects of the insulating silica (SiO_2) shell thickness on the resulting permittivity of the core-shell particles.

Chapter 4 shows the use of Ag@SiO_2 core-shell particles (hydrophobized through the surface treatment with alkyl silanes) as filler for the preparation of nanocomposites with PDMS. The investigation of the dielectric and mechanical properties of the resulting nanocomposites is the key topic of this chapter, and steps towards the optimization of the nanocomposite properties are featured.

Another alternative for the hydrophobization of the Ag@SiO_2 core-shell particles is shown in Chapter 5. Here, the Ag@SiO_2 core-shell particles are subjected to the surface-initiated atom transfer radical polymerization (SI-ATRP) which provides the possibility of conducting polymerizations on the particle surface. By polymerizing monomers such as methyl methacrylate (MMA), the particle surface is rendered hydrophobic and allows their redispersion in organic, non-polar solvents which would enhance their compatibility with hydrophobic media.

The chapters were originally written as manuscripts for peer-reviewed journals, and therefore certain texts and references might be repeated in the process. While Chapters 2, 3 and 4 have already been accepted for publication (*J. Phys. Chem. C* **2014**, 118, 11093-11103, *RSC Adv.* **2013**, 3, 6964-6971 and *J. Mater. Chem. A* **2015**, 3, 14675-14685), Chapter 5 is still outstanding. The appendix exhibits additional results, including the synthesis of AgNPs through the inverse miniemulsions technique as well as the dielectric properties of nanocomposites using different sizes of AgNPs (with constant SiO_2 shell thickness). They are placed in the appendix as they were either aborted projects or do not give results substantial for publications. The arrangement of the chapters is mainly based

1. Introduction

on the steps towards the preparation of the nanocomposites and do not necessarily correspond to the chronological order of events.

1.11 References

- (1) Rao, Y.; Wong, C. P. Novel Ultra-High Dielectric Constant Polymer Based Composite Development for Embedded Capacitor Application. *4th Electron. Packag. Technol. Conf. 2002*. **2002**, 65–69.
- (2) Wilk, G. D.; Wallace, R. M.; Anthony, J. M. High-K Gate Dielectrics: Current Status and Materials Properties Considerations. *J. Appl. Phys.* **2001**, 89, 5243–5275.
- (3) Kingon, A. I.; Maria, J.; Streiffer, S. K. Alternative Dielectrics to Silicone Dioxide for Memory and Logic Devices. *Nature* **2000**, 406, 1032–1038.
- (4) Barber, P.; Balasubramanian, S.; Anguchamy, Y.; Gong, S.; Wibowo, A.; Gao, H.; Ploehn, H. J.; zur Loye, H.-C. Polymer Composite and Nanocomposite Dielectric Materials for Pulse Power Energy Storage. *Materials (Basel)* **2009**, 2, 1697–1733.
- (5) Pelrine, R.; Sommer-Larsen, P.; Kornbluh, R.; Heydt, R.; Kofod, G.; Pei, Q.; Gravesen, P. Applications of Dielectric Elastomer Actuators. *Proc. SPIE* **2001**, 4329, 335–349.
- (6) Dang, Z.-M.; Yuan, J.-K.; Zha, J.-W.; Zhou, T.; Li, S.-T.; Hu, G.-H. Fundamentals, Processes and Applications of High-Permittivity Polymer–matrix Composites. *Prog. Mater. Sci.* **2012**, 57, 660–723.
- (7) Röntgen, W. C. Ueber Die Durch Elektrizität Bewirkten Form-Und Volumenänderungen von Dielektrischen Körpern. *Ann. Phys.* **1880**, 247, 771–786.
- (8) Pelrine, R.; Kornbluh, R.; Kofod, G. High-Strain Actuator Materials Based on Dielectric Elastomers. *Adv. Mater.* **2000**, 12, 1223–1225.
- (9) Keplinger, C.; Kaltenbrunner, M.; Arnold, N.; Bauer, S. Röntgen’s Electrode-Free Elastomer Actuators without Electromechanical Pull-in Instability. *Proc. Natl. Acad. Sci. U. S. A.* **2010**, 107, 4505–4510.
- (10) Akbari, S.; Shea, H. R. Microfabrication and Characterization of an Array of Dielectric Elastomer Actuators Generating Uniaxial Strain to Stretch Individual Cells. *J. Micromechanics Microengineering* **2012**, 22, 045020.

1. Introduction

- (11) Kovacs, G.; Lochmatter, P.; Wissler, M. An Arm Wrestling Robot Driven by Dielectric Elastomer Actuators. *Smart Mater. Struct.* **2007**, *16*, S306–S317.
- (12) Ashley, S. Artificial Muscles. *Sci. Am.* **2003**, *289*, 52–59.
- (13) Ha, S. M.; Yuan, W.; Pei, Q.; Pelrine, R.; Stanford, S. Interpenetrating Polymer Networks for High-Performance Electroelastomer Artificial Muscles. *Adv. Mater.* **2006**, *18*, 887–891.
- (14) Mirfakhrai, T.; Madden, J. D. W.; Baughman, R. H. Polymer Artificial Muscles. *Mater. Today* **2007**, *10*, 30–38.
- (15) Biddiss, E.; Chau, T. Dielectric Elastomers as Actuators for Upper Limb Prosthetics: Challenges and Opportunities. *Med. Eng. Phys.* **2008**, *30*, 403–418.
- (16) Bar-Cohen, Y. *Electroactive Polymer (EAP) Actuators as Artificial Muscles: Reality, Potential, and Challenges*; 2nd ed.; SPIE Press: Bellingham, Washington, 2004.
- (17) O'Halloran, A.; O'Malley, F.; McHugh, P. A Review on Dielectric Elastomer Actuators, Technology, Applications, and Challenges. *J. Appl. Phys.* **2008**, *104*, 071101.
- (18) Carpi, F. *The European Scientific Network for Artificial Muscles and the EuroEAP Conference*.
- (19) Carpi, F.; Kornbluh, R.; Sommer-Larsen, P.; Alici, G. Electroactive Polymer Actuators as Artificial Muscles: Are They Ready for Bioinspired Applications? *Bioinspir. Biomim.* **2011**, *6*, 045006.
- (20) Brochu, P.; Pei, Q. Advances in Dielectric Elastomers for Actuators and Artificial Muscles. *Macromol. Rapid Commun.* **2010**, *31*, 10–36.
- (21) Pei, Q.; Rosenthal, M. Multifunctional Electroelastomer Roll Actuators and Their Application for Biomimetic Walking Robots. *Proceeding SPIE, Electroact. Polym. Actuators Devices* **2003**, *5051*, 281–290.
- (22) Pelrine, R. E. R.; Kornbluh, R. R. D. R.; Joseph, J. J. P. J.; International, S. R. I.; Ave, R.; Park, M. Electrostriction of Polymer Dielectrics with Compliant Electrodes as a Means of Actuation. *Sensors Actuators A Phys.* **1998**, *64*, 77–85.
- (23) McKay, T. G.; O'Brien, B. M.; Calius, E. P.; Anderson, I. A. Soft Generators Using Dielectric Elastomers. *Appl. Phys. Lett.* **2011**, *98*, 2009–2012.

1. Introduction

- (24) Koh, S. J. A.; Keplinger, C.; Li, T.; Bauer, S.; Suo, Z. Dielectric Elastomer Generators: How Much Energy Can Be Converted? *IEEE/ASME Trans. Mechatronics* **2011**, *16*, 33–41.
- (25) Pelrine, R.; Kornbluh, R. D.; Eckerle, J.; Jeuck, P.; Oh, S.; Pei, Q.; Stanford, S. Dielectric Elastomers: Generator Mode Fundamentals and Applications. *SPIE's 8th Annu. Int. Symp. Smart Struct. Mater.* **2001**, 4329, 148–156.
- (26) Pelrine, R.; Kornbluh, R.; Pei, Q.; Joseph, J. High-Speed Electrically Actuated Elastomers with Strain Greater than 100%. *Science* **2000**, 287, 836–840.
- (27) Pelrine, R.; Kornbluh, R.; Joseph, J.; Heydt, R.; Pei, Q.; Chiba, S. High-Field Deformation of Elastomeric Dielectrics for Actuators. *Mater. Sci. Eng. C* **2000**, *11*, 89–100.
- (28) Kim, H.; Park, J.; Chuc, N. H.; Choi, H. R.; Nam, J. D.; Lee, Y.; Jung, H. S.; Koo, J. C.; Huu Chuc, N. Development of Dielectric Elastomer Driven Micro-Optical Zoom Lens System. *Proc. SPIE 6524, Electroact. Polym. Actuators Devices* **2007**, 6524, 65241V – 65241V – 10.
- (29) Rosset, S.; Shea, H. R. Flexible and Stretchable Electrodes for Dielectric Elastomer Actuators. *Appl. Phys. A Mater. Sci. Process.* **2013**, *110*, 281–307.
- (30) *Dielectric Elastomers as Electromechanical Transducers*; Carpi, F.; De Rossi, D.; Kornbluh, R.; Pelrine, R.; Sommer-Larsen, P., Eds.; Elsevier: Amsterdam, 2008.
- (31) Opris, D. M.; Molberg, M.; Walder, C.; Ko, Y. S.; Fischer, B.; Nüesch, F. a. New Silicone Composites for Dielectric Elastomer Actuator Applications In Competition with Acrylic Foil. *Adv. Funct. Mater.* **2011**, *21*, 3531–3539.
- (32) Racles, C.; Cazacu, M.; Fischer, B.; Opris, D. M. Synthesis and Characterization of Silicones Containing Cyanopropyl Groups and Their Use in Dielectric Elastomer Actuators. *Smart Mater. Struct.* **2013**, *22*, 104004.
- (33) Galantini, F.; Carpi, F.; Gallone, G. Effects of Plasticization of a Soft Silicone for Dielectric Elastomer Actuation. *Smart Mater. Struct.* **2013**, *22*, 104020.
- (34) Shankar, R.; Ghosh, T. K.; Spontak, R. J. Electromechanical Response of Nanostructured Polymer Systems with No Mechanical Pre-Strain. *Macromol. Rapid Commun.* **2007**, *28*, 1142–1147.
- (35) Drobny, J. G. *Polymers for Electricity and Electronics*; John Wiley & Sons, Inc.: Hoboken, New Jersey, 2012.

1. Introduction

- (36) Harper, C. A. *Handbook of Plastics, Elastomers, and Composites*; Mc Graw-Hill Companies Inc.: New York, 2002.
- (37) Cervantes, J.; Zárraga, R.; Salazar-Hernández, C. Organotin Catalysts in Organosilicon Chemistry. *Appl. Organomet. Chem.* **2012**, *26*, 157–163.
- (38) Lewis, L. N.; Stein, J.; Gao, Y.; Colborn, R. E.; Hutchins, G. Platinum Catalysts Used in the Silicone Industry. *Platin. Metals Rev.* **1997**, *41*, 66–75.
- (39) Li, Z.; Hansen, K.; Yao, Y.; Ma, Y.; Moon, K.; Wong, C. P. The Conduction Development Mechanism of Silicone-Based Electrically Conductive Adhesives. *J. Mater. Chem. C* **2013**, *1*, 4368–4374.
- (40) Sangermano, M.; Marchi, S.; Meier, P.; Kornmann, X. UV-Activated Hydrosilation Reaction for Silicone Polymer Crosslinking. *J. Appl. Polym. Sci.* **2013**, *128*, 1521–1526.
- (41) Lv, Y.; Lin, Z.; Svec, F. “Thiol-Ene” Click Chemistry: A Facile and Versatile Route for the Functionalization of Porous Polymer Monoliths. *Analyst* **2012**, *137*, 4114–4118.
- (42) Müller, U.; Kunze, A.; Herzig, C.; Weis, J. Photocrosslinking of Silicones. Part 13. Photoinduced Thiol-Ene Crosslinking of Modified Silicones. *J. Macromol. Sci. Part A* **1996**, *33*, 439–457.
- (43) Rissing, C.; Son, D. Y. Thiol-Ene Reaction for the Synthesis of Multifunctional Branched Organosilanes. *Organometallics* **2008**, *27*, 5394–5397.
- (44) Dünki, S. J.; Ko, Y. S.; Nüesch, F. A.; Opris, D. M. Self-Repairable , High Permittivity Dielectric Elastomers with Large Actuation Strains at Low Electric Fields. *Adv. Funct. Mater.* **2015**, *25*, 2467–2475.
- (45) Tieke, B. *Makromolekulare Chemie: Eine Einführung*; VCH: Weinheim, 1997.
- (46) Kuhn, W. Beziehungen Zwischen Molekülgrösse, Statistischer Molekülgestalt Und Elastischen Eigenschaften Hochpolymerer Stoffe. *Colloid Polym. Sci.* **1936**, *76*, 258–271.
- (47) Rubinstein, M.; Panyukov, S. Elasticity of Polymer Networks. *Macromolecules* **2002**, *35*, 6670–6686.
- (48) Rubinstein, M.; Colby, R. *Polymers Physics*; Oxford, 2003.
- (49) Treloar, L. R. G. *The Physics of Rubber Elasticity*; Oxford university press, 1975.

1. Introduction

- (50) Kramer, O. Non-Equilibrium Mechanical Properties of Model Networks. *Br. Polym. J.* **1985**, *17*, 129–133.
- (51) *Broadband Dielectric Spectroscopy*; Kremer, F.; Schönhals, A., Eds.; Springer Berlin Heidelberg: Berlin, Heidelberg, 2003.
- (52) Chen, L.; Ong, C.; Neo, C. Electromagnetic Properties of Materials. In *Microwave Electronics: Measurement and Materials Characterization*; John Wiley & Sons, Ltd: Chichester, UK, 2004.
- (53) Ieda, M.; Nagao, M.; Hikita, M. High-Field Conduction and Breakdown in Insulating Polymers. Present Situation and Prospects. *IEEE Trans. Dielectr. Electr. Insul.* **1994**, *1*, 934–945.
- (54) Ieda, M. Dielectric Breakdown Process of Polymers. *IEEE Trans. Electr. Insul.* **1980**, *EI-15*, 206–224.
- (55) Huang, J.; Shian, S.; Diebold, R. M.; Suo, Z.; Clarke, D. R. The Thickness and Stretch Dependence of the Electrical Breakdown Strength of an Acrylic Dielectric Elastomer. *Appl. Phys. Lett.* **2012**, *101*, 122905.
- (56) Koh, S. J. A.; Li, T.; Zhou, J.; Zhao, X.; Hong, W.; Zhu, J.; Suo, Z. Mechanisms of Large Actuation Strain in Dielectric Elastomers. *J. Polym. Sci. Part B Polym. Phys.* **2011**, *49*, 504–515.
- (57) Michel, S.; Chu, B. T. T.; Grimm, S.; Nüesch, F. A.; Borgschulte, A.; Opris, D. M. Self-Healing Electrodes for Dielectric Elastomer Actuators. *J. Mater. Chem.* **2012**, *22*, 20736.
- (58) La, T.; Lau, G.; Shiao, L.; Tan, A. W. Muscle-like High-Stress Dielectric Elastomer Actuators with Oil Capsules. *Smart Mater. Struct.* **2014**, *23*, 105006.
- (59) Schneuwly, A.; Groning, P.; Schlapbach, L. Breakdown Behavior of Oil-Im Polypropylene as Dielectric in Film Capacitors. *IEEE Trans. Dielectr. Electr. Insul.* **1998**, *5*, 862–868.
- (60) Yuan, W.; Brochu, P.; Ha, S. M.; Pei, Q. Dielectric Oil Coated Single-Walled Carbon Nanotube Electrodes for Stable, Large-Strain Actuation with Dielectric Elastomers. *Sensors Actuators, A Phys.* **2009**, *155*, 278–284.
- (61) Van Rysselberghe, P. Remarks Concerning The Clausius-Mossotti Law. *J. Phys. Chem.* **1929**, *49*, 1152–1155.

1. Introduction

- (62) Lorentz, H. A. Über Die Beziehung Zwischen Der Fortpflanzungsgeschwindigkeit Des Lichtes Und Der Körperdichte. *Ann. Phys.* **1879**, 245, 641–665.
- (63) Onsager, L. Electric Moments of Molecules in Liquids. *J. Am. Chem. Soc.* **1936**, 58, 1486–1493.
- (64) Kirkwood, J. G. The Dielectric Polarization of Polar Liquids. *J. Chem. Phys.* **1939**, 7, 911–919.
- (65) Fröhlich, H. Theoretical Dipolar Interaction. *Trans. Faraday Soc.* **1946**, 42, A003.
- (66) Kirkwood, G. The Influence of Hindered Molecular Rotation on the Dielectric Polarization of Polar Liquids. *Trans. Faraday Soc.* **1946**, 42, A007.
- (67) Fröhlich, H. *Theory of Dielectrics: Dielectric Constant and Dielectric Loss*; Monographs on the physics and chemistry of materials; Clarendon Press: Oxford, 1958.
- (68) Chen, D.; Yi, S.; Fang, P.; Zhong, Y.; Huang, C.; Wu, X. Synthesis and Characterization of Novel Room Temperature Vulcanized (RTV) Silicone Rubbers Using Octa[(trimethoxysilyl)ethyl]-POSS as Cross-Linker. *React. Funct. Polym.* **2011**, 71, 502–511.
- (69) Racles, C.; Alexandru, M.; Bele, A.; Musteata, V. E.; Cazacu, M.; Opris, D. M. Chemical Modification of Polysiloxanes with Polar Pendant Groups by Co-Hydrosilylation. *RSC Adv.* **2014**, 4, 37620–37628.
- (70) Risse, S.; Kussmaul, B.; Krüger, H.; Kofod, G. A Versatile Method for Enhancement of Electromechanical Sensitivity of Silicone Elastomers. *RSC Adv.* **2012**, 2, 9029–9035.
- (71) Madsen, F. B.; Dimitrov, I.; Daugaard, A. E.; Hvilsted, S.; Skov, A. L. Novel Cross-Linkers for PDMS Networks for Controlled and Well Distributed Grafting of Functionalities by Click Chemistry. *Polym. Chem.* **2013**, 4, 1700–1707.
- (72) Risse, S.; Kussmaul, B.; Krüger, H.; Waché, R.; Kofod, G. DEA Material Enhancement with Dipole Grafted PDMS Networks. *Proc. SPIE, Electroact. Polym. Actuators Devices* **2011**, 7976, 79760N – 79760N – 7.
- (73) Kussmaul, B.; Risse, S.; Kofod, G.; Waché, R.; Wegener, M.; McCarthy, D. N.; Krüger, H.; Gerhard, R. Enhancement Of Dielectric Permittivity And Electromechanical Response In Silicone Elastomers: Molecular Grafting Of Organic Dipoles To The Macromolecular Network. *Adv. Funct. Mater.* **2011**, 21, 4589–4594.

1. Introduction

- (74) Madsen, F. B.; Yu, L.; Daugaard, A. E.; Hvilsted, S.; Skov, A. L. A New Soft Dielectric Silicone Elastomer Matrix with High Mechanical Integrity and Low Losses. *RSC Adv.* **2015**, *5*, 10254–10259.
- (75) Myroshnychenko, V.; Brosseau, C. Finite-Element Modeling Method for the Prediction of the Complex Effective Permittivity of Two-Phase Random Statistically Isotropic Heterostructures. *J. Appl. Phys.* **2005**, *97*.
- (76) Brosseau, C. Modelling and Simulation of Dielectric Heterostructures: A Physical Survey from an Historical Perspective. *J. Phys. D. Appl. Phys.* **2006**, *39*, 1277–1294.
- (77) Maxwell Garnett, J. C. Colours in Metal Glasses and in Metallic Films. *Phil. Trans. R. Soc. Lond.* **1904**, *203*, 385–420.
- (78) Koh, G. Effective Dielectric Constant of a Medium with Spherical Inclusions. *IEEE Trans. Geosci. Remote Sens.* **1992**, *30*, 184–186.
- (79) Sihvola, A.; Saastamoinen, S.; Heiska, K. Mixing Rules and Percolation. *Remote Sens. Rev.* **1994**, *9*, 39–50.
- (80) Qi, L.; Lee, B. I.; Chen, S.; Samuels, W. D.; Exarhos, G. J. High-Dielectric-Constant Silver-Epoxy Composites as Embedded Dielectrics. *Adv. Mater.* **2005**, *17*, 1777–1781.
- (81) Shen, Y.; Lin, Y.; Li, M.; Nan, C.-W. High Dielectric Performance of Polymer Composite Films Induced by a Percolating Interparticle Barrier Layer. *Adv. Mater.* **2007**, *19*, 1418–1422.
- (82) Sihvola, A. Mixing Rules with Complex Dielectric Coefficients. *Subsurf. Sens. Technol. Appl.* **2000**, *1*, 393–415.
- (83) Nguyen, H. C.; Doan, V. T.; Park, J.; Koo, J. C.; Lee, Y.; Nam, J.; Choi, H. R. The Effects of Additives on the Actuating Performances of a Dielectric Elastomer Actuator. *Smart Mater. Struct.* **2008**, *18*, 015006.
- (84) Stiubianu, G.; Bele, A.; Tugui, C.; Musteata, V. New Dielectric Elastomers with Improved Properties for Energy Harvesting and Actuation. *Proc. SPIE* **2015**, 9258, 925808.
- (85) Hashin, Z.; Rosen, B. W. The Elastic Moduli of Fiber-Reinforced Materials. *J. Appl. Mech.* **1964**, *63*, 223–232.

1. Introduction

- (86) Krimmer, A. A Direct Approach for the Explicit Determination of the in-Situ Modulus of Matrices in Fibre Reinforced Plastics. In *ECCM15 - 15th European Conference on Composite Materials*; Venice, Italy, 2012; pp. 24–28.
- (87) Beer, F. Die Festigkeitseigenschaften Kreuzweise Bewehrter Kunststoffe. *VDI-Zeitschrift* **1959**, *101*, 463–468.
- (88) Bigg, D. M. Mechanical Properties of Particulate Filled Polymers. *Polym. Compos.* **1987**, *8*, 115–122.
- (89) Opris, D. M.; Crespy, D.; Löwe, C.; Molberg, M.; Nüesch, F. Phtalocyanine and Encapsulated Polyaniline Nanoparticles as Fillers for Dielectric Elastomers. *Proc. SPIE, Electroact. Polym. Actuators Devices (EAPAD)Electroactive Polym. Actuators Devices* **2009**, 7287, 72870L – 72870L – 8.
- (90) Dang, Z.-M.; Yu, Y.-F.; Xu, H.-P.; Bai, J. Study on Microstructure and Dielectric Property of the BaTiO₃/epoxy Resin Composites. *Compos. Sci. Technol.* **2008**, *68*, 171–177.
- (91) Choi, H.-W.; Heo, Y.-W.; Lee, J.-H.; Kim, J.-J.; Lee, H.-Y.; Park, E.-T.; Chung, Y.-K. Effects of BaTiO₃ on Dielectric Behavior of BaTiO₃–Ni–polymethyl Methacrylate Composites. *Appl. Phys. Lett.* **2006**, *89*, 132910.
- (92) Vrejoiu, I.; Pedarnig, J. D.; Dinescu, M.; Bäuerle, D. Rapid Communication Flexible Ceramic – Polymer Composite Films with Temperature-Insensitive and Tunable Dielectric Permittivity. *Appl. Phys. A* **2002**, *409*, 407–409.
- (93) Gallone, G.; Carpi, F.; De Rossi, D.; Levita, G.; Marchetti, A. Dielectric Constant Enhancement in a Silicone Elastomer Filled with Lead Magnesium Niobate-Lead Titanate. *Mater. Sci. Eng. C* **2007**, *27*, 110–116.
- (94) Stoyanov, H.; Brochu, P.; Niu, X.; Della Gaspera, E.; Pei, Q. Dielectric Elastomer Transducers with Enhanced Force Output and Work Density. *Appl. Phys. Lett.* **2012**, *100*, 2010–2013.
- (95) Kurimoto, M.; Okubo, H.; Kato, K.; Hanai, M.; Hoshina, Y.; Takei, M.; Hayakawa, N. Dielectric Properties of Epoxy/alumina Nanocomposite Influenced by Control of Micrometric Agglomerates. *IEEE Trans. Dielectr. Electr. Insul.* **2010**, *17*, 662–670.
- (96) Molberg, M.; Crespy, D.; Rupper, P.; Nüesch, F.; Månson, J.-A. E.; Löwe, C.; Opris, D. M. High Breakdown Field Dielectric Elastomer Actuators Using Encapsulated Polyaniline as High Dielectric Constant Filler. *Adv. Funct. Mater.* **2010**, *20*, 3280–3291.

1. Introduction

- (97) Yuan, J.-K.; Dang, Z.-M.; Yao, S.-H.; Zha, J.-W.; Zhou, T.; Li, S.-T.; Bai, J. Fabrication and Dielectric Properties of Advanced High Permittivity Polyaniline/poly(vinylidene Fluoride) Nanohybrid Films with High Energy Storage Density. *J. Mater. Chem.* **2010**, *20*, 2441–2447.
- (98) Li, G.; Yu, S.; Sun, R.; Lu, D. Clean and in-Situ Synthesis of Copper-Epoxy Nanocomposite as a Matrix for Dielectric Composites with Improved Dielectric Performance. *Compos. Sci. Technol.* **2014**, *110*, 95–102.
- (99) Wang, Q.; Chen, G. Effect of Nanofillers on the Dielectric Properties of Epoxy Nanocomposites. *Adv. Mater. Res.* **2012**, *1*, 93–107.
- (100) Jayasundere, N.; Smith, B. V. Dielectric Constant for Binary Piezoelectric 0-3 Composites. *J. Appl. Phys.* **1993**, *73*, 2462–2466.
- (101) Opris, D. M.; Nüesch, F. A.; Löwe, C.; Molberg, M.; Nagel, M. Synthesis, Characterization, and Dielectric Properties of Phthalocyanines with Ester and Carboxylic Acid Functionalities. *Chem. Mater.* **2008**, *53*, 6889–6896.
- (102) Nalwa, H. S. *Handbook of Low and High Dielectric Constant Materials and Their Applications, Two-Volume Set*; Academic Press: San Diego, 1999.
- (103) Niu, Y.; Yu, K.; Bai, Y.; Wang, H.; Member, S. Enhanced Dielectric Performance of BaTiO₃ / PVDF Composites Prepared by Modified Process for Energy Storage Applications. *IEEE Trans. Ultrason. Ferroelectr. Freq. Control* **2015**, *62*, 108–115.
- (104) Dang, Z.-M.; Lin, Y.-H.; Nan, C.-W. Novel Ferroelectric Polymer Composites with High Dielectric Constants. *Adv. Mater.* **2003**, *15*, 1625–1629.
- (105) Singh, V.; Kulkarni, A. R.; Mohan, T. R. R. Dielectric Properties of Aluminum – Epoxy Composites. *J. Appl. Polym. Sci.* **2003**, *90*, 3602–3608.
- (106) Nelson, J. K.; Linhardt, R. J.; Schadler, L. S.; Hillborg, H. Effect of High Aspect Ratio Filler on Dielectric Properties of Polymer Composites: A Study on Barium Titanate Fibers and Graphene Platelets. *IEEE Trans. Dielectr. Electr. Insul.* **2012**, *19*, 960–967.
- (107) Goswami, K.; Daugaard, A. E.; Skov, A. L. Dielectric Properties of Ultraviolet Cured Poly(dimethyl Siloxane) Sub-Percolative Composites Containing Percolative Amounts of Multi-Walled Carbon Nanotubes. *RSC Adv.* **2015**, *5*, 12792–12799.
- (108) Wang, L.; Dang, Z.-M. Carbon Nanotube Composites with High Dielectric Constant at Low Percolation Threshold. *Appl. Phys. Lett.* **2005**, *87*, 042903.

1. Introduction

- (109) Nayak, S.; Kumar Chaki, T.; Khastgir, D. Development of Poly(dimethylsiloxane)/BaTiO₃ Nanocomposites as Dielectric Material. *Adv. Mater. Res.* **2012**, 622-623, 897–900.
- (110) Grannan, D. M.; Garland, J. C.; Tanner, D. B. Critical Behavior of the Dielectric Constant of a Random Composite near the Percolation Threshold. *Phys. Rev. Lett.* **1981**, 46, 375–379.
- (111) Xu, J.; Wong, C. P. Effects of the Low Loss Polymers on the Dielectric Behavior of Novel Aluminum-Filled High-K Nano-Composites. *2004 1st IEEE Consum. Commun. Netw. Conf. (IEEE Cat. No.04EX745)* 158–170.
- (112) Rajesh, S.; Sonoda, K.; Uusimaki, A.; Yang, K. H.; Lu, H. Y.; Jantunen, H. Effective Dielectric Response of Polymer Composites with Ceramic Coated Silver Flakes. *J. Mater. Sci. Mater. Electron.* **2012**, 24, 191–195.
- (113) Dang, Z.-M.; Peng, B.; Xie, D.; Yao, S.-H.; Jiang, M.-J.; Bai, J. High Dielectric Permittivity Silver/polyimide Composite Films with Excellent Thermal Stability. *Appl. Phys. Lett.* **2008**, 92, 112910.
- (114) Lu, J.; Moon, K.-S.; Xu, J.; Wong, C. P. Synthesis and Dielectric Properties of Novel High-K Polymer Composites Containing in-Situ Formed Silver Nanoparticles for Embedded Capacitor Applications. *J. Mater. Chem.* **2006**, 16, 1543–1548.
- (115) Lu, J.; Moon, K.-S.; Wong, C. P. Silver/polymer Nanocomposite as a High-K Polymer Matrix for Dielectric Composites with Improved Dielectric Performance. *J. Mater. Chem.* **2008**, 18, 4821–4826.
- (116) Xu, J.; Moon, K.-S. K. S. K.-S.; Tison, C.; Wong, C. P. P. A Novel Aluminum-Filled Composite Dielectric for Embedded Passive Applications. *IEEE Trans. Adv. Packag.* **2006**, 29, 295–306.
- (117) Lin, Y.; Jiang, L.; Zhao, R.; Nan, C.-W. High-Permittivity Core/shell Structured NiO-Based Ceramics and Their Dielectric Response Mechanism. *Phys. Rev. B* **2005**, 72, 014103.
- (118) Dang, Z.-M.; Wang, L.; Yin, Y.; Zhang, Q.; Lei, Q.-Q. Giant Dielectric Permittivities in Functionalized Carbon-Nanotube/ Electroactive-Polymer Nanocomposites. *Adv. Mater.* **2007**, 19, 852–857.
- (119) Tian, M.; Wei, Z.; Zan, X.; Zhang, L.; Zhang, J.; Ma, Q.; Ning, N.; Nishi, T. Thermally Expanded Graphene Nanoplates/polydimethylsiloxane Composites with High

1. Introduction

Dielectric Constant, Low Dielectric Loss and Improved Actuated Strain. *Compos. Sci. Technol.* **2014**, 99, 37–44.

(120) Andrey, L.; Sau, T. K. *Complex-Shaped Metal Nanoparticles : Bottom-Up Syntheses and Applications*; WILEY-VCH Verlag: Weinheim, 2012.

(121) Li, Z.; Moon, K. S.; Kim, S.; Wong, C. P. Enhancement of Dielectric Strength and Processibility of High Dielectric Constant Al Nanocomposite by Organic Molecule Treatment. *Proc. - Electron. Components Technol. Conf.* **2011**, 2073–2078.

(122) Lee, Y.; Choi, J.-R.; Lee, K. J.; Stott, N. E.; Kim, D. Large-Scale Synthesis of Copper Nanoparticles by Chemically Controlled Reduction for Applications of Inkjet-Printed Electronics. *Nanotechnology* **2008**, 19, 415604.

(123) Xu, J.; Moon, K.-S.; Tison, C.; Wong, C. P. A Novel Aluminum-Filled Composite Dielectric for Embedded Passive Applications. *IEEE Trans. Adv. Packag.* **2006**, 29, 295–306.

(124) Reszczyńska, J.; Jurek, A.; Łacka, I.; Skwarek, E.; Zaleska, A. Preparation of Silver Nanoparticles in Reverse Micelles and Antibacterial Activity of Silver Modified-Paints. *Adv. Mater. Sci.* **2010**, 10, 12–20.

(125) Sharma, V. K.; Yngard, R. A.; Lin, Y. Silver Nanoparticles: Green Synthesis and Their Antimicrobial Activities. *Adv. Colloid Interface Sci.* **2009**, 145, 83–96.

(126) Goyal, A.; Kumar, A.; Patra, P. K.; Mahendra, S.; Tabatabaei, S.; Alvarez, P. J. J.; John, G.; Ajayan, P. M. In Situ Synthesis of Metal Nanoparticle Embedded Free Standing Multifunctional PDMS Films. *Macromol. Rapid Commun.* **2009**, 30, 1116–1122.

(127) Yu, M. K.; Jeong, Y. Y.; Park, J.; Park, S.; Kim, J. W.; Min, J. J.; Kim, K.; Jon, S. Drug-Loaded Superparamagnetic Iron Oxide Nanoparticles for Combined Cancer Imaging and Therapy in Vivo. *Angew. Chemie - Int. Ed.* **2008**, 47, 5362–5365.

(128) Lee, H.; Yu, M. K.; Park, S.; Moon, S.; Min, J. J.; Jeong, Y. Y.; Kang, H.-W.; Jon, S. Thermally Cross-Linked Superparamagnetic Iron Oxide Nanoparticles: Synthesis and Application as a Dual Imaging Probe for Cancer in Vivo. *J. Am. Chem. Soc.* **2007**, 129, 12739–12745.

(129) Hu, M.; Chen, J.; Li, Z.-Y.; Au, L.; Hartland, G. V.; Li, X.; Marquez, M.; Xia, Y. Gold Nanostructures: Engineering Their Plasmonic Properties for Biomedical Applications. *Chem. Soc. Rev.* **2006**, 35, 1084–1094.

1. Introduction

- (130) Xu, R.; Wang, D.; Zhang, J.; Li, Y. Shape-Dependent Catalytic Activity of Silver Nanoparticles for the Oxidation of Styrene. *Chem. - An Asian J.* **2006**, *1*, 888–893.
- (131) Burda, C.; Chen, X.; Narayanan, R.; El-Sayed, M. A. Chemistry and Properties of Nanocrystals of Different Shapes. *Chem. Rev.* **2005**, *105*, 1025–1102.
- (132) Daniel, M.-C.; Astruc, D. Gold Nanoparticles: Assembly, Supramolecular Chemistry, Quantum-Size-Related Properties, and Applications toward Biology, Catalysis, and Nanotechnology. *Chem. Rev.* **2004**, *104*, 293–346.
- (133) Lu, J.; Su, F.; Huang, Z.; Zhang, C.; Liu, Y.; Ma, X.; Gong, J. N-Doped Ag/TiO₂ Hollow Spheres for Highly Efficient Photocatalysis under Visible-Light Irradiation. *RSC Adv.* **2013**, *3*, 720–724.
- (134) Atwater, H. A.; Polman, A. Plasmonics for Improved Photovoltaic Devices. *Nat. Mater.* **2010**, *9*, 205–213.
- (135) Qi, J.; Dang, X.; Hammond, P. T.; Belcher, A. M. Highly Efficient Plasmon-Enhanced Dye-Sensitized Solar Cells through Metal@Oxide Core-Shell Nanostructure. **2011**, *5*, 7108–7116.
- (136) Tavakoli, A.; Sohrabi, M.; Kargari, A. A Review of Methods for Synthesis of Nanostructured Metals with Emphasis on Iron Compounds. *Chem. Pap.* **2007**, *61*, 151–170.
- (137) Klabunde, K. J. *Nanoscale Materials in Chemistry*; Wiley-Interscience: New York, 2001.
- (138) Wang, Y.; Xia, Y. Bottom-up and Top-down Approaches to the Synthesis of Monodispersed Spherical Colloids of Low Melting-Point Metals. *Nano Lett.* **2004**, *4*, 2047–2050.
- (139) LaMer, V. K.; Dinegar, R. H. . Theory, Production and Mechanism of Formation of Monodispersed Hydrosols. *J. Am. Chem. Soc.* **1950**, *72*, 4847–4854.
- (140) Tao, A. R.; Habas, S.; Yang, P. Shape Control of Colloidal Metal Nanocrystals. *Small* **2008**, *4*, 310–325.
- (141) Wang, D.; Möhwald, H. Template-Directed Colloidal Self-Assembly - the Route to “Top-down” Nanochemical Engineering. *J. Mater. Chem.* **2004**, *14*, 459–468.
- (142) Kim, D.; Jeong, S.; Moon, J. Synthesis of Silver Nanoparticles Using the Polyol Process and the Influence of Precursor Injection. *Nanotechnology* **2006**, *17*, 4019–4024.

1. Introduction

- (143) Murray, C. B.; Kagan, C. R.; Bawendi, M. G. Synthesis and Characterization of Monodisperse Nanocrystals and Close-Packed Nanocrystal Assemblies. *Annu. Rev. Mater. Sci.* **2000**, *30*, 545–610.
- (144) De Mello Donegá, C.; Liljeroth, P.; Vanmaekelbergh, D. Physicochemical Evaluation of the Hot-Injection Method, a Synthesis Route for Monodisperse Nanocrystals. *Small* **2005**, *1*, 1152–1162.
- (145) Krutyakov, Y. A.; Kudrinskiy, A. A.; Olenin, A. Y.; Lisichkin, G. V. Synthesis and Properties of Silver Nanoparticles: Advances and Prospects. *Russ. Chem. Rev.* **2008**, *77*, 233–257.
- (146) Notarianni, M.; Vernon, K.; Chou, A.; Aljada, M.; Liu, J.; Motta, N. Plasmonic Effect of Gold Nanoparticles in Organic Solar Cells. *Sol. Energy* **2014**, *106*, 23–37.
- (147) Thompson, D. Michael Faraday's Recognition of Ruby Gold : The Birth of Modern Nanotechnology His 1857 Lecture to the Royal Society in London. *Gold Bull.* **2007**, *40*, 267–269.
- (148) Choi, H.; Lee, J.-P.; Ko, S.-J.; Jung, J.-W.; Park, H.; Yoo, S.; Park, O.; Jeong, J.-R.; Park, S.; Kim, J. Y. Multipositional Silica-Coated Silver Nanoparticles for High-Performance Polymer Solar Cells. *Nano Lett.* **2013**, *13*, 2204–2208.
- (149) Rycenga, M.; Cobley, C. M.; Zeng, J.; Li, W.; Moran, C. H.; Zhang, Q.; Qin, D.; Xia, Y. Controlling the Synthesis and Assembly of Silver Nanostructures for Plasmonic Applications. *Chem. Rev.* **2011**, *111*, 3669–3712.
- (150) Liang, X.; Yu, S.; Sun, R.; Luo, S.; Wan, J.; Yu, S.; Sun, R.; Luo, S.; Liang, X.; Wan, J.; et al. Microstructure and Dielectric Behavior of the Three-Phase Ag@SiO₂/BaTiO₃/PVDF Composites with High Permittivity. *J. Mater. Res.* **2012**, *27*, 991–998.
- (151) Yang, X. H.; Fu, H. T.; Wong, K.; Jiang, X. C.; Yu, A. B. Hybrid Ag@TiO₂ Core-Shell Nanostructures with Highly Enhanced Photocatalytic Performance. *Nanotechnology* **2013**, *24*, 415601.
- (152) Chin, S. F.; Pang, S. C.; Dom, F. E. I. Sol-Gel Synthesis of Silver/titanium Dioxide (Ag/TiO₂) Core-Shell Nanowires for Photocatalytic Applications. *Mater. Lett.* **2011**, *65*, 2673–2675.
- (153) Cobley, C. M.; Rycenga, M.; Zhou, F.; Li, Z.-Y.; Xia, Y. Etching and Growth: An Intertwined Pathway to Silver Nanocrystals with Exotic Shapes. *Angew. Chem. Int. Ed. Engl.* **2009**, *48*, 4824–4827.

1. Introduction

- (154) Farrell, Z.; Shelton, C.; Dunn, C.; Green, D. Straightforward, One-Step Synthesis of Alkanethiol-Capped Silver Nanoparticles from an Aggregative Model of Growth. *Langmuir* **2013**, 29, 9291–9300.
- (155) Pastoriza-Santos, I.; Liz-Marzán, L. Formation and Stabilization of Silver Nanoparticles through Reduction by *N, N*-Dimethylformamide. *Langmuir* **1999**, 15, 948–951.
- (156) Hiramatsu, H.; Osterloh, F. E. Communications A Simple Large-Scale Synthesis of Nearly with Exchangeable Surfactants. *Chem. Mater.* **2004**, 16, 801–802.
- (157) Sarkar, A.; Kapoor, S.; Mukherjee, T. Preparation, Characterization, and Surface Modification of Silver Nanoparticles in Formamide. *J. Phys. Chem. B* **2005**, 109, 7698–7704.
- (158) Yin, Y.; Li, Z.-Y.; Zhong, Z.; Gates, B.; Xia, Y.; Venkateswaran, S. Synthesis and Characterization of Stable Aqueous Dispersions of Silver Nanoparticles through the Tollens process. *J. Mater. Chem.* **2002**, 12, 522–527.
- (159) Zhang, Q.; Li, W.; Wen, L.-P.; Chen, J.; Xia, Y. Facile Synthesis of Ag Nanocubes of 30 to 70 nm in Edge Length with CF₃COOAg as a Precursor. *Chem. - A Eur. J.* **2010**, 16, 10234–10239.
- (160) Creighton, J. A.; Blatchford, C. G.; Albrecht, M. G. Plasma Resonance Enhancement of Raman Scattering by Pyridine Adsorbed on Silver or Gold Sol Particles of Size Comparable to the Excitation Wavelength. *J. Chem. Soc. Faraday Trans. 2* **1979**, 75, 790–798.
- (161) Korgel, B. A.; Fitzmaurice, D. Self-Assembly of Silver Nanocrystals into Two-Dimensional Nanowire Arrays. *Adv. Mater.* **1998**, 10, 661–665.
- (162) Nickel, U.; Mansyreff, K.; Schneider, S. Production of Monodisperse Silver Colloids by Reduction with Hydrazine: The Effect of Chloride and Aggregation on SER(R)S Signal Intensity. *J. Raman Spectrosc.* **2004**, 35, 101–110.
- (163) Riddick, J. A. *Organic Solvents: Physical Properties and Methods of Purification*; Bunger, W. B.; Sakano, T. K., Eds.; Techniques of chemistry; 4th ed.; New York, N.Y.: Wiley, 1986; Vol. vol.2.
- (164) Pastoriza-Santos, I.; Liz-Marzán, L. M.; Santos, I.; Marzán, L. Reduction of Silver Nanoparticles in DMF. Formation of Monolayers and Stable Colloids. *Pure Appl. Chem* **2000**, 72, 83–90.

1. Introduction

- (165) Pastoriza-Santos, I.; Liz-Marzán, L. Formation of PVP-Protected Metal Nanoparticles in DMF. *Langmuir* **2002**, *18*, 2888–2894.
- (166) Pastoriza-Santos, I.; Liz-Marzán, L. Synthesis of Silver Nanoprisms in DMF. *Nano Lett.* **2002**, *2*, 903–905.
- (167) Pastoriza-Santos, I.; Liz-Marzán, L. M. N , N -Dimethylformamide as a Reaction Medium for Metal Nanoparticle Synthesis. *Adv Funct Mater* **2009**, *19*, 679–688.
- (168) Kemp, M.; Slotnick, H. Silver Mirror. *J. Chem. Educ.* **1981**, *58*, 655–656.
- (169) Qu, L.; Dai, L. Novel Silver Nanostructures from Silver Mirror Reaction on Reactive Substrates. *J. Phys. Chem. B* **2005**, *109*, 13985–13990.
- (170) Niitsoo, O.; Couzis, A. Facile Synthesis of Silver Core - Silica Shell Composite Nanoparticles. *J. Colloid Interface Sci.* **2011**, *354*, 887–890.
- (171) Kvitek, L.; Prucek, R.; Panacek, A.; Novotny, R.; Hrbac, J.; Zboril, R. The Influence of Complexing Agent Concentration on Particle Size in the Process of SERS Active Silver Colloid Synthesis. *J. Mater. Chem.* **2005**, *15*, 1099–1105.
- (172) Dondi, R.; Su, W.; Griffith, G. A.; Clark, G.; Burley, G. A. Highly Size- and Shape-Controlled Synthesis of Silver Nanoparticles via a Templated Tollens Reaction. *Small* **2012**, *8*, 770–776.
- (173) Hsu, S. L. C.; Wu, R. T. Synthesis of Contamination-Free Silver Nanoparticle Suspensions for Micro-Interconnects. *Mater. Lett.* **2007**, *61*, 3719–3722.
- (174) Liu, T.; Li, D.; Yang, D.; Jiang, M. Size Controllable Synthesis of Ultrafine Silver Particles through a One-Step Reaction. *Mater. Lett.* **2011**, *65*, 628–631.
- (175) Pandey, S.; Pandey, S. K.; Parashar, V.; Mehrotra, G. K.; Pandey, A. C. Ag/PVA Nanocomposites: Optical and Thermal Dimensions. *J. Mater. Chem.* **2011**, *21*, 17154–17159.
- (176) Turkevich, J.; Stevenson, P. C.; Hillier, J. A Study of the Nucleation and Growth Processes in the Synthesis of Colloidal Gold. *Discuss. Faraday Soc.* **1951**, *11*, 55–75.
- (177) Lee, P. C.; Meisel, D. Adsorption and Surface-Enhanced Raman of Dyes on Silver and Gold Sols. *J. Phys. Chem.* **1982**, *86*, 3391–3395.
- (178) Dong, X.; Ji, X.; Wu, H.; Zhao, L.; Li, J.; Yang, W. Shape Control of Silver Nanoparticles by Stepwise Citrate Reduction. *J. Phys. Chem. C* **2009**, *113*, 6573–6576.

1. Introduction

- (179) Yang, Z.; Qian, H.; Chen, H.; Anker, J. N. One-Pot Hydrothermal Synthesis of Silver Nanowires via Citrate Reduction. *J. Colloid Interface Sci.* **2010**, *352*, 285–291.
- (180) Pyatenko, A.; Yamaguchi, M.; Suzuki, M. Synthesis of Spherical Silver Nanoparticles with Controllable Sizes in Aqueous Solutions. *J. Phys. Chem. C* **2007**, *111*, 7910–7917.
- (181) Wiley, B.; Sun, Y.; Xia, Y. Synthesis of Silver Nanostructures with Controlled Shapes and Properties. *Acc. Chem. Res.* **2007**, *40*, 1067–1076.
- (182) Wiley, B.; Sun, Y.; Mayers, B.; Xia, Y. Shape-Controlled Synthesis of Metal Nanostructures: The Case of Silver. *Chem. - A Eur. J.* **2005**, *11*, 454–463.
- (183) Wiley, B.; Herricks, T.; Sun, Y.; Xia, Y. Polyol Synthesis of Silver Nanoparticles: Use of Chloride and Oxygen to Promote the Formation of Single-Crystal, Truncated Cubes and Tetrahedrons. *Nano Lett.* **2004**, *4*, 1733–1739.
- (184) Liang, H.; Wang, W.; Huang, Y.; Zhang, S.; Wei, H.; Xu, H. Controlled Synthesis of Uniform Silver Nanospheres †. *J. Phys. Chem. C* **2010**, *114*, 7427–7431.
- (185) Sun, Y.; Mayers, B.; Herricks, T.; Xia, Y. Polyol Synthesis of Uniform Silver Nanowires: A Plausible Growth Mechanism and the Supporting Evidence. *Nano Lett.* **2003**, *3*, 955–960.
- (186) Xiong, Y.; Siekkinen, A. R.; Wang, J.; Yin, Y.; Kim, M. J.; Xia, Y. Synthesis of Silver Nanoplates at High Yields by Slowing down the Polyol Reduction of Silver Nitrate with Polyacrylamide. *J. Mater. Chem.* **2007**, *17*, 2600–2602.
- (187) Hu, Y.; Ge, J.; Lim, D.; Zhang, T.; Yin, Y. Size-Controlled Synthesis of Highly Water-Soluble Silver Nanocrystals. *J. Solid State Chem.* **2008**, *181*, 1524–1529.
- (188) Sun, Y.; Xia, Y. Shape-Controlled Synthesis of Gold and Silver Nanoparticles. *Science* **2002**, *298*, 2176–2179.
- (189) Skrabalak, S.; Wiley, B.; Kim, M.; Formo, E.; Xia, Y. On the Polyol Synthesis of Silver Nanostructures: Glycolaldehyde as a Reducing Agent. *Nano Lett.* **2008**, *8*, 2077–2081.
- (190) Silvert, P.; Herrera-Urbina, R.; Tekaiia-Elhsissen, K. Preparation of Colloidal Silver Dispersions by the Polyolprocess. *J. Mater. Chem.* **1997**, *6*, 573–577.

1. Introduction

- (191) Nishioka, M.; Miyakawa, M.; Kataoka, H.; Koda, H.; Sato, K.; Suzuki, T. M. Continuous Synthesis of Monodispersed Silver Nanoparticles Using a Homogeneous Heating Microwave Reactor System. *Nanoscale* **2011**, *3*, 2621–2626.
- (192) Mehenni, H.; Sinatra, L.; Mahfouz, R.; Katsiev, K.; Bakr, O. M. Rapid Continuous Flow Synthesis of High-Quality Silver Nanocubes and Nanospheres. *RSC Adv.* **2013**, *3*, 22397–22403.
- (193) Zhang, Q.; Li, H.; Poh, M.; Xia, F.; Cheng, Z. An All-Organic Composite Actuator Material with a High Dielectric Constant. *Nature* **2002**, *419*, 284–287.
- (194) Huang, C.; Zhang, Q. M.; deBotton, G.; Bhattacharya, K. All-Organic Dielectric-Percolative Three-Component Composite Materials with High Electromechanical Response. *Appl. Phys. Lett.* **2004**, *84*, 4391.
- (195) Lucchini, M. A.; Testino, A.; Ludwig, C.; Kambolis, A.; El-Kazzi, M.; Cervellino, A.; Riani, P.; Canepa, F. Continuous Synthesis of Nickel Nanopowders: Characterization, Process Optimization, and Catalytic Properties. *Appl. Catal. B Environ.* **2014**, *156-157*, 404–415.
- (196) Park, B. K.; Jeong, S.; Kim, D.; Moon, J.; Lim, S.; Kim, J. S. Synthesis and Size Control of Monodisperse Copper Nanoparticles by Polyol Method. *J. Colloid Interface Sci.* **2007**, *311*, 417–424.
- (197) Xu, J.; Wong, C. P. Low-Loss Percolative Dielectric Composite. *Appl. Phys. Lett.* **2005**, *87*, 082907.
- (198) *CRC Handbook of Chemistry and Physics*; Weast, R. C., Ed.; CRC Press: Boca Raton, FL, 1979.
- (199) Graf, C.; Vossen, D. L. J.; Imhof, A.; van Blaaderen, A. A General Method To Coat Colloidal Particles with Silica. *Langmuir* **2003**, *19*, 6693–6700.
- (200) Kobayashi, Y.; Katakami, H.; Mine, E.; Nagao, D.; Konno, M.; Liz-Marzán, L. M. Silica Coating of Silver Nanoparticles Using a Modified Stober Method. *J. Colloid Interface Sci.* **2005**, *283*, 392–396.
- (201) Mine, E.; Yamada, A.; Kobayashi, Y.; Konno, M.; Liz-Marzán, L. M. Direct Coating of Gold Nanoparticles with Silica by a Seeded Polymerization Technique. *J. Colloid Interface Sci.* **2003**, *264*, 385–390.
- (202) Liz-Marzan, L.; Mulvaney, P. The Assembly of Coated Nanocrystals. *J. Phys. Chem. B* **2003**, *107*, 7312–7326.

1. Introduction

- (203) Mulvaney, P.; Liz-Marzán, L. M.; Giersig, M.; Ung, T. Silica Encapsulation of Quantum Dots and Metal Clusters. *J. Mater. Chem.* **2000**, *10*, 1259–1270.
- (204) Stöber, W.; Fink, A.; Bohn, E. Controlled Growth of Monodisperse Silica Spheres in the Micron Size Range. *J. Colloid Interface Sci.* **1968**, *69*, 62–69.
- (205) Baida, H.; Billaud, P.; Marhaba, S.; Christofilos, D.; Cottancin, E.; Crut, a; Lermé, J.; Maioli, P.; Pellarin, M.; Broyer, M.; et al. Quantitative Determination of the Size Dependence of Surface Plasmon Resonance Damping in Single Ag@SiO₂ Nanoparticles. *Nano Lett.* **2009**, *9*, 3463–3469.
- (206) Rainville, L.; Dorais, M.-C.; Boudreau, D. Controlled Synthesis of Low Polydispersity Ag@SiO₂ Core-shell Nanoparticles for Use in Plasmonic Applications. *RSC Adv.* **2013**, *3*, 13953.
- (207) Gao, T.; Jelle, B. P.; Gustavsen, A. Core-Shell-Typed Ag@SiO₂ Nanoparticles as Solar Selective Coating Materials. *J. Nanoparticle Res.* **2013**, *15*, 1370.
- (208) Li, J.; Zhang, B.; Wang, F.; Liu, C. Silver/carbon-Quantum-Dot Plasmonic Luminescent Nanoparticles. *New J. Chem.* **2011**, *35*, 554–557.
- (209) Yang, J.; Zhang, F.; Chen, Y.; Qian, S.; Hu, P.; Li, W.; Deng, Y.; Fang, Y.; Han, L.; Luqman, M.; et al. Core-Shell Ag@SiO₂@mSiO₂ Mesoporous Nanocarriers for Metal-Enhanced Fluorescence. *Chem. Commun. (Camb)*. **2011**, *47*, 11618–11620.
- (210) Bai, Z.; Chen, R.; Si, P.; Huang, Y.; Sun, H.; Kim, D. H. Fluorescent pH Sensor Based on Ag@SiO₂ Core-Shell Nanoparticle. *ACS Appl. Mater. Interfaces* **2013**, *5*, 5856–5860.
- (211) Liu, S. H.; Han, M. Y. Synthesis, Functionalization, and Bioconjugation of Monodisperse, Silica-Coated Gold Nanoparticles: Robust Bioprobes. *Adv. Funct. Mater.* **2005**, *15*, 961–967.
- (212) Ung, T.; Liz-Marzan, L. M. Controlled Method for Silica Coating of Silver Colloids . Influence of Coating on the Rate of Chemical Reactions. *Langmuir* **1998**, *14*, 3740–3748.
- (213) Wang, W.; Zhipeng, L.; Baohua, G.; Zhenyu, Z.; Hongxin, X. Ag@SiO₂ Core-Shell Nanoparticles for Probing Spatial Distribution of Electromagnetic Field Enhancement via Surface-Enhanced Raman Scattering. **2009**, *3*, 3493–3496.
- (214) Xue, C.; Chen, X.; Hurst, S. J.; Mirkin, C. A. Self-Assembled Monolayer Mediated Silica Coating of Silver Triangular Nanoprisms. *Adv. Mater.* **2007**, *19*, 4071–4074.

1. Introduction

- (215) Graf, C.; Gao, Q.; Schütz, I.; Noufele, C. N.; Ruan, W.; Posselt, U.; Korotianskiy, E.; Nordmeyer, D.; Rancan, F.; Hadam, S.; et al. Surface Functionalization of Silica Nanoparticles Supports Colloidal Stability in Physiological Media and Facilitates Internalization in Cells. *Langmuir* **2012**, *28*, 7598–7613.
- (216) Liu, S.; Han, M.-Y. Silica-Coated Metal Nanoparticles. *Chem. Asian J.* **2010**, *5*, 36–45.
- (217) Yin, Y.; Lu, Y.; Sun, Y.; Xia, Y. Silver Nanowires Can Be Directly Coated with Amorphous Silica To Generate Well-Controlled Coaxial Nanocables of Silver/Silica. *Nano Lett.* **2002**, *2*, 427–430.
- (218) Bahadur, N. M.; Furusawa, T.; Sato, M.; Kurayama, F.; Siddiquey, I. A.; Suzuki, N. Fast and Facile Synthesis of Silica Coated Silver Nanoparticles by Microwave Irradiation. *J. Colloid Interface Sci.* **2011**, *355*, 312–320.
- (219) Bastakoti, B. P.; Guragain, S.; Yusa, S.; Nakashima, K. Novel Synthesis Route for Ag@SiO₂ Core-shell Nanoparticles via Micelle Template of Double Hydrophilic Block Copolymer. *RSC Adv.* **2012**, *2*, 5938–5940.
- (220) Prasad, B. L. V; Arumugam, S. K.; Bala, T.; Sastry, M. Solvent-Adaptable Silver Nanoparticles. *Langmuir* **2005**, *21*, 822–826.
- (221) Chen, X.; Mao, S. S. Titanium Dioxide Nanomaterials: Synthesis, Properties, Modifications, and Applications. *Chem. Rev.* **2007**, *107*, 2891–2959.
- (222) Zhang, N.; Liu, S.; Fu, X.; Xu, Y. Synthesis of M@TiO₂ (M= Au, Pd, Pt) Core-shell Nanocomposites with Tunable Photoreactivity. *J. Phys. Chem. C* **2011**, *2*, 9136–9145.
- (223) Yang, X.; Fu, H.; Yu, A.; Jiang, X. Large-Surface Mesoporous TiO₂ Nanoparticles: Synthesis, Growth and Photocatalytic Performance. *J. Colloid Interface Sci.* **2012**, *387*, 74–83.
- (224) Pastoriza-Santos, I.; Koktysh, D. One-Pot Synthesis of Ag@TiO₂ Core-Shell Nanoparticles and Their Layer-by-Layer Assembly. *Langmuir* **2000**, *16*, 2731–2735.
- (225) Hirakawa, T.; Kamat, P. V; Uni, V.; Dame, N. Charge Separation and Catalytic Activity of Ag@TiO₂ Core - Shell Composite Clusters under UV - Irradiation. *J. Am. Chem. Soc.* **2005**, *127*, 3928–3934.
- (226) Sun, H.; He, J.; Wang, J.; Zhang, S.-Y.; Liu, C.; Sritharan, T.; Mhaisalkar, S.; Han, M.-Y.; Wang, D.; Chen, H. Investigating the Multiple Roles of Polyvinylpyrrolidone for a General Methodology of Oxide Encapsulation. *J. Am. Chem. Soc.* **2013**, *135*, 9099–9110.

1. Introduction

- (227) Dong, Q.; Yu, H.; Jiao, Z.; Lu, G.; Bi, Y. New Facile Synthesis of One-Dimensional Ag@TiO₂ Anatase Core-shell Nanowires for Enhanced Photocatalytic Properties. *RSC Adv.* **2014**, *4*, 59114–59117.
- (228) Li, W.; Yang, J.; Wu, Z.; Wang, J.; Li, B.; Feng, S.; Deng, Y.; Zhang, F.; Zhao, D. A Versatile Kinetics-Controlled Coating Method to Construct Uniform Porous TiO₂ Shells for Multifunctional Core-Shell Structures. *J. Am. Chem. Soc.* **2012**, *134*, 11864–11867.
- (229) Aguirre, M. E.; Rodríguez, B.; Rom, E. S.; Feldho, A.; Grela, M. A. Ag @ ZnO Core A Shell Nanoparticles Formed by the Timely Reduction of Ag⁺ Ions and Zinc Acetate Hydrolysis in *N,N*-Dimethylformamide: Mechanism of Growth and Photocatalytic Properties. *J. Phys. Chem. C* **2011**, *115*, 24967–24974.
- (230) Encina, E. R.; Pérez, M. A.; Coronado, E. A. Synthesis of Ag@ZnO Core-shell Hybrid Nanostructures: An Optical Approach to Reveal the Growth Mechanism. *J. Nanoparticle Res.* **2013**, *15*, 1688.
- (231) Tom, R. T.; Nair, A. S.; Singh, N.; Aslam, M.; Nagendra, C. L.; Philip, R.; Vijayamohanan, K. .; Pradeep, T. Freely Dispersible Au@TiO₂, Au@TiO₂, and Ag@ ZrO₂ Core-Shell Nanoparticles: One-Step Synthesis, Characterization, Spectroscopy, and Optical Limiting Properties. *Langmuir* **2003**, *19*, 3439–3445.
- (232) Moran, C. H.; Rycenga, M.; Zhang, Q.; Xia, Y. Replacement of Poly(vinyl Pyrrolidone) by Thiols: A Systematic Study of Ag Nanocube Functionalization by Surface-Enhanced Raman Scattering. *J. Phys. Chem. C. Nanomater. Interfaces* **2011**, *115*, 21852–21857.
- (233) Gries, K.; Bubel, K.; Wohlfahrt, M.; Agarwal, S.; Koert, U.; Greiner, A. Preparation of Gold Nanoparticle–Poly (L-Menthyl Methacrylate) Conjugates via ATRP Polymerization. *Macromol. Chem. Phys.* **2011**, *212*, 2551–2557.
- (234) Quaroni, L.; Chumanov, G. Preparation of Polymer-Coated Functionalized Silver Nanoparticles. *J. Am. Chem. Soc.* **1999**, *121*, 10642–10643.
- (235) Mandal, T. K.; Fleming, M. S.; Walt, D. R. Preparation of Polymer Coated Gold Nanoparticles by Surface-Confined Living Radical Polymerization at Ambient Temperature. *Nano Lett.* **2002**, *2*, 3–7.
- (236) Ohno, K.; Koh, K.; Tsujii, Y.; Fukuda, T. Synthesis of Gold Nanoparticles Coated with Well-Defined, High-Density Polymer Brushes by Surface-Initiated Living Radical Polymerization. *Macromolecules* **2002**, *35*, 8989–8993.

1. Introduction

- (237) Nuss, S.; Böttcher, H. Gold Nanoparticles with Covalently Attached Polymer Chains. *Angew. Chemie (International ed. English)* **2001**, *40*, 4016–4018.
- (238) Li, D.; He, Q.; Cui, Y.; Wang, K.; Zhang, X.; Li, J. Thermosensitive Copolymer Networks Modify Gold Nanoparticles for Nanocomposite Entrapment. *Chem. - A Eur. J.* **2007**, *13*, 2224–2229.
- (239) Dong, H.; Zhu, M.; Yoon, J. A.; Gao, H.; Jin, R.; Matyjaszewski, K. One-Pot Synthesis of Robust Core/shell Gold Nanoparticles. *J. Am. Chem. Soc.* **2008**, *130*, 12852–12853.
- (240) Mi, H.-Y.; Li, Z.; Turng, L.-S.; Sun, Y.; Gong, S. Silver Nanowire/thermoplastic Polyurethane Elastomer Nanocomposites: Thermal, Mechanical, and Dielectric Properties. *Mater. Des.* **2014**, *56*, 398–404.

1. Introduction

Chapter 2: Continuous Production of Tailored Silver Nanoparticles by Polyol Synthesis and Reaction Yield Measured by X-ray Absorption Spectroscopy: Towards a Growth Mechanism.

Declaration: The SFTR was modified by Dr. Andrea Testino for the experiments, who also conducted the XRD experiments and particle size measurement with the BI-XDC. XANES measurements were conducted by Dr. Sonia Pin and Dr. Thomas Huthwelker. The nanoparticles synthesis as well as the analysis (TEM, SEM, DLS, UV-vis) were performed by Jose Enrico Q. Quinsaat.

Jose Enrico Q. Quinsaat¹, Andrea Testino^{2()}, Sonia Pin³, Thomas Hutwelker³, Frank A. Nüesch¹, Paul Bowen⁴, Heinrich Hofmann⁴, Christian Ludwig^{2,5}, and Dorina M. Opris^{1(*)}*

¹Swiss Federal Laboratories for Materials Science and Technology (Empa), Laboratory for Functional Polymers, Überlandstrasse 129, 8600 Dübendorf, Switzerland

²General Energy Research Department, Paul Scherrer Institut, Villigen PSI, 5303 Villigen, Switzerland

³Swiss Light Source (SLS), Paul Scherrer Institut, Villigen PSI, 5303 Villigen, Switzerland

⁴Ecole Polytechnique Fédérale de Lausanne (EPFL), Materials Institute, Powder Technology Laboratory (LTP), 1015 Lausanne, Switzerland

⁵École Polytechnique Fédérale de Lausanne, School of Architecture, Civil and Environmental Engineering, EPFL ENAC, 1015 Lausanne, Switzerland

2. Continuous Production of Tailored Silver Nanoparticles by Polyol Synthesis and Reaction Yield Measured by X-ray Absorption Spectroscopy: Towards a Growth Mechanism.

Abstract: In this paper two complementary topics are discussed: (i) the continuous production of silver nanoparticles (AgNPs) and (ii) the measurement of reaction yield by X-ray Absorption Near Edge Spectroscopy (XANES). The continuous *polyol synthesis* of AgNPs in grams amount and in the size range of 7-104 nm was carried out in the Segmented Flow Tubular Reactor (SFTR). Particle size was tailored by controlling the synthesis parameters such as temperature, reactant concentrations, and polyvinylpyrrolidone (PVP) molecular weight. The continuous production was tested for 4 h and the product has shown constant particle size distribution over the whole production time. Reliable continuous production of $2.3 \text{ g}\cdot\text{h}^{-1}$ of about 100 nm AgNPs can be achieved with a lab-scale SFTR. The produced particles were fully characterized with respect to size, size distribution and chemical purity. To better understand the growth mechanism, synchrotron-radiation high-resolution X-ray diffraction and X-ray absorption spectroscopy data were collected directly on the AgNPs suspension. In particular, from XANES experiments the conversion yield of Ag^+ to Ag^0 was measured. The results are consistent with a two steps process where PVP controls the particle nucleation while growth is ensured by thermally induced ethylene glycol oxidation.

2.1. Introduction

Over the last couple of decades, noble metal nanoparticles have attracted significant interest in science and industry due to their wide range of applications. Thanks to their interesting optical properties, AgNPs have gained a lot of attention in applications such as surface-enhanced Raman spectroscopy,^{1,2} optical sensing,³⁻⁵ electronics⁶ and plasmonic enhancement of absorption.⁷ Noble metal nanoparticles have also excellent surface properties that find application in catalysis⁸. AgNPs in the size range 20-50 nm are required for the preparation of conductive paste for ink-jet⁹⁻¹² or screen printing^{13,14} as well as for joining of power electronics components.¹⁵⁻¹⁷ For these latter applications, a narrow particle size distribution is mandatory because few larger particles cause nozzle clogging

2. Continuous Production of Tailored Silver Nanoparticles by Polyol Synthesis and Reaction Yield Measured by X-ray Absorption Spectroscopy: Towards a Growth Mechanism.

or defects in the conductive wires or joining layers. Excellent electrical and thermal properties, very close to the silver bulk values, are obtained upon sintering. When flexible organic substrates are used (e.g. polymeric films) the sintering temperature has to be as low as possible, ideally below 250 °C. Sintering temperature decreases with particle size driving the technology toward AgNPs. Nevertheless, very high solid loads (> 50 wt%) are required in metal pastes in order to produce optimal electrical and thermal conductivities but such ultrafine particles are very difficult to retrieve quantitatively from the synthesis mother solution. Thus, a trade-off between a low sintering temperature and facile particle retrieving is for instance the use of larger particles (30-100 nm).

Moreover, AgNPs are particularly interesting as conductive filler for the preparation of composite materials with high dielectric properties. Epoxy-based nanocomposites using Ag as filler with dielectric constants up to 300 have been reported so far.^{18,19} For this application, AgNPs with an average size up to 200 nm and narrow particle size distribution are of great interest.

Liquid phase chemical reduction is a simple and popular method to prepare metal nanoparticles from salts, since no hazardous by-products are generated. Among these methods, the polyol synthesis, intensively investigated by Xia and co-workers,^{20,21} stands out as a convenient and environmentally friendly way to generate silver nanostructures.

Different stabilizers have been used in the polyol synthesis, which include polyacrylamide,²² polyacrylic acid (PAA)²³ and polyvinylpyrrolidinone (PVP).²⁴ By tuning the synthesis parameters such as concentration,²⁴ precursor addition rate and method, temperature²⁵, average molecular weight of the stabilizer,^{26,27} reactant stoichiometry^{28, 29} or additives,³⁰⁻³³ size and shape of the nanocrystals can be controlled.

One of the limitations in producing high quality AgNPs is the poor control of mixing conditions, stirring efficiency, temperature inhomogeneity, heating and cooling rates, in the batch type reactors used. This hampers the reproducibility and product quality and

2. Continuous Production of Tailored Silver Nanoparticles by Polyol Synthesis and Reaction Yield Measured by X-ray Absorption Spectroscopy: Towards a Growth Mechanism.

uniformity.^{24,34,35} Despite the influence of the aforementioned parameters, good product quality may be obtained when working with low reactant concentrations; the product quality degradation, such as particle size distributions broadening, becomes very pronounced when attempting to scale up e.g. by increasing the reaction volume or increasing the precursor concentration. The preparation of AgNPs in batch conditions with different reaction volumes show the differing product properties and indicate that the reproducibility of the small scale reaction cannot be obtained by simply increasing the reaction volume (see Supporting Information). The heat transfer in a small volume is more efficient than in a large volume, and this affects the nucleation process. The batch reaction at smaller reaction volume yields smaller particles since there is a more rapid nucleation due to the faster heating of the reaction mixture. This also manifests itself on the better particle size distribution achieved in small scale reactions. Overall, the obtained yields of the reactions were around 70 %. The difficulty of the upscaling of the reaction can also be seen in ref. [24] where the best particle variation coefficient was obtained at a AgNO_3 concentration of around 31 mM. A further increase in the concentration, despite keeping the precursor ratio constant, led to a deterioration of the particle size distribution. A possibility to overcome scaling up problems is by multiplying or “numbering up” the small batch syntheses but can become cumbersome and expensive. An alternative is to use a continuous flow reactor. Few attempts for the continuous production of AgNPs have been reported in literature, mainly focused on small particle sizes (< 10 nm) prepared by microfluidic devices³⁶⁻³⁸ or in a tubular reactors³⁹ and syringe pumps⁴⁰ (semi-continuous): these papers deal with flow rates $< 1 \text{ ml}\cdot\text{min}^{-1}$, millimolar Ag concentrations and limited treated volumes, thus not suitable for a relatively large production (few $\text{g}\cdot\text{h}^{-1}$). An interesting experimental work is reported by Nishioka³⁸ *et al.*, where AgNPs are produced in a tubular reactor heated in a microwave oven. The authors claim that by conventional heating in an oil bath, metal silver is deposited on the tubular reactor wall and the product quality deteriorates over time while by microwave heating the process is reliable over time. Similar fouling problems are reported by Lin and coworkers.⁴⁰

2. Continuous Production of Tailored Silver Nanoparticles by Polyol Synthesis and Reaction Yield Measured by X-ray Absorption Spectroscopy: Towards a Growth Mechanism.

In this work we present the continuous polyol synthesis of AgNPs in the size range 10-120 nm using high precursor concentrations ($[\text{Ag}^+] \approx 120 \text{ mM}$ in the reaction mixture). The reaction was carried out in the Segmented Flow Tubular Reactor (SFTR)⁴¹ heated in a conventional oil bath. A prominent feature in this experimental set-up is that an inert and immiscible solvent is introduced into the system and separates the reaction mixture into identical micro-volumes before transporting them into the reactor. This principle avoids back-mixing of the reaction mixture and creates identical conditions for the produced micro-volumes in terms of heat transfer and residence time within the reactor. Moreover, as already shown for several precipitation reactions^{42,43} and here presented for the first time for AgNPs production, the immiscible fluid protects the internal tubular wall reactor allowing long production time without product quality deterioration or fouling. In this paper the effects of the reaction temperature and the average molecular weight of PVP on the resulting particle size and distribution are investigated. The products were fully characterized by Transmission Electron Microscopy (TEM), high resolution X-ray Diffraction (XRD), Thermogravimetric Analysis (TGA), Inductively Coupled Plasma Mass Spectrometry (ICP-MS), Dynamic Light Scattering (DLS), Ultraviolet-Visible Spectroscopy (UV-vis), and X-ray Disk Centrifuge Particle Size Analysis (Brookhaven Instrument, BI-XDC).

Synchrotron radiation was used both for X-ray diffraction (XRD) and for X-ray absorption spectroscopy (XAS). X-ray diffraction patterns were collected on dried powder as well as directly on the as prepared suspensions. X-ray Absorption Near Edge Spectroscopy (XANES) was used for the first time to directly measure the reaction yield.

Additionally, a correlation between the major plasmon peak in the UV-vis spectra and the TEM particle size was identified. It is demonstrated that a series of relevant analytical data can be measured directly on the particle suspension. The combination of the applied analytical techniques allowed a growth mechanism to be proposed which can explain the experimental results obtained in the continuous production using the SFTR.

2.2. Experimental Section

2.2.1. Continuous Segmented Flow Tubular Reactor (SFTR)

A schematic view of the Continuous Segmented Flow Tubular Reactor (SFTR) is illustrated in Fig. 23. More details are published elsewhere.⁴¹⁻⁴³ The SFTR is composed of a micromixer which ensures that the reactants are efficiently mixed, a segmenter, and a PTFE tubular reactor, placed in a thermostatic bath. Small suspension volumes (about 0.2 cm³) are thus created, producing microdroplets or microreactors in an immiscible fluid (*n*-dodecane, *n*-C₁₂), where the reaction – in this case Ag⁺ reduction and Ag precipitation – takes place. This small volume ensures a high homogeneity of the droplets and each of them is facing the identical *history* (e.g., residence time and heat exchange) throughout the tube.

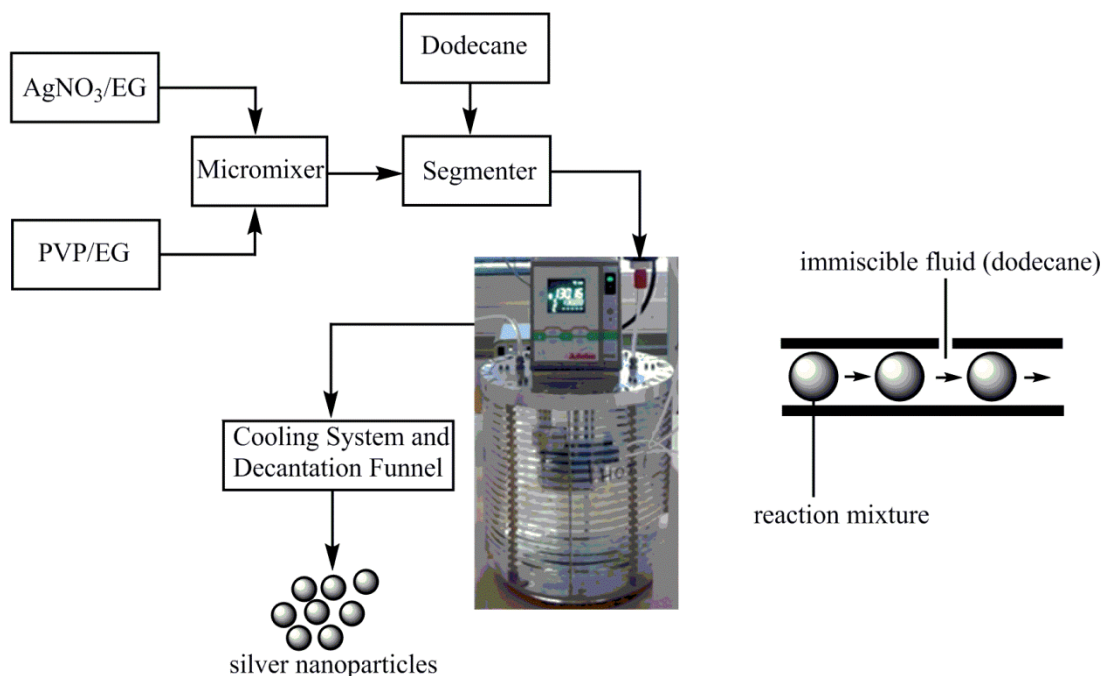


Fig. 23: Schematic illustration of the SFTR. The two reactants are introduced separately into the system and pass through various systems (micromixer, segmenter) in order to produce reaction

2. Continuous Production of Tailored Silver Nanoparticles by Polyol Synthesis and Reaction Yield Measured by X-ray Absorption Spectroscopy: Towards a Growth Mechanism.

microdroplets prior to going through the heated reactor where the formation of the particles occurs. The reaction or the precipitation occurs in the mixing chamber and/or induced by the rapid temperature change when the microreactors are heated in the thermostatic bath. According to fluid dynamic modelling, the temperature of the droplets reaches 95 % and 99 % of the bath temperature within 6 and 10 s, respectively.⁴⁴ Fouling on the inner tubular reactor wall is avoided due to the immiscible fluid by forming a thin film on the tube surface^{42,45} and thus allowing long continuous process times (> 12 h). The residence time is determined by the pump flow rates and the tube length and adjusted according to the specific reaction kinetics. This is a steady-state process in which each step (mixing and reaction) is well separated, leading to a better control and reproducibility. If needed, after the tubular reactor, in the process line, a heat-exchanger can be placed to cool down the reacting mixture and quench the reaction. Finally, a separation unit or decanter allows the separation of the product from the immiscible fluid; the product – particle in suspension – is collected, while the immiscible fluid is recycled in the process for environmental and cost concerns.

2.2.2 Polyol Synthesis of Silver Nanoparticles in the SFTR

All chemicals were purchased from Sigma Aldrich and used as received. Ethylene glycol (EG) was distilled prior to use. A modified procedure from Xia and co-workers was applied for AgNPs synthesis.⁴⁶ Two separate solutions of AgNO₃ (0.236 M) and PVP 10: $M_w = 10'000 \text{ g}\cdot\text{mol}^{-1}$ or PVP 40: $M_w = 40'000 \text{ g}\cdot\text{mol}^{-1}$ (2.16 M in terms of repeating units) were prepared. PVP and AgNO₃ were dissolved at 70 °C under sonication and at room temperature under magnetic stirring, respectively. In order to protect the AgNO₃ solution from sunlight, the container was shielded off by wrapping aluminium foil around it. The two reactants were introduced into the reactor system by pumping with two HPLC pumps at a rate of 1.5 mL/min. After forming the reaction mixture in the micromixer, the micro-volumes were made in the segmenter by passing through *n*-C₁₂ at a speed of 24.8 mL/min.

2. Continuous Production of Tailored Silver Nanoparticles by Polyol Synthesis and Reaction Yield Measured by X-ray Absorption Spectroscopy: Towards a Growth Mechanism.

In the experimental trial, the temperature range was kept between 120 and 150 °C. The residence time of the micro-volumes within the tube in the thermostatic bath was 12 min. In a second tubular section, the segmented suspension was cooled down. The silver sol was then collected in the decantation funnel and *n*-C₁₂ separated. The theoretical AgNPs production (100 % yield) corresponds to 2.26 g AgNPs h⁻¹.

2.2.3. Materials and Methods

Particles were characterized by TEM images (Philips CM30) measuring over 400 particles, DLS (Malvern Zetasized Nano ZS), BI-XDC (Brookhaven Instruments) and UV-vis (Cary 50 Spectrophotometer). TGA was carried out with a Mettler Toledo TGA/SDTA 851e in the temperature range 25-500 °C (heating rate 5 K min⁻¹). About 20 mg of Ag powders were treated in Ar/O₂ (20 % O₂, 15 ml·min⁻¹) atmosphere. A second run under reducing atmosphere Ar/H₂ (5 % H₂, 10 mL·min⁻¹) was carried out on selected samples. Chemical analysis was carried out with an Agilent 7700x ICP-MS after digestion of the samples in HNO₃ and dilution in milliQ water, using external calibration standards. XRD patterns and XANES measurements were done at the Swiss Light Source (SLS, Paul Scherrer Institut, Villigen PSI, Switzerland). XRD were collected at the Material Science beam line (X04SA), at 25 keV and using a 0.3 mm glass capillary.⁴⁷ Cell parameters were calculated by Rietveld refinement using the GSAS (General Structural Analysis Software)⁴⁸ and ICSD (Inorganic Crystal Structure Database).⁴⁹ Crystallite sizes (d_{XRD}) were estimated from the full path refinement using the GSAS (profile function #4).⁵⁰ Moreover, diffraction patterns were collected directly on the as prepared suspension, through a liquid cell sample holder with 10 mm of optical path.

2. Continuous Production of Tailored Silver Nanoparticles by Polyol Synthesis and Reaction Yield Measured by X-ray Absorption Spectroscopy: Towards a Growth Mechanism.

In order to understand the influence of the key parameters on the precipitation process, the reaction yield (Y) needs to be measured. Y is defined as

$$Y = \frac{Ag_n^0}{Ag_T} \quad (\text{Eq. 42})$$

where Ag_n^0 and Ag_T are the amount of AgNPs obtained and the overall amount of silver in the system, respectively. Experimentally we notice that when the reaction is complete ($Y = 100\%$) the as-prepared particle suspensions are stable over time with a shelf-time of several months.

For $Y < 100\%$, silver mirror was formed over time on the storing vessel because of the reducing environment and the unreacted Ag^+ . Thus, the overall amount of silver is:

$$Ag_T = Ag_n^0 + Ag_m^0 + Ag^+ \quad (\text{Eq. 43})$$

where Ag_m^0 and Ag^+ are metal silver deposited on the vessel as mirror and the unreacted silver ions, respectively.

The measurement of the reaction yield is not a trivial analytical problem to solve since: (i) it is not always possible to retrieve the solid quantitatively from the suspension; (ii) it is difficult to carry out chemical analysis on the supernatant because of the presence of residual particles in suspension; (iii) the chemical method, e.g. by titration with chlorine ions without AgNPs separation, may be affected by the nanoparticles interference. A different approach needs to be found out that (i) it is sensitive to the Ag^+/Ag^0 ratio,

2. Continuous Production of Tailored Silver Nanoparticles by Polyol Synthesis and Reaction Yield Measured by X-ray Absorption Spectroscopy: Towards a Growth Mechanism.

(ii) does not require solid-liquid separation, (iii) can be carried out on the liquid suspension just after the synthesis, ideally on-line, when $Ag_m^0 = 0$.

Here, a novel approach to measure the reaction yield by X-ray Absorption Near Edge Spectroscopy (XANES) is presented. XANES is a direct method to quantify the oxidation state of the absorbing atom. By fitting (Linear Combination Fitting, see later in this section), the relative amount of Ag^+ and Ag^0 can be calculated. Thus, when $Ag_m^0 = 0$, the reaction yield is calculated as

$$Y = \left(1 + \frac{Ag^+}{Ag_n^0}\right)^{-1} \quad (\text{Eq. 44})$$

In this paper, two Ag absorption edges were measured (K and L_3) and compared in terms of analytical results and experimental requirements.

The Ag L_3 -edge XANES spectra were collected at the PHOENIX beamline (X07MA). The beamline was equipped with a Si(111) monochromator tuned to the Ag L_3 -edge, assigned to 3351 eV using a thin Ag metal foil, also used as a standard for Ag^0 specie. The experimental set-up closely follows the one reported in ref. [51]. The measurements were carried out in fluorescence mode, at room temperature in a 100 mbar He atmosphere. An appropriate sample concentration was chosen, in order to give the maximum contrast at the Ag- L_3 edge and minimize the over-absorption effects. Actually, the as-synthesized suspensions were used without dilution because preliminary tests demonstrate that over-absorption effects were negligible. To measure the incoming photon flux (I_0), a polyester foil (Goodfellow), coated with 50 nm of Ni, was put into the beam at the exit of the focusing optics, thus behind the last aperture before the sample. The total electron yield generated on the foil by the beam served as measure of I_0 .

2. Continuous Production of Tailored Silver Nanoparticles by Polyol Synthesis and Reaction Yield Measured by X-ray Absorption Spectroscopy: Towards a Growth Mechanism.

The Ag-K edge XANES spectra were collected at the Super-XAS beamline (X10DA). The intensity of the incident beam (I_0) was measured with an argon filled ion chamber. The Ag^+ standard and the sample suspensions were properly diluted in order to minimize hole-effects and then placed in 1 mm glass capillaries. X-ray absorption data from the sample were measured in transmission mode. A second argon filled ion chamber was used to measure I_1 . A thin sample of Ag metal foil was used for calibration and also as a standard for Ag^0 specie. The calibration measurement was made with a third argon filled ion chamber (I_2) placed after I_1 . The position of the metal absorption edge (Ag, 25514 eV) could then be determined by placing the Ag metal standard between ion chambers I_1 and I_2 and measuring the absorption coefficient of the metal standard. In both XAS experiments a solution of Ag^+ , stabilized with HNO_3 , was used as standard for Ag^+ species.

The XANES spectra were analysed by using the Linear Combination Fitting (LCF)⁵²⁻⁵⁵ option available in ATHENA.⁵⁶ With this method, the X-ray absorption spectrum is modelled by least squares fitting using linear combination of known species to fit the unknown spectrum. The underlying principle is the additive nature of the absorption from each species in the sample. The total absorption coefficient can be written as a sum of the chemical forms or species. Mathematically, $Model = \sum_i f_i(STD_i)$ where $Model$ is the least square fit to the sample spectrum over a selected energy range, and f_i is the scaling factors applied to each spectrum of the corresponding standard (STD_i) across the energy range of the fit. The scaling factors obtained from LCF represent the fraction of each standard species in the unknown sample. The LC fit has been carried out in the energy range 25400 – 25700 eV for the Ag-K edge and in the 3300 – 3450 eV range for the Ag-L₃ edge. The relative weights of the two reference standards (Ag^0 and Ag^+) are allowed to vary from 0 to 1, and the absorption edge energies, previously aligned, are kept fixed during the analysis.

2.3. Results

Following a single droplet within the tubular reactor, a clear colour evolution occurs over time, from colourless transparent to pale transparent yellow to deep red or dark suspensions. The colour change is due to the well-known localized surface plasmon resonance spectra that highly depend upon their size, shape, and surrounding environment. The transparent solution indicates that no reduction occurs during mixing at room temperature, while the reaction starts, induced by the temperature, in the thermostatic bath. The colour change is thus due to the AgNPs nucleation and growth. Dark suspensions are obtained at high reaction yield and for rather large particle (> 60 nm).

The collected products, in form of suspensions, were characterized both as suspension and as washed and dried powders. Tab. 4 summarizes the synthesis condition and the average particle size of the 7 series of samples produced. The samples were collected for about 30 minutes of continuous production. At $T = 120$ °C and PVP 40k, the reaction does not occur. It is worth noting that, in the tested temperature conditions (≤ 150 °C), if the process is carried out without PVP, the silver reduction does not occur. Fig. 24 shows representative TEM images of the samples G0, G1, G2, and G3 prepared with PVP 10k. The average particle size obtained ranged from 23(4), 25(4), 47(8) and 58(7) nm by conducting the experiments at temperature 120, 130, 140 and to 150 °C, respectively. In the parenthesis, the measured standard deviation of the particle population is reported, which evaluates the particle size distribution span. Fig. 25 show the products (samples G4, G5 and G7) obtained when PVP 40k was used. The particle sizes was 7(2), 79(15) and 104(20) nm for temperatures of 130, 140 and 150 °C, respectively. The particle size distribution measured from the TEM images are also reported as inset (Fig. 24 and Fig. 25).

2. Continuous Production of Tailored Silver Nanoparticles by Polyol Synthesis and Reaction Yield Measured by X-ray Absorption Spectroscopy: Towards a Growth Mechanism.

Tab. 4: Summary of the *polyol synthesis* of AgNPs in the SFTR. In the parenthesis is reported the measured standard deviation of the particle population.

Sample	Temperature (°C)	PVP M_w (g·mol ⁻¹)	TEM size (nm)	Mean diameter (nm) ^a
G0	120	10k	23 (4)	14 (4)
G1	130	10k	25 (4)	20 (8)
G2	140	10k	47 (8)	33 (12)
G3	150	10k	58 (7)	56 (17)
G4	130	40k	7 (2)	9 (2)
G5	140	40k	79 (15)	107 (30)
G7	150	40k	104 (20)	123 (32)

^aMean numerical diameter. In the parenthesis is reported the measured standard deviation of the particle population.

2. Continuous Production of Tailored Silver Nanoparticles by Polyol Synthesis and Reaction Yield Measured by X-ray Absorption Spectroscopy: Towards a Growth Mechanism.

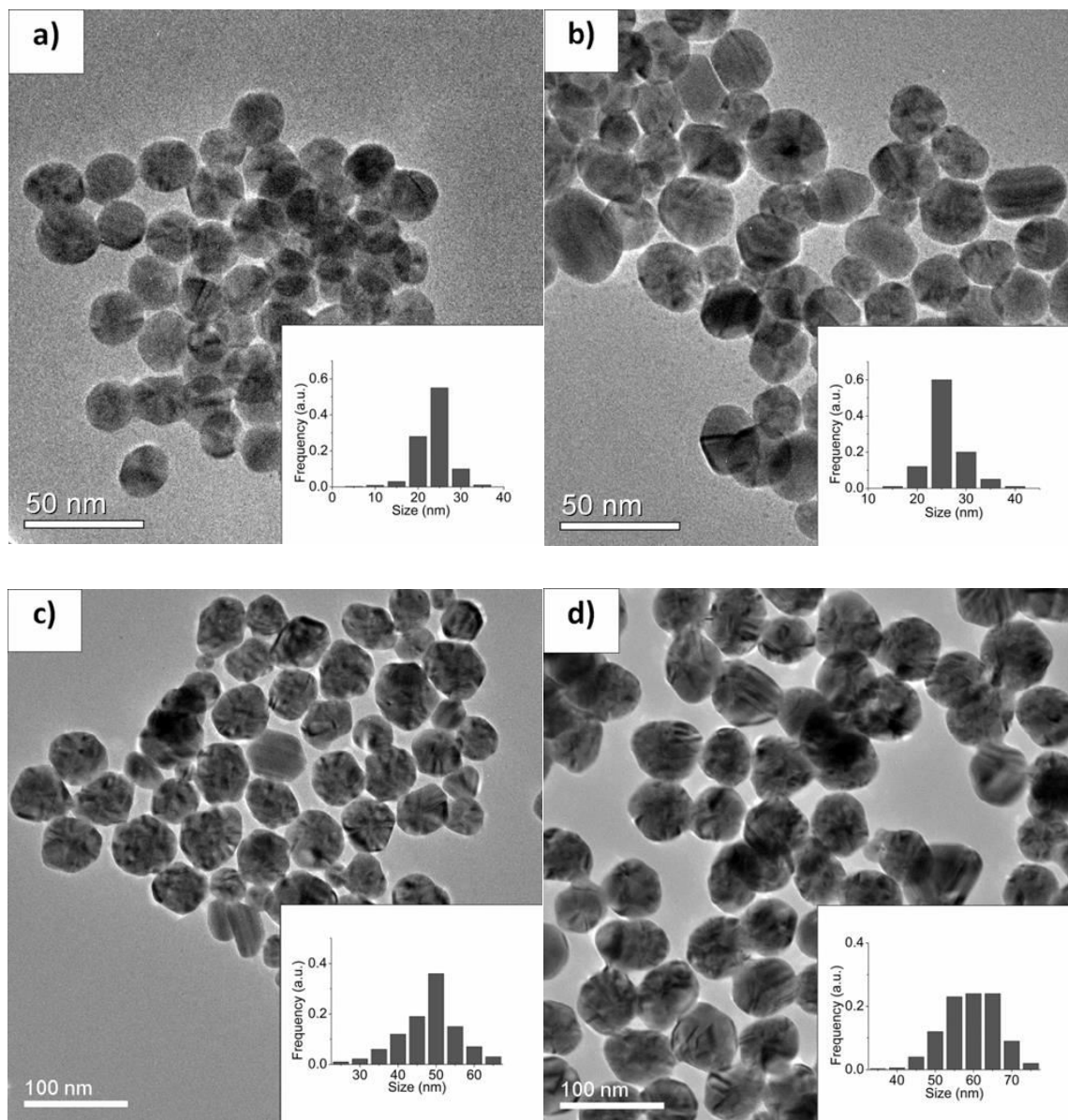


Fig. 24: AgNPs prepared with PVP 10k: (a) G0, (b) G1, (c) G2 and (d) G3.

2. Continuous Production of Tailored Silver Nanoparticles by Polyol Synthesis and Reaction Yield Measured by X-ray Absorption Spectroscopy: Towards a Growth Mechanism.

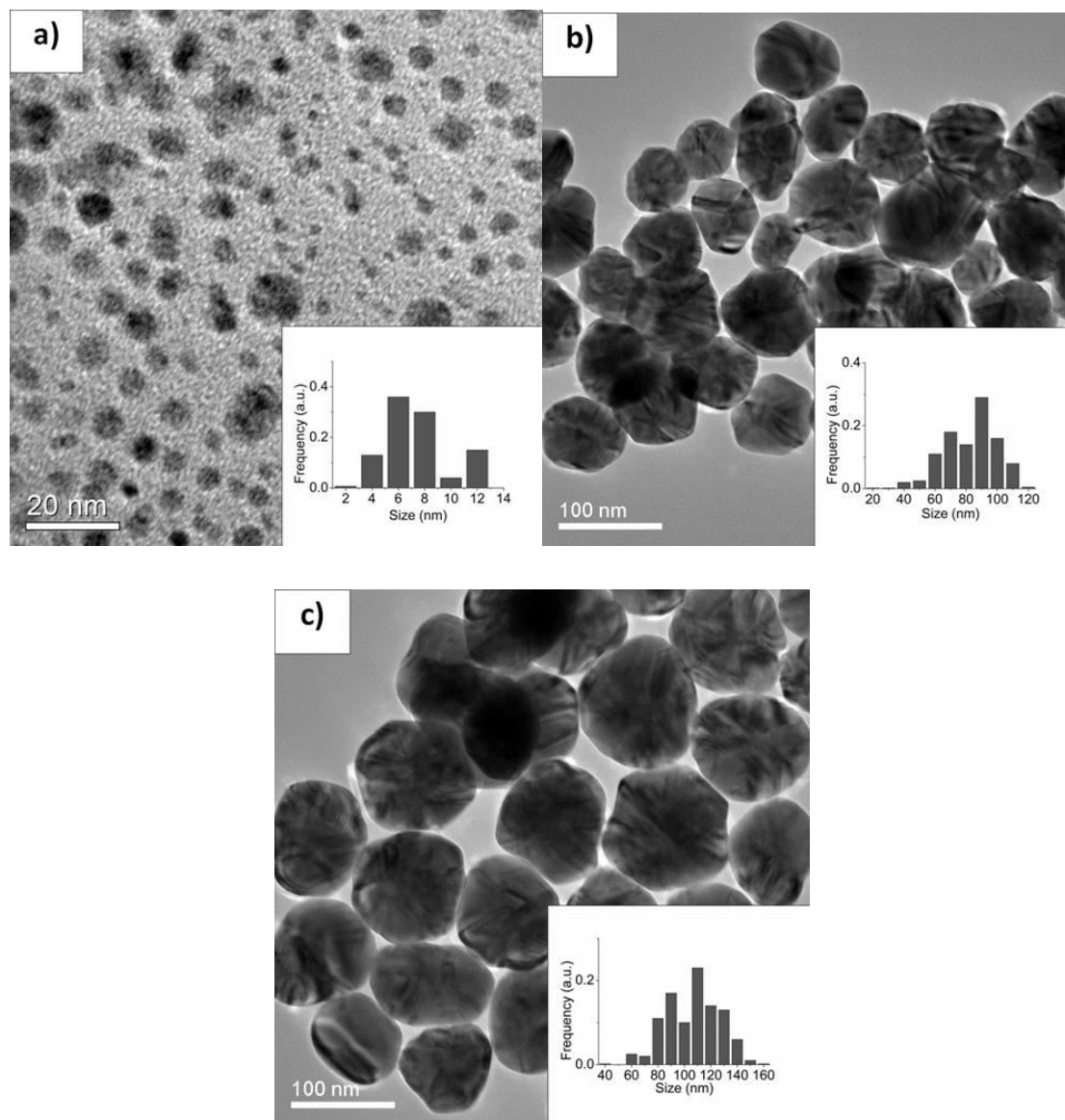


Fig. 25: AgNPs prepared with PVP 40k: (a) G4, (b) G5 and (c) G7.

2. Continuous Production of Tailored Silver Nanoparticles by Polyol Synthesis and Reaction Yield Measured by X-ray Absorption Spectroscopy: Towards a Growth Mechanism.

After washing, the surface plasmon bands in the visible region were measured by UV-Vis spectrometry. A bathochromic shift of the major plasmon peak λ_{\max} from 402 to 453 nm was observed as the average TEM diameter increases from 7 to 104 nm (Fig. 26 and Fig. 27). This correlation is shown in Fig. 26. The position of λ_{\max} depends on the solvent used for the measurements.⁵⁷ The presence of a second broad plasmon peak for the sample with particles of 23 nm diameter might be indicative for some occurring agglomeration, although the DLS spectrum (Fig. 28) and TEM images did not provide substantial proof for their existence. Nevertheless, particle agglomeration can be assumed, especially with decreasing particle size due to enhanced attractive forces acting between them. The shoulders evident on the UV-vis spectra of the sample G0 can also be explained either by the occurrence of non-spherical shapes within the particle population e.g. oblate spheroids. This effect is pronounced for small particle sizes, but vanishes at larger particle sizes due to the larger particle size distribution.⁵⁸

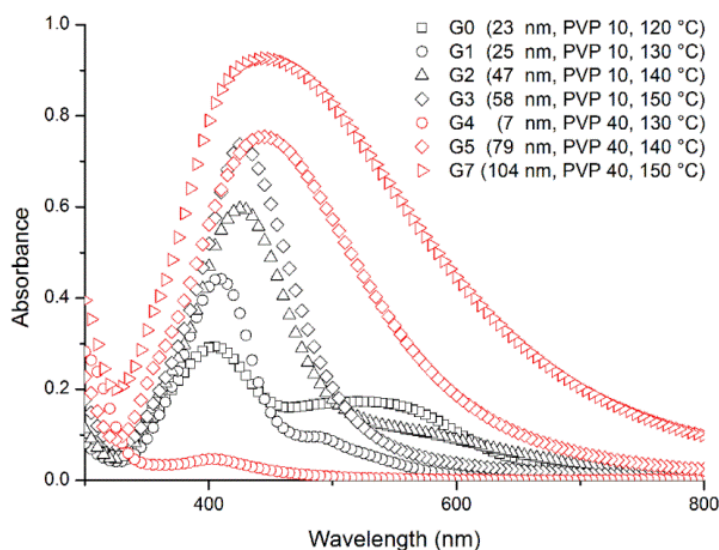


Fig. 26: UV-vis spectra of the AgNPs prepared with the SFTR.

2. Continuous Production of Tailored Silver Nanoparticles by Polyol Synthesis and Reaction Yield Measured by X-ray Absorption Spectroscopy: Towards a Growth Mechanism.

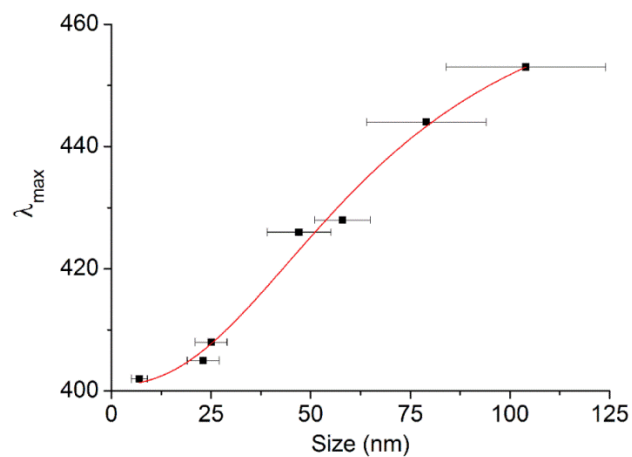


Fig. 27: Correlation of the mean particle diameter (measured with TEM) with the position of the absorption maxima in the UV-vis spectra.

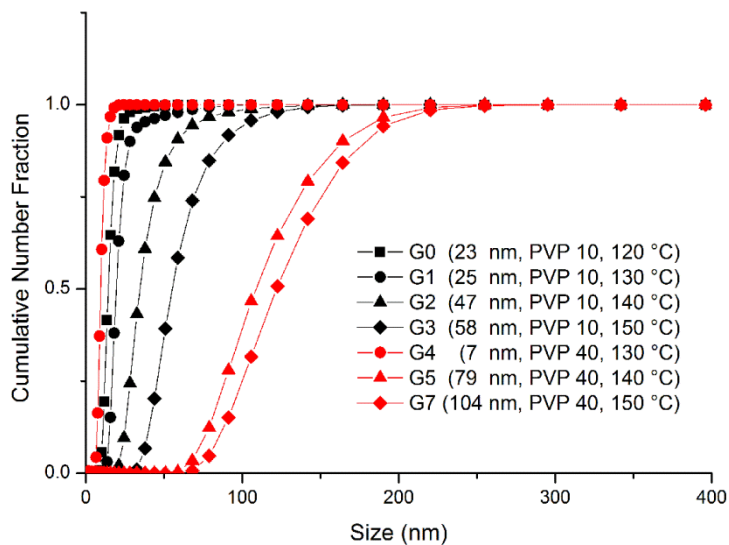


Fig. 28: Particle size number distribution measured by DLS of the AgNPs prepared with the SFTR.

2. Continuous Production of Tailored Silver Nanoparticles by Polyol Synthesis and Reaction Yield Measured by X-ray Absorption Spectroscopy: Towards a Growth Mechanism.

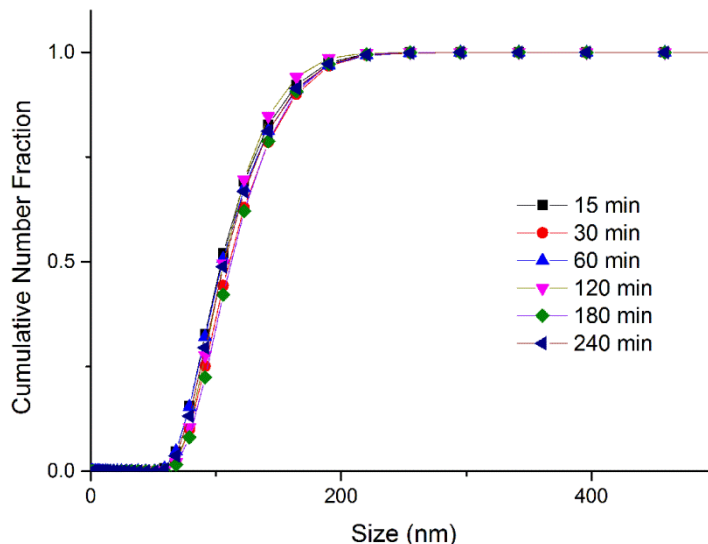


Fig. 29: Particle size number distribution measured by DLS of the AgNPs prepared during the long term reaction (L1). Particles were analysed at different reaction times.

The synthesis reliability against time was conducted by producing AgNPs for about 4 h at 150 °C using PVP 40k (sample L1, equivalent to sample G7). These synthesis conditions have been selected because complete reduction to Ag^0 was obtained (see later in this section). Suspension aliquots were taken at regular times and DLS particle size distributions recorded. Fig. 29 shows the overlapping particle size distributions and Tab. 5 shows the percentile diameters d_{n10} , d_{n50} and d_{n90} against time. The mean particle diameter of the collective samples (all L1 aliquots) was measured by DLS, by TEM image, as well as by BI-XDC. Results are summarized in Tab. 6.

2. Continuous Production of Tailored Silver Nanoparticles by Polyol Synthesis and Reaction Yield Measured by X-ray Absorption Spectroscopy: Towards a Growth Mechanism.

Tab. 5: Percentile Diameters measured with DLS for AgNPs (L1) prepared at 150 °C running over 4 hours.

Aliquot taken after reaction time (min)	d_{n10} (nm)	d_{n50} (nm)	d_{n90} (nm)	Mean diameter ^a (nm)
15	73	99	146	110 (27)
30	76	104	154	112 (29)
60	69	96	146	104 (30)
120	71	95	139	105 (25)
180	76	104	152	106 (30)
240	72	98	147	101 (30)

^aMean numerical diameter. The measured standard deviation of the particle population is reported in parenthesis.

Tab. 6: Mean diameter for AgNPs (L1) prepared at 150 °C running over 4 hours. In the parenthesis is reported the measured standard deviation of the particle population.

	DLS d_{n50} (nm)	TEM (nm)	XDC (nm)
Particle size	100 (30)	87 (17)	91 (26)

The reaction yield was determined on selected samples by XANES spectroscopy. Both the Ag L₃-edge and K-edge XANES spectra have been collected. The normalized $\mu(E)$ data obtained for the two Ag species (Ag⁺ and Ag⁰) were linearly combined to fit the

2. Continuous Production of Tailored Silver Nanoparticles by Polyol Synthesis and Reaction Yield Measured by X-ray Absorption Spectroscopy: Towards a Growth Mechanism.

normalized $\mu(E)$ data of selected samples using the Linear Combination Fitting (LCF) method.⁴⁹⁻⁵² The low energy of the Ag-L₃ edge (3351 eV) allows reducing the radiation damage on the samples during the measurements, but the interference from other edges (i.e. Ag-L₂ at 3524 eV) cannot be excluded, limiting the energy range in which the samples can be measured. Moreover, the low energy of the Ag-L₃ edge challenges the measurement from the point of view of the experimental set-up and materials needed for the optical windows. For these reasons, on selected samples, Ag-K edge (25514 eV) XANES spectra have been collected as well. In this case, because of the higher energy used, the beam damage is more probable, but the measurement can be much faster and the experimental setup as simple as a standard glass capillary.

The percentage of Ag⁺ and Ag⁰, the corresponding errors, the goodness-of-fit (*R*-factor, i.e. a measure of mean square sum of the misfit at each data point), the calculated yield, and the gravimetric yield, which was measured by weighting the collected product after 3 consecutive washing and centrifugation cycles, is reported in Tab. 7. The reported incertitude on the measurement is obtained from the ATHENA software and refers to the error on the LCF. Sample G7 and L1 are completely converted to Ag⁰ and the fitting is actually not necessary because their XANES spectra overlap the Ag metal standard. It is worth noting that the incertitude of the measurement technique has to be experimentally evaluated by *ad-hoc* trials. For the time being, based on our experience and the literature⁵⁹⁻⁶¹, the measurement incertitude can be estimate below 3 %.

As example, Fig. 30 reports the normalized of Ag L₃-edge and K-edge XANES spectra for the sample G3 and G4, respectively. The goodness-of-fit can also be seen from the little difference (plotted as green line) between the experimental and LC fitted data.

2. Continuous Production of Tailored Silver Nanoparticles by Polyol Synthesis and Reaction Yield Measured by X-ray Absorption Spectroscopy: Towards a Growth Mechanism.

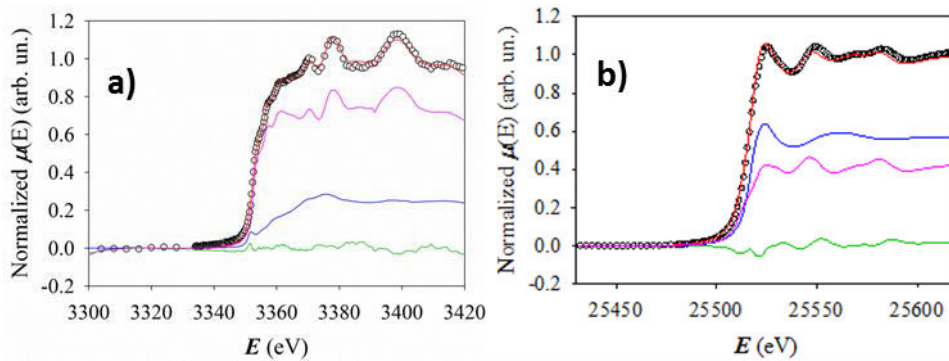


Fig. 30: Example of LC fit for (a) Sample G3 (Ag-L₃) and (b) Sample G4 (Ag-K) edge XANES spectrum. Circles: experimental data; Red line: LC fit; Blue line: fraction of Ag⁺ making up the fit; Pink line: fraction of Ag⁰ making up the fit; Green line: Difference between experimental data and LC fit.

Tab. 7: Summary of the amount of Ag⁺ and Ag⁰ of selected samples determined by XANES spectroscopy (L₃-edge or K-edge). The yield is determined by (Eq. 42).

	Ag ⁰ (%)	Ag ⁺ (%)	R- factor (%) [*]	Yield XANES (%)	Yield gravim. (%)
G3 (L ₃ -edge)	74 ± 1	25 ± 1	0.002	75 ± 2	73 ± 5
G4 (K-edge)	57 ± 2	41 ± 2	0.006	58 ± 4	<i>n.d.</i>
G5 (K-edge)	92 ± 1	5 ± 1	0.002	95 ± 2	89 ± 5
G5 (L ₃ -edge)	93 ± 1	6 ± 1	0.002	94 ± 2	89 ± 5
G7 (L ₃ -edge)	> 97	-	-	> 97	95 ± 5
L1 (L ₃ -edge)	> 97	-	-	> 97	95 ± 5

^{*} defined as $R = \frac{\sum (XANES_{measured} - XANES_{calculated})^2}{\sum (XANES_{measured})^2} \times 100$

2. Continuous Production of Tailored Silver Nanoparticles by Polyol Synthesis and Reaction Yield Measured by X-ray Absorption Spectroscopy: Towards a Growth Mechanism.

Tab. 7 reports the yield measured by the gravimetric method. In this case the product needs to be washed and retrieved by centrifuging for at least three times. This procedure was not possible for sample G4 because of the small particle size. The gravimetric yields are in good agreement with the XANES values, considering that a fraction of NPs can be lost during the washing and centrifugation treatments.

The purity of selected solid samples, after centrifugation, washing, and drying were analyzed by ICP-MS and TGA. The chemical analysis carried out on samples G3 and G7 showed no relevant contaminants ($\text{Fe} \approx 20 \text{ ppm}$; $\text{Na} \approx 5 \text{ ppm}$; Ni , Zn , $\text{Mo} \approx 2 \text{ ppm}$) and the Ag content were about 90 % and 97 %, respectively. These results are coherent with the TGA experiments which show that the weight loss against temperature (Fig. 31) may be attributed to organic residuals on the particle surface. The organics are completely burned out at about 280 °C for samples L1 and G7. Sample G3 shows a different behaviour with a clear two-step weight loss. The reason of the second weight loss, which is completed at 500 °C, is under investigation, but could be ascribed to the lower molecular weight of PVP used in the synthesis.

A subsequent thermal treatment under reducing conditions (5 % H_2 , balance Ar) up to 500 °C (not shown) was performed. The absence of weight changes confirm that the samples were not oxidized due to the thermal treatment carried out in air.

2. Continuous Production of Tailored Silver Nanoparticles by Polyol Synthesis and Reaction Yield Measured by X-ray Absorption Spectroscopy: Towards a Growth Mechanism.

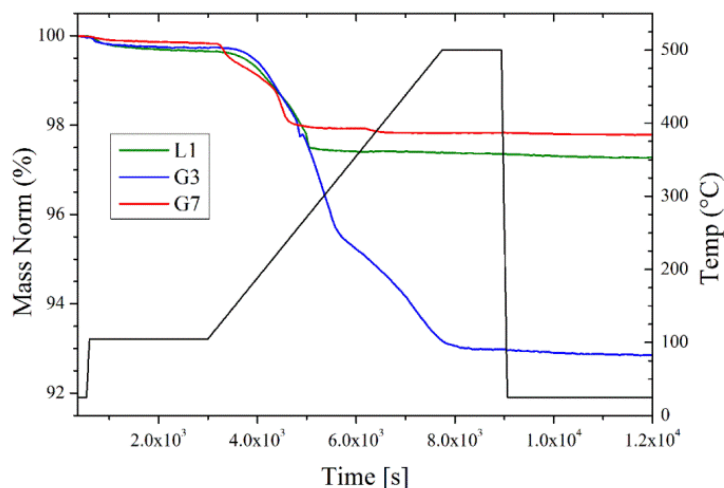


Fig. 31: TGA measurements conducted on the recovered powders from samples G3, G7 and L1.

High resolution XRD patterns on powders were collected on selected samples (G3, G4, G5, G7). As example, Fig. 32 shows the powder diffraction pattern for sample G7. Organic residues, in agreement with the TGA experiments, gave a relevant background contribution. The best fit obtained by Rietveld refinement suggests the presence of two populations of crystallites of about 10 nm and 80 nm. The calculated crystallite size is smaller than the TEM particle size but in agreement with the multi-domain substructure of the particles (Fig. 24 and Fig. 25). The diffraction patterns do not show any crystalline secondary phases. Fig. 32 shows the diffraction patterns collected on the as prepared suspensions (G3, G4, G5) as well. In these cases, the peak broadening is a complex convolution of particle size and the liquid suspension thickness under analysis but the collected patterns show good signal-to-noise ratio. It can be seen that sample G4 has no diffraction peaks because the particles are both small (7 nm) and few (low conversion yield), while G3 and G5 (and G7, not showed) gave excellent signals. Again, no secondary phases were detected.

2. Continuous Production of Tailored Silver Nanoparticles by Polyol Synthesis and Reaction Yield Measured by X-ray Absorption Spectroscopy: Towards a Growth Mechanism.

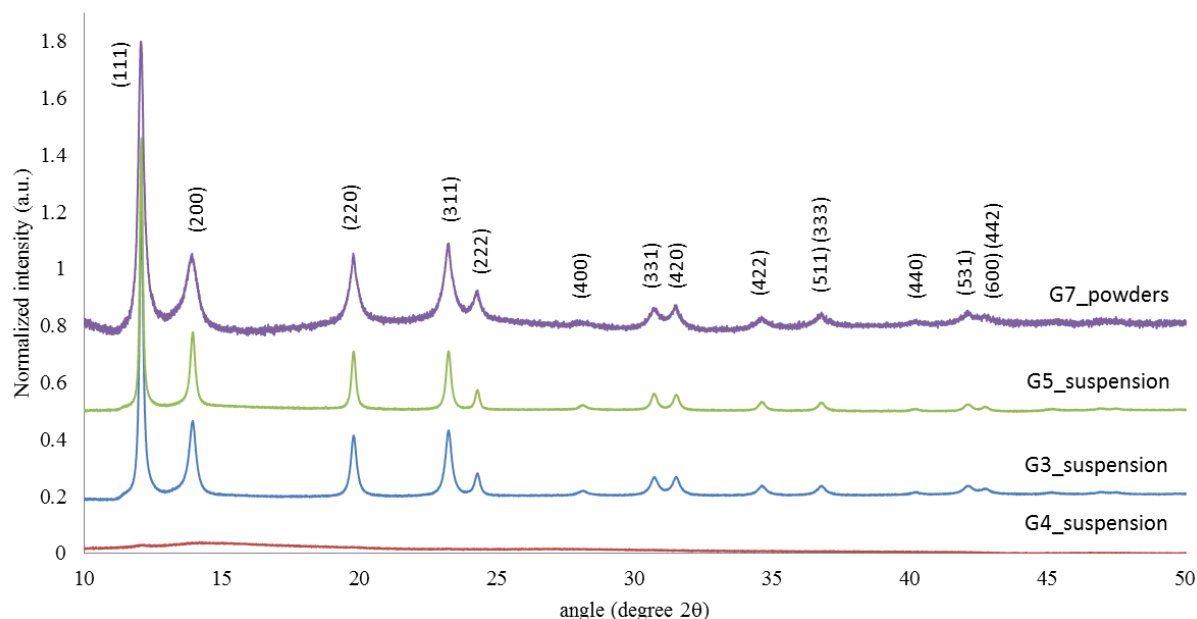


Fig. 32: Diffraction patterns collected on powder (G7) or on the as prepared suspension (G3, G4, G5) after background subtraction.

2.4. Discussion

Due to the evident colour change during the reaction progress (due the surface plasmon effect which strongly depends on the Ag^0 particle size), the drop-to-drop homogeneity can be easily verified along the tubular reactor. The constant and reproducible colour of the droplets is a clear demonstration of the system stability. However, in some cases, for instance when a small gas bubble was dosed by one pump at the beginning of an experimental trial, a droplet of different colour was immediately recognized in the tube due the chemical difference of that droplet with respect to the neighbours' droplets.

The powders produced over 4 h shows constant particle size distribution, demonstrating that the preparation of AgNPs can be extended for a long production time with constant product properties.

2. Continuous Production of Tailored Silver Nanoparticles by Polyol Synthesis and Reaction Yield Measured by X-ray Absorption Spectroscopy: Towards a Growth Mechanism.

Thermogravimetric measurements and chemical analysis gave coherent results: the product consists of pure Ag and organic residues (about 3 wt%), most probably PVP on the particles surface. The organic residues are burned out at about 250 °C. The overall metallic contaminants concentration is below 50 ppm.

The particle size distributions of the produced samples were measured by several techniques and a general good agreement among the measurements were demonstrated. We can conclude that the most convenient method is DLS because (i) limited amount of product is needed, (ii) it is fast and (iii) inexpensive, and (iv) reliable results are obtained. The major drawback is that DLS is an offline method. Nevertheless, the correlation between TEM size and UV-Vis spectroscopy (Fig. 27) open the possibility to monitor particle size on-line using UV-Vis spectroscopy.

The AgNP_s conversion yield was measured from XANES spectra using both K and L₃-edges, giving comparable results (Sample G5, Tab. 4). The higher energy of the K-edge greatly simplifies the experimental set-up and the feasibility of the direct measurement of the reaction yield on the suspension was demonstrated (Fig. 30). Similarly, X-ray diffraction patterns of the powder may be efficiently measured from the suspension with a liquid sample holder cell, as demonstrated in Fig. 32. It turns out that these investigations may be carried out directly on the as prepared suspension, ideally *in situ* in the SFTR reactor. In principle, the most relevant particle formation parameters such as primary particle size by XRD (the crystallite size), secondary particle size by UV-vis spectroscopy (thanks to correlation with the TEM size) the particles, and conversion yield by XANES might be studied *in situ* and time-resolved, allowing the detailed kinetic study of particle formation.

As shown in Tab. 4, average particle diameter can be tuned by changing the reaction temperature and the PVP average molecular weight. The effect of the temperature has also a relevant influence on the conversion yield and size: higher temperatures gave higher yields and bigger particle sizes. Moreover, the particle size distribution span remains

2. Continuous Production of Tailored Silver Nanoparticles by Polyol Synthesis and Reaction Yield Measured by X-ray Absorption Spectroscopy: Towards a Growth Mechanism.

almost unchanged against yield. Such behaviour may be explained by a two stage process where nucleation and growth occur on two different times scales. It is plausible to consider that particle nucleation occurs only in a limited time frame at the beginning of the precipitation – which visually corresponds to the time frame from colourless solution to pale yellow suspension – producing a defined number of small particles. Then, this population of particles grow over time, consuming Ag^+ ions, confirming that reduction to Ag^0 occurs. The reducing agent is the *in situ* generated glycolaldehyde formed by oxidation of EG at elevated temperatures. It should be mentioned here that this oxidation process is strongly accelerated by the temperature.⁶² For this reason, at 130 °C and 12 min of reaction time, the conversion yield is very low while at 150 °C the reaction is quantitative for the same reaction time.

Nucleation could be controlled by PVP.⁶³ This hypothesis is supported by the fact that (i) tests carried out without PVP led to no precipitation of AgNPs at all, (ii) it is known that PVP acts both as stabilizer and reductant,⁶⁴ and (iii) the particle size decreases with PVP molecular weight. Commercially available PVP are commonly terminated with hydroxyl (-OH) end-groups⁶⁵. These terminal groups act as reducing agent: keeping constant the ratio between polymer repetition unit and silver, the number of terminal groups increases for shorter polymer backbone, i.e., PVP 10k has more hydroxyl groups compared to PVP 40k. Thus, provided that the particles can grow (i.e., the temperature is high enough), PVP 10k can produce more nuclei, (i.e., smaller particles) than PVP 40k.

We conclude that our experimental results are coherent with a two sub-sequent steps: (i) nucleation, which is controlled by the amount of PVP terminal groups and (ii) particle growth, which is tuned by the temperature through its influence on the EG reduction potential. In order to consolidate these findings, a detailed experimental trial on precipitation kinetics is currently in progress.

2.5. Conclusions

A novel method to prepare AgNPs in a continuous way has been presented. Here, the segmented flow kept in the reactor provides optimization beyond to state-of-the-art of continuous synthesis methods by creating more homogenous reaction conditions. The variation of the reaction temperature and the average molecular weight of the PVP lead to the systematic change in the average particle sizes and reaction yield. Our experimental data suggest that PVP is controlling the nucleation step while particle growth is tuned by the temperature through its influence on the EG reduction potential.

Particle size and reaction yield data have been combined in order to outline a rational (nucleation and growth) formation path. The method to measure the reaction yield was one of the most relevant achievements of this experimental work. Yield was measured directly in the produced particle suspension by linear fit of XANES spectra. Synchrotron-light diffraction patterns were also collected from the suspension. Moreover, a clear correlation between TEM size and the major plasmon peak of the UV-Vis spectra has been identified. We have demonstrated that key parameters such as primary particle size, secondary particle size, and conversion yield may be investigated *in situ* and time-resolved. Thus, a comprehensive particle formation mechanism can be investigated.

Finally, the potential of the SFTR to prepare high amounts of AgNPs over a long period was demonstrated by running the reaction for 4 h, obtaining constant particle size distribution with production rate $> 2 \text{ g}\cdot\text{h}^{-1}$.

2.6 Acknowledgements

We gratefully acknowledge the Swiss National Science Foundation, the Swiss Federal Laboratories for Materials Science and Technology (Empa, Dübendorf) and Paul-Scherrer Institut (Villigen) for providing financial support and infrastructure for our research. We

2. Continuous Production of Tailored Silver Nanoparticles by Polyol Synthesis and Reaction Yield Measured by X-ray Absorption Spectroscopy: Towards a Growth Mechanism.

thank Dr. Luca Quaroni, Dr. Antonio Cervellino, Dr. Mohammed Tarik, and Mr. Albert Schuler for their contribution to the sample characterization. The XRD and FTIR data were collected at the X01DC and X04SA-MS beamlines of the Swiss Light Source (PSI).

2.7 References

- (1) Evanoff, D. D. Jr.; Chumanov, G. Synthesis and Optical Properties of Silver Nanoparticles and Arrays. *ChemPhysChem* **2005**, *6*, 1221.
- (2) Rycenga, M.; Cobley, C. M.; Zeng, J.; Li, W.; Moran, C. H.; Zhang, Q.; D. Qin, D.; Xia, Y. Controlling the Synthesis and Assembly of Silver Nanostructures for Plasmonic Applications. *Chem. Rev.* **2011**, *111*, 3669-3712.
- (3) Cobley, C. M.; Skrabalak, S. E.; Campbell, D. J.; Xia, Y. Shape-Controlled Synthesis of Silver Nanoparticles for Plasmonics and Sensing Applications. *Plasmonics* **2009**, *4*, 171-179.
- (4) McFarland, A. D.; Van Duyne, R. P. Single Silver Nanoparticles as Real-Time Optical Sensors with Zeptomole Sensitivity. *Nano Lett.* **2003**, *3*, 1057-1062.
- (5) Lee, K. -Y.; El-Sayed, M. A. Gold and Silver Nanoparticles in Sensing and Imaging: Sensitivity of Plasmon Response to Size, Shape and Metal Composition. *J. Phys. Chem B* **2006**, *110*, 19220-19225.
- (6) Gittins, D. I.; Bethell, D.; Schiffrin, D. J.; Nichols, R. J. A Nanometre-Scale Electronics Switch Consisting of a Metal Cluster and Redox Addressable Groups. *Nature* **2000**, *408*, 67-69.
- (7) Atwater, H. A.; Polman, A. Plasmonics for Improved Photovoltaic Devices. *Nat. Mat.* **2010**, *9*, 205-213.

2. Continuous Production of Tailored Silver Nanoparticles by Polyol Synthesis and Reaction Yield Measured by X-ray Absorption Spectroscopy: Towards a Growth Mechanism.

- (8) Crooks, R. M.; Zhao, M.; Sun, L.; Chechik, V.; Yeung, L. K. Dendrimer-Encapsulated Metal Nanoparticles: Synthesis, Characterization, Applications to Catalysis. *Acc. Chem. Res.* **2001**, *34*, 181-190.
- (9) Lee, H. -H.; Chou, K. -S.; Huang, K. -C. Inkjet Printing of Nanosized Silver Colloids. *Nanotechnology* **2005**, *16*, 2436-2441.
- (10) Kim, D.; Jeong, S.; Lee, S.; Park, B. K.; Moon, J. Organic Thin Film Transistor Using Silver Electrodes by the Ink-Jet Printing Technology. *Thin Solid Films* **2007**, *515*, 7692-7696.
- (11) Balantrapu, K.; Goia, D. Silver Nanoparticles for Printable Electronics and Biological Applications. *J. Mat. Res.* **2009**, *24*, 2828-2836.
- (12) Balantrapu, K.; McMurrin, M.; Goia, D. Inkjet Printable Silver Dispersions: Effect of Bi-modal Particle Size Distribution on Film Formation and Electrical Conductivity. *J. Mat. Res.* **2010**, *25*, 821-827.
- (13) Yin, W.; Lee, D. -H.; Choi, J.; Park, C.; Cho, S. M. Screen Printing of Silver Nanoparticle Suspension for Metal Interconnects. *Kor. J. Chem. Eng.* **2008**, *25*, 1358-1361.
- (14) Jakubowska, M.; Jarosz, M.; Kielbasinski, K.; Mlozniak, A. New Conductive Thick-Film Paste Based on Silver Nanopowder for High Power and High Temperature Applications. *Microelectron. Reliab.* **2011**, *51*, 1235-1240.
- (15) Suganuma, K.; Sakamoto, S.; Kagami, N.; Wakuda, D.; Kim, K. -S.; Nogi, M. Low-Temperature Low-Pressure Die Attach with Hybrid Silver Particle Paste. *Microelectron. Reliab.* **2012**, *52*, 375-380.
- (16) Kisiel, R.; Szczepanski, Z. Die-Attachment Solutions for SiC Power Devices. *Microelectron. Reliab.* **2009**, *49*, 627-629.

2. Continuous Production of Tailored Silver Nanoparticles by Polyol Synthesis and Reaction Yield Measured by X-ray Absorption Spectroscopy: Towards a Growth Mechanism.

- (17) Hu, A.; Guo, J. Y.; Alarifi, H.; Patane, G.; Zhou, Y.; Compagnini, G.; Xu, C. X. Low Temperature Sintering of Ag Nanoparticles for Flexible Electronics Packaging. *Appl. Phys. Lett.* **2010**, *97*, 153117-3.
- (18) Qi, L.; Lee, B. I.; Chen, S.; Samuels, W. D.; Exarhos, G. J. High-Dielectric-Constant Silver-Epoxy Composites as Embedded Dielectrics. *Adv. Mater.* **2005**, *17*, 1777-1781.
- (19) Rajesh, S.; Sonoda, K.; Uusimäki, A.; Yang, K. H.; Lu, H. Y.; Jantunen, H. Effective Dielectric Response of Polymer Composites with Ceramic Coated Silver Flakes *J. Mater. Sci.: Mater. Electron* **2013**, *24*, 191-195.
- (20) Wiley, B.; Sun, Y.; Mayers, B.; Xia, Y. Shape-Controlled Synthesis of Metal Nanostructures. *Chem. Eur. J.* **2005**, *11*, 454-463.
- (21) Wiley, B.; Sun, Y.; Xia, Y. Synthesis of Silver Nanostructures with Controlled Shapes and Properties. *Acc. Chem. Res.* **2007**, *40*, 1067-1076.
- (22) Xiong, Y.; Siekkinen, A. R.; Wang, J.; Yin, Y.; Kim, M. J.; Xia, Y. Synthesis of Silver Nanoplates at High Yields by Slowing Down the Polyol Reduction of Silver Nitrate with Polyacrylamide. *J. Mater. Chem.* **2007**, *17*, 2600-2602.
- (23) Hu, Y.; Ge, J.; Lim, D.; Zhang, T.; Yin, Y. Size-Controlled Synthesis of Highly Water-Soluble Silver Nanocrystals. *Solid State Chem.* **2008**, *181*, 1524-1529.
- (24) Silvert, P. -Y.; Herrera-Urbina, R.; Duvauchelle, N.; Vijayakrishnan, V.; Elhsissen, K. T. Preparation of Colloidal Silver Dispersions by the Polyol Process. *J. Mater. Chem.* **1996**, *6*, 573-577.
- (25) Kim, D.; Jeong, S.; Moon, J. Synthesis of Silver Nanoparticles Using the Polyol Process and the Influence of Precursor Injection. *Nanotechnology* **2006**, *17*, 4019-4024.

2. Continuous Production of Tailored Silver Nanoparticles by Polyol Synthesis and Reaction Yield Measured by X-ray Absorption Spectroscopy: Towards a Growth Mechanism.

- (26) Shin, H. S.; Yang, H. J.; Kim, S. B.; Lee, M. S. Mechanism of Growth of Colloidal Silver Nanoparticles Stabilized by Polyvinyl Pyrrolidinone in γ -Irradiated Silver Nitrate Solution. *Colloid Interface Sci.* **2004**, 274, 89-94.
- (27) Tsuji, M.; Nishizawa, Y.; Matsumoto, K.; Kubokawa, M.; Miyamae, N.; Tsuji, T. Effects of Chain Length of Polyvinyl Pyrrolidinone for the Synthesis of Silver Nanostructures by a Microwave-Polyol Method. *Mater. Lett.* **2006**, 60, 834-838.
- (28) Sun, Y.; Xia, Y. Shape-Controlled Synthesis of Gold and Silver Nanoparticles. *Science* **2002**, 298, 2176-2179.
- (29) Zhao, T.; Sun, R.; Yu, S.; Zhang, Z.; Zhou, L.; Huang, H.; Du, R. Size-Controlled Preparation of Silver Nanoparticles by a Modified Polyol Method. *Colloids and Surfaces A: Physicochem. Eng. Aspects* **2010**, 366, 197-202.
- (30) Washio, I.; Xiong, Y.; Yin, Y.; Xia, Y. Reduction by the End-Groups of Poly(vinyl pyrrolidinone): A New and Versatile Route to the Kinetically Controlled Synthesis of Ag Triangular Nanoplates. *Adv. Mater.* **2006**, 18, 1745-1749.
- (31) Xiong, Y.; Siekkinen, A. R.; Wang, J.; Yin, Y.; Kim, M. J.; Xia, Y. Synthesis of Silver Nanoplates at High Yields by Slowing Down the Polyol Reduction of Silver Nitrate with Polyacrylamide. *J. Mater. Chem.* **2007**, 17, 2600-2602.
- (32) Sun, Y.; Mayers, B.; Herricks, T.; Xia, Y. Polyol Synthesis of Uniform Silver Nanowires: A Plausible Growth Mechanism and Supporting Evidence. *Nano Lett.* **2003**, 3, 955-960.
- (33) Siekkinen, A. R.; McLellan, J. M.; Chen, J.; Xia, Y. Rapid Synthesis of Small Nanocubes by Mediating Polyol Reduction with a Trace Amount of Sodium Sulfide or Sodium Hydrosulfide. *Chem. Phys. Lett.* **2006**, 432, 491-496.

2. Continuous Production of Tailored Silver Nanoparticles by Polyol Synthesis and Reaction Yield Measured by X-ray Absorption Spectroscopy: Towards a Growth Mechanism.

- (34) Yen, B. K. H.; Stott, N. E.; Jensen, K. F.; Bawenchi, M. G. A Continuous-Flow Microcapillary Reactor for the Preparation of a Size Series of CdSe Nanocrystals. *Adv. Mater.* **2003**, *15*, 1858-1862.
- (35) Yan, J.; Zou, G.; Wang, X.; Bai, H.; Mu, F.; Wu, A. In *A Study on the Low Temperature Sintering-Bonding Through In-situ Formation of Ag Nanoparticles Using Ag₂O Microparticles*. Proceedings of the International Conference on Electronic Packaging Technology and High Density Packaging, 12th, Shanghai, China, Aug. 8-11.
- (36) Silvestrini, S.; Carofiglio, T.; Maggini, M. Shape-Selective Growth of Silver Nanoparticles under Continuous Flow Photochemical Conditions. *Chem. Comm.* **2013**, *49*, 84-86.
- (37) He, S. T.; Liu, Y. L.; Maeda, H. Controlled Synthesis of Colloidal Silver Nanoparticles in Capillary Micro-Flow Reactor. *J. Nanopart. Res.* **2008**, *10*, 209-215.
- (38) Nishioka, M.; Miyakawa, M.; Kataoka, H.; Koda, H.; Sato, K.; Suzuki, T. M. Continuous Synthesis of Monodispersed Silver Nanoparticles Using a Homogenous Heating Microwave Reactor System. *Nanoscale* **2011**, *3*, 2621-2626.
- (39) Huang, J.; Lin, L.; Li, Q.; Sun, D.; Wang, Y.; Lu, Y.; He, N.; Yang, K.; Yang, X.; Wang, H.; Wang, W.; Lin, W. Continuous-Flow Biosynthesis of Silver Nanoparticles by Lixivium of Sundried *Cinnamomum Camphora* Leaf in Tubular Microreactors. *Ind. Eng. Chem. Res.* **2008**, *47*, 6081-6090.
- (40) Lin, X. Z.; Terepka, A. D.; Yang, H. Synthesis of Silver Nanoparticles in a Continuous Flow Tubular Reactor. *Nano Lett.* 2004, *4*, 2227-2232.
- (41) Jongen, N.; Donnet, M.; Bowen, P.; Lemaitre, J.; Hofmann, H.; Schenk, R.; Hofmann, C.; Aoun-Habbache, M.; Guillermet-Fritsch, S.; Sarrias, J. et al. Development of a Continuous Segmented Flow Tubular Reactor and the “Scale-out” Concept – In Search of Perfect Powders. *Chem. Eng. Techn.* 2003, *26*, 303-305.

2. Continuous Production of Tailored Silver Nanoparticles by Polyol Synthesis and Reaction Yield Measured by X-ray Absorption Spectroscopy: Towards a Growth Mechanism.

- (42) Aimable, A.; Jongen, N.; Testino, A.; Donnet, M.; Lemaitre, J.; Hofmann, H.; Bowen, P. Precipitation of Nanosized and Nanostructured Powders: Process Intensification Using SFTR, Applied to BaTiO₃, CaCO₃ and ZnO. *Chem. Eng. Tech.* 2011, 34, 344-352.
- (43) Lucchini, M. A.; Testino, A.; Ludwig, C.; Kambolis, A.; El-Kazzi, M.; Cervellino, A.; Riani, P.; Canepa, F. Continuous Synthesis of Nickel Nanopowders: Characterization, Process Optimization, and Catalytic Properties”, *Appl. Cat., B*, 2014, accepted.
- (44) Testino, A. Aqueous Synthesis of BaTiO₃ Nanopowders. Experiments and Kinetic Modelling. Ph.D. dissertation, University of Genoa, 2004.
- (45) Kashid, M. N.; Agar, W. D. Hydrodynamics of Liquid-Liquid Slug Flow Capillary Microreactor: Flow Regimes, Slug Size and Pressure Drop. *Chem. Eng. J.* 2007, 131, 1-13.
- (46) Wiley, B. J.; Im, S. H.; Li, Z. Y.; McLellan, J.; Siekkinen, A.; Xia, Y. Maneuvering the Surface Plasmon Resonance of Silver Nanostructures Through Shape-Controlled Synthesis. *J. Phys. Chem. B* 2006, 110, 15666-15675.
- (47) Willmott, P. R.; Meister, D.; Leake, S. J.; Lange, M.; Bergamaschi, A.; Böge, M.; Calvi, M.; Cancellieri, C.; Casati, N.; Cervellino, A. *et al.* The Material Science Beamline Upgrade at the Swiss Light Source. *J. Synchrotron Rad.* **2013**, 20, 667-682.
- (48) A. C. Larson, R. B. Von Dreele, General Structure Analysis System (GSAS), Technical Report LAUR 86-748; Los Alamos National Laboratory: New Mexico, **2000**.
- (49) Inorganic Crystal Structure Database (ICSD), Fachinformationsezentrum Karlsruhe and Gemlin Institute, Karlsruhe **1997**: Ni # 41508.
- (50) GSAS Manual (<http://www.ccp14.ac.uk/solution/gsas/>).
- (51) Rouff, A. A.; Rabe, S.; Nachtegaal, M.; Vogel, F. X-Ray Absorption Fine Structure Study of the Effect of Protonation on Disorder and Multiple Scattering in Phosphate Solutions and Solids. *J. Phys. Chem. A* **2009**, 113 (25), 6895-6903.

2. Continuous Production of Tailored Silver Nanoparticles by Polyol Synthesis and Reaction Yield Measured by X-ray Absorption Spectroscopy: Towards a Growth Mechanism.

- (52) Ajiboye, B.; Akinremi, O.; Jurgensen, A. Experimental Validation of Quantitative XANES Analysis for Phosphorous Speciation. *Soil. Sci. Soc. Am.* **2007**, *71*, 1288-1291.
- (53) Berry, A. J.; Hack, A.C.; Mavrogenes, J. A.; Newville, M.; Sutton, S.R. A XANES Study of Cu Speciation in High-Temperature Brines Using Synthetic Fluid Inclusions. *Am. Mineral.* **2006**, *91*, 1773-1782.
- (54) Takaoka, M.; Yamamoto, T.; Shiono, A.; Takeda, N.; Oshita, K.; Matsumoto, T.; Tanaka, T. The Effect of Copper Speciation on the Formation of Chlorinated Aromatics on Real Municipal Solid Waste Incinerator Fly Ash. *Chemosphere* **2005**, *59*, 1497-1503.
- (55) Kretschmer, X. C.; Meitzner, G.; Gardea, J. L.; Webb, R. Determination of Cu Environments in the Cyanobacterium *Anabaena Flos-Aquae* by X-Ray Absorption Spectroscopy. *Appl. and Environ. Microbiol.* **2004**, *70*, 771-780.
- (56) Ravel, B.; Newville, M. Athena, Artemis, Hephaestus: Data Analysis for X-Ray Absorption Spectroscopy Using IFEFFIT. *J. Synchrotron Rad.* **2005**, *12*, 537-541.
- (57) Slistan-Grijalva, A.; Herrera-Urbina, R.; Rivas-Silva, J. F.; Avalos-Borja, M.; Castillon-Barraza, F. F.; Posada-Amarillas, A. Classical Theoretical Characterization of the Surface Plasmon Absorption Band for Silver Spherical Nanoparticles Suspended in Water and Ethylene Glycol. *Physica* **2005**, *27*, 104-112.
- (58) Lance Kelly, K.; Coronado; E. Zhao, L. L.; Schatz, G. C. The Optical Properties of Metal Nanoparticles: The Influence of Size, Shape and Dielectric Environment. *J. Phys. Chem. B.* **2003**, *107* (3), 668-677.
- (59) Huang, Y. -J.; Paul Wang, H.; Hsiao, M. C.; Tai, C. C.; Huang, H.-L.; Liu, S. H. Speciation of Copper in Micropores. *Water, Air, and Soil Pollution* **2004**, *153*, 187-194.
- (60) Arcon, I.; Kolar, J.; Kodre, A.; Hanzel, D.; Strlic, M. XANES Analysis of Fe Valence in Iron Gall Inks. *X-Ray Spectrom.* **2007**, *36*, 199-205

2. Continuous Production of Tailored Silver Nanoparticles by Polyol Synthesis and Reaction Yield Measured by X-ray Absorption Spectroscopy: Towards a Growth Mechanism.

- (61) Døelsch, E.; Basile-Døelsch, I.; Rose, J.; Masion, A.; Borschneck, D.; Hazemann, J.-L.; Saint Macary, H.; Bottero, J.-Y. New Combination of EXAFS Spectroscopy and Density Fractionation for the Speciation of Chromium Within an Andosol. *Environ. Sci. Technol.* **2006**, *40*, 7602-7608
- (62) Skrabalak, S. E.; Wiley, B. J.; Kim, M.; Formo, E.; Xia, Y. On the Polyol Synthesis of Silver Nanostructures: Glycoaldehyde as a Reducing Agent. *Nano Lett.* **2008**, *8*, 2077-2081.
- (63) Yun, H.; Lee, I. -M.; Im, S. H.; Lee, S. -Y.; Lee, B. Site-Selective Synthesis of Silver Nanoparticles in Pre-Patterned Trenches and their Localized Surface Plasmon Resonances. *Nanotechnology* **2012**, *23*, 015306.
- (64) Tao, A. R.; Habas, S.; Yang, P. Shape Control of Colloidal Metal Nanocrystals. *Small* **2008**, *4*, 310-325
- (65) Xiong, Y.; Washio, I.; Chen, J.; Cai, H.; Li, Z. -Y.; Xia, Y. Poly(vinyl pyrrolidinone): A Dual Functional Reductant and Stabilizer for the Facile Synthesis of Noble Metal Nanoplates in Aqueous Solutions. *Langmuir* **2006**, *22*, 8563-8570.

2.8 Supporting information

Experimental Part

Three different batch reactions were performed at 150 °C with different reaction volumes (Tab. 8). Briefly, PVP 40 ($M_w = 40'000$ g/mol) was dissolved in ethylene glycol (EG) under sonication. Thereafter, AgNO₃ solution in EG was added, the resulting mixture stirred at 25 °C for a minute before placing the reaction vessel into a preheated oil bath (150 °C). The reaction mixture was stirred for 1 h where color changes were observed (from yellow to olive). Then, the vessel was cooled in a water bath, the mixture diluted with acetone, centrifuged, decanted and further washed thrice with an EtOH/acetone mixture before redispersion in EtOH for further analysis. The yield of the reaction was determined by measuring the collected powder after washing and centrifugation followed by drying *in vacuo*.

Tab. 8: Different batch reactions with constant AgNO₃/PVP ratio performed at 150 °C. The reaction volume was varied for each reaction by a factor of 10.

Entry	m(AgNO ₃)/g	m(PVP)/g	V(EG)/mL	Yield (%)
Ag_1	0.02	0.12	1	72 ± 5
Ag_2	0.2	1.2	10	72 ± 5
Ag_3	2	12	100	68 ± 5

2. Continuous Production of Tailored Silver Nanoparticles by Polyol Synthesis and Reaction Yield Measured by X-ray Absorption Spectroscopy: Towards a Growth Mechanism.

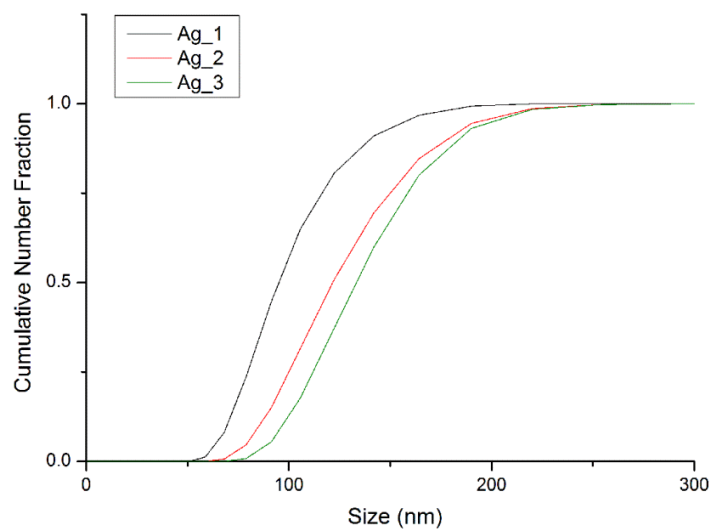


Fig. 33: DLS spectra of the samples Ag_1, Ag_2 and Ag_3.

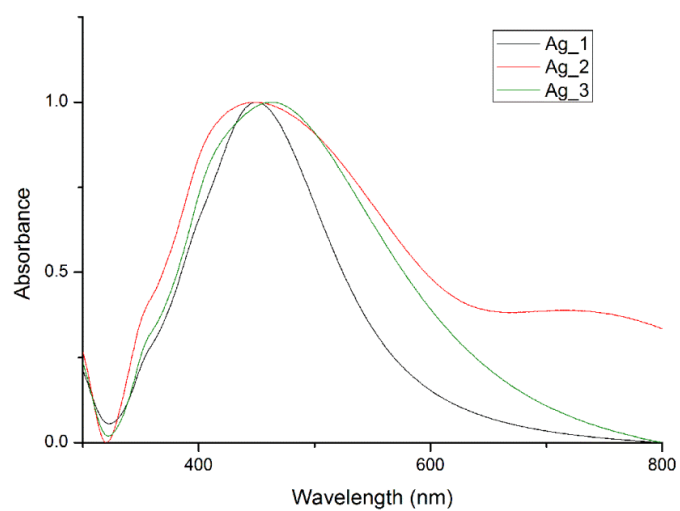


Fig. 34: UV-vis spectra of the samples Ag_1, Ag_2 and Ag_3.

2. Continuous Production of Tailored Silver Nanoparticles by Polyol Synthesis and Reaction Yield Measured by X-ray Absorption Spectroscopy: Towards a Growth Mechanism.

Tab. 9: Percentile and mean diameters of the samples Ag_1, Ag_2 and Ag_3.

Entry	d_{n10} (nm) ^a	d_{n50} (nm) ^a	d_{n90} (nm) ^a	Mean diameter (nm) ^a	TEM size (nm)
Ag_1	66	88	129	94(24)	71(13)
Ag_2	80	112	163	118(32)	79(21)
Ag_3	92	125	174	127(31)	92(21)

^a Mean numerical diameter. Mean value of 3 measurements, performed by DLS.

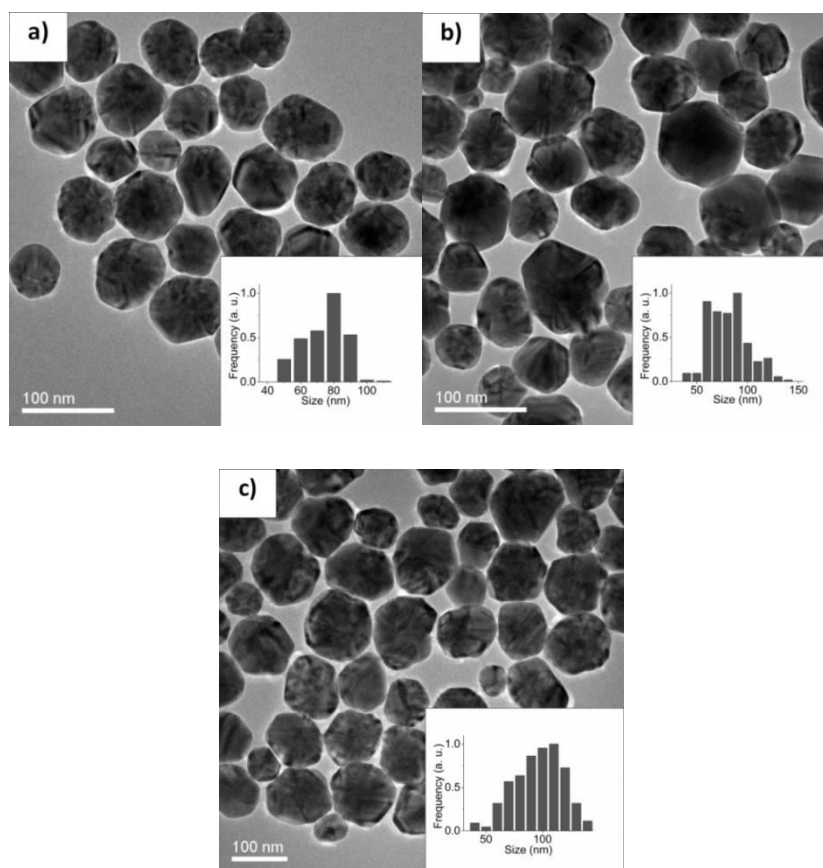


Fig. 35: TEM micrographs of the samples (a) Ag_1, (b) Ag_2 and (c) Ag_3 with corresponding particle size distribution (PSD).

Chapter 3: Dielectric Properties of Silver Nanoparticles Coated with Silica Shells of Different Thicknesses

Declaration: The nanoparticles synthesis and functionalization as well as the microscopy analysis with TEM/SEM were conducted by Jose Enrico Q. Quinsaat, while the dielectric measurements of the particles that were pressed into pellets were conducted by Dr. Dorina Opris.

Jose Enrico Q. Quinsaat^{1,2}, Frank A. Nüesch¹, Heinrich Hofmann², Dorina M. Opris^{1}*

¹Swiss Federal Laboratories for Materials Science and Technology (Empa), Laboratory for Functional Polymers, Überlandstrasse 129, 8600 Dübendorf, Switzerland

²Ecole Polytechnique Fédérale de Lausanne (EPFL), Materials Institute, Powder Technology Laboratory (LTP), 1015 Lausanne, Switzerland

3. Dielectric Properties of Silver Nanoparticles Coated with Silica Shells of Different Thicknesses

Abstract: Core/shell nanoparticles having metallic silver nanoparticle cores of ~ 38 nm in diameter and silica shells of different thicknesses ranging from ~ 3.6 – 20 nm were prepared. For the silica coating, a slightly modified Stöber method was used which allowed preparing grams of core/shell nanoparticles for the first time. The particles were characterized by UV-vis spectroscopy, dynamic light scattering, scanning electron microscopy, transmission electron microscopy, and energy-dispersive X-ray scattering. Their dielectric properties were measured as pellets in parallel-plate capacitors. It was found that the permittivity is much influenced by the silica shell thickness with an increase in permittivity for thinner shells. A shell thickness of 20 ± 2 nm allowed fabrication of capacitors which have similar characteristics to those of silica, thus, there is no influence of the metal core on the dielectric properties anymore. However, by decreasing the silica shell to 17 ± 2 , 8 ± 1.5 , and 6.6 ± 1.5 nm the permittivity at high frequencies is increasing from 10, 34, to 41, respectively. The insulator to metal transition was observed for a silica shell thickness of 3.6 ± 1 nm. Functionalization of the silica surface with a hydrophobic coating removes surface adsorbed water as observed by the flat dielectric permittivity over a large frequency domain.

3.1 Introduction

Properties of metals change significantly when going from macroscopic to nanoparticle sizes.¹ In the last couple of years, much development has been done with respect to the synthesis of metal nanoparticles and quite some understanding of how to prepare different shapes and sizes was achieved.² Blending such nanoparticles in polymeric, ceramic matrices allowed fabrication of new materials with unprecedented properties which might find their way in optical, electrical, and magnetic applications. Materials with high dielectric permittivity (ϵ') are of great interest for future electronic capacitors with high energy storage densities and low operating voltage.³ For such applications not only high ϵ' is required, but also low conductivity and high breakdown field are desired properties.

3. Dielectric Properties of Silver Nanoparticles Coated with Silica Shells of Different Thicknesses

These two properties have a direct impact on the device lifetime and also on the maximum energy density of the capacitor which is given by:

$$U_e = \frac{1}{2} \epsilon' \epsilon_0 E_b^2 \quad (\text{Eq. 45})$$

Here, ϵ' is the relative dielectric permittivity, E_b is the electric breakdown strength, and ϵ_0 the vacuum permittivity (8.85542×10^{-12} F/m).³ The energy loss due to dissipation by the dielectric material is given by

$$W = \pi \epsilon' E f \tan \delta \quad (\text{Eq. 46})$$

where E is the electric field strength, f is the frequency, and $\tan \delta$ is the loss factor. Thus a low dielectric loss material will have a low energy loss, especially for high frequency applications.

Several approaches have been used in order to produce materials with high ϵ' which include blends with highly polarizable ceramic particles,^{4,5} polymers with polar functional groups,⁶ and composite materials with conductive fillers.⁷

According to the percolation theory, the effective ϵ' of composites increases rapidly at concentrations approaching the percolation threshold, when the conductive paths are hindered by a dielectric matrix.⁸ Various conductive fillers like metal particles, conjugated polymers, or carbon black have been used for percolative composites with polymers as matrix materials.⁹⁻¹³ However, although the reported ϵ' values were high, the blended materials showed high dielectric loss due to agglomeration of the fillers leading to conductive pathways. Several approaches were used to overcome this limitation. For

3. Dielectric Properties of Silver Nanoparticles Coated with Silica Shells of Different Thicknesses

example, Xu *et al.* used Al particles covered with an Al_2O_3 insulating shell, and obtained composites with low dielectric losses.¹⁴ Kempa *et al.* used silica coated conductive particles and observed that the shape and monodispersity of the nanoparticles strongly affect the dielectric properties of the composites. Li *et al.* used effective medium approximation of a composite made of three-phase material and showed that the effective ϵ' , the breakdown strength, and the electrical energy density are strongly affected by the microstructure of the nanocomposite and therefore must be carefully controlled.¹⁵

From the literature, it became clear that in order to prepare reliable materials the percolation paths in composites containing conductive fillers should be avoided. This can be achieved by surrounding the particles with an insulating shell that precisely defines the minimum approach distance of twice the shell thickness (Fig. 36).¹⁶

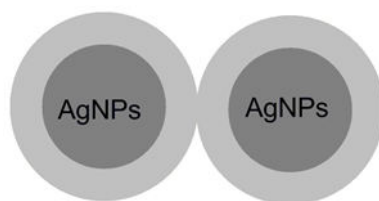


Fig. 36: Insulator shell (light grey) on conductive Ag nanoparticles (dark grey) defining the minimum distance between the cores as twice the shell thickness.

Several approaches were already reported in the literature on how to prepare core/shell particles.¹⁷ The most common one uses wet chemistry on preformed cores including interfacial polymerization of the shell onto the core, controlled phase separation techniques, and heterocoagulation.¹⁸ Although high temperature formation of dielectric oxide shell is occasionally used, it is less attractive since the shell thickness is difficult to control.¹⁹ Another way of preparing core/shell particles is by using layer by layer deposition.²⁰ Despite these advances in the synthesis of core/shell particles, a challenge

3. Dielectric Properties of Silver Nanoparticles Coated with Silica Shells of Different Thicknesses

which still needs to be overcome is the up-scaling of the synthesis allowing preparation of sufficient material to be used for further investigations.

Despite the large number of publications dealing with percolated materials, there is limited information on the ϵ' of monodisperse metal nanoparticles coated with an insulator shell of different thicknesses and/or composites of such well-defined particles in a matrix.

It is the aim of this work to prepare structurally well-defined core/shell particles having AgNP cores and silica as insulating shell (denoted as Ag@SiO₂(x), where x is the silica shell thickness taken from TEM measurements) and measure their dielectric properties as a function of shell thickness. Apart from many studies that concentrate on optical measurements with Ag@SiO₂ particles, dielectric measurements of such particles are not known. To be able to run such measurements large quantities of particles are required. Thus, a slightly modified Stöber method was developed that allowed us preparing grams of core/shell particles at higher concentrations as compared to the literature. The silica shells prevent the AgNPs from touching each other and also keep the AgNP cores at a defined minimum distance. The dielectric properties of such particles were measured for the first time in pellets in parallel-plate capacitors and the influence of the insulator shell thickness on the dielectric properties was investigated.

3.2 Experimental Section

3.2.1 Synthesis of Silver Nanoparticles (38 nm)

The synthesis of the AgNPs was based on an existing protocol.²¹ A solution of polyvinyl pyrrolidinone (PVP) (40.5 g, 361 mmol) in ethylene glycol (EG, 0.3 L) was heated in a thermostat at 130°C for 30 min. Then, a solution of AgNO₃ (6 g, 36 mmol) dissolved in EG (4 mL) and nanopure water (3 mL) was added via rapid injection and the mixture was stirred at 130°C for further 30 min. Afterwards, the mixture was cooled, washed with

3. Dielectric Properties of Silver Nanoparticles Coated with Silica Shells of Different Thicknesses

acetone, and centrifuged. The washing procedure was repeated twice before redispersion of the residue in ethanol (EtOH) (100 mL). AgNPs were prepared in 81% yield.

3.2.2 Synthesis of Silica Coated Silver Nanoparticles Ag@SiO₂(x nm)

The encapsulation of the AgNPs with SiO₂ was based on an existing protocol.²² From the above dispersion of AgNPs in ethanol, 5 ml was taken and diluted with ethanol to 31.5 ml in order to obtain a conc. of 46 mM AgNPs. This dispersion was treated with NH₄OH (29 %, 1.3 mL) under gentle stirring (Tab. 10) at 25 °C followed by the dropwise addition of different concentrations of tetraethoxysilane (TEOS) in EtOH (3 mL) which was completed after 60 s (For concentrations see Tab. 10). The reaction mixture was stirred for further 20 h, then diluted with acetone, washed, centrifuged (4'000 rpm, 45 min) and decanted. The washing procedure was repeated 3 times. The residue was redispersed in MeOH for further analysis. The particles were dried in high vacuum at 25 °C for 8 h.

3. Dielectric Properties of Silver Nanoparticles Coated with Silica Shells of Different Thicknesses

Tab. 10: The amount of reagents used for the coating of AgNPs with different thickness silica shell.

^aWhere x is the silica shell thickness and y is the deviation of the silica shell from TEM, stirring rate: ^b550 rpm, ^c500 rpm, and ^d400 rpm, ^e31.5 ml of 46 mM AgNP dispersed in ethanol was used.

Sample Ag@SiO ₂ ($x \pm y$ nm) ^a	Vol % TEOS in EtOH [3 mL] ^e	Particles size by TEM (nm)	Particles size by DLS (nm)
Ag@SiO ₂ (20 \pm 2 nm) ^b	20%	78	79
Ag@SiO ₂ (17 \pm 2 nm) ^b	15%	72	72
Ag@SiO ₂ (8 \pm 1.5 nm) ^c	8%	54	57
Ag@SiO ₂ (6.6 \pm 1.5 nm) ^c	5%	51	54
Ag@SiO ₂ (3.6 \pm 1 nm) ^d	2.5%	45	366

3.2.3 Synthesis of Hydrophobic Coating: (Ag@SiO₂(17 nm))@alkylsilane)

Ag@SiO₂ (60 mg) was dispersed in EtOH (10 mL) and treated with dimethylamine (DMA) (40%, 166 μ L, 1.34 mmol) under gentle stirring (500 rpm) followed by the dropwise addition of *n*-octyldimethylmethoxysilane (334 μ L, 1.34 mmol) which was completed within a minute. The mixture was stirred for further 48 h, then diluted with acetone, washed, centrifuged (13'000 rpm, 25 min) and decanted followed by redispersion and further washing in isopropanol (13'000 rpm, 25 min) for 4 times. The particles were dried in high vacuum at 25 °C for 8 h.

3.3 Materials and Methods

All chemicals were purchased from Aldrich and used as received.

The nanoparticles were observed by SEM on a Hitachi S-4800 and FEI NovaNanoSEM 230, TEM were done with Philips CM30 TEM and JEOL 2200FS TEM/STEM, UV-vis absorption spectra were recorded with a Cary 50 spectrophotometer, DLS were done with a

3. Dielectric Properties of Silver Nanoparticles Coated with Silica Shells of Different Thicknesses

Malvern Zetasized Nano ZS, and ^{29}Si NMR spectra were recorded with a Bruker Avance-400 spectrometer. Image analysis was used for the TEM micrographs to estimate the particles size. The number of particles measured was about 400 for Ag core by using ImageJ and about 100 for the coated particles with the help of a ruler for Windows. Permittivity measurements were done in the frequency range of 100 Hz to 1 MHz using an HP 4284A LCR meter. The amplitude of the probing AC electric signal applied to the samples was 1 V. The permittivity was determined from the capacitance: $C = \epsilon_0 \epsilon_r A/d$, where A is the electrode area, d is the thickness of the capacitor, and ϵ_0 is the vacuum permittivity. Before use, the samples were dried for 8 h at 2×10^{-2} mbar. Pellets were prepared by pressing at 3 tons ($\varnothing = 3$ mm) and were then covered with silver paste electrodes. Their microstructures were measured with SEM (see supporting information) All the samples were measured immediately after pellet preparation in order to avoid changes in the water content.

3.4 Results

3.4.1 Synthesis and Characterization of AgNPs Coated with SiO_2

A wide range of different shapes and sizes of AgNPs have been prepared including sphere, spheroid, cube, octahedron, tetrahedron, bipyramid, rod, and wire starting from cheap and readily available silver salts.²³ For a general overview of the state of the art on the shape controlled syntheses of AgNPs the reader is referred to the excellent review article by Xia *et al.*²⁴ The most common way for preparing AgNPs includes the reduction of silver salt by boron hydrides, polyols, or hydrogen.²⁵

We prepared AgNPs by reduction of AgNO_3 with EG in the presence of PVP as capping agent at 130°C . The particles were stabilized by polyvinylpyrrolidone (PVP). The reactions were initially done on a small scale (0.2 g AgNO_3), however in order to be able to make dielectric investigations of AgNPs, gram quantities are required. Thus, the possibility of up-scaling the synthesis was investigated. Since the reaction temperature influences

3. Dielectric Properties of Silver Nanoparticles Coated with Silica Shells of Different Thicknesses

particles size, an accurate control of the temperature was required. In order to achieve this, a reactor heated with a thermostat was used. This setup enabled control within $\pm 1^\circ\text{C}$ during the synthesis. Fig. 37 shows the TEM images of the prepared AgNPs on 6 g scale. By TEM it was found that the average particles size was about 38 ± 2 nm in diameter (particle diameter of majority of the particles is between 35-40 nm) and by DLS that they have a reasonable size distribution (0.2).

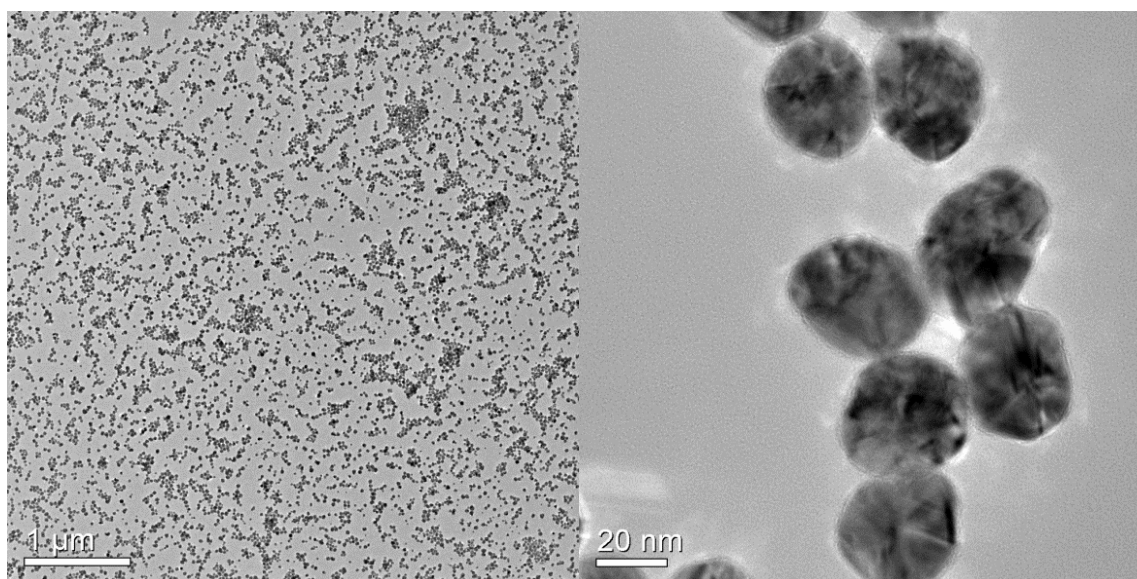


Fig. 37: TEM images of AgNPs prepared by reduction of AgNO_3 with ethylene glycol. The reaction was done starting with 6 g AgNO_3 .

Silica is well known for its good insulator properties. Core/shell particles with SiO_2 shell having controllable thickness were prepared by the Stöber method.²⁶ This layer by layer technique was intensely used for example to prepare polystyrene-silica, gold-silica core/shell particles with controlled shell thickness from a few nanometers to several hundreds.²⁷ Ag particles²⁸ and nanowires²⁹ were also coated with amorphous silica shells of different thickness by using TEOS as silica precursor. We also used Stöber method for the silica coating of AgNPs. The silica shells not only hinder agglomeration of AgNPs and

3. Dielectric Properties of Silver Nanoparticles Coated with Silica Shells of Different Thicknesses

enhance their stability, but also allow surface functionalization.³⁰ In a typical synthesis, the AgNPs are dispersed at a certain concentration in ethanol and TEOS is hydrolyzed and deposited on the surface of the nanoparticles. A disadvantage of Stöber method is the high dilution required (typical concentration range from 0.01 mM to 1 mM) which made up-scaling of the process unpractical. We therefore slightly modified the reaction conditions and systematically increased the concentration of AgNPs (46 mM) such that about 0.1 g of AgNPs per batch was coated. The strong contrast between the black silver core and the gray shell in the TEM images (Fig. 38) confirms that core/shell nanoparticles were formed. Despite the use of NH_4OH which was thought to trigger the dissolution of the silver cores, no core-free silica shells were observed in the TEM images. In comparison, the use of DMA as catalyst for the hydrolysis of TEOS did not give uniform and spherical silica shells as suggested in the literature.³¹ Furthermore, the presence of the silica shell was confirmed by EDX done on the naked AgNPs and on the coated particles as shown in Fig. 39. Only in the latter spectrum, silicon is detected. The Cu and C peaks correspond to the carbon-coated copper grid on which the particles were deposited for this test.

3. Dielectric Properties of Silver Nanoparticles Coated with Silica Shells of Different Thicknesses

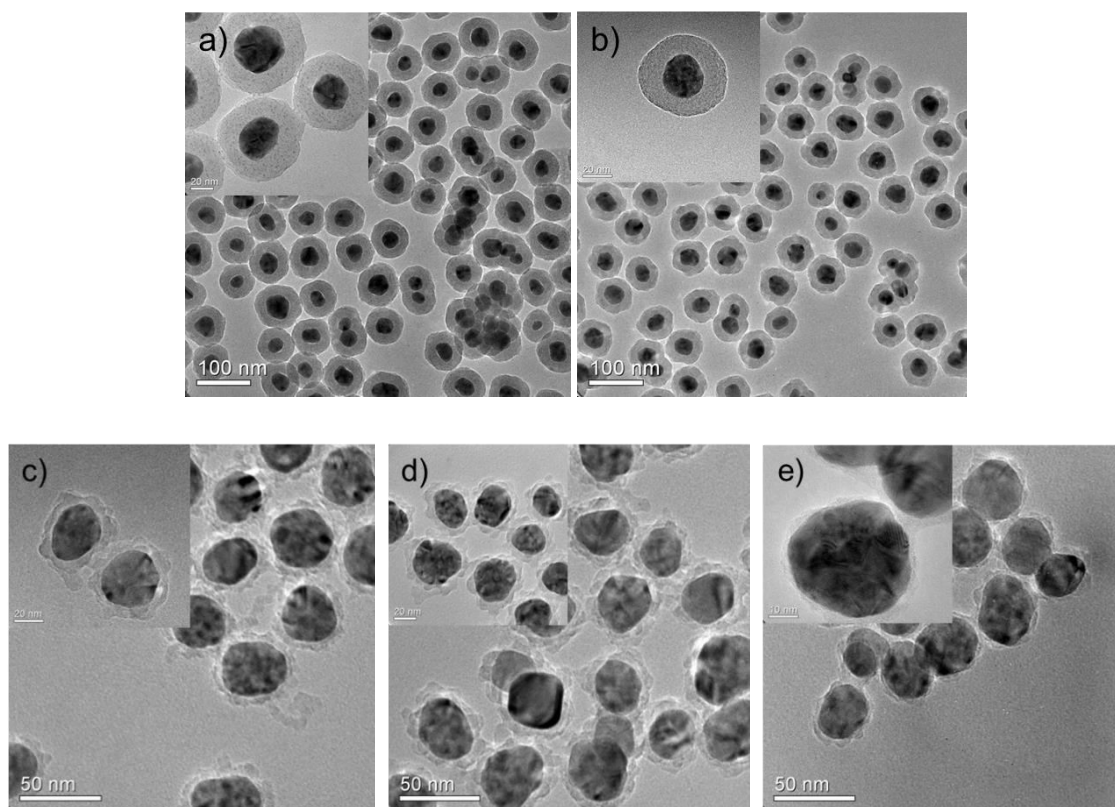


Fig. 38: TEM images of the AgNPs coated with a silica shell. The average diameters of AgNPs were 38 nm while the SiO₂ shells were about 20 ± 2 nm (a); 17 ± 2 nm (b); 8 ± 1.5 nm (c); 6.6 ± 1.5 nm (d); 3.6 ± 1 nm (e).

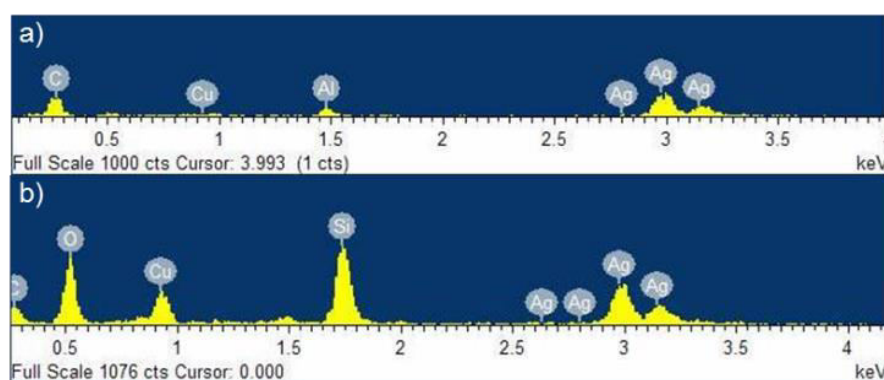


Fig. 39: EDX of the naked AgNPs (a) and of the AgNPs coated with SiO₂ (b).

3. Dielectric Properties of Silver Nanoparticles Coated with Silica Shells of Different Thicknesses

The silica shell thickness could be varied by altering the initial TEOS concentration. The growth of very thin silica shells requires slow and careful addition of TEOS into the solution.³² The silica shell grown on the silver nanoparticles was quite uniform and also spherical in shape when the shell thickness was about 17 nm or higher, but was less uniform for the thinner shells. This effect was also observed by others. For example Yin *et al.* coated Ag nanowires and found that when a thin silica shell of about 2 nm was formed, the thickness of the shell varied considerably. Thicker shells were smoother and more uniform.²⁹ It was also observed that the specific morphology of the particles is preserved in the coating process. Graf *et al.* used PVP adsorbed on various colloidal particles and coated these particles with silica shells of variable thickness. The length of the polymer used strongly influenced the homogeneity and the smoothness of the initial silica coating.³³ Fig. 38 shows TEM images of AgNPs with SiO₂ shells of different thickness. Additionally, the TEM images clearly show that the SiO₂ shell thickness can be changed by altering the amount of TEOS used. The surface plasmon resonance of AgNPs is sensitive to size, shape, and the dielectric material surrounding the nanoparticles. While the naked Ag particles give rise to a maximum absorption peak at $\lambda_{\text{max}} = 415$ nm, a small bathochromic shift (Fig. 40) with increasing the silica shell from 425 nm for 6.6 nm particles to 437 nm for 20 nm particles was observed. This can be explained by the change of the surrounding medium of the AgNPs, since silica possesses a higher refractive index than the solvent (MeOH). When the silica shell thickness was reduced to around 3.6 nm, the UV-vis spectrum featured broadened peaks. For the thicker shells, silica is completely covering the AgNPs. Because of the basic conditions, the surface hydroxyl groups are deprotonated and therefore electrostatic stabilization is the mechanism preventing agglomeration. The nanoparticles with thin and partial silica coating behave like conventional hard spheres in a Lennard-Jones potential and therefore aggregate. We assume that the surface coverage with silica is patchy and that agglomeration comes about by contact between particles at the surface parts which either have a very thin silica layer or are even free of silica. Then van der Waals forces are strong and result in agglomeration. Whether there is any residual PVP on the surface with little or no silica cannot be said at present. The size increases with

3. Dielectric Properties of Silver Nanoparticles Coated with Silica Shells of Different Thicknesses

increasing the silica shell is also reflected by DLS and further confirms the coating (Fig. 41). Interestingly, while almost all dispersed particles have similar sizes as those determined by TEM, the size of Ag@SiO₂ (3.6 ± 1) with a TEM diameter of 45 nm appears much larger (Tab. 10) a sign for agglomerated particles. A direct comparison of our results with the literature is not possible since no DLS data are given for metal particles coated with a silica shell.

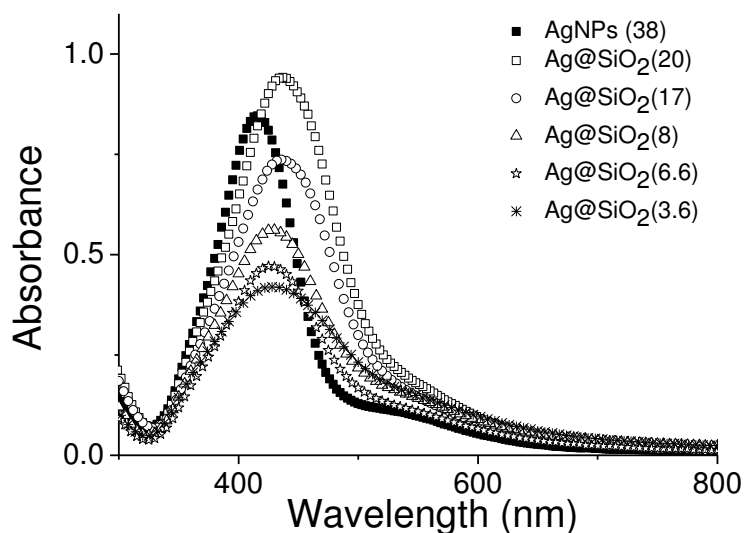


Fig. 40: UV-vis absorption spectra of AgNPs and of AgNPs coated with a silica shell recorded in MeOH. A small bathochromic shift can be seen with increasing shell thickness.

3. Dielectric Properties of Silver Nanoparticles Coated with Silica Shells of Different Thicknesses

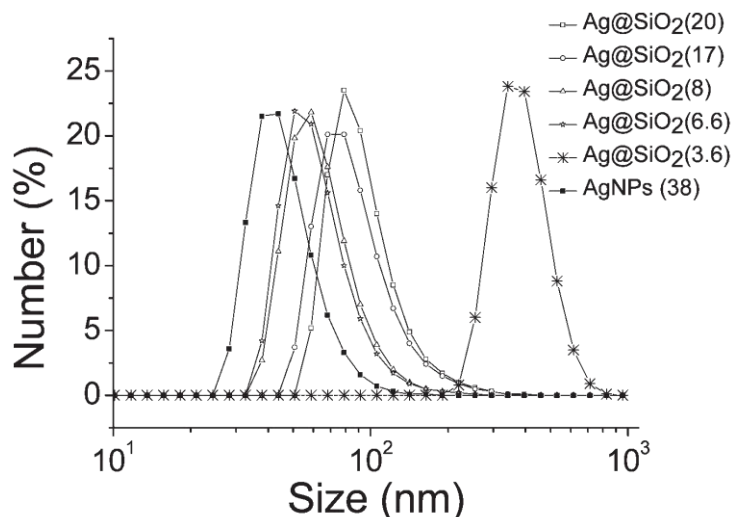


Fig. 41: Hydrodynamic diameter D_H determined by DLS of AgNPs before and after coating with silica shell recorded in EtOH. An increase in particle size is observed with increasing shell thickness, except for Ag@SiO₂ (3.6) the D_H -value of which does not match single particle size. For explanations, see text.

3.4.2 Dielectric Properties of Ag@SiO₂ in Pressed Pellets

The real part of the dielectric function ϵ' of pressed pellets of powder samples composed of Ag@SiO₂ nanoparticles were obtained by measuring the capacitance of the pellets using the sandwich architecture Ag/ Ag@SiO₂ /Ag in the frequency range of 100 Hz to 1 MHz (see experimental part). The dielectric response of Ag@SiO₂ pellets is given in Fig. 42. As expected, an increase in ϵ' with decreasing shell thickness was observed at all frequencies. Concretely, for shell thicknesses of 20 ± 2 , 17 ± 2 , 8 ± 1.5 , and 6.6 ± 1.5 nm ϵ' -values of 4.6, 10, 34 and 41, respectively, were obtained (Fig. 42). AgNPs coated with a very thin insulating shell of about 3.6 ± 1 nm were conductive and it was not possible to run the dielectric measurement. For thicker shells, the ϵ' of Ag@SiO₂ pellets is almost constant at high frequencies but increases at lower frequencies. The reason for this might be due to the presence of traces of ions and residual water absorbed on the silica surface which is rather difficult to remove which would increase the ion conductivity at low frequencies.

3. Dielectric Properties of Silver Nanoparticles Coated with Silica Shells of Different Thicknesses

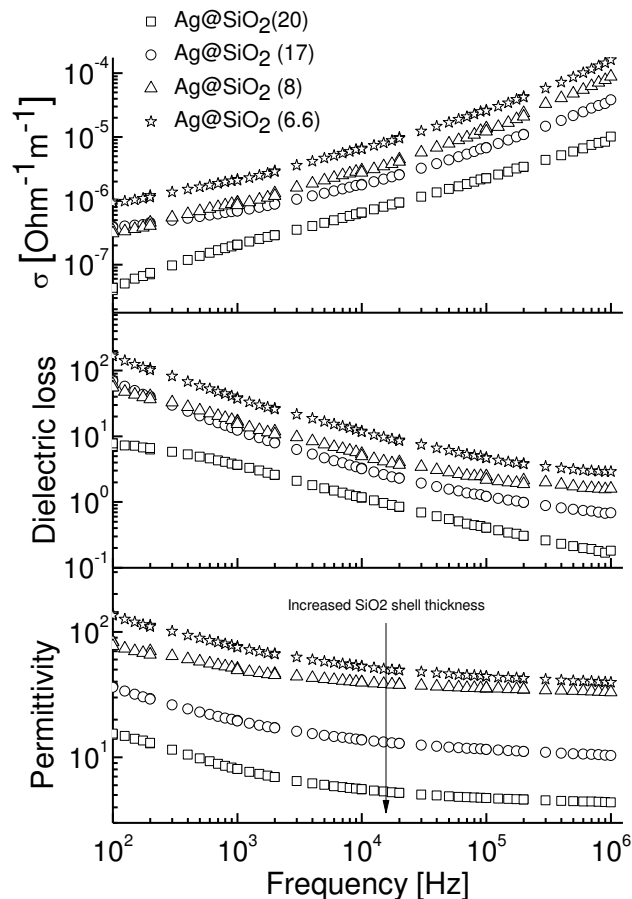


Fig. 42: Permittivity, dielectric loss, and conductivity of AgNPs coated with silica shells of different thickness as function of frequency.

In order to exclude traces of water which may have caused the ϵ' values to scatter, the powder sample of AgNPs with a shell thickness of 17 ± 2 nm was hydrophobized with a silane reagent. The wettability test done in water/toluene as well as the presence of the signal at $\delta = 13$ ppm in the ^{29}Si NMR spectrum characteristic for the Si-C are clear indications that the silylation was successfully achieved (see Supporting information). The dielectric properties of silylated sample showed ϵ' values that remained constant even at lower frequencies (Fig. 43). As mentioned before, the rising permittivity of the non-silylated nanoparticle samples is likely due to ionic impurity conduction which is favored

3. Dielectric Properties of Silver Nanoparticles Coated with Silica Shells of Different Thicknesses

by water adsorption in the porous nanoparticle film. Silylation creates a hydrophobic shell around the Ag nanoparticles and removes the water from the surface. At high frequencies, typically above 10^4 Hz, the ion conduction mechanism no longer contributes to the permittivity of the nanoporous samples. The difference between silylated and non-silylated samples in the high frequency region is rather small and is attributed to slightly different packing of the nanoparticle in the pellets and to the experimental uncertainty. Since the ϵ' of air is rather low, and the air voids are filled by alkyl chains which have a ϵ' of about 2, a slight increase in the ϵ' should be observed for the hydrophobized sample. Such effect was observed by others. For example the permittivity of bulk TiO_2 value of 80 decreased to 58 for TiO_2 nanoparticles due to the presence of voids.³⁴

3. Dielectric Properties of Silver Nanoparticles Coated with Silica Shells of Different Thicknesses

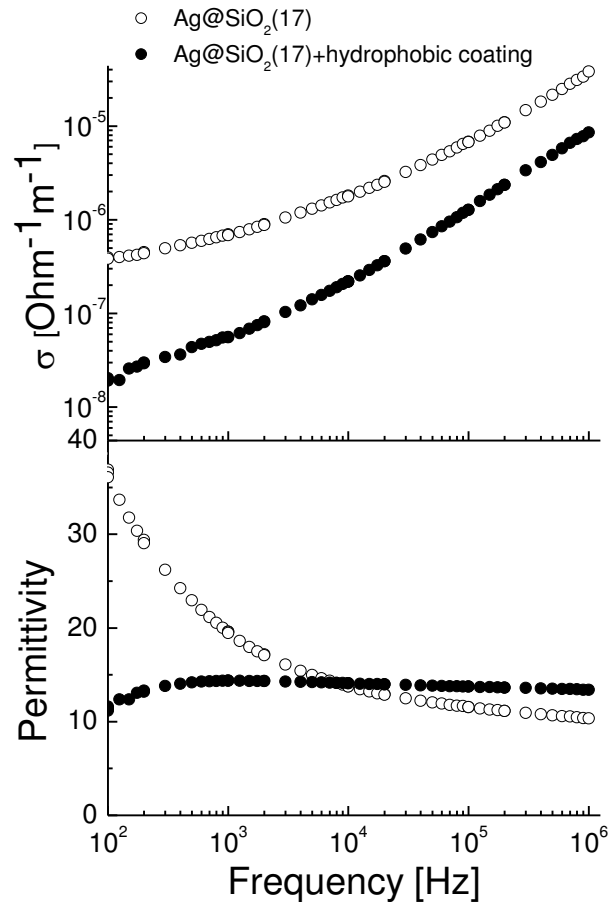


Fig. 43: The permittivity and conductivity of AgNPs coated with a 17 ± 2 nm silica shell and of a silica hydrophobized with a silane reagent.

The dielectric loss increases with the thinning of silica shell (Fig. 42). This loss of charges is also reflected by the conductivity of the samples. The AC conductivity is given by $\sigma = 2\pi\vartheta\epsilon_0\epsilon''$, where ϵ'' is the imaginary part of the complex dielectric function ϵ' , ϵ_0 is the permittivity of vacuum and ϑ is the frequency. If the universal response function $\sigma(\vartheta) = A\vartheta^s$ is fitted to the measured AC conductivity (Fig. 42), a frequency exponent between 0.49 and 0.56 is obtained, depending on the thickness of the silica shell.³⁵ A frequency exponent $s < 1$, is typical for non-Debye type relaxation caused by hopping or tunnelling of charges.³⁶ The trend that s decreases with decreasing the silica shell thickness is characteristic for a system in which conductivity increases.³⁷ Through the

3. Dielectric Properties of Silver Nanoparticles Coated with Silica Shells of Different Thicknesses

hydrophobization of the silica surface the conductivity of the sample decreases significantly at all frequencies as compared to the sample where no hydrophobic coating was used. Hydrophobization of the silica surface is required not only to stabilize the dielectric properties of the Ag@SiO₂ but it helps to compatibilize the particles with an organic matrix where such particles could be used as high ϵ' filler. Further work is presently going in this direction.

Our samples can be considered as percolating conductive particles held apart by the twice the thickness of the insulating shell. If we do not have water inclusion in our pellet samples, the voids can be considered to be filled with air. Therefore the calculation of the effective electrical permittivity of the samples amounts to calculation of highly concentrated core-shell particles in an air matrix ($\epsilon_m = 1$). It is well known that only effective medium theories such as the one derived by Bruggemann can reasonably well describe non-dilute particle inclusion in a matrix.³⁸ Here we applied an effective-medium theory that has been developed for two-phase random composites with an interfacial shell given by³⁹

$$(1-F) \frac{\epsilon_{eff} - \epsilon_m}{2\epsilon_{eff} + \epsilon_m} + F \frac{\epsilon_{eff} - \epsilon_c}{2\epsilon_{eff} + \epsilon_c} = 0 \quad (\text{Eq. 47})$$

$$\epsilon_{eff} = \frac{F(3\epsilon_c - 3\epsilon_m) + 2\epsilon_m - \epsilon_c + \sqrt{[F^2(9\epsilon_m^2 - 18\epsilon_c\epsilon_m + 9\epsilon_c^2) - F(12\epsilon_m^2 - 18\epsilon_c\epsilon_m + 6\epsilon_c^2) + 4\epsilon_m^2 + 4\epsilon_c\epsilon_m + \epsilon_c^2]}}{4} \quad (\text{Eq. 48})$$

$$\text{with } \epsilon_c = \epsilon_1 \frac{2\epsilon_1 + \epsilon_2 + 2\alpha(\epsilon_2 - \epsilon_1)}{2\epsilon_1 + \epsilon_2 - \alpha(\epsilon_2 - \epsilon_1)} \quad (\text{Eq. 49})$$

3. Dielectric Properties of Silver Nanoparticles Coated with Silica Shells of Different Thicknesses

where ϵ_{eff} is the effective permittivity, ϵ_1 the permittivity of the shell ($\epsilon_{silica} = 3.9$), ϵ_2 the permittivity of the core ($\epsilon_{Ag} = 10000$),⁴⁰ ϵ_c the dielectric permittivity of the core-shell particles, α is the volume fraction of core in the core-shell particles $\alpha = (r_0/R)^3$, where r_0 is the radius of Ag nanoparticles and R is the radius of the core-shell particles. For the calculations ideal spheres were used. Their closed-packed arrangement (*hcp*) leads to volume fraction F of 74 %. Given the deviation of the experimental particles from spherical structure it is difficult to indicate a precise packing density. From the SEM images of pellets (see Supporting information) we infer a tight packing. Therefore we have chosen the highest packing density that can be achieved with identical spheres. The calculated and measured effective permittivity as a function of shell thickness is displayed in Tab. 11. The measured values are clearly larger than the calculated ones which could be due to the failure of the model at the percolation limit, even though the theory proved to fit the permittivity of polymer composites with a volume fraction of BaTiO₃ particles up to 70% or might be due to traces of water that are rather hard to remove.

Tab. 11: The calculated and measured ϵ' for different silica thicknesses.

Entry	ϵ_{eff}' calc. ^a	ϵ' measured ^b
Ag@SiO ₂ (20)	3.9	4.6
Ag@SiO ₂ (17)	4.2	10
Ag@SiO ₂ (8)	6.9	34
Ag@SiO ₂ (6.6)	8.0	41
Ag@SiO ₂ (3.6)	13.5	conductive

^a $\epsilon_m=1$ for air, $\epsilon'_{SiO_2} = 3.9$. ^bIn order to avoid ionic conductivity contributions, the permittivity at the frequency of 10^4 Hz is given.

3.5 Conclusions

We report an upscale of the synthesis of Ag nanoparticles of 38 nm size as well as their coating with a silica shell of different thicknesses by the Stöber method. The silica shell was varied from ~ 3.6 nm to ~ 20 nm. The core/shell structure of the prepared particles was clearly proven by using a combination of techniques: UV-vis, DLS, SEM, TEM, and EDX. Parallel-plate capacitors of pellets composed of pressed powder of Ag nanoparticles coated with different silica shells were made and the dielectric properties were investigated as function of the shell thickness. For a shell of 3.6 ± 1 nm, the insulator layer is too thin and the particles are conductive while increasing the shell thickness to 6.6 ± 1.5 nm, a shift from conductive to dielectric behaviour was observed. A further increase in the shell to 20 ± 2 nm hides the presence of the metal core and the resulting particles behave similar to silica. The conductivity of the samples due to absorbed water on the silica surface can be reduced by hydrophobization of the surface with an alkyl silane. Such hydrophobized particles have high permittivity, small dielectric losses, and are readily dispersible in nonpolar solvents and are therefore attractive fillers particularly for polydimethylsiloxane material for transducer and more generally for large energy storage capacitors.

3.6 Acknowledgments

We gratefully acknowledge D. Schreier for helping with the TEM and SEM measurements, Dr. F. La Mattina for providing us with the infrastructure for the impedance measurements (all Empa), Dr. D. Rentsch for the ^{29}Si NMR measurement, and B. Sinnet from Eawag for helping with DLS measurement. We also gratefully acknowledge Swiss National Science Foundation (SNF132101) and Swiss Federal Laboratories for Materials Science and Technology (Empa, Dübendorf) for financial support.

3.7 References

- (1) Kelly, L. K.; Coronado, E.; Zhao, L. L.; Schatz, G. C. The Optical Properties of Metal Nanoparticles: The Influence of Size, Shape, and Dielectric Environment. *J. Phys. Chem. B*, **2003**, *107*, 668-677; Welles, A. E. Silver Nanoparticles Properties, Characterization and Applications, Nova Science Pub. Inc. New York **2012**; Alivisatos, A. P. Semiconductor Clusters, Nanocrystals, and Quantum Dots. *Science*, **1996**, *271*, 933-937; Murphy, C. J.; Jana, N. R. Controlling the Aspect Ratio of Inorganic Nanorods and Nanowires. *Adv. Mater.* **2002**, *14*, 80-82.
- (2) Zeng, J.; Xia, X.; Rycenga, M.; Henneghan, P.; Li, Q.; Xia, Y. Successive Deposition of Silver on Silver Nanoplates: Lateral Versus Vertical Growth. *Angew. Chem. Int. Ed.* **2011**, *50*, 244–249.
- (3) Guo, N.; DiBenedetto, S. A.; Tewari, P.; Lanagan, M. T.; Ratner, M. A.; Marks, T. J. Nanoparticle, Size, Shape, and Interfacial Effects on Leakage Current Density, Permittivity, and Breakdown Strength of Metal Oxide-Polyolefin Nanocomposites: Experiment and Theory. *Chem. Mater.* **2010**, *22*, 1567–1578; Pan, J.; Li, K.; Li, J.; Hsu, T.; Wang, Q. Dielectric Characteristics of Poly (ether ketone ketone) for High Temperature Capacitive Energy Storage. *Appl. Phys. Lett.* **2009**, *95*, 022902; Claude, J.; Lu, Y.; Li, K.; Wang, Q. Electrical Storage in Poly(vinylidene fluoride) based Ferroelectric Polymers: Correlating Polymer Structure to Electrical Breakdown Strength. *Chem. Mater.* **2008**, *20*, 2078–2080; B. Chu, B.; X. Zhou, X.; K. Ren, K.; Neese, B.; Lin, M.; Wang, Q.; Bauer, F.; Zhang, Q. M. A Dielectric Polymer with High Electric Energy Density and Fast Discharge Speed. *Science*, **2006**, *313*, 334–336.
- (4) Bai, Y.; Cheng, Z.-Y.; Bharti, V.; Xu, H. S.; Zhang, Q. M. High-Dielectric-Constant Ceramic-Powder Polymer Composites. *Appl. Phys. Lett.* **2000**, *76*, 3804-3806; Li, J.; Seok, S.; Chu, B.; Dogan, F.; Zhang, Q.; Wang, Q. Nanocomposites of Ferroelectric Polymers with TiO₂ Nanoparticles Exhibiting Significantly Enhanced Electrical Energy Density. *Adv. Mater.* **2009**, *21*, 217–221; Gallone, G.; Carpi, F.; De Rossi, D.; Levita, G.;

3. Dielectric Properties of Silver Nanoparticles Coated with Silica Shells of Different Thicknesses

Marchetti, A. Dielectric Constant Enhancement in Silicone Elastomer Filled with Lead Magnesium Niobate-Lead Titanate. *Mat. Sci. Eng. C* **2007**, 27, 110–116; Stoyanov, H.; Kollosche, M.; Risse, S.; McCarthy, D. N.; Kofod, G. Elastic Block Copolymer Nanocomposites with Controlled Interfacial Interactions for Artificial Muscles with Direct Voltage Control. *Soft Matter* **2011**, 7, 194-202.

(5) Z. Li, Z.; L. A. Fredin, L. A.; P. Tewari, P.; S. A. DiBenedetto, S. A.; M. T. Lanagan, M. T.; M. A. Ratner, M. A.; T. J. Marks, T. J. *In Situ* Catalytic Encapsulation of Core-Shell Nanoparticles Having Variable Shell Thickness: Dielectric and Energy Storage Properties of High Permittivity Metal Oxide Nanocomposites. *Chem. Mater.* **2010**, 22, 5154-5164.

(6) P. Hedvin, Dielectric Spectroscopy of Polymers, Adam Higler LTD, Budapest, 1977.

(7) Huang, C.; Zhang, Q. Enhanced Dielectric and Electromechanical Responses in High Dielectric Constant All-Polymer Percolative Composites. *Adv. Funct. Mater.* **2004**, 14, 501-506; Kirkparck, S. Percolation and Conduction. *Rev. Mod. Phys.* **1973**, 45, 574-588; Nan, C. W. Physics of Inhomogenous Inorganic Materials. *Prog. Mater. Sci.* **1993**, 37, 1-116; Pecharroman, C.; Moya, J. S. Experimental Evidence of a Giant Capacitance in Insulator-Conductor Composites at the Percolation Threshold. *Adv. Mater.* **2000**, 12, 294-297; Dang, Z.-M., Shen, S.; Nan, C. W. Dielectric Behavior of Three-Phase Percolative Ni-BaTiO₃/Polyvinylidene Fluoride Composites. *Appl. Phys. Lett.* **2002**, 81, 4814-4816.

(8) Moya, J. S. Experimental Evidence of a Giant Capacitance in Insulator-Conductor Composites at the Percolation Threshold. *Adv. Mater.* **2000**, 12, 294-297;

(9) Rao, Y.; Wong, C. P.; Xu, J. High Dielectric Polymer Composites and Methods of Preparation Thereof. US Pat. 6864306, 2005; Choi, H. W.; Heo, Y. W.; Lee, J. H.; E. Park, E. T.; Chung, Y. K. Effects of BaTiO₃ on Dielectric Behavior of BaTiO₃-Ni-Polymethyl Methacrylate Composites. *Appl. Phys. Lett.* **2006**, 89, 132910; Lu, J.; K. Moon, K. S.; Xu, J.; Wong, C. P. Synthesis and Dielectric Properties of Novel High-K Polymer Composites Containing In-Situ Formed Silver Nanoparticles for Embedded Capacitor Applications. *J. Mat. Chem.* **2006**, 16, 1543-1548.

3. Dielectric Properties of Silver Nanoparticles Coated with Silica Shells of Different Thicknesses

- (10) Qi, L.; Lee, B. I.; Chen, S.; Samuels, W. D.; Exarhos, G. J. High-Dielectric-Constant Silver-Epoxy Composites as Embedded Dielectrics. *Adv. Mater.* **2005**, *17*, 1777-1781.
- (11) Shen, Y.; Lin, Y.; Li, M.; Nan, C. W. High Dielectric Performance of Polymer Composite Films Induced by a Percolating Interparticle Barrier. *Adv. Mat.* **2007**, *19*, 1418-1422.
- (12) T. Kempa, T.; Carnahan, D.; Olek, M.; Correa, M.; Giersig, M.; Cross, M.; Benham, G.; Sennett, M.; Ren, Z.; Kempa, K. Dielectric Media Based on Isolated Metallic Nanostructures. *J. Appl. Phys.* **2005**, *98*, 034310.
- (13) Yang, T. I.; Brown, R. N. C.; Kempel, L. C.; Kofinas, P.; Controlled Synthesis of Core-Shell Iron-Silica Nanoparticles and Their Magneto-Dielectric Properties in Polymer Composites. *Nanotechnology* **2011**, *22*, 105601.
- (14) Xu, J.; Wong, C. P. Low-Loss Percolative Dielectric Composite. *Appl. Phys. Lett.* **2005**, *87*, 082907.
- (15) Li, J. Y.; Zhang, L.; Ducharme, S. Electric Energy Density of Dielectric Nanocomposite. *Appl. Phys. Lett.* **2007**, *90*, 132901.
- (16) Wilkinson, D.; Langer, J. S.; Sen, P. N. Enhancement of the Dielectric-Constant Near a Percolation Threshold. *Phys. Rev. B* **1983**, *28*, 1081-1087.
- (17) Goh, H.; Lee, H. -J.; Nam, B.; Lee, Y. B.; Choi, W. S. A Chemical Reactor for Hierarchical Nanomaterials with Tuneable Structures: A Metal-Triggered Reaction in the Confined Heat Chamber. *Chem. Mat.* **2011**, *23*, 4832-4837; Niitsoo, O.; Couzis, A. Facile Synthesis of Silver Core-Silica Shell Composite Nanoparticles. *J. Coll. Interf. Sci.* **2011**, *354*, 887-890; Schmidt, A. M. The Synthesis of Magnetic Core-Shell Nanoparticles by Surface-Initiated Ring-Opening Polymerization of ϵ -Caprolactone. *Macromol. Rapid Commun.* **2005**, *26*, 93-97; Li, H.; Han, J.; Panioukhine, A.; Kumacheva, E. From Heterocoagulated Colloids to Core-Shell Particles. *J. Coll. Interf. Sci.* **2002**, *255*, 119-128; Vogel, N.; Fernandez-Lopez, C.; Perez-Juste, C. J.; Liz-Marzan, L. M.; Landfester, K.;

3. Dielectric Properties of Silver Nanoparticles Coated with Silica Shells of Different Thicknesses

Weiss, C. K. Ordered Arrays of Gold Nanostructures From Interfacially Assembled Au@PNIPAM Hybrid Nanoparticles. *Langmuir* **2012**, 28, 8985-8993.

(18) Pham, H. H.; Kumacheva, E. Core-Shell Particles: Building Blocks for Advanced Polymer Materials. *Macromol. Symp.* **2003**, 192, 191-205.

(19) Burns, G. P. Titanium Dioxide Dielectric Films Formed by Rapid Thermal Oxidation. *J. Appl. Phys.* **1988**, 65, 2095-2097; Biener, J.; Farfan-Arriba, E.; Bienel, M.; C. Friend, C. M.; Madix, R. J. Synthesis of TiO₂ Nanoparticles on the Au(111) Surface. *J. Chem. Phys.* **2005**, 123, 094705-1-094705-6.

(20) Guerrero-Martinez, A.; Perez-Juste, J.; Liz-Marzan, L. M. Recent Progress on Silica Coating of Nanoparticles and related Nanomaterials. *Adv. Mater.* **2010**, 22, 1182-1195; Iijima, M.; Kaniya, H. Layer-by-Layer Surface Modification of Functional Nanoparticles for Dispersion in Organic Solvents. *Langmuir* **2010**, 26, 17943-17948; Fernandez-Lopez, C.; Mateo-Mateo, C.; Alvarez-Puebla, R. A.; Perez-Juste, J.; Pastoriza-Santos, I.; Liz-Marzan, L. M. Highly Controlled Silica-Coating of PEG-Capped Metal Nanoparticles and Preparation of SERS-Encoded Particles. *Langmuir* **2009**, 25, 13894-13899.

(21) Wiley, B. J.; Im, S. H.; Li, Z. Y.; McLellan, J.; Siekkinen, A.; Xia, Y. Maneuvering the Surface Plasmon Resonance of Silver Nanostructures Through Shape-Controlled Synthesis. *J. Phys. Chem. B*, **2006**, 110, 15666-15675; Kim, D.; Jeong, S.; Moon, J. Synthesis of Silver Nanoparticles Using the Polyol Synthesis and the Influence of Precursor Injection. *Nanotechnology* **2006**, 17, 4019-4024.

(22) Baida, H.; Billaud, P.; Marhaba, S.; Christofilos, D.; Cottancin, E.; Crut, A.; Lermé, J.; Maioli, P.; Pellarin, M.; Broyer, M.; Del Fatti, N.; Vallée, F. Quantitative Determination of the Size Dependence of Surface Plasmon Resonance Damping in Single Ag@SiO₂ Nanoparticles. *Nano Lett.* **2009**, 9, 3463-3469; Zhang, F.; Braun, G.; Shi, Y.; Zhang, Y.; Sun, X.; Reich, N.; Zhao, D.; Stucky, G. Fabrication of Ag@SiO₂@Y₂O₃:Er Nanostructures for Bioimaging: Tuning of the Upconversion Fluorescence with Silver Nanoparticles. *J. Am. Chem. Soc.* **2010**, 132, 2850-2851.

3. Dielectric Properties of Silver Nanoparticles Coated with Silica Shells of Different Thicknesses

- (23) Im, S. H.; Lee, Y. T.; Wiley, B.; Xia, Y. Large-Scale Synthesis of Silver Nanocubes: The Role of HCl in Promoting Cube Perfection and Monodispersity. *Angew. Chem.* **2005**, *117*, 2192-2195; Yu, D.; Yam, V. W. -W. Controlled Synthesis of Monodisperse Silver Nanocubes in Water. *J. Am. Chem. Soc.* **2004**, *126*, 13200-13201.
- (24) Xia, Y.; Xiong, Y.; Lim, B.; Skrabalak, S. E. Shape-Controlled Synthesis of Metal Nanocrystals: Simple Chemistry Meets Complex Physics? *Angew. Chem. Int. Ed.* **2009**, *48*, 60-103.
- (25) Siekkinen, A. R.; McLellan, J. M.; Chen, J.; Xia, Y. Rapid Synthesis of Small Silver Nanocubes by Mediating Polyol Reduction with a Trace Amount of Sodium Sulfide or Sodium Hydrosulfide. *Chem. Phys. Lett.* **2006**, *432*, 491-496; D. D. Evanoff, D. D.; G. Chumanov, G. Size-Controlled Synthesis of Nanoparticles. 1. "Silver-Only" Aqueous Suspensions via Hydrogen Reduction. *J. Phys. Chem. B* **2004**, *108*, 13948-13956.
- (26) Stöber, W.; Fink, A.; Bohn, E. Controlled Growth of Monodisperse Silica Spheres in the Micron Size Range. *J. Colloid Interface Sci.* **1968**, *26*, 62-69
- (27) Caruso, F.; Caruso, R. A.; Möhwald, H. Nanoengineering of Inorganic and Hybrid Hollow Spheres by Colloidal Templating. *Science* **1998**, *282*, 1111-1114; Lu, Y.; McLellan, J.; Xia, Y. Synthesis and Crystallization of Hybrid Spherical Colloids Composed of Polystyrene Cores and Silica Shells. *Langmuir*, **2004**, *20*, 3464-3470.
- (28) Xu, K.; Wang, J. -X.; Kang, X. -L.; Chen, J. -F. Fabrication of Antibacterial Monodispersed Ag-SiO₂ Core-Shell Nanoparticles with High Concentration. *Mat. Lett.* **2009**, *63*, 31-33; Ung, T.; Liz-Marzan, L. M.; Mulvaney, P. Controlled Method for Silica Coating of Silver Colloids. Influence of Coating on the Rate of Chemical Reactions. *Langmuir* **1998**, *14*, 3740-3748; Hardikar, V. V.; Matijevic, E. Coating of Nanosize Silver Particles with Silica. *J. Colloid Interace. Sci.* **2000**, *221*, 133-136; Han, Y.; Jiang, J.; Lee, S. S.; Ying, J. Y. Reverse Microemulsion-Mediated Synthesis of Silica-Coated Gold and Silver Nanoparticles. *Langmuir* **2008**, *24*, 5842-5848.

3. Dielectric Properties of Silver Nanoparticles Coated with Silica Shells of Different Thicknesses

- (29) Yin, Y.; Lu, Y.; Sun, Y.; Xia, Y. Silver Nanowires Can Be Directly Coated with Amorphous Silica To Generate Well-Controlled Coaxial Nanocables of Silver/Silica. *Nano Lett.* **2002**, 2, 427-430.
- (30) Kong, X.; Yu, Q.; Zhang, X.; Du, X.; Gong, H.; Jiang, H. Synthesis and Application of Surface Enhanced Raman Scattering (SERS) tags of Ag@SiO₂ Core/Shell Nanoparticles in Protein Detection. *J. Mater. Chem.* **2012**, 22, 7767-7774.
- (31) Kobayashi, Y.; Katakami, Y. H.; Mine, E.; Nagao, D.; Konno, M.; Liz-Marzan, L. M. Silica Coating of Silver Nanoparticles Using a Modified Stöber Method. *J. Colloid. Interface Sci.* **2005**, 283, 392-396
- (32) Yang, J.; Zhang, F.; Chen, Y.; Qian, S.; Hu, P.; Li, W.; Deng, Y.; Fang, Y.; Han, L.; Luqman, M.; Zhao, D. Core-Shell Ag@SiO₂@mSiO₂ Mesoporous Nanocarriers for Metal-Enhanced Fluorescence. *Chem. Commun.* **2011**, 47, 11618-11620.
- (33) Graf, C.; Vossen, D. L. J.; Imhof, A.; van Blaaderen, A. A General Method To Coat Colloidal Particles with Silica. *Langmuir* **2003**, 19, 6693-6700.
- (34) Balasubramanian, B.; Kraemer, K. L.; Reding, N. A.; Skomski, R.; Ducharme, S.; Sellyer, D. J. Synthesis of Monodisperse TiO₂-Paraffin Core-Shell Nanoparticles for Improved Dielectric Properties. *ACS Nano* **2010**, 4, 1893-1900.
- (35) Ahmad, M. M.; Makhoulf, S. A.; Khalil, K. M. S. Dielectric Behavior and AC Conductivity Study of NiO/Al₂O₃ Nanocomposites in Humid Atmosphere. *J. Appl. Phys.* **2006**, 100, 094232; Garcia-Belmonte, G.; Kytin, V.; Dittrich, T.; Bisquert, J. Effect of Humidity on the AC Conductivity of Nanoporous TiO₂. *J. Appl. Phys.* **2003**, 94, 155262.
- (36) Jonscher, A. K. The Universal Dielectric Response. *Nature* **1977**, 267, 673-679.
- (37) Elliott, S. R. AC Conduction in Amorphous Chalcogenide and Pnictide Semiconductors. *Adv. Phys.* **1987**, 36, 135-217.

3. Dielectric Properties of Silver Nanoparticles Coated with Silica Shells of Different Thicknesses

(38) Tinga, W. R. Progress in Electromagnetics Research; Dielectric Properties of Heterogeneous Materials, eds. Kong, J. A., Priou, A. Elsevier Science Publishing Co. Inc., New York, 1992.

(39) Xue, Q. J. Effective-Medium Theory for Two-Phase Random Composites with an Interfacial Shell. *Mater. Sci. Technol.* **2000**, *16*, 367-369.

(40) Bowman, D. R.; Strout, D. Model for Dielectric Breakdown in Metal-Insulator Composites. *Phys. Rev. B* **1989**, *40*, 4641. For metal insulator composites, the permittivity diverges close to the percolation threshold of the metallic fillers. In order to reflect this behavior using the effective medium theory applied in our paper, an infinite value for ϵ_{Ag} would have to be chosen. Here, an arbitrary high enough ϵ_{Ag} number that yields the same results as an infinite ϵ_{Ag} value was chosen.

3.8 Supporting Information



Fig. 44: Wettability test in water/toluene for the Ag@SiO₂ (left) and that of hydrophobized with silane reagent (right). The hydrophobized particles are transferred in organic phase.

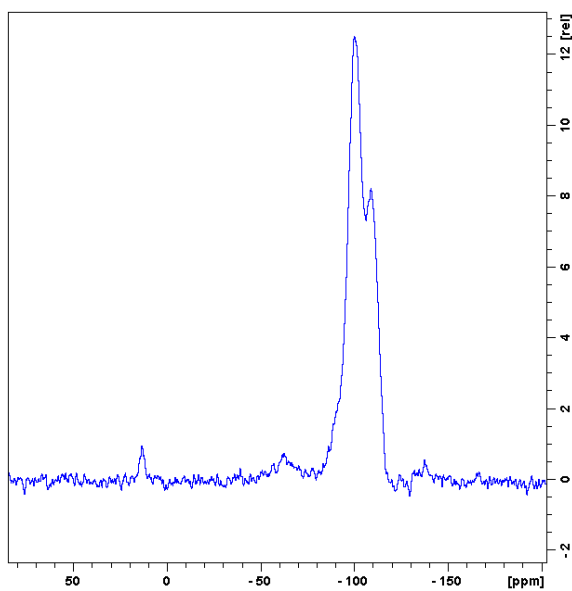


Fig. 45: Solid-state ²⁹Si CP-MAS NMR spectrum of silver nanoparticles coated with silica shell and surface functionalized with octyl chains showing the chemical shift for the silicon nucleus of the surface- bound alkyl chains at $\delta = 13$ ppm.

3. Dielectric Properties of Silver Nanoparticles Coated with Silica Shells of Different Thicknesses

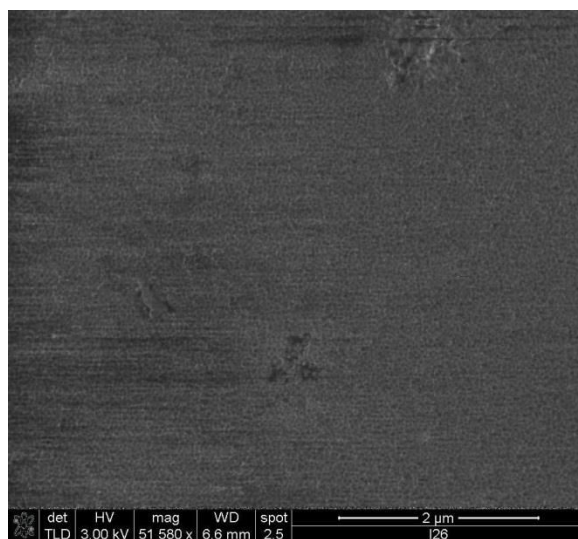


Fig. 46: SEM image of Ag@SiO₂ (6.6 nm) powder in pressed pellet. The sample was measured in high vacuum mode using 3 kV and a TLD detector.

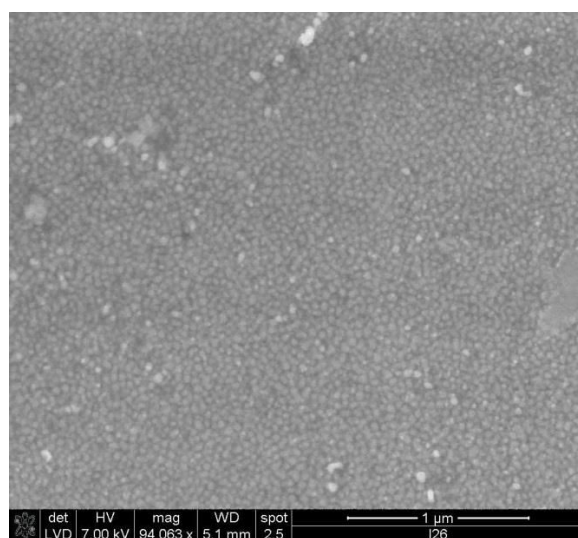


Fig. 47: SEM image of Ag@SiO₂ (6.6 nm) powder in pressed pellet. The sample was measured in low vacuum mode using 7 kV and a LVD detector.

3. Dielectric Properties of Silver Nanoparticles Coated with Silica Shells of Different Thicknesses

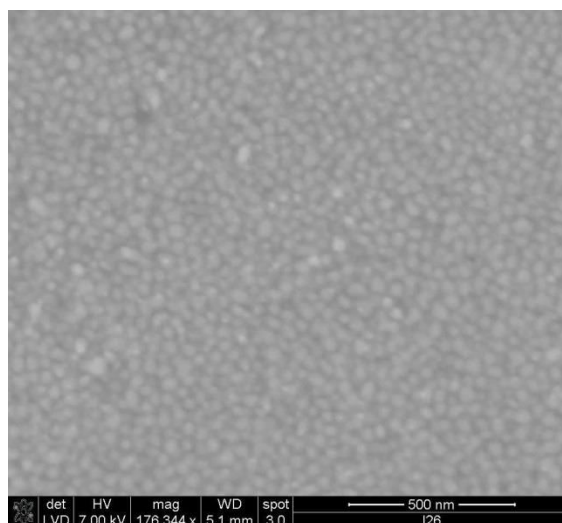


Fig. 48: SEM image of Ag@SiO₂ (6.6 nm) powder in pressed pellet. The sample was measured in low vacuum mode using 7 kV and a LVD detector.

Chapter 4: Highly Stretchable Dielectric Elastomer Composites Containing High Volume Fraction of Silver Nanoparticles (AgNPs)

Declaration: The nanoparticles synthesis and functionalization, the microscopy analysis with TEM/SEM, the nanocomposite formation as well as the mechanical tests were conducted by Jose Enrico Q. Quinsaat, while dielectric measurements of the filler and the resulting nanocomposite were conducted by Dr. Dorina Opris. The high molecular weight PDMS was prepared by Dr. Mihaela Alexandru, while Dr. Borgschulte performed the XPS measurements for the nanoparticles.

*Jose Enrico Q. Quinsaat^{1,2}, Mihaela Alexandru¹, Frank A. Nüesch^{1,2}, Heinrich Hofmann², Andreas Borgschulte³ and Dorina M. Opris^{*1}*

¹ *Swiss Federal Laboratories for Materials Science and Technology (Empa), Laboratory for Functional Polymers, Überlandstrasse 129, 8600 Dübendorf, Switzerland*

² *Ecole Polytechnique Fédérale de Lausanne (EPFL), Materials Institute, 1015 Lausanne, Switzerland*

³ *Swiss Federal Laboratories for Materials Science and Technology (Empa), Laboratory for Advanced Analytical Technologies, Überlandstrasse 129, 8600 Dübendorf, Switzerland*

Abstract: The relative permittivity (ϵ') of a polymeric material can be significantly increased when blended with conductive fillers at concentrations approaching percolation threshold. However, reproducible synthesis of such composites is after decades of research still a major challenge and a bottleneck for their application. Difficulties arise in controlling size and shape of the filler as well as in its homogenous distribution within the composite. These parameters strongly affect the dielectric as well as the mechanical properties of the composite. While a substantial amount of literature is dealing with the influence of conductive filler on the dielectric properties of composites, little is known about their mechanical properties. It is therefore still an important goal to synthesize materials with simultaneously high ϵ' and good mechanical properties. Here, we report the synthesis of dielectric elastomers that combine key properties such as high flexibility and stretchability, high thermal stability, increased ϵ' , low dielectric loss and conductivity. Such materials were prepared by solution processing using quasi-spherical silver nanoparticles (AgNPs) of defined size in a polydimethylsiloxane matrix ($M_w = 692$ kDa). To prevent percolation, the AgNPs were coated with a thin silica shell (< 4 nm). To increase their compatibility with the silicone matrix, these core/shell nanoparticles were passivated with a silane reagent. The insulating silica shell around the particles precisely defines the minimum approach distance between the cores as twice the shell thickness. The dielectric properties of those passivated particles (filler) were measured in pellets and found to have an almost frequency independent values of $\epsilon' = 90$ and a very low loss factor $\tan \delta = 0.023$ at high frequencies. When such particles were used as filler in a polydimethylsiloxane matrix, composites with low dielectric losses were obtained. A composite containing 31 vol% filler with $\epsilon' = 21$ and a $\tan \delta = 0.03$ at ~ 1 kHz was achieved. At a AgNPs volume fraction of 20%, the composite has a $\epsilon' = 5.9$ at ~ 1 kHz, a dielectric strength of 13.4 V/ μm , elastic modulus as low as 350 kPa at 100 % strain, and a strain at break of 800 %. Due to the high specific energy density *per* volume at low electric fields, these composites are attractive materials in applications involving low electric fields.

4.1 Introduction

Next generation electronic devices require materials that combine elasticity with electronic, optoelectronic and thermal properties and open exciting challenges for material scientists.¹ During the last couple of years, much research has been devoted to prepare elastomers that show increased permittivity (ϵ'), low dielectric losses (ϵ''), high dielectric strength (E_b) and high flexibility.^{2,3} Such elastomers are attractive dielectrics in dielectric elastomer transducers (DET) which are elastic capacitors that either elongate under a high electric field (actuator mode of operation) or harvest energy upon stretching and charging (generator mode of operation).^{4,5} The amount of energy harvested per cycle increases when materials with high strain at break, high ϵ' , and high breakdown field are used.⁶ However, for certain application, in the vicinity of human body, high voltages should be avoided. High ϵ' materials are also attractive dielectric in capacitors.

Cross-linked polydimethylsiloxanes elastomers (silicones) have excellent environmental properties, low glass transition temperature, and mechanical properties that do not change much with temperature and frequency and were intensively used by the DET community.^{7–11} However, the ϵ' of silicones is lower than 3. Several approaches have been used to increase the ϵ' of a silicone by, for example, chemical modification with organic dipoles^{12–14} or blending with conductive fillers¹⁵ as well as high ϵ' ceramics.^{16–19} Chemical modification of silicones with organic dipoles is a promising approach to increase ϵ' but other materials parameters such as flexibility, elasticity, elastic moduli, and strain at break, are also affected. Additionally, tedious synthetic steps have to be followed. Blends with ceramic fillers show also an increase in ϵ' , however, a significant increase in ϵ' is obtained at volume fractions exceeding 50 vol% which, in turn, has a detrimental effect on elastic properties. Conductive filler composites look like a promising approach to high ϵ' materials since the ϵ' increases according to a power law as the filler concentration approaches a critical value corresponding to the percolation threshold (Eq. 50):²⁰

$$\epsilon'_{eff} = \frac{\epsilon_{mr'}}{(f_c - f)^q} \quad (\text{Eq. 50})$$

4. Highly Stretchable Dielectric Elastomer Composites Containing High Volume Fraction of AgNPs

whereby ϵ_{eff}' and ϵ_{mr}' are the permittivity of the composite and of the polymer matrix respectively, f_c is the percolation threshold fraction, f is the volume fraction of the filler, and q is a scaling constant. Metal particles, metal oxide particles, carbon black, carbon nanotubes, and conductive polymers have been used as conductive fillers.^{6,21–26}

Conductive polymer fillers have the advantage of being lightweight and easy to prepare. However, when blended in a polymer matrix, the morphology of the filler is rather difficult to control and phase separation is often observed.^{27,28} Since permittivity is sensitive to the morphology, shape and size of the conductive filler, special care has to be taken to control these parameters.²⁹ In addition, the interfacial interaction shifts the percolation threshold toward lower volume fraction of nanoparticles and starts to be effective when the proportion between the radius of the nanoparticles and the thickness of the shell approaches a value of 10.³⁰ If the filler has a large size or is agglomerated, and if its size is close to that of the film thickness, discharge between electrodes happens.³¹ In many cases, the addition of conductive nanoparticles enhances ϵ' but increases the dielectric losses, making the potential gain in ϵ' useless. Therefore, to synthesize composites with reliable and reproducible properties, the size of the filler and its dispersion in the composites must be carefully controlled.³²

Metal nanoparticles (MNPs) are easy to polarize and their shape and size can be precisely controlled and are therefore very good model systems. When applied as fillers in the above context, agglomeration of MNPs has to be avoided when dispersed into a matrix. Otherwise conductive paths can form which are detrimental to the properties. MNPs can be incorporated into a polymer matrix using *in situ* or *ex situ* approaches.^{33,34} In the former, the particles are formed through reduction or decomposition of a metal salt that was dispersed in polymer matrix.³⁵ However, the morphology, the shape, and the size of the MNPs in the matrix is difficult to control and composites with rather low volume fraction of metal are formed.^{36,37} Furthermore, the residual components formed during reduction/decomposition of the metal source are either left in the composite or have to be removed by tedious swelling/extraction steps. We considered this approach therefore

4. Highly Stretchable Dielectric Elastomer Composites Containing High Volume Fraction of AgNPs

unattractive for our goal. In the latter approach, preformed particles are blended into a polymer matrix. Here, the incompatibility and the agglomeration of the metal filler in the polymer matrix are problems that have to be overcome. Although there has been substantial amount of work devoted to the dielectric properties of MNPs polymer composites, fillers were used that were either polydisperse, or had large particles size and non-uniform shapes, as well as undefined/or no insulating coating. As mentioned above, such MNPs were not attractive for our purpose.

Silver (Ag) has a high reduction potential and can be prepared in different size and shapes and was therefore selected for our investigations.^{38,39} Polymer composites containing silver nanoparticles (AgNPs) are known. Shen and coworkers used AgNPs coated with an organic shell as filler in an epoxy matrix.⁴⁰ The organic shells were tuned from 4-6 nm up to 8-10 nm. They showed that nanocomposites with the particles surrounded by thinner shells featured a higher ϵ' than the nanocomposite with thicker shells. The rather low dielectric breakdown of the composites of less than 1 V/ μm which is significantly lower as compared to the epoxy matrix used (30 V/ μm), clearly shows the importance of the type and the thickness of the insulating shell used. Very important is also the influence of the volume content of MNPs on the mechanical properties of the resulting materials. Unfortunately, to the best of our knowledge, no detailed characterization of the mechanical properties of composites containing high vol% of metal filler exist. Furthermore, elastic composites containing high vol% of MNPs that show large reversible deformations are not known.

It was thus a prime goal of the present work to provide robust access to metal particles that are not susceptible to chemical oxidation and which have defined size. The present work also aims to prepare surface-treated core/shell Ag/silica nanoparticles which we refer to as Ag@SiO₂ and to use them as filler in polydimethylsiloxane (PDMS) matrix to create high-profile composite materials that allowed us investigating the influence of the filler on the mechanical and dielectric properties of the composite. This would allow us elucidating how much the ϵ' can be increased and how other properties like dielectric loss, conductivity and dielectric breakdown are affected, keeping an eye also on the mechanical

4. Highly Stretchable Dielectric Elastomer Composites Containing High Volume Fraction of AgNPs

properties. The preparation of large amounts of AgNPs was possible by using the polyol synthesis, while the silica coating was achieved by using an optimized Stöber method.^{41,42} To ensure optimum performance of the composite, the compatibility of the Ag@SiO₂ particles with the PDMS matrix was significantly increased by treating the surface of the particles with hexamethyldisilazane (HMDS). Composites of surface-treated Ag@SiO₂ filler in PDMS were made by solution processing. The dielectric and mechanical properties of different vol% of Ag@SiO₂ filler in PDMS were investigated for the first time.

4.2 Experimental Section

4.2.1 Materials and Methods

AgNO₃, poly(vinyl pyrrolidinone) (PVP), ethylene glycol (EG), octamethylcyclotetrasiloxane (D₄), H₂SO₄, hexamethyldisilazane (HMDS), ammonia (NH₄OH), and dibutyltin dilaurate (Sn) catalysts were purchased from Aldrich and used as received. Linear hydroxyl end-functionalized polydimethylsiloxane (PDMS) ($M_w = 139$ kDa) by ABCR (25-35 % methylhydrosiloxane)-dimethylsiloxane-copolymer (AB109380) cross-linker by ABCR. Higher molecular weight hydroxyl end-functionalized polydimethylsiloxane ($M_w = 692$ kDa) was prepared according to the literature.⁴³

The nanoparticles were observed by SEM on a FEI NovaNanoSEM 230 using a BSED detector, TEM analysis were done with Philips CM30 TEM and JEOL 2200FS TEM/STEM, UV-vis absorption spectra were recorded with a Cary 50 spectrophotometer, DLS were done with a Malvern Zetasized Nano ZS, the thermogravimetric analysis (TGA) was conducted with a Perkin Elmer TGA7 at a heating rate of 20 °C min⁻¹ under a He gas flow. *In situ*-XPS surface analysis are performed in a modified VG EscaLab spectrometer with the base pressure $< 1 \times 10^{-10}$ mbar. XPS spectra were collected with a SPECS PHOIBOS 100 analyzer using a non-monochromated X-ray source (Al K α : 1486.6 eV, twin anode Mg K α /Al K α). Image analysis was used for the TEM micrographs to estimate the particles size. The number of particles measured was about 400 for Ag core and about

4. Highly Stretchable Dielectric Elastomer Composites Containing High Volume Fraction of AgNPs

100 for the coated particles with the help of a ruler for Windows. For the determination of the amount of silver in the composites, about 50 mg of material was transferred to a pre-cleaned quartz vessel. Thereafter, 3 mL of nitric acid (65 %) and 1 mL of H₂O₂ (30 %) was added to the components. The contents were transferred into a microwave vessel which contained 5 mL of deionized water (Milli-Q-Quality) and 1 mL H₂O₂. The nanocomposite was decomposed in the microwave MLS 1200. The clear solution was transferred into a 15 mL PP Centrifuge tube with deionized water and diluted to 10 mL. For the quantification of the silver content in the nanocomposite, the prepared solution was once again diluted by a factor of 100. Standard silver solutions containing 1, 2, 5, 10, 20 and 50 mg/L prepared from a commercially available 1 g/L silver standard solution were used for the calibration of the ICP-OES (Vista pro Varian). The particle dispersions in toluene were prepared with a tip sonicator (Sonics VCX-500 Model CV33).

The microstructures of the films were measured with SEM on samples prepared by the freeze-breaking method in liquid nitrogen. Permittivity measurements were done in the frequency range of 1 Hz to 1 MHz using an Novocontrol Alpha-A Frequency Analyzer using a Hewlett Packard 16451B dielectric test fixture equipped with round electrodes. Prior to the measurements, Au electrodes with a thickness of 50 nm were sputtered on both sides of the films. The diameter of the electrodes was 12.5 mm (A series), 7 mm (B series) or 21 mm (B₂₀). To ensure a good contact and a uniform “pressure” over the samples (because of the round electrode used), gold plates slightly smaller than the coated electrodes were used. No dependence of the dielectric properties with the electrode size was observed, which is supportive for homogenous materials. The amplitude of the probing ac electric signal applied to the samples was 1 V. The permittivity was determined from the capacitance: $C = \epsilon\epsilon_0 A/d$, where A is the electrode area, d is the thickness of the capacitor, and ϵ_0 is the vacuum permittivity.

The tensile tests were performed using a Zwick Z010 tensile test machine with a crosshead speed of 500 mm/min. Tensile test specimens with a gauge width of 2 mm and a gauge length of 18 mm were prepared by die cutting. The strain was determined using a traverse moving sensor. The curves were averaged from 3 independent experiments. The tensile

4. Highly Stretchable Dielectric Elastomer Composites Containing High Volume Fraction of AgNPs

modulus was determined from the slope of the stress-strain curves using a linear fit to the data points within 10% strain. Dynamic mechanical analysis was carried out on a RSA 3 DMA from TA Instruments. Stripes of 10 mm wide, 24 mm long, and 58 μm thick were measured under a dynamic load of 2 g, at 1 % strain in the frequency range of 0.01 to 10 Hz, at 26 °C, and 65% humidity.

4.2.2 Synthesis of AgNPs

In a 250 mL round-bottom flask, PVP ($M_w = 40$ kDa) was dissolved in EG (100 mL) under sonication. After complete dissolution of the polymer, the flask was stirred in an oil bath at 130 °C for 30 min, then an aqueous solution of AgNO_3 (2 mL, 1 g/mL) was injected rapidly and the reaction mixture was stirred further for 1 h at a speed of 900 rpm. The flask was later removed from the oil bath, cooled in a water bath and the reaction mixture was diluted with acetone, centrifuged at 5'000 rpm for 1 h and decanted. The resulting precipitate was further washed with acetone and water 3 times before redispersion in EtOH. The reaction was repeated 20 times and the products were redispersed in 1.5 L of EtOH. Yield: 14.2 g (57 %).

4.2.3 Synthesis Ag@SiO₂ Core-shell Particles

The silica-coating was performed based on existing protocols of the modified Stöber method.⁴¹ From the stock solution of AgNPs prepared as described above, 200 mL was filled in a 1 L flask and diluted to 600 mL with EtOH. The suspension was treated with NH_4OH (29 %, 25 mL) and with an ethanolic solution of TEOS (50 mL, 0.6 vol% TEOS) and stirred at 25 °C for 19 h. The mixture was diluted with acetone, centrifuged at 5'000 rpm for 30 min, decanted, and redissolved in EtOH. The products were washed with acetone for further 3 times before redispersion in EtOH. The reaction was performed 7 times to obtain Ag@SiO₂ core-shell particles with a very thin silica shell of 3.3 ± 0.7 nm (~ 100 particles measured).

4.2.4 Synthesis of Ag@SiO₂@Si(CH₃)₃

The ethanolic suspension of Ag@SiO₂ core-shell particles was centrifuged. Most of the ethanol was removed by decantation and the residue was redispersed in anhydrous toluene (200 mL) and stirred at 500 rpm. To this suspension, hexamethyldisilazane (HMDS) (23 mL) was added and stirred for 6 h. The particles were recovered by centrifugation, washed once again with toluene to obtain the surface-treated Ag@SiO₂ core-shell particles. Yield: 13.5 g (> 95 %).

4.2.5 Synthesis of Composites of Series A

The Ag@SiO₂@Si(CH₃)₃, PDMS (M_w ~139 kDa), and (25-35 % methylhydrosiloxane)-dimethylsiloxane-copolymer cross-linker were mechanically mixed to a homogenous dispersion. Toluene was used to adjust the viscosity of the mixture. The dibutyltin dilaurate was then added and films were prepared by doctor blading. The samples were aged for about one month before testing. For the amounts used please see Tab. 13.

4.2.6 Synthesis of Composites of Series B

The Ag@SiO₂@Si(CH₃)₃ was first dispersed in toluene by using a tip sonication operated at a power of 40 % for at least 10 min. To this, PDMS (M_w = 692 kDa) and (25-35 % methylhydrosiloxane)-dimethylsiloxane-copolymer cross-linker were added and a homogenous composite was made by mechanically mixing. The Sn-catalyst was then added and films were prepared by doctor blading. The samples were aged for about one month before testing.

4.2.7 Synthesis of Composite B₃₁

The Ag@SiO₂@Si(CH₃)₃ filler, PDMS (M_w = 692 kDa), and (25-35 % methylhydrosiloxane)-dimethylsiloxane-copolymer cross-linker were mechanically mixed

to a homogenous dispersion using cyclohexane solvent to adjust the viscosity. After obtaining a good dispersion, the catalyst was added. Cyclohexane was selected as solvent, because it is more facile to be removed in high vacuum at room temperature and therefore the speed of cross-linking reaction is lowered. To avoid agglomeration of the particles, a sonicator bath was used during the evaporation. A sticky powder formed after the solvent evaporation which was pressed in pellets by using an IR press, heated at 80 °C for 5 h. Platinum electrodes were sputtered on the pellet before the dielectric measurements were done.

4.3 Results and Discussion

4.3.1 Synthesis and Characterization of the Filler Particles

We selected Ag as metal source because AgNPs are stable against oxidation and can be prepared in different sizes and shapes. Since other metal nanoparticles such as aluminum, zinc, iron, nickel and copper form an insulating oxide layer when exposed to air, we did not consider using them because their dielectric properties might change in time or when exposed to elevated temperatures due to surface oxidation.^{44–48}

AgNPs were prepared by using the so called polyol synthesis. Briefly, an aqueous silver nitrate solution was injected into a preheated solution of poly(vinyl pyrrolidone) (PVP) stabilizer in ethylene glycol (EG) at 130°C for 60 min. The particles were purified by washing several times with ethanol/acetone. Fig. 49 shows the TEM images of the prepared AgNPs. The average particles size was 57 ± 10 nm and DLS confirmed a reasonable size distribution (Fig. 50 and Fig. 51). Dried particles kept in normal atmosphere for four months did not show any change in their chemical composition as proved by XRD and XPS spectra where no signals typical for silver oxide were observed (see Supp. Inform.). The particles have a cubic structure with peaks at 2θ : 38.1 (111), 44.3 (200), 64.5 (220), 77.4 (311), and 81.5 (222) that are in agreement with the published data (see Supporting Information).⁴⁹ The XPS analysis shows a peak at 368.2 eV due to metallic

4. Highly Stretchable Dielectric Elastomer Composites Containing High Volume Fraction of AgNPs

silver. A small peak at 365.8 eV due to surface silver atoms surrounded by the PVP chain and no peak at 367.4 eV typical for silver oxide was observed. It can be concluded that the polyol synthesis, which is performed at temperatures exceeding 100 °C under normal atmosphere, does not lead to an oxidation of the silver surface neither during the synthesis nor during storage of the particles in the laboratory.

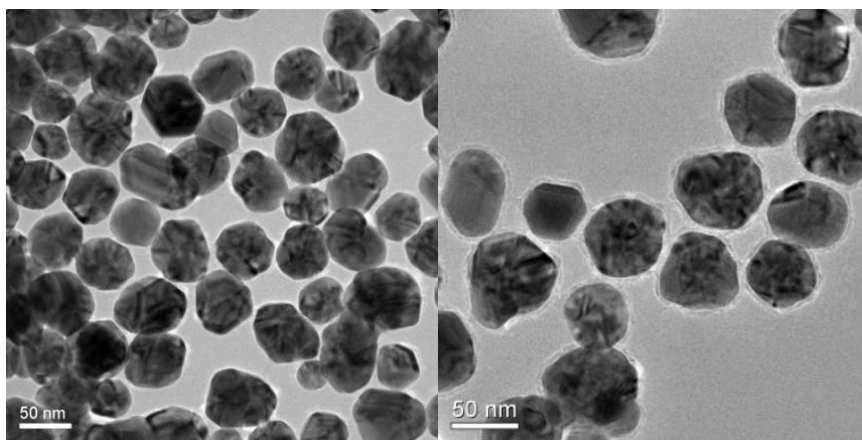


Fig. 49a-b: TEM micrographs of AgNPs prepared by reduction of AgNO_3 with ethylene glycol (left) and of their coating with a thin silica shell of about 3.3 nm (right).

To avoid conductive paths through the material, AgNPs were surface-coated with an insulating shell prior blending. Instead of using an oxidation process, we used a hydrolysis step for the coating. We have recently showed that it is possible to synthesize AgNPs coated with a thin insulating silica shell and also to scale-up this procedure.⁵⁰ Silica is an excellent insulator and has a good compatibility with the silicone matrix. A slightly modified so called Stöber method was used.⁵¹ Our previous investigations have shown that a silica shell thickness of less than 4 nm is optimal to avoid electrical conductivity and to increase ϵ' of the resulting nanocomposites concurrently.⁵⁰ This coating was achieved by dispersing the AgNPs at a certain concentration in ethanol and let tetraethoxysilane (TEOS) to hydrolyze under basic conditions and deposit on the Ag surface. The silica-coating is facilitated by the presence of residual PVP around the Ag cores since it serves as

4. Highly Stretchable Dielectric Elastomer Composites Containing High Volume Fraction of AgNPs

an anchoring group for the growing SiO₂ layer.^{51,52} The successful coating was proven by TEM, UV-vis, DLS and EDX. TEM images show a strong contrast between the black silver cores and the grey silica shell which clearly proves the formation of Ag@SiO₂ core/shell structures (Fig. 49). Further evidence for the coating is provided by surface plasmon resonance. Upon coating the AgNPs with a thin silica shell (3.3 ± 0.7 nm), a slight bathochromic shift of the absorption peak from $\lambda = 436$ nm to $\lambda = 437$ nm in the UV-vis spectra is observed (Tab. 12 and Fig. 50) as a result of the higher dielectric constant of SiO₂ as the new medium compared to PVP/EtOH. DLS also confirms a slight increase in the hydrodynamic radius after the silica-coating of the particles (Fig. 51). Generally, the presence of the silicon peak in the EDX of the coated AgNPs further supports the presence of the silica shell (see Supporting Information). It is important to note that each individual AgNPs is coated with a silica shell of about the same thickness and also that no agglomeration of the AgNPs occurred during the coating. We can also confirm that the molecular weight of the PVP used for the synthesis is important for the functionalization of the particles with the silica shell.⁵¹ For example PVP of $M_w = 40$ kDa allowed formation of uniform silica shells as compared to PVP of $M_w = 10$ kDa where the silica shell was less uniform. This effect is even more pronounced when a very thin silica shell is desired. Thin uniform silica shells are more difficult to prepare than the thick shells. According to the literature, lower molecular weight PVP might even lead to the agglomeration of the core-shell particles due to the lack of shielding off the silver cores from the attractive van der Waals forces.²⁵

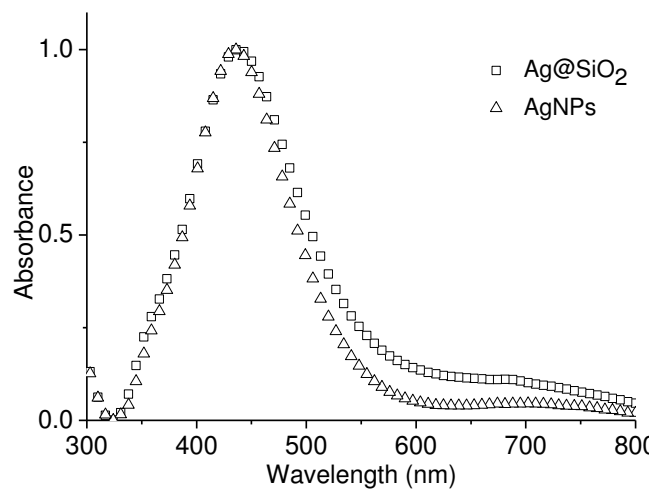


Fig. 50: UV-vis spectra of AgNPs (Δ) and silica-coated Ag@SiO₂ core-shell particles (\square) recorded in ethanol.

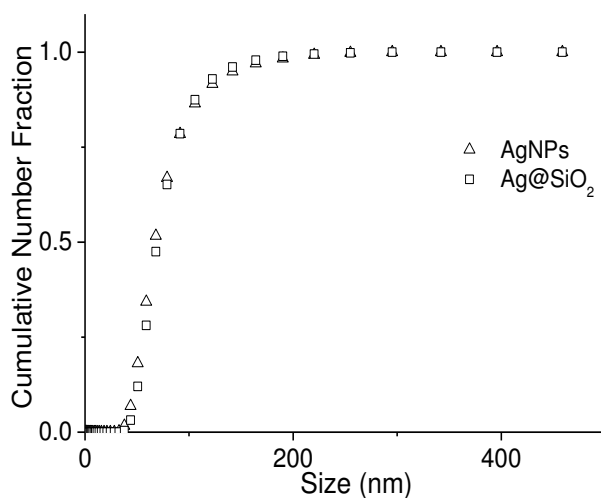


Fig. 51: DLS spectra of AgNPs (Δ) and silica-coated Ag@SiO₂ core-shell particles (\square) recorded in ethanol.

Tab. 12: Size and λ_{\max} data of AgNPs and Ag@SiO₂ obtained by TEM, DLS and UV-vis of the core-shell particles before and after the surface treatment with HMDS.

Entry	Sample	TEM (nm)	DLS (nm) ^a	λ_{\max} (nm)
1	AgNPs	57(10)	60(24)	436
2	Ag@SiO ₂	64(11)	68(27)	437
3	Ag@SiO ₂ @Si(CH ₃) ₃	-	68(26)	439

^a Mean numerical diameter. In the parenthesis is reported the measured standard deviation of the particle population.

The silica surface is quite reactive and needs to be passivated by a hydrophobic layer prior to blending. Three different reagents were tried to achieve this: hexamethyldisilazane (HMDS), methoxy(dimethyl)octylsilane, and *n*-octyldimethylchlorosilane. HMDS was preferred since the resulting particles (Ag@SiO₂@Si(CH₃)₃ – filler) formed stable dispersions in toluene as can be seen in the wettability test (Fig. 52). Furthermore, the reaction occurs seemingly fast and does not require inert conditions.⁵³ In addition to the wettability test, the increase in the carbon content in elemental analysis of the surface-treated particles as compared to the starting one further confirms the functionalization. The elemental analysis data show an increase in the carbon content for the HMDS treated particles as compared to the silica coated one. The functionalized particles Ag@SiO₂@Si(CH₃)₃ were kept wet in order to avoid their agglomeration. Tab. 12 summarizes the sizes of the as prepared AgNPs, of Ag@SiO₂, and of Ag@SiO₂@Si(CH₃)₃ obtained from TEM, DLS and UV-vis measurements.

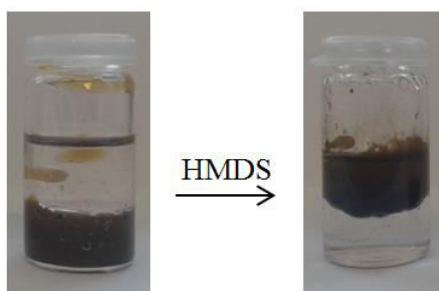


Fig. 52: Wetting test of Ag@SiO₂ core-shell particles conducted in toluene/water mixture before (left) and after (right) surface functionalization with HMDS.

4.3.2 Synthesis and Characterization of AgNP Composites

Two series of composites were prepared and are named as Xy, where X represents the name of the series synthesized with PDMS of different M_w and y represents the Ag vol%. Since the particles were kept wet all the time, the amount of Ag in the composites was determined by Inductively Coupled Plasma-Optical Emission Spectrometry (ICP-OES) and is given as y in the samples' code. As matrix, a commercial and a home-made hydroxyl end-functionalized polydimethylsiloxane (PDMS) $M_w = 139$ kDa (for Series A) and $M_w = 692$ kDa (for series B) were used, respectively. These PDMS polymers were cross-linked via a condensation reaction of the hydroxyl end-groups with the hydrosilane groups of (25-35 % methylhydrosiloxane)-dimethylsiloxane-copolymer cross-linker (CL) (see Experimental Section). Different volumes of highly concentrated filler solution in toluene were dispersed in PDMS matrix. To these mixtures the CL and the Sn-catalyst were added. Films were prepared by doctor blade technique. Depending on the Ag volume fraction the color of the composites changes from brown (below 10-15 vol%) to grey (> 15 %). Tab. 13 gives an overview of the reagents used for the synthesis of materials of series A and B. The use of organotin catalyst is also known as Room Temperature Vulcanization (RTV) or 'cold vulcanization' which allows the formation of elastomers in about 24 h.⁵⁴ Nevertheless, the samples were aged for 1 month prior to performing the mechanical measurements to ensure the complete evaporation of residual toluene and to allow sufficient time for the finalization of the condensation reactions. Our

4. Highly Stretchable Dielectric Elastomer Composites Containing High Volume Fraction of AgNPs

attempts to use a silicone matrix that is cross-linked via a hydrosilylation which requires shorter reaction time at elevated temperatures were not successful.

The Scanning electron microscopy (SEM) images were recorded with a backscatter electron detector (BSED) which is designed to illustrate differences in molecular densities. Here, the particles are featured as small bright spots due to their higher scattering intensity compared to the PDMS matrix (Fig. 53). The present particle agglomerates within the nanocomposites are depicted as large, bright ensembles. SEM images of the samples A prepared by freeze-breaking in liquid nitrogen illustrate that even at a low Ag vol% some agglomeration can be observed, while with increasing Ag vol% more agglomerates with dimensions reaching tens of microns were observed. Films of the series B feature a better dispersion of the filler with fewer agglomerates.

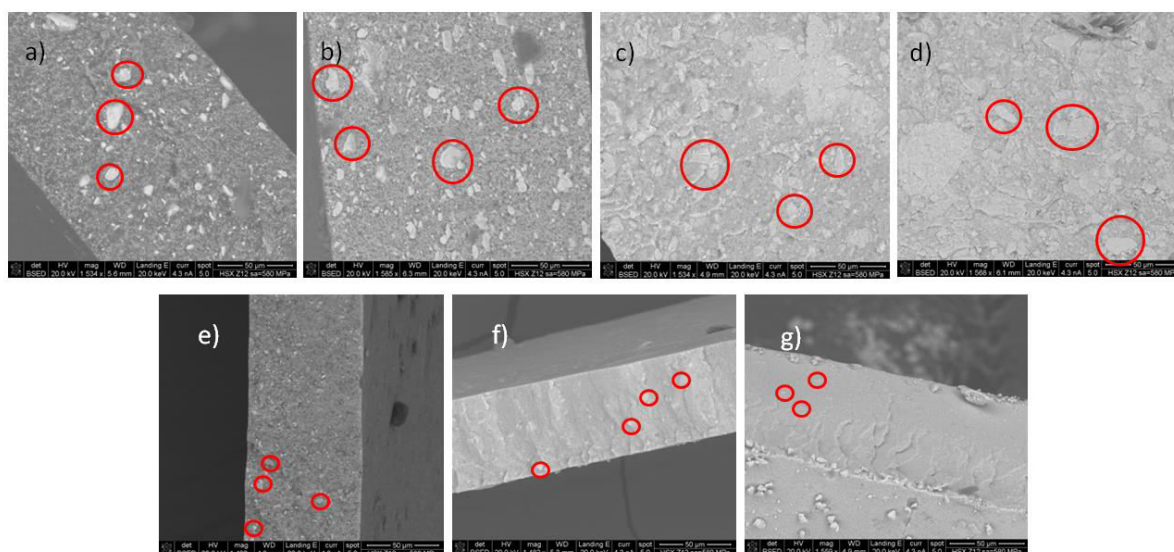


Fig. 53a-g: SEM images of the freeze-broken Ag/PDMS nanocomposites of series A containing 5, 12, 18, 25 vol% and Ag (a-d) and of series B containing 9, 14, and 20 vol% Ag (e-g). Some present agglomerates are shown in the red circles. The scale bar is 50 μm .

4. Highly Stretchable Dielectric Elastomer Composites Containing High Volume Fraction of AgNPs

The mechanical properties of the composites were studied by tensile tests. The results are summarized in Tab. 14. The stress-strain curves, averaged from three independent tests are shown in Fig. 54. Material A₅ shows an elastic behavior, while material A₂₅ retains flexibility but it is plastically deformed. The strain at break decreases with increasing amount of Ag from about 52 % for A₅ to 8.8 % for A₂₅. As expected, an increase in the stiffness of the materials with increasing the Ag vol% was observed.

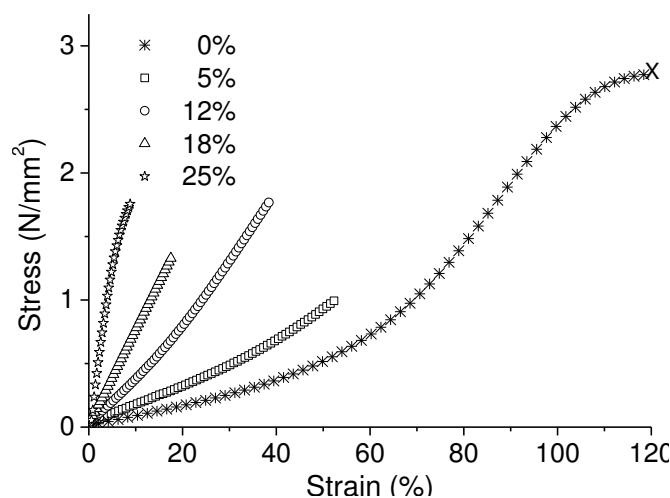


Fig. 54: Stress–strain curves of the composites of series A containing different vol% of Ag and of the neat matrix. The vol% of Ag was determined after the films were cross-linked by using ICP-OES.

It is well known that the mechanical properties of an elastomer are affected by both the molecular weight of the polymer as well as the amount of cross-linker used. Therefore, to further improve the elastic properties of the composites, a hydroxyl end-functionalized PDMS of a high molecular weight ($M_w = 692$ kDa, GPC) was used which allowed us the synthesis of composites of series B. This polymer was synthesized by cationic ring-opening polymerization of octamethylcyclotetrasiloxane (D₄) in the presence of H₂SO₄.⁴³ Highly stretchable and flexible materials with strain at break much higher as compared to the matrix formed (Fig. 54). As expected an increase in the elastic moduli at all strains with increasing the amount of filler used was observed. The influence of the filler on the

4. Highly Stretchable Dielectric Elastomer Composites Containing High Volume Fraction of AgNPs

mechanical properties is more pronounced in the low strain regime, while with increasing the strain, the filler influence is less pronounced (see Fig. 55 insert and Tab. 13). Two composites with 20 vol% Ag but different amount of cross-linker were first prepared (^{stiff}B₂₀ and B₂₀) (for the amounts used, please see Tab. 13). Composite ^{stiff}B₂₀ has a strain at break of 270 % and elastic moduli at low strains in the 6 MPa regime. For composite B₂₀ the amount of cross-linker used was reduced to half. Composite B₂₀ despite of its high Ag vol% content, shows excellent elastic properties with a strain at break as high as 800 % and moduli of elasticity as low as 350 kPa at 100 % strain. The Ag vol% content was further reduced for materials B₁₄ and B₉. These composite show a slightly increase in the strain at break and decrease in the elastic moduli as compared to B₂₀. Composites B₁₄ and B₂₀ were further subjected to extension-relaxation cycles. An initial load of 0.01 N was used. Fig. 56 shows the behavior of a freshly prepared specimen in its first five cycles of extension-relaxation to a maximum of 50 % strain. As can be seen, for the second extension-relaxation cycle the stress required on reloading is reduced as compared to the initial loading and the hysteresis observed for the subsequent cycles was rather low.

4. Highly Stretchable Dielectric Elastomer Composites Containing High Volume Fraction of AgNPs

Tab. 13: The amount of components used for the synthesis of the matrix and of materials of series A and B.

Entry	PDMS [g]	CL [μL] ^{c)}	Density ρ [g/cm ³]	V(toluene) [mL]
A ₀	1.9 ^{a)}	800	0.99	2
A ₅	0.9 ^{a)}	380	1.52	1.3
A ₁₂	0.8 ^{a)}	340	2.21	2.8
A ₁₈	0.7 ^{a)}	295	2.94	3.5
A ₂₅	0.4 ^{a)}	168	3.66	2.9
^{stiff} B ₂₀	0.15 ^{b)}	32	3.05	3
B ₂₀	0.15 ^{b)}	16	3.05	3
B ₁₄	0.15 ^{b)}	16	2.46	3
B ₉	0.15 ^{b)}	16	1.83	3
B ₀	0.3	32	0.98	3.5

Hydroxyl end-functionalized PDMSs were used: a) $M_w = 139$ kDa and b) $M_w = 692$ kDa. c) For all composites a solution of Sn-catalyst in toluene (50 wt%) was used and the proportion between cross-linker/catalyst was 4. Toluene was used to adjust the viscosity of the composites. The amount of Ag contained in the composite was determined after cross-linking by ICP-OES.

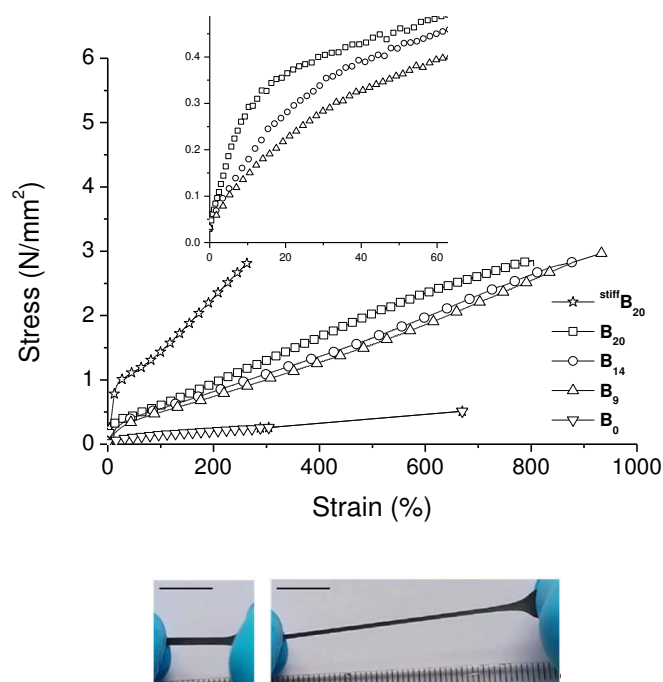


Fig. 55: Stress-strain curves of the matrix B₀, ^{stiff}B₂₀, B₂₀, B₁₄, and B₉; the enlargement for the low strains (insert); and photos of B₂₀ in its relaxed and strained form (bottom) (the scale bar represents 1 cm).

The same sample was subjected to successively higher strains from 50% up to 450% followed by the return to the original gauge length (see Supporting Information). A strong dependence of the stress-strain curves upon increasing the strain level was observed. This stress softening phenomenon is typical for filled rubber materials and is known as the *Mullins effect*. Different mechanisms have been proposed to explain this effect including reorganization of the polymer network, reorganization of the filler-filler networks, and/or the detachment of the polymer network from the filler.⁵⁵ Material B₂₀ was aged for 5 days at 150 °C and its stress-strain and the cyclic relaxation behavior was compared with that of a B₂₀ sample aged at 25 °C for 10 days (see Supporting Information). The elastic properties were only slightly affected by the temperature. Material B₂₀ is slightly stiffer after this aging and the strain at break decreased, but the elastic property is retained. The cyclic tests show some differences for the first strain-release cycle and a small difference between the cycles at the used strain.

The hysteresis loop at the first strain-release cycle is more pronounced for the sample that was aged at elevated temperatures (see Supporting Information). Additionally, dynamic mechanical analysis has been carried out on B₂₀ (Fig. 56 right). The elastic modulus measured at low strains (1%) and at 0.01 Hz was 2.4 MPa while by increasing the frequency to 0.1 Hz an increase in the elastic modulus to 3.4 MPa was observed. The viscoelastic losses ($\tan \delta$) are rather low ($\tan \delta < 0.2$ at all frequencies) and further support the good elastic properties of B₂₀. Silicones are generally characterized by a pronounced thermal stability and a single weight loss step at high temperatures. It has been demonstrated that PDMS degrades through the depolymerisation of PDMS to give cyclic oligomeric siloxanes.^{56,57} The silicone matrix used by us (B₀) is stable up to 400 °C where it starts to decompose (Fig. 57). The decomposition of the composites of series B proceeds in one step and the degradation of the polymer is shifted to values above 500 °C. The incorporation of filler to the PDMS restricts the chain mobility and therefore the degradation of the nanocomposites is delayed compared to the pure silicone rubber.^{58,59} An increase in the amount of filler does not lead to a further change in the thermal properties of the nanocomposites. As expected, the amount of residue left due to the Ag@SiO₂ filler increases with increasing the Ag vol% and clearly shows that the composites have high filler content. The amount of residue roughly corresponds to the amount of Ag@SiO₂ used.

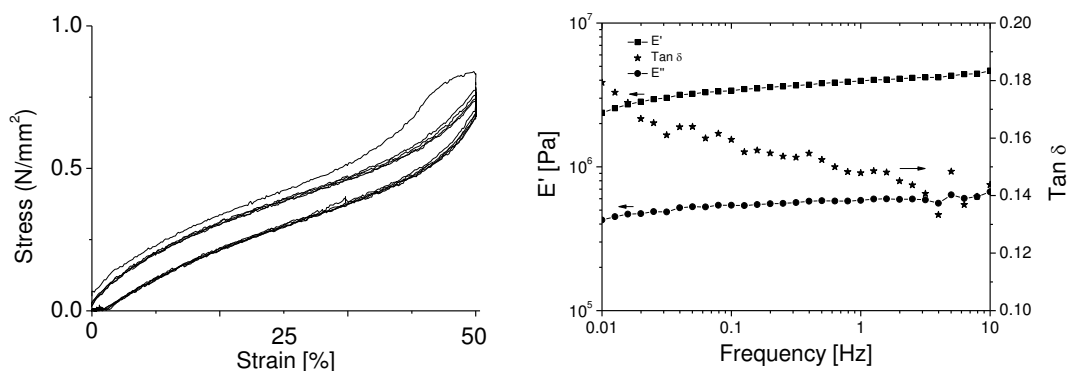


Fig. 56: Cyclic stress-strain relaxation curves of B₁₄ at 50 % strain (left) and dynamic mechanical analysis for B₂₀ at different frequencies (right).

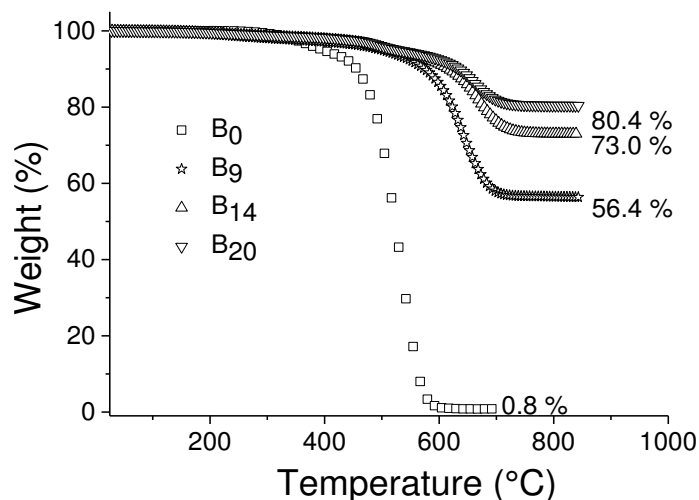


Fig. 57: TGA curves of composites B and of the matrix under helium.

4.3.3 Dielectric Properties of the Filler and Composites

The dielectric properties of the filler, matrix, and composites were measured using an impedance spectrometer in a frequency range from 1 Hz to 10^6 Hz at 1 V amplitude at room temperature (Fig. 58). The dielectric properties of the pure filler were measured in pellet that was obtained by pressing the dried particles using an IR press. Two platinum electrodes were sputtered on both sides. An almost constant frequency dependent ϵ_r' with a value of about 90 at 10^3 Hz and rather low loss factor $\tan \delta$ at high frequencies was observed (see Tab. 14, Fig. 58). Furthermore, the low conductivity at low frequency of 9×10^{-11} S/cm is supportive for a core/shell structure. The composites of series A show an expected increase in ϵ_r' with the Ag vol% from 3 for the silicone matrix to 4.4 for 5%, to 5.6 for 12% and reaches a max value of 7.8 for 18 %. The dielectric losses and also the conductivity slightly increase with increasing the amount of filler, but remain at low values characteristic for dielectric materials. For example, all composites have a conductivity that is lower than 3×10^{-13} S/cm at low frequencies. A further increase in the AgNPs volume fraction to 25 % results in inhomogeneous films with a rough surface, therefore complicating the accurate measurement of film thickness.⁶⁰ As mentioned above, for series

4. Highly Stretchable Dielectric Elastomer Composites Containing High Volume Fraction of AgNPs

B, a PDMS of a higher molecular weight was used. The concentration of silver was varied between 9 and 31 vol% Ag. High quality films were prepared for concentrations up to 20 % by the doctor blade technique. However, a further increase in the concentration of the filler resulted in non-homogenous films. To nevertheless find how the dielectric properties are changing when the filler vol% approaches the concentration where the particles are percolating (this “mechanical” percolation should not be confused with the conductive percolation), a different strategy was used (see Experimental Section) which allowed us the synthesis of B₃₁. The dielectric properties of series B are similar to those of series A. Also here, composites with very low conductivity and low dielectric losses were obtained. Composite B₃₁ with a Ag vol% of 31 % has a permittivity as high as 21, a low loss factor of 0.03 at 1 kHz with a value for the permittivity that remains almost constant with the frequency. A value of $\epsilon' = 5.9$ for B₂₀ which is also highly stretchable. It was reported before that the conductive filler/insulator composites show a percolation like increase in the ϵ' , however a linear increase in the permittivity with increasing the Ag vol% was observed in our case (see Supporting Information). The increase in the ϵ' for the two series is slightly different. This might be due to the different ways of dispersing the filler in the polymer matrix: mechanical mixing for series A while tip sonication was used for series B. Through the dispersion of the filler by mechanical mixing, agglomerates in the size of tens of microns are still present within the matrix (Fig. 53) while when the sonicator tip was used to disperse the particles, more homogenous dispersion of the particles within the matrix was observed. The particles within the agglomerates are in closer proximity to each other, resulting in a collective response to the electric field from the present short-range order of the particles, which is absent in a well dispersed, agglomerate-free system.⁶¹ It has also been reported elsewhere that the presence of agglomerates within the nanocomposite leads to higher ϵ' values compared to the well dispersed system, as a direct result of moisture inclusion as well as specific effects resulting from the agglomerated structure.⁶² The breakdown field of the resulting composites was also measured (see Tab. 14 and Supporting Information). The breakdown experiments were conducted using a setup similar to that described by Kollosche⁶³ and also in capacitor devices that had round electrodes ($\varnothing = 8$ mm). It should be also mentioned here that no actuation of the materials

4. Highly Stretchable Dielectric Elastomer Composites Containing High Volume Fraction of AgNPs

was observed when conducting the breakdown measurement. The dielectric breakdowns are higher for series B as compare to series A which are supportive for a better dispersion of the filler in the composites of series B as well as the increase in the molecular weight of the polymer matrix.^{60,64} A decrease in the breakdown field with increasing Ag vol% was observed from 23.1 V/ μm for B₉ to 13.4 V/ μm for B₂₀. The dielectric breakdown of a material is strongly affected by the elastic moduli.⁶⁵ The dielectric breakdown of our composites is significantly higher as compared to the epoxy composites containing AgNPs coated with an organic shell,⁴⁰ despite that herein a soft matrix was used.

Tab. 14: Summary of the permittivity, loss factor, and breakdown field of the composites of series A and B.

Sample	^a ϵ'	^a $\tan \delta$	E_B [V/ μm] ^b	E_B [V/ μm] ^c	Y^d [MPa]	Max Strain [%]
A ₀	3.0	0.0017	77.0	-	0.78	119
A ₅	4.4	0.0307	16.6	11.8	1.43	52
A ₁₂	5.6	0.0234	8.8	8.8	3.74	38
A ₁₈	7.8	0.0609	10.4	3.5	7.51	17
B ₃₁	21	0.0300	-	1.3	-	-
stiff B ₂₀	6.8	0.0142	19.0	5.8	5.98	268
B ₂₀	5.9	0.0078	13.4	5.9	1.44	805
B ₁₄	5.7	0.0144	21.4	12.3	1.23	878
B ₉	4.7	0.0083	23.1	29.4	0.89	935
B ₀	3.0	0.0003	63	40.0	0.23	670

^aThe values for the permittivity were taken at ~ 1 kHz, which is sufficiently high frequency to avoid the ion conduction and interfacial polarization effects. ^bMeasurements conducted using small electrodes (1 mm²). About 10 samples were measured and the data were averaged. ^cMeasurements conducted with electrodes with a diameter of 8 mm. ^dYoung's modulus calculated at a strain of 10 %.

4. Highly Stretchable Dielectric Elastomer Composites Containing High Volume Fraction of AgNPs

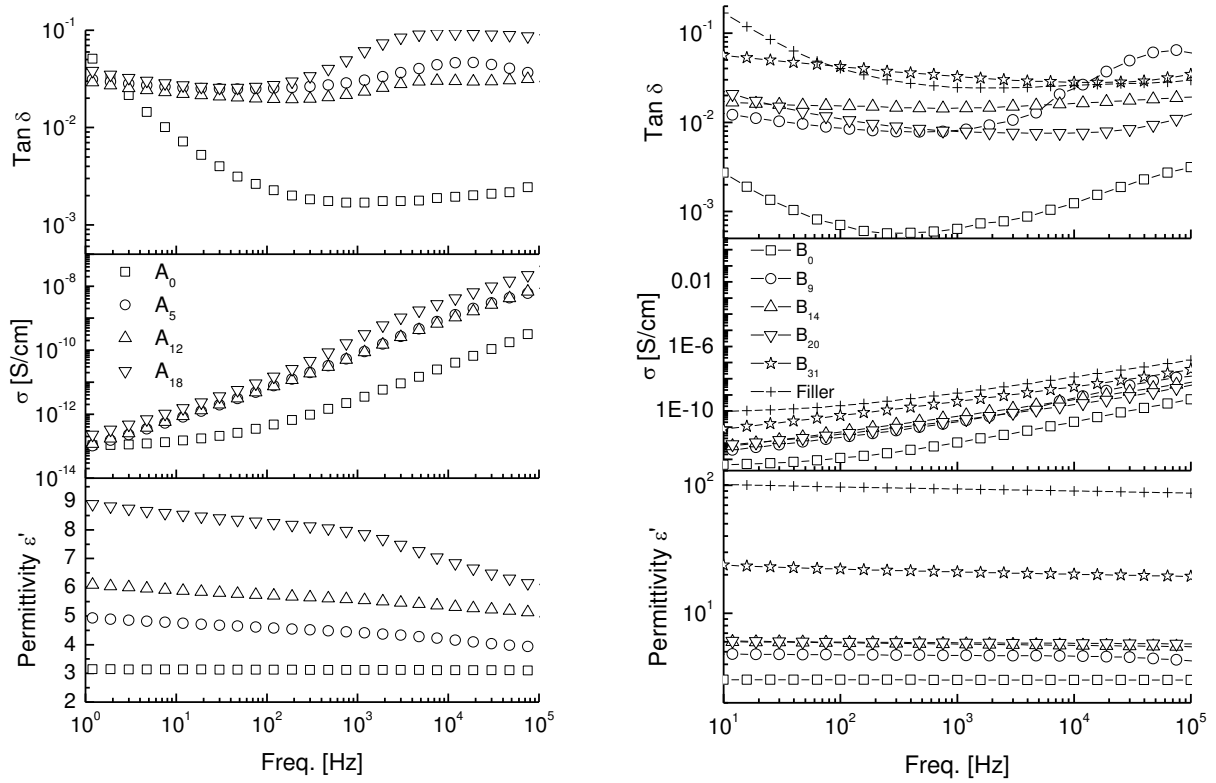


Fig. 58: Permittivity, $\tan \delta$, and conductivity as function of frequency for series A (left) and series B and the filler (right).

As mentioned in the introduction, dielectric elastomers with increased permittivity can find applications in dielectric elastomer generator (DEG) for energy harvesting.⁶⁶ For this purpose, the DEG undergo a working cycle which involves: (a) stretching the area, (b) charging, (c) mechanical relaxation followed by (d) energy harvesting.^{5,6} The output of the system is quantified by the specific energy density per volume $\Delta W/\text{Vol}$ (Eq. 51). The specific energy density per volume of the nanocomposites for a corresponding electric field is shown in Fig. 59. The parameter $\Delta W/\text{Vol}$ is limited by the electric breakdown field E_B of the nanocomposites and can be calculated by⁶

4. Highly Stretchable Dielectric Elastomer Composites Containing High Volume Fraction of AgNPs

$$\frac{\Delta W}{Vol} = \frac{1}{2} \varepsilon' \varepsilon_0 E_B^2 \left(1 - \frac{1}{(s_{\max} + 1)^2} \right) \quad (\text{Eq. 51})$$

where, ε_0 is the vacuum permittivity and s_{\max} is the maximum strain at break for the corresponding elastomers. As shown in Fig. 59, the breakdown field of the nanocomposites is lower as compared to the silicone matrix and despite of the increase in the permittivity and the high strain at break, the maximum amount of energy that can be harvested with these composites is lower as compared to the silicone matrix. For example at an electric field of 20 V/ μm the maximum amount of energy per cycle increases from 5.2 mJ/cm³ for the B₀ silicone matrix, to 8.2 mJ/cm³ for B₉ and to 10 mJ/cm³ for B₁₄. Therefore, these nanocomposites might be useful as dielectric in energy harvester operated at low electric fields.

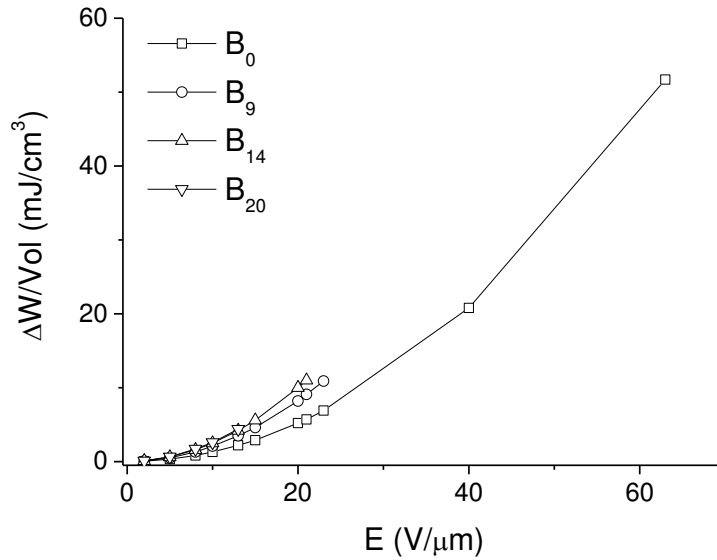


Fig. 59: Specific energy density per volume at a given electric field.

4.4 Conclusions and Outlook

Core/shell Ag/silica nanoparticles with Ag core of 57 nm surrounded by a thin silica shell of ~ 4 nm and passivated by a trimethylsilyl layer show a $\epsilon' = 90$ very low dielectric losses. These particles were used as filler in a polydimethylsiloxane matrix to synthesize composites with different Ag vol%. It was shown that by a careful selection of matrix and cross-linker amount, it is possible to prepare materials with concentrations of filler as high as 20 vol% that have an elastic modulus as low as 350 kPa at 100 % strain and a strain at break as high as 800 %. The stress relaxation tests show a minor hysteresis from the first to the second cycle and almost no hysteresis for the subsequent cycles. Additionally, composites with increased ϵ' , low dielectric losses, and high dielectric breakdowns were obtained. An increase in the ϵ' with increasing the vol% of Ag was observed. For example, a composite containing 31 vol% filler has a $\epsilon' = 21$ and a loss factor of 0.03 at ~ 1 kHz. The low dielectric losses of these materials are supportive of a good encapsulation of the metallic Ag in an insulating silica shell. A composite containing 20 vol% AgNPs has a $\epsilon' = 5.9$ at ~ 1 kHz, a dielectric strength of 13.4 V/ μm . Because of the increased permittivity and high strain at break, these materials might find application as dielectric in energy harvesting devices operated at low electric fields. Furthermore, since the Ag core can in principle be replaced by other metals, the described procedure can be used for the synthesis of other polymer/metal composites and suggests a broad applicability of the method that would allow the synthesis of other functional materials.

4.5 Acknowledgements

We gratefully acknowledge D. Schreier and Dr. Y. Arroyo for helping with the TEM and SEM measurements, S. Dünki for the DMA measurements, B. Fischer for the TGA measurements, A. Wichser for helping with the ICP-OES measurements (all Empa) and M. Schneider from the Micro-laboratory of the Laboratory for Organic Chemistry (ETH Zurich) for elemental analysis measurements. We thank B. Sinnet from Eawag for helping

with DLS measurement. DMO thanks Dr. Racles from PPI for her kind support with the Sciex project. We also gratefully acknowledge Swiss National Science Foundation (SNF132101), Sciex (12.192), and Swiss Federal Laboratories for Materials Science and Technology (Empa, Dübendorf) for financial support.

4.6 References

- (1) Chae, S. H.; Yu, W. J.; Bae, J. J.; Duong, D. L.; Perello, D.; Jeong, H. Y.; Ta, Q. H.; Ly, T. H.; Vu, Q. A.; Yun, M.; et al. Transferred Wrinkled Al₂O₃ for Highly Stretchable and Transparent Graphene-Carbon Nanotube Transistors. *Nat. Mater.* **2013**, *12*, 403–409.
- (2) Brochu, P.; Pei, Q. Advances in Dielectric Elastomers for Actuators and Artificial Muscles. *Macromol. Rapid Commun.* **2010**, *31*, 10–36.
- (3) Biggs, J.; Danielmeier, K.; Hitzbleck, J.; Krause, J.; Kridl, T.; Nowak, S.; Orselli, E.; Quan, X.; Schapeler, D.; Sutherland, W.; et al. Electroactive Polymers: Developments of and Perspectives for Dielectric Elastomers. *Angew. Chemie - Int. Ed.* **2013**, *52*, 9409–9421.
- (4) *Dielectric Elastomers as Electromechanical Transducers*; Carpi, F.; De Rossi, D.; Kornbluh, R.; Pelrine, R.; Sommer-Larsen, P., Eds.; Elsevier: Amsterdam, 2008.
- (5) Pelrine, R.; Kornbluh, R. D.; Eckerle, J.; Jeuck, P.; Oh, S.; Pei, Q.; Stanford, S. Dielectric Elastomers: Generator Mode Fundamentals and Applications. *SPIE's 8th Annu. Int. Symp. Smart Struct. Mater.* **2001**, *4329*, 148–156.
- (6) Molberg, M.; Crespy, D.; Rupper, P.; Nüesch, F.; Månson, J.-A. E.; Löwe, C.; Opris, D. M. High Breakdown Field Dielectric Elastomer Actuators Using Encapsulated Polyaniline as High Dielectric Constant Filler. *Adv. Funct. Mater.* **2010**, *20*, 3280–3291.
- (7) Stoyanov, H.; Brochu, P.; Niu, X.; Della Gaspera, E.; Pei, Q. Dielectric Elastomer Transducers with Enhanced Force Output and Work Density. *Appl. Phys. Lett.* **2012**, *100*, 2010–2013.
- (8) Goswami, K.; Skov, A. L.; Daugaard, A. E. UV-Cured, Platinum-Free, Soft Poly(dimethylsiloxane) Networks. *Chem. - A Eur. J.* **2014**, *20*, 9230–9233.
- (9) Bejenariu, A. G.; Yu, L.; Skov, A. L. Low Moduli Elastomers with Low Viscous Dissipation. *Soft Matter* **2012**, *8*, 3917–3923.

4. Highly Stretchable Dielectric Elastomer Composites Containing High Volume Fraction of AgNPs

- (10) Galantini, F.; Carpi, F.; Gallone, G. Effects of Plasticization of a Soft Silicone for Dielectric Elastomer Actuation. *Smart Mater. Struct.* **2013**, *22*, 104020.
- (11) Madsen, F. B.; Yu, L.; Daugaard, A. E.; Hvilsted, S.; Skov, A. L. A New Soft Dielectric Silicone Elastomer Matrix with High Mechanical Integrity and Low Losses. *RSC Adv.* **2015**, *5*, 10254–10259.
- (12) Kussmaul, B.; Risse, S.; Kofod, G.; Waché, R.; Wegener, M.; McCarthy, D. N.; Krüger, H.; Gerhard, R. Enhancement Of Dielectric Permittivity And Electromechanical Response In Silicone Elastomers: Molecular Grafting Of Organic Dipoles To The Macromolecular Network. *Adv. Funct. Mater.* **2011**, *21*, 4589–4594.
- (13) Madsen, F. B.; Dimitrov, I.; Daugaard, A. E.; Hvilsted, S.; Skov, A. L. Novel Cross-Linkers for PDMS Networks for Controlled and Well Distributed Grafting of Functionalities by Click Chemistry. *Polym. Chem.* **2013**, *4*, 1700–1707.
- (14) Racles, C.; Cazacu, M.; Fischer, B.; Opris, D. M. Synthesis and Characterization of Silicones Containing Cyanopropyl Groups and Their Use in Dielectric Elastomer Actuators. *Smart Mater. Struct.* **2013**, *22*, 104004.
- (15) Gallone, G.; Carpi, F.; De Rossi, D.; Levita, G.; Marchetti, A. Dielectric Constant Enhancement in a Silicone Elastomer Filled with Lead Magnesium Niobate-Lead Titanate. *Mater. Sci. Eng. C* **2007**, *27*, 110–116.
- (16) Carpi, F.; Gallone, G.; Galantini, F.; De Rossi, D. Silicone-Poly(hexylthiophene) Blends as Elastomers with Enhanced Electromechanical Transduction Properties. *Adv. Funct. Mater.* **2008**, *18*, 235–241.
- (17) Hu, W.; Zhang, S. N.; Niu, X.; Liu, C.; Pei, Q. 40_An Aluminum Nanoparticle–acrylate Copolymer Nanocomposite as a Dielectric Elastomer with a High Dielectric Constant. *J. Mater. Chem. C* **2014**, *2*, 1658–1666.
- (18) Galantini, F.; Bianchi, S.; Castelvetro, V.; Anguillesi, I.; Gallone, G. Properties of a Dielectric Elastomer Actuator Modified by Dispersion of Functionalised Carbon Nanotubes. *Adv. Sci. Technol.* **2012**, *79*, 41–46.
- (19) Goswami, K.; Daugaard, A. E.; Skov, A. L. Dielectric Properties of Ultraviolet Cured Poly(dimethyl Siloxane) Sub-Percolative Composites Containing Percolative Amounts of Multi-Walled Carbon Nanotubes. *RSC Adv.* **2015**, *5*, 12792–12799.
- (20) Grannan, D. M.; Garland, J. C.; Tanner, D. B. Critical Behavior of the Dielectric Constant of a Random Composite near the Percolation Threshold. *Phys. Rev. Lett.* **1981**, *46*, 375–379.

- (21) Dang, Z.-M.; Wang, L.; Yin, Y.; Zhang, Q.; Lei, Q.-Q. Giant Dielectric Permittivities in Functionalized Carbon-Nanotube/ Electroactive-Polymer Nanocomposites. *Adv. Mater.* **2007**, *19*, 852–857.
- (22) Yang, X. H.; Fu, H. T.; Wong, K.; Jiang, X. C.; Yu, A. B. Hybrid Ag@TiO₂ Core-Shell Nanostructures with Highly Enhanced Photocatalytic Performance. *Nanotechnology* **2013**, *24*, 415601.
- (23) Berdel, K.; Member, S. S.; Rivas, J. G. J.; Bolívar, P. H.; Maagt, P. De; Member, S. S.; Kurz, H. Temperature Dependence of the Permittivity and Loss Tangent of High-Permittivity Materials at Terahertz Frequencies. *IEEE Trans. Microwav. Theor.* **2005**, *53*, 1266–1271.
- (24) Nelson, J. K.; Linhardt, R. J.; Schadler, L. S.; Hillborg, H. Effect of High Aspect Ratio Filler on Dielectric Properties of Polymer Composites: A Study on Barium Titanate Fibers and Graphene Platelets. *IEEE Trans. Dielectr. Electr. Insul.* **2012**, *19*, 960–967.
- (25) Romasanta, L. J.; Hernández, M.; López-Manchado, M. A.; Verdejo, R. Functionalised Graphene Sheets as Effective High Dielectric Constant Fillers. *Nanoscale Res. Lett.* **2011**, *6*, 508.
- (26) Zhou, Y.; Chen, Y.; Wang, H.; Wong, C. P. Creation of a Multilayer Aluminum Coating Structure Nanoparticle Polyimide Filler for Electronic Applications. *Mater. Lett.* **2014**, *119*, 64–67.
- (27) Opris, D. M.; Crespy, D.; Löwe, C.; Molberg, M.; Nüesch, F. Phtalocyanine and Encapsulated Polyaniline Nanoparticles as Fillers for Dielectric Elastomers. *Proc. SPIE, Electroact. Polym. Actuators Devices (EAPAD) Electroactive Polym. Actuators Devices* **2009**, 7287, 72870L – 72870L – 8.
- (28) Huang, C.; Zhang, Q. M.; Su, J. High-Dielectric-Constant All-Polymer Percolative Composites. *Appl. Phys. Lett.* **2003**, *82*, 3502–3504.
- (29) Kempa, T.; Carnahan, D.; Olek, M.; Correa, M.; Giersig, M.; Cross, M.; Benham, G.; Sennett, M.; Ren, Z.; Kempa, K. Dielectric Media Based on Isolated Metallic Nanostructures. *J. Appl. Phys.* **2005**, *98*, 3–6.
- (30) Li, J. Y.; Zhang, L.; Ducharme, S. Electric Energy Density of Dielectric Nanocomposites. *Appl. Phys. Lett.* **2007**, *90*, 28–31.
- (31) Qi, L.; Lee, B. I.; Chen, S.; Samuels, W. D.; Exarhos, G. J. High-Dielectric-Constant Silver-Epoxy Composites as Embedded Dielectrics. *Adv. Mater.* **2005**, *17*, 1777–1781.

4. Highly Stretchable Dielectric Elastomer Composites Containing High Volume Fraction of AgNPs

- (32) Guo, N.; DiBenedetto, S. A.; Tewari, P.; Lanagan, M. T.; Ratner, M. A.; Marks, T. J. Nanoparticle, Size, Shape, and Interfacial Effects on Leakage Current Density, Permittivity, and Breakdown Strength of Metal Oxide–Polyolefin Nanocomposites: Experiment and Theory. *Chem. Mater.* **2010**, *22*, 1567–1578.
- (33) Grubbs, R. B. Hybrid Metal-Polymer Composites from Functional Block Copolymers. *J. Polym. Sci. Part A Polym. Chem.* **2005**, *43*, 4323–4336.
- (34) Pastoriza-Santos, I.; Pérez-Juste, J.; KICKELBICK, G.; Liz-Marzán, L. M. Optically Active Poly(dimethylsiloxane) Elastomer Films Through Doping with Gold Nanoparticles. *J. Nanosci. Nanotechnol.* **6**, 453–458.
- (35) Lu, J.; Moon, K.-S.; Wong, C. P. Silver/polymer Nanocomposite as a High-K Polymer Matrix for Dielectric Composites with Improved Dielectric Performance. *J. Mater. Chem.* **2008**, *18*, 4821–4826.
- (36) Ellison, J.; Wykoff, G.; Paul, A.; Mohseni, R.; Vasiliev, A. Efficient Dispersion of Coated Silver Nanoparticles in the Polymer Matrix. *Colloids Surfaces A Physicochem. Eng. Asp.* **2014**, *447*, 67–70.
- (37) Hoppe, C. E.; Rodríguez-Abreu, C.; Lazzari, M.; López-Quintela, M. A.; Solans, C. One-Pot Preparation of Gold-Elastomer Nanocomposites Using PDMS-Graft-PEO Copolymer Micelles as Nanoreactors. *Phys. Status Solidi* **2008**, *205*, 1455–1459.
- (38) Wiley, B.; Sun, Y.; Mayers, B.; Xia, Y. Shape-Controlled Synthesis of Metal Nanostructures: The Case of Silver. *Chem. - A Eur. J.* **2005**, *11*, 454–463.
- (39) Kim, D.; Jeong, S.; Moon, J. Synthesis of Silver Nanoparticles Using the Polyol Process and the Influence of Precursor Injection. *Nanotechnology* **2006**, *17*, 4019–4024.
- (40) Shen, Y.; Lin, Y.; Li, M.; Nan, C.-W. High Dielectric Performance of Polymer Composite Films Induced by a Percolating Interparticle Barrier Layer. *Adv. Mater.* **2007**, *19*, 1418–1422.
- (41) Baida, H.; Billaud, P.; Marhaba, S.; Christofilos, D.; Cottancin, E.; Crut, A.; Lermé, J.; Maioli, P.; Pellarin, M.; Broyer, M.; et al. Quantitative Determination of the Size Dependence of Surface Plasmon Resonance Damping in Single Ag@SiO₂ Nanoparticles. *Nano Lett.* **2009**, *9*, 3463–3469.
- (42) Guerrero-Martínez, A.; Pérez-Juste, J.; Liz-Marzán, L. M. Recent Progress on Silica Coating of Nanoparticles and Related Nanomaterials. *Adv. Mater.* **2010**, *22*, 1182–1195.
- (43) Cazacu, M.; Racles, C.; Vlad, A.; Antohe, M.; Forna, N. Silicone-Based Composite for Relining of Removable Dental Prosthesis. *J. Compos. Mater.* **2009**, *43*, 2045–2055.

4. Highly Stretchable Dielectric Elastomer Composites Containing High Volume Fraction of AgNPs

- (44) Xu, J.; Wong, C. P. Low-Loss Percolative Dielectric Composite. *Appl. Phys. Lett.* **2005**, 87, 082907.
- (45) Putson, C.; Jaaoh, D.; Meauma, N.; Muensit, N. Effect of Micro- and Nano-Particle Fillers at Low Percolation Threshold on the Dielectric and Mechanical Properties of Polyurethane/Copper Composites. *J. Inorg. Organomet. Polym. Mater.* **2012**, 22, 1300–1307.
- (46) Zhang, Y.; Wang, Y.; Deng, Y.; Li, M.; Bai, J. Enhanced Dielectric Properties of Ferroelectric Polymer Composites Induced by Metal-Semiconductor Zn-ZnO Core-Shell Structure. *ACS Appl. Mater. Interfaces* **2012**, 4, 65–68.
- (47) Lucchini, M. A.; Testino, A.; Ludwig, C.; Kambolis, A.; El-Kazzi, M.; Cervellino, A.; Riani, P.; Canepa, F. Continuous Synthesis of Nickel Nanopowders: Characterization, Process Optimization, and Catalytic Properties. *Appl. Catal. B Environ.* **2014**, 156-157, 404–415.
- (48) Park, B. K.; Jeong, S.; Kim, D.; Moon, J.; Lim, S.; Kim, J. S. Synthesis and Size Control of Monodisperse Copper Nanoparticles by Polyol Method. *J. Colloid Interface Sci.* **2007**, 311, 417–424.
- (49) Liu, C.; Yang, X.; Yuan, H.; Zhou, Z.; Xiao, D. Preparation of Silver Nanoparticle and Its Application to the Determination of Ct -DNA. *Sensors* **2007**, 7, 708–718.
- (50) Quinsaat, J. E. Q.; Nüesch, F. A.; Hofmann, H.; Opris, D. M. Dielectric Properties of Silver Nanoparticles Coated with Silica Shells of Different Thicknesses. *RSC Adv.* **2013**, 3, 6964–6971.
- (51) Graf, C.; Vossen, D. L. J.; Imhof, A.; van Blaaderen, A. A General Method To Coat Colloidal Particles with Silica. *Langmuir* **2003**, 19, 6693–6700.
- (52) Liu, S.; Han, M.-Y. Silica-Coated Metal Nanoparticles. *Chem. Asian J.* **2010**, 5, 36–45.
- (53) Gun'ko, V.; Vedamuthu, M.; Henderson, G.; Blitz, J. Mechanism and Kinetics of Hexamethyldisilazane Reaction with a Fumed Silica Surface. *J. Colloid Interface Sci.* **2000**, 228, 157–170.
- (54) Cervantes, J.; Zárraga, R.; Salazar-Hernández, C. Organotin Catalysts in Organosilicon Chemistry. *Appl. Organomet. Chem.* **2012**, 26, 157–163.
- (55) Boyce, M. C.; Yeh, O.; Socrate, S.; Kear, K.; Shaw, K. Micromechanics of Cyclic Softening in Thermoplastic Vulcanizates. *J. Mech. Phys. Solids* **2001**, 49, 1343–1360.

4. Highly Stretchable Dielectric Elastomer Composites Containing High Volume Fraction of AgNPs

- (56) Grassie, N. .; Macfarlane, I. G. . The Thermal Degradation of Polysiloxanes-I. *Eur. Polym. J.* **1978**, *14*, 875–884.
- (57) Lewicki, J. P.; Liggat, J. J.; Patel, M. The Thermal Degradation Behaviour of Polydimethylsiloxane/montmorillonite Nanocomposites. *Polym. Degrad. Stab.* **2009**, *94*, 1548–1557.
- (58) Silva, V. P.; Gonçalves, M. C.; Yoshida, I. V. P. Biogenic Silica Short Fibers as Alternative Reinforcing Fillers of Silicone Rubbers. *J. Appl. Polym. Sci.* **2006**, *101*, 290–299.
- (59) Norkhairunnisa, M.; Azizan, A.; Mariatti, M.; Ismail, H.; Sim, L. Thermal Stability and Electrical Behavior of Polydimethylsiloxane Nanocomposites with Carbon Nanotubes and Carbon Black Fillers. *J. Compos. Mater.* **2011**, *46*, 903–910.
- (60) Calebrese, C.; Hui, L.; Schadler, L.; Nelson, J. A Review on the Importance of Nanocomposite Processing to Enhance Electrical Insulation. *IEEE Trans. Dielectr. Electr. Insul.* **2011**, *18*, 938–945.
- (61) Tan, Q.; Cao, Y.; Irwin, P. DC Breakdown in Polyetherimide Composites and Implication for Structural Engineering. *2007 IEEE Int. Conf. Solid Dielectr.* **2007**, 411–414.
- (62) Kurimoto, M.; Okubo, H.; Kato, K.; Hanai, M.; Hoshina, Y.; Takei, M.; Hayakawa, N. Dielectric Properties of Epoxy/alumina Nanocomposite Influenced by Control of Micrometric Agglomerates. *IEEE Trans. Dielectr. Electr. Insul.* **2010**, *17*, 662–670.
- (63) Kollosche, M.; Kofod, G. Electrical Failure in Blends of Chemically Identical, Soft Thermoplastic Elastomers with Different Elastic Stiffness. *Appl. Phys. Lett.* **2010**, *96*, 12–15.
- (64) Claude, J.; Lu, Y.; Wang, Q. Effect of Molecular Weight on the Dielectric Breakdown Strength of Ferroelectric Poly(vinylidene Fluoride-Chlorotrifluoroethylene)s. *Appl. Phys. Lett.* **2007**, *91*, 2–5.
- (65) Stark, K. H.; Garton, C. G. Electric Strength of Irradiated Polyethene. *Nature* **1955**, *175*, 642–643.
- (66) R. Kornbluh, R. Pelrine, Q. Pei, R. Heydt, S. Stanford, S. Oh and J. Eckerle, *Proc. SPIE Smart Struct. Mater.* **2002**, 4698, 254–270.

4.7 Supporting Information

Highly stretchable dielectric elastomers composites containing high silver nanoparticles volume fraction

*Jose Enrico Q. Quinsaat, Mihaela Alexandru, Frank A. Nüesch, Heinrich Hofmann, Andreas Borgschulte, and Dorina M. Opris**

J. E. Q. Quinsaat, Dr. M. Alexandru, Prof. Frank A. Nüesch, Dr. D. M. Opris

Swiss Federal Laboratories for Materials Science and Technology (Empa), Laboratory for Functional Polymers, Überlandstrasse 129, 8600 Dübendorf, Switzerland

E-mail: dorina.opris@empa.ch

J. E. Q. Quinsaat, Prof. H. Hofmann, Prof. F. A. Nüesch, Ecole Polytechnique Fédérale de Lausanne (EPFL), Materials Institute, 1015 Lausanne, Switzerland

Dr. A. Borgschulte, Swiss Federal Laboratories for Materials Science and Technology (Empa), Laboratory for Hydrogen and Energy, Überlandstrasse 129, 8600 Dübendorf, Switzerland

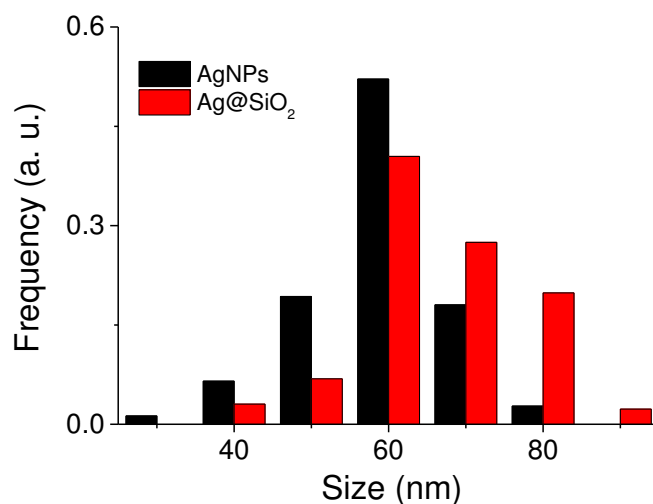


Fig. 60: Size distribution of AgNPs and Ag@SiO₂ core-shell. The sizes were determined through TEM image analysis.

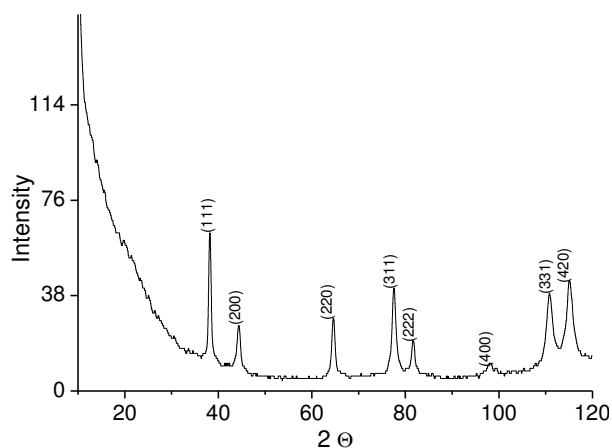


Fig. 61: XRD pattern of the AgNPs prepared by polyol synthesis at 130 °C. The typical cubic silver diffraction was observed.

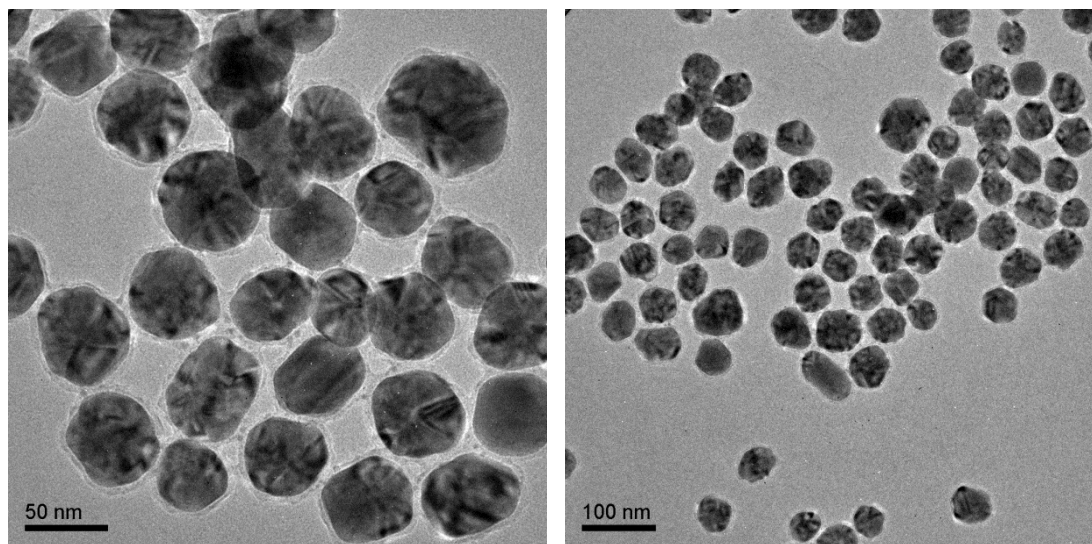


Fig. 62: TEM micrographs of the Ag@SiO₂ produced via upscaling through the addition of 0.6 vol% ethanolic TEOS solution into the reaction mixture.

4. Highly Stretchable Dielectric Elastomer Composites Containing High Volume Fraction of AgNPs

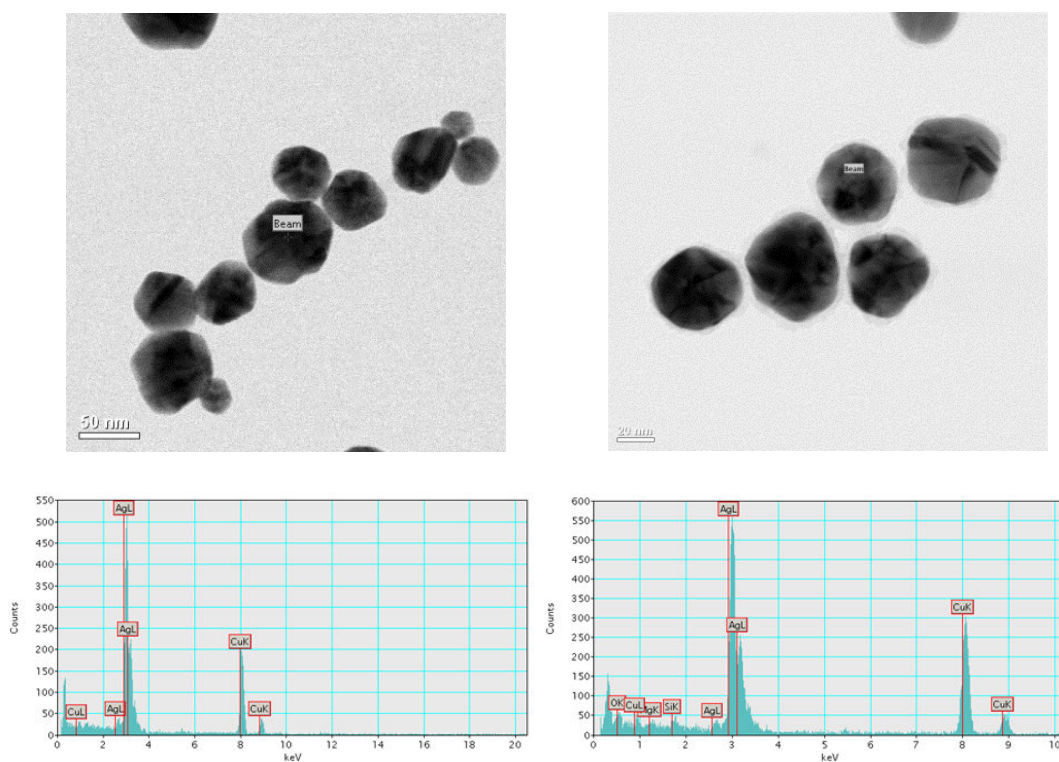


Fig. 63: TEM micrographs of the AgNPs (left) and Ag@SiO₂ core-shell particles (right) and their corresponding EDX spectrum below.

Sample	Elemental analysis		
	C [%]	H [%]	N [%]
Ag@SiO ₂	1.11	0.19	0.24
Ag@SiO ₂ @Si(CH ₃) ₃	1.75	0.28	0.33

Fig. 64: Elemental analysis of the core-shell particles before and after surface treatment with HMDS.

4. Highly Stretchable Dielectric Elastomer Composites Containing High Volume Fraction of AgNPs

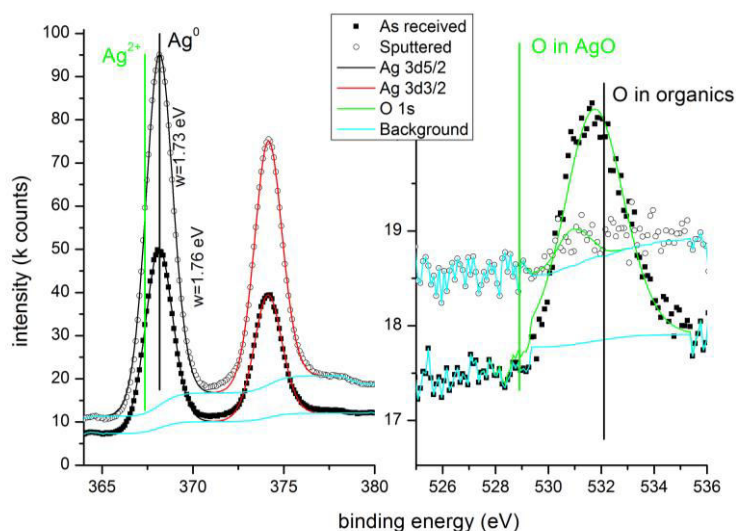


Fig. 65: XPS spectra of AgNPs prepared with the polyol synthesis at 130 °C. The peak indicative for the oxidized silver species is missing.

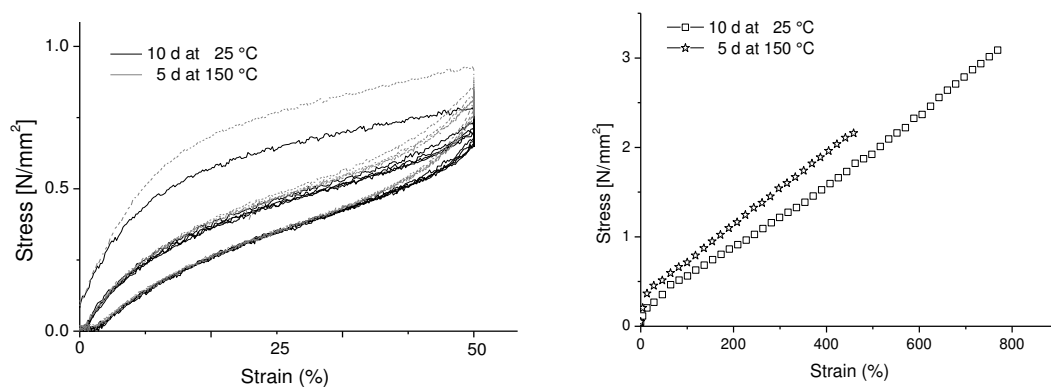


Fig. 66: The mechanical properties of B₂₀ aged at room temperature for 10 days and at 150 °C for 5 days: the cyclic (left) and the stress-strain (right) tests.

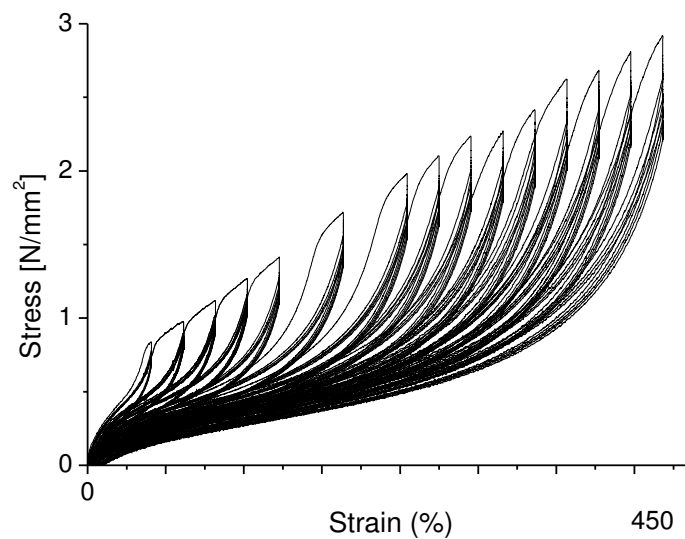


Fig. 67: The strain reloading stress-strain curves after initial strain excursions of 50, 75, 100, all the way up to 450 % for B₁₄.

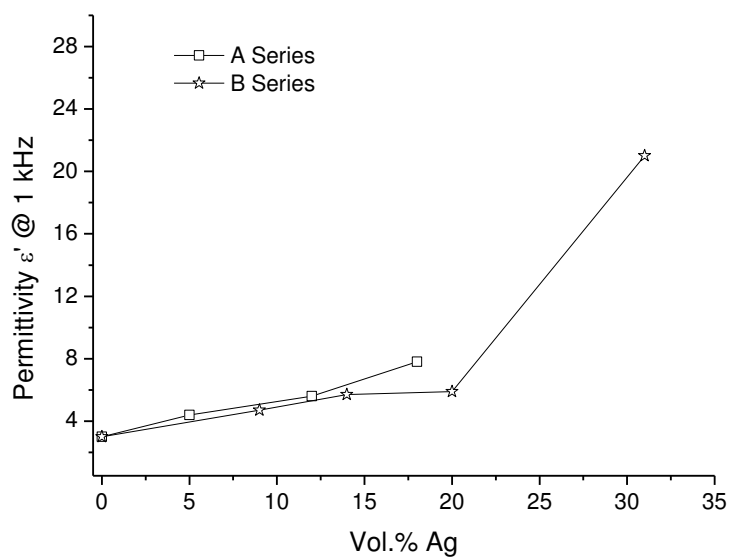


Fig. 68: Permittivity as function of filler content of the composite of series A and B.

4. Highly Stretchable Dielectric Elastomer Composites Containing High Volume Fraction of AgNPs

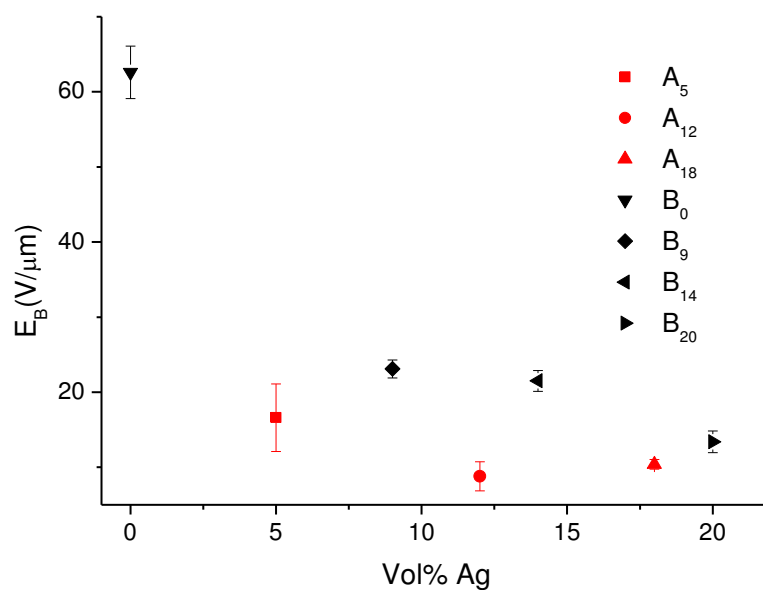


Fig. 69: Breakdown field E_B as function of filler content of the composite of series A (red) and B (black). The averaged values are depicted with error bars and were obtained from the measurements using the electrodes with an area of 1 mm^2 .



Fig. 70: Electrodes used for breakdown strength measurements and the overall set-up of the system (from left to right).

4. Highly Stretchable Dielectric Elastomer Composites Containing High Volume Fraction of AgNPs



Fig. 71: The setup used for measuring the dielectric properties.

The thicknesses of the samples used for the dielectric measurements were below 50 μm and were measured using a Heidenhein high accuracy gage. The samples were measured using Hewlett Packard 16451B dielectric test fixture equipped with round electrodes (left). To ensure a good contact and a uniform “pressure” over the samples (because of the round electrode used), gold plates slightly smaller than the coated electrodes were used. The setup shown above (left), allows a tender touch of the sample by the top electrode that is connected to a micrometer. So, there should be no displacement or pressure in the samples. The sample coated with 21 mm electrode was also measured using the setup with which the Novocontrol Alpha-A Frequency Analyzer is equipped (right) and the dielectric results were similar to those obtained using the other setup. Because rather thin samples were used, which were coated with conductive layers of defined surface, even when the right setup was used and more pressure was applied to the sample by screwing, no change in the permittivity was observed.

4. Highly Stretchable Dielectric Elastomer Composites Containing High Volume Fraction of AgNPs

Chapter 5: Surface Hydrophobization of Silver Nanoparticles (AgNPs) through Surface-initiated Atom Transfer Radical Polymerization (SI-ATRP)

Declaration: The nanoparticle synthesis, functionalization as well as the TEM image analysis were conducted by Jose Enrico Q. Quinsaat.

Jose Enrico Q. Quinsaat^{1,2}, Frank A. Nüesch¹, Heinrich Hofmann², Dorina M. Opris^{1}*

¹Swiss Federal Laboratories for Materials Science and Technology (Empa), Laboratory for Functional Polymers, Überlandstrasse 129, 8600 Dübendorf, Switzerland

²Ecole Polytechnique Fédérale de Lausanne (EPFL), Materials Institute, Powder Technology Laboratory (LTP), 1015 Lausanne, Switzerland

Abstract: This work describes the preparation of poly(methyl methacrylate) (PMMA)-coated Ag@SiO₂ core-shell particles by conducting a Surface-initiated Atom Transfer Radical Polymerization (SI-ATRP). Prior to conducting the polymerization, Silver nanoparticles (AgNPs) formed by the polyol synthesis were subjected to preliminary surface functionalization which includes the encapsulation in an insulating SiO₂ shell. The growth of an additional organic PMMA shell yields inorganic/organic core-shell particles with an enhanced dispersibility in non-polar solvents.

5.1 Introduction

Silver Nanoparticles (AgNPs) are widely employed in different scientific fields due to their array of properties. The current application fields of AgNPs include biology,¹⁻³ optics,⁴⁻⁶ catalysis^{7,8} and electronics.⁹⁻¹² The properties of AgNPs depend on both their size and shape, and it is essential to gain control over them in order to tune their properties. While the continuous preparation of AgNPs in flow reactors have enabled the control over the size and distribution of the particles,¹³⁻¹⁶ the polyol synthesis has established itself as a reliable and facile method to prepare different silver nanostructures which includes wires, cubes, spheres, bipyramids and triangles.¹⁷ The surface functionalization is essential for both the stability and further use of AgNPs in different application fields. Inorganic materials such as TiO₂ and SiO₂ have been used to encapsulate the AgNPs with an oxide layer in order to give core-shell particles. While Ag@TiO₂ particles are exploited for their resulting photocatalytic activity,¹⁸⁻²⁰ Ag@SiO₂ have been prepared in order to control their plasmonic properties.²¹⁻²³ Furthermore, Ag@SiO₂ core-shell particles also feature good dielectric properties with both low conductivities and dielectric losses.^{24,25} Previous studies on the dielectric properties of the core-shell particles revealed the control over the dielectric properties with the variation of the silica shell thickness.²⁶ Therefore, core-shell particles are promising candidates to be used as high permittivity filler for the preparation of materials with enhanced dielectric properties. However, the SiO₂ shell is highly hydrophilic and has to be rendered hydrophobic in order to compatibilize it with matrices

5. Surface Hydrophobization of AgNPs through SI-ATRP

such as polydimethylsiloxane (PDMS), polyacrylates or polyolefins. Hybrid organic/inorganic nanocomposites find potential applications in optics, electronics and biomedicine.^{27,28} Although surface hydrophobization can be achieved with alkyl silanes^{29–32} or by emulsion polymerization,³³ this work exploits the possibility of growing an outer polymer layer on the core-shell particles by conducting a Surface-initiated (SI) Atom Transfer Radical Polymerization (ATRP).^{34,35} SI-ATRP has previously been used to prepare organic/inorganic hybrid particles. In most of the cases, the growth of polymers such as polystyrenes, polymethacrylates and polyacrylonitriles has been demonstrated on SiO₂ particles or Si-surfaces.^{36–38} Apart from SiO₂ nanoparticles, SI-ATRP has also been demonstrated on metal surfaces and particles such as Au, where a thiol-functionalized ATRP-initiator was grafted directly on the particle surface.^{39–44} The resulting hybrid particles featured good dispersability and thus compatibility in hydrophobic media as well as high mechanical and thermal stability.^{27,36,45} These features are the targeted properties of the polymer (PMMA)-coated Ag@SiO₂ core-shell particles which were prepared in this work (Fig. 72 and Fig. 73).

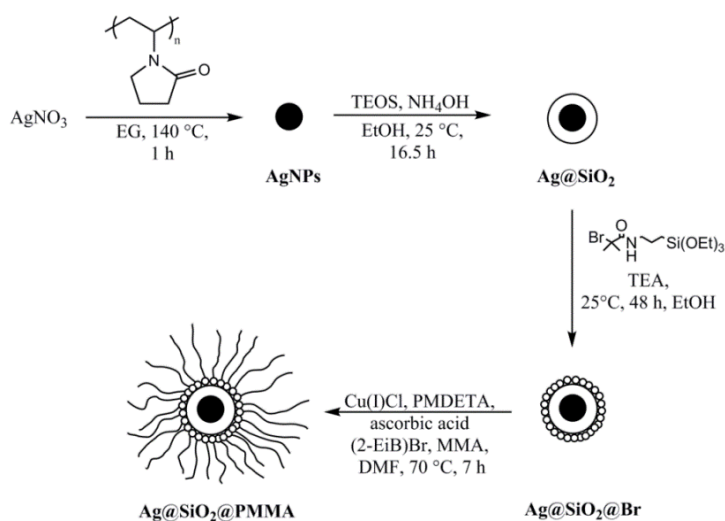


Fig. 72: General scheme towards the preparation of PMMA-coated Ag@SiO₂ core-shell particles.

5.2 Experimental Section

5.2.1 Materials and Methods

AgNO₃, poly(vinyl pyrrolidinone) (PVP), ethylene glycol (EG), tetrahydrofuran (THF), ethanol (EtOH), methanol (MeOH), α -bromoisobutyryl bromide, ammonia (29 % solution, NH₄OH), triethylamine (TEA), tetraethoxysilane (TEOS), aminopropyl triethoxysilane (APTES), CuCl, *N,N',N'',N''*-pentamethyldiethylenetriamine (PMDETA), ascorbic acid, ethyl- α -bromoisobutyrate (2-(EiB)Br), methyl methacrylate (MMA) were purchased from Aldrich. While EG and MMA were distilled prior use, all other chemicals were used as received. Monomer conversion in the polymerization reaction was monitored and analyzed with a Bruker Avance III 400 NMR spectrometer using a 5 mm BBO Prodigy™ CryoProbe at 400.18, 100.63 and 79.50 MHz, respectively. Gel permeation chromatography (GPC) measurements were done with an Agilent 1100/PSS WinGPC 8.1 system in tetrahydrofuran calibrated with poly(methyl methacrylate) (PMMA) standards (Polymer Standards Service). Prior to the analysis by GPC, the polymers were subjected to cycles of purification which consists of dissolving them in THF followed by the precipitation in MeOH. The nanoparticles were observed with TEM using a Philips CM30 TEM. For the observation of PMMA-coated core-shell particles, the TEM grid was stained with 2 wt% aqueous solution of phosphotungstic acid. UV-vis absorption spectra were recorded with a Cary 50 spectrophotometer, DLS measurements were done with a Malvern Zetasized Nano ZS, the thermogravimetric analysis (TGA) was conducted with a Perkin Elmer TGA7 at a heating rate of 20 °C min⁻¹ under a helium gas flow. The number of particles measured for the statistical determination of the particle size was about 400 for Ag core and about 120-150 for the SiO₂ and PMMA-coated particles with the help of the software Imagej and a ruler for Windows, respectively.

5. Surface Hydrophobization of AgNPs through SI-ATRP

5.2.2 Synthesis of AgNPs

In a 100 mL round-bottom flask, PVP (6 g, 54 mmol, $M_w = 40$ kDa) was dissolved in EG (50 mL) under sonication. After complete dissolution of the polymer, the flask was stirred in an oil bath at 140 °C for 30 min, then an aqueous solution of AgNO₃ (1 mL, 1 g/mL) was injected rapidly and the reaction mixture was stirred further for 1 h at a speed of 900 rpm. The flask was later removed from the oil bath, cooled in a water bath and the reaction mixture was diluted with acetone, centrifuged at 5'000 rpm for 0.5 h and decanted. The resulting precipitate was further washed with acetone and water 3 times before redispersion in EtOH. The reaction was repeated 18 times and the particles were redispersed in 400 mL of EtOH. Yield: 9.26 g (82 %). Size: 59 ± 22 nm.

5.2.3 Synthesis of Ag@SiO₂ Core-shell Particles

The silica-coating was performed based on existing protocols of the modified Stöber method.²⁶ For the silica-coating, 2 x 190 mL of the AgNPs dispersion in EtOH was transferred each in a 2 L flask, diluted with EtOH (600 mL) and treated with NH₄OH (29 %, 21.25 mL), ethanolic TEOS solution (2.2 vol%, 45 mL) and stirred at 25 °C for 16 h. The mixture was diluted with acetone, centrifuged and decanted. The particles were redispersed in EtOH and the washing procedure was repeated thrice in order to obtain the core-shell particles (8 g) which were redispersed in EtOH (250 mL). Size: 65 ± 14 nm.

5.2.4 Synthesis of APTES-Br

APTES-Br was prepared according to a previous protocol.⁴⁶ A mixture containing APTES (10 mL, 43 mmol) and triethylamine (7.8 mL, 57 mmol) in dry THF (200 mL) was treated dropwise with α -bromoisobutryl bromide (5.55 mL, 51 mmol) at 0 °C. After completing the addition, the mixture was stirred at 0 °C for further 30 min, and then warmed to 25 °C and stirred overnight. The mixture was filtered, concentrated *in vacuo* to give APTES-Br

5. Surface Hydrophobization of AgNPs through SI-ATRP

(13.1 g, 86 %) as yellow oil. ^1H NMR (CDCl_3 , 400 MHz): 0.6-0.7 (m, 2H, SiCH_2), 1.25 (t, 9H, $\text{CH}_3\text{CH}_2\text{OSi}$), 1.63-1.73 (m, 2H, CH_2), 2.00 (s, 6H, CCH_3), 3.3 (q, 2H, CH_2N). 3.85 (q, 6H, CH_2CH_3), 6.9 (s, 1H, NH).

5.2.5 Synthesis of Initiator-coated Ag@SiO₂ Core-shell Particles (Ag@SiO₂@Br)

The Ag@SiO₂ core-shell particles (230 mL out of the 250 mL stock solution) were transferred to a 500 mL round bottom flask, stirred at 25 °C and treated with triethylamine (5.4 mL, 39.1 mmol) and a mixture of APTES-Br (5.4 g, 14.6 mmol) in EtOH (20 mL). The mixture was stirred for 2 days, then diluted with acetone, centrifuged and decanted. The residue was redispersed in EtOH, diluted with acetone, centrifuged and decanted. The washing cycle was repeated 6× in order to obtain the initiator-coated core-shell particles (6.4 g, 80 %) which were redispersed in EtOH (100 mL).

5.2.6 Surface-initiated (SI) ATRP on Initiator Coated Ag@SiO₂ Core-shell Particles

The initiator-coated Ag@SiO₂ core-shell particles (4 g, ~ 0.54 mmol APTES-Br grafted on the surface), MMA (35.7 mL, 336 mmol), 2-(EiB)Br (55 μL , 0.35 mmol) in DMF (10 mL) were transferred to a 250 mL Schlenk flask, and subjected to three freeze-dry-pump-thaw cycles. In a separate flask, a solution of CuCl (80 mg, 0.80 mmol), PMDETA (210 μL , 1 mmol), and ascorbic acid (44 mg, 0.25 mmol) in DMF (15 mL) was degassed with Ar for 30 min and then transferred to the Schlenk flask containing the particles via a cannula. The flask was then placed in a preheated oil bath and stirred at 70 °C. During the reaction, aliquots were taken after defined time intervals. The reaction was terminated after 7 h by exposing the reaction to air followed by cooling the reaction mixture down to room temperature. The mixture was dissolved in acetone, centrifuged and decanted. The washing procedure was repeated 7 times until no free polymer chain was detected in the mother liquor. Eventually, PMMA-coated core-shell particles (1.8 g) were obtained after the

5. Surface Hydrophobization of AgNPs through SI-ATRP

purification process.

5.3 Results and Discussion

5.3.1 Synthesis of AgNPs and Surface Functionalization with SiO₂

The AgNPs were prepared by the polyol synthesis, an established method to prepare nanoparticles in relatively large amounts per batch reaction.²⁶ The average particle diameter was 59 nm (Fig. 73). The silica-coating was conducted with a modified Stöber method to give core-shell particles in gram quantities with a thin SiO₂-shell of ~ 3 nm (Fig. 73).^{19,21,26} The subsequent change in the dielectric medium of the AgNPs (from PVP/EtOH to SiO₂) led to a bathochromic shift from 434 to 443 nm in the corresponding UV-vis spectra (Fig. 74). As previously investigated, it is essential to keep the SiO₂-shell very thin in order to preserve the metallic character of the core-shell particles e.g. the dielectric constant.²⁶ However, the thin silica shell seemed to be insufficient in stabilizing the AgNPs from forming some agglomerates which can be attributed to the strong van der Waals interactions acting between the cores. The formation of some agglomerates between the particles is indicated by the broadening of the peaks in the UV-vis spectra although DLS does not detect it.

5.3.2 Surface-initiated (SI) ATRP on the Ag@SiO₂ Core-shell Particles

Although the direct growth of polymers on gold nanoparticles (AuNPs) functionalized with thiol-terminated initiators has previously been reported, a main drawback of this approach is the relatively weak Au-S bond (~ 40 kcal/mol) which can undergo bond dissociation at temperatures > 60 °C.⁴⁰ In comparison, the Ag-S bond dissociation energy amounts 52 kcal/mol, which is a bit higher than the Au-S bond energy but will also undergo the same fate at high temperatures.⁴⁷ Since the polymerization has to be conducted at ambient temperatures in order to circumvent this issue, the choice of polymerizable monomers becomes limited. To overcome this problem the APTES-Br initiator was chemically grafted to the silica surface of the Ag@SiO₂ core-shell particles. The SiO₂ shell serves as a

5. Surface Hydrophobization of AgNPs through SI-ATRP

protection barrier for the AgNPs towards agglomeration as a result of electrostatic stabilization and allows chemical functionalization of the surface through the presence of the hydroxyl groups.

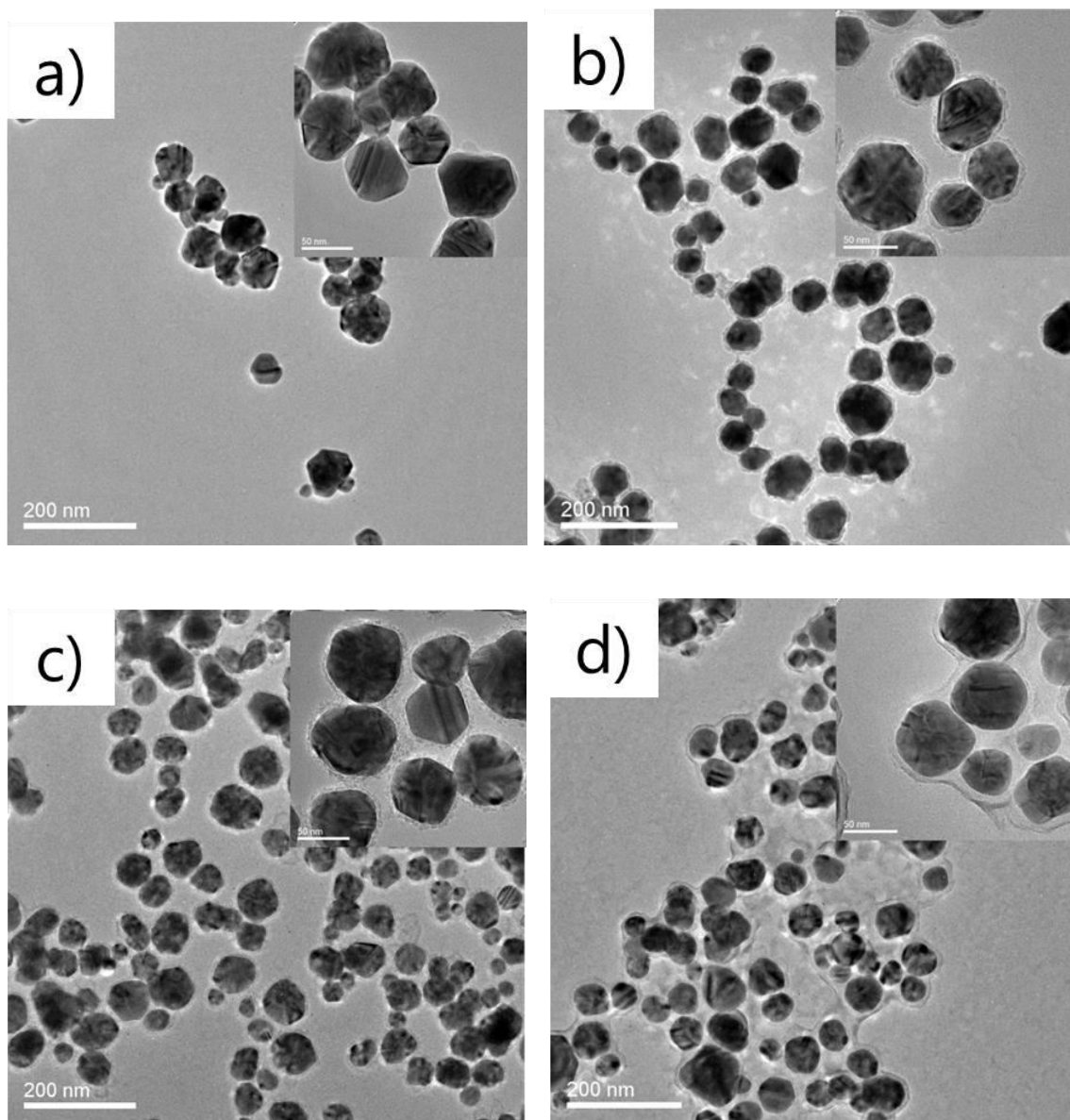


Fig. 73: TEM micrographs of AgNPs (a), Ag@SiO₂ (b), APTES-Br (c) and PMMA-coated Ag@SiO₂ core-shell particles (d).

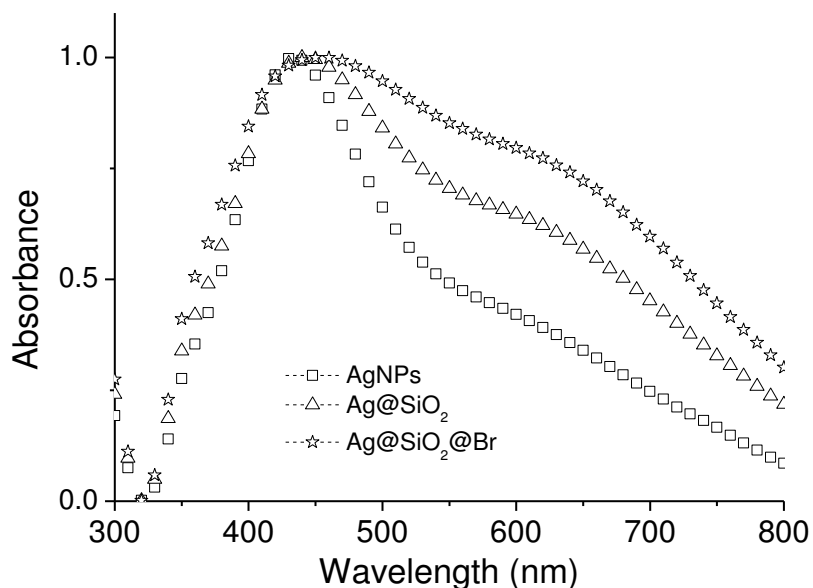


Fig. 74: UV-vis spectra of AgNPs, Ag@SiO₂ and APTES-Br coated Ag@SiO₂ core-shell particles. The spectra were recorded in EtOH.

Similarly, Au@SiO₂@PMMA particles have been prepared in the same fashion by Matsui *et al.*⁴⁸ Such a three-layered hybrid particle assembly has been used by Liang *et al.* to produce hairy hybrid microrattles upon etching away the intermediate SiO₂ layer.⁴⁹ Eventually, the Au core is trapped in a hollow cavity surrounded by a polymeric shell consisting either of poly(ethylene glycol) (PEG) or poly(*N*-isopropylacrylamide). As reported earlier, the use of NH₄OH as alkaline catalyst for the initiator fixation induces agglomeration, and therefore TEA was used for this procedure to minimize the risk, and despite the broadened UV-vis signal for the APTES-Br coated core-shell particles (Fig. 74) which is indicative for some agglomeration formation, the DLS measurements and TEM micrographs do not support this findings (Fig. 73 and Fig. 75).⁵⁰ TEA can deprotonate the silanol groups thus enabling the alkoxysilane initiators to attach onto the SiO₂ surface.^{51–53} The immobilization of the initiator on the particle surface was verified by elemental analysis which determined the Br content to be 1.08 wt%, thus giving about 125 μmol of

5. Surface Hydrophobization of AgNPs through SI-ATRP

Br/g of nanoparticle. By assuming a spherical shape of the core-shell particles and a silanol group density of $5/\text{nm}^2$,⁵⁴ the initiator density becomes around 7-8 molecules/ nm^2 which is higher than the reported in the literature and the theoretically possible grafting densities, but could be attributed to the formation of multilayered networks of the APTES-Br on the surface.^{50,55} However, the calculated polymer chain density was ~ 0.1 chains/ nm^2 , a value which is smaller than the ones reported previously (see TGA spectra).^{44,50} The SI-ATRP was performed at 70°C in order to control the molecular weight distribution of the polymers as well as to prevent potential effects of the present copper salts in the solution on the morphology of the AgNPs.⁵⁶ Free “sacrificial” initiator (2-(EtB)Br) was introduced in order to achieve control over the polymerization through the accumulation of sufficient amounts of Cu(II) species via radical termination.^{50,57} The use of CuCl in this work rather than CuBr was attributed to the fact that ATRP reactions conducted with CuBr generally led to higher polymer dispersion index (PDI) compared to the reactions which employed CuCl catalyst.^{58,59} The polymerization was terminated after 7 h, which led to an overall monomer conversion of 46 %. An increase in the particle size as a result of the growing insulating layer was observed in both the TEM micrographs as well as in the DLS spectra of the corresponding particles at each functionalization stage (Fig. 73 and Fig. 75). Unfortunately, it was difficult to differentiate the SiO_2 - and PMMA-shell from each other due to the amorphous nature and poor electron density featured by both entities, but an increase in the size of the core-shell particles after the polymerization was observed in the corresponding TEM micrographs (Fig. 73) although the size of the PMMA-coated core-shell particles is much lower than the value obtained from the DLS measurements (Tab. 15). This can be explained by the fact that the hydrodynamic diameter of the particles is larger in solution due to the swelling of the tethered polymer chains in organic solvents. A similar observation was made by Ohno *et al.* where the hydrodynamic diameter D_H of the particles obtained from DLS measurements surpasses the size determined from the TEM micrographs.⁵⁰ In contrast, the polymers collapse in the dry state and form compact core-shell structures thus leading to the smaller particle size observed by TEM. Additionally, some chains might undergo interdigitation as a result of attractive forces occurring between them thus leading to a compression of the PMMA shell.⁴⁸

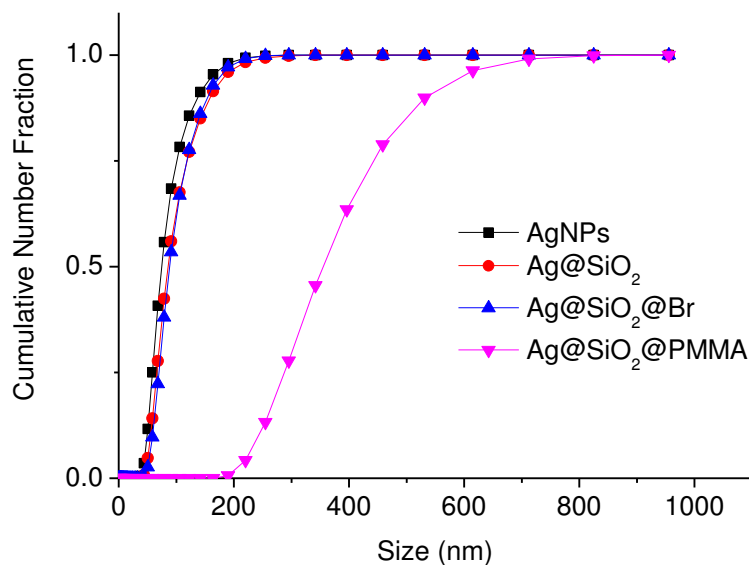


Fig. 75: DLS spectra of AgNPs, Ag@SiO₂, APTES-Br and PMMA-coated Ag@SiO₂ core-shell particles recorded in EtOH.

Concerning the image analysis performed on the TEM micrographs of the Ag@SiO₂@PMMA core-shell particles, the average diameter of the particles was increased by ~ 20 nm, therefore the resulting polymer shell composed of PMMA chains in the dry state is estimated to be around 10 nm thick (Fig. 76). An overview of the determined parameters for the particles after each functionalization step is shown in Tab. 15. The corresponding UV-vis spectrum of the PMMA-coated core-shell particles was recorded in THF due to its enhanced solubility in non-polar solvents and is shown in Fig. 77. For comparison reasons, the spectrum of the APTES-Br coated core-shell particles was also recorded in THF. After the polymerization on the APTES-Br coated core-shell particles, the maximum absorption peak λ_{\max} initially experiences a blue shifting from 457 to 455 nm which could be explained by the increase in the interparticle distance through the growing of the polymer chains as well as the change in the dielectric medium of the particles ($\epsilon_{\text{PMMA}} < \epsilon_{\text{SiO}_2}$).⁶⁰ The narrower peaks of the PMMA-coated Ag@SiO₂ core-shell

5. Surface Hydrophobization of AgNPs through SI-ATRP

particles compared to the uncoated counterpart in the UV-vis spectra could be indicative for a better dispersion of the particles in THF as a result of rendering the surface hydrophobic. With increasing polymerization time, λ_{\max} experiences a small bathochromic shift from 455 to 460 nm which might be caused by the enhanced interactions of the particles as a result of the previously mentioned interdigitation of the polymers attributed to the increase in the molecular weight. Despite the steric repulsion between the dangling polymer chains, they might be able to form tight ensembles with each other due to the entanglement/interdigitation caused by hydrophobic/hydrophobic interactions. This can manifest itself in the broadening of the UV-vis spectra (Fig. 77) after 7h of polymerization.

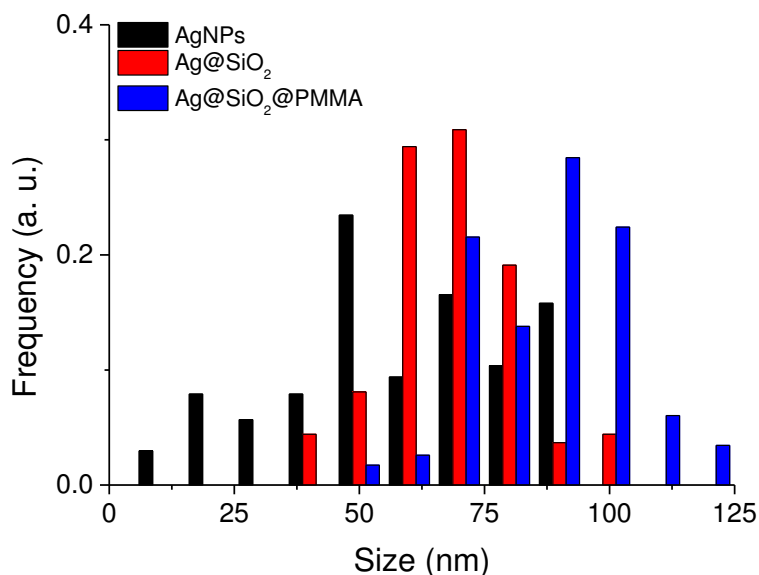


Fig. 76: Particle size distribution of AgNPs, Ag@SiO₂ core-shell particles and PMMA-coated Ag@SiO₂ core-shell particles obtained from the image analysis of TEM micrographs.

5. Surface Hydrophobization of AgNPs through SI-ATRP

Tab. 15: Determined size parameters of AgNPs, Ag@SiO₂ core-shell particles (before and after immobilization of APTES-Br) and PMMA-coated Ag@SiO₂ core-shell particles.

	Size (TEM)	Size (DLS) ^a	λ_{\max}
AgNPs	59 (22)	75 (29) ^b	434 ^b
Ag@SiO ₂	65 (14)	83 (35) ^b	443 ^b
Ag@SiO ₂ @Br	-	86 (32) ^b	453 ^b
Ag@SiO ₂ @PMMA	84 (16)	342 (99) ^c	460 ^c

^a Mean numerical diameter. In the parenthesis is reported the measured standard deviation of the particle population

^b measured in EtOH

^c measured in THF

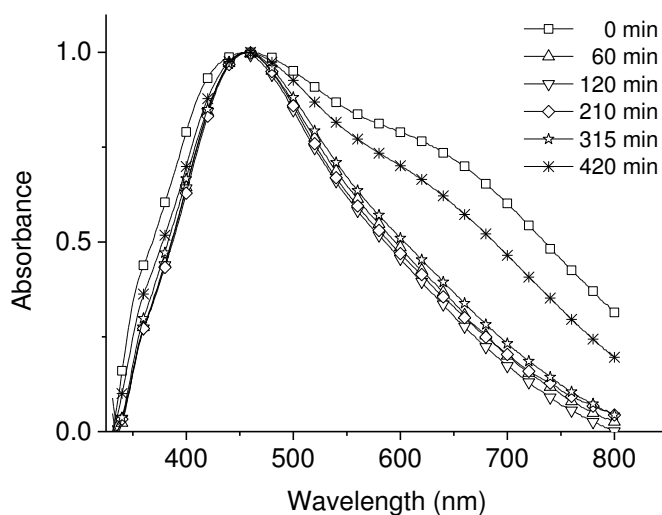


Fig. 77: UV-vis spectra of APTES-Br coated Ag@SiO₂ core-shell particles and PMMA-coated Ag@SiO₂ core-shell obtained from the aliquots taken after a prescribed amount of time. The spectra were recorded in THF.

5. Surface Hydrophobization of AgNPs through SI-ATRP

In Fig. 78, water/toluene extraction tests of the particles after each corresponding functionalization step are illustrated. The particles remained hydrophilic even after the immobilization of the APTES-Br initiator which is in agreement with the literature.⁵¹

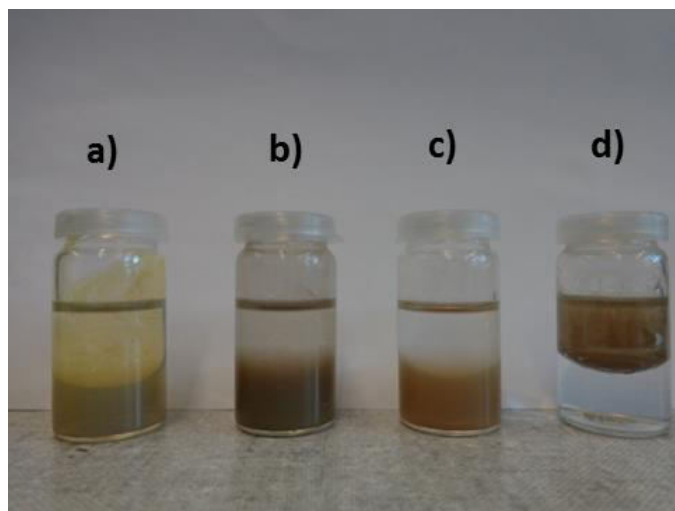


Fig. 78: Water/toluene extraction tests of AgNPs (a), Ag@SiO₂ (b), APTES-Br-coated Ag@SiO₂ (c) and PMMA-coated Ag@SiO₂ core-shell particles (d). The organic phase is above the aqueous phase.

As expected, the grafting of PMMA on the initiator-coated Ag@SiO₂ core-shell particles led to a transfer of the particles into the hydrophobic phase due to the hydrophobic polymer chains on the surface. The PMMA-coated core-shell particles were dispersible in a variety of organic solvents which includes toluene, THF and acetone. In order to control and analyze the polymerization, aliquots were taken out of the reaction solution after defined time intervals. The reaction was terminated after a monomer conversion of 46 % (Fig. 79).

5. Surface Hydrophobization of AgNPs through SI-ATRP

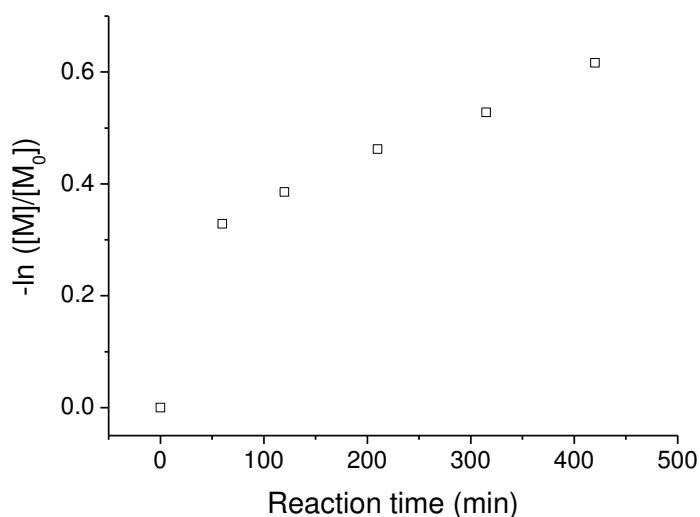


Fig. 79: Semi-logarithmic plot of the monomer conversion versus the polymerization reaction time.

It is well known that the molecular weight and molecular weight distribution of polymers formed by ATRP on surfaces are basically identical to the values obtained from polymers that were prepared with free initiators.^{44,61} Therefore, the characteristics of the isolated polymer formed from the reaction of the free, “sacrificial” initiator should be representative for the grafted polymers. GPC measurements gave a molecular weight $M_n = 100'000$ g/mol for the free polymer after 7 h of polymerization (Fig. 80 and Fig. 81). Unfortunately, the PDI deteriorated in the course of the polymerization reaction, namely from 1.6 to 2.6 despite the careful choice of reaction parameters. This might be the direct result of the deterioration of the stirring of the reaction mixture due to the increased viscosity of the system during the course of the reaction. This affected the uniform heat transfer within the system, especially for a large reaction volume where such effects become more pronounced as was the case here. The TGA measurements under He atmosphere were performed for Ag@SiO₂, APTES-Br, and PMMA-coated Ag@SiO₂ core-shell particles. The results shown in Fig. 82 illustrate the increase in the amount of decomposed materials and the decrease in residual mass with each functionalization step due to the degradation of the organic components. The TGA curve of the PMMA-coated

5. Surface Hydrophobization of AgNPs through SI-ATRP

core-shell particles show different stages of degradation, a feature observed for the decomposition of PMMA prepared through radical initiation. The different stages of decomposition are a result of different polymer degradation mechanisms found in PMMA which are described elsewhere.^{62–65} Overall, the residual mass after the degradation of PMMA-coated Ag@SiO₂ core-shell particles is about 79.9 wt%, indicating a polymer content of 14.2 wt% by taking the residual mass of APTES-Br functionalized core-shell particles after thermal degradation into account (Fig. 82). In volumetric terms, the Ag content in the core-shell particles is still around 20–30 vol%, and is within the vicinity of the percolation threshold described for Ag-based nanocomposites.^{10,66}

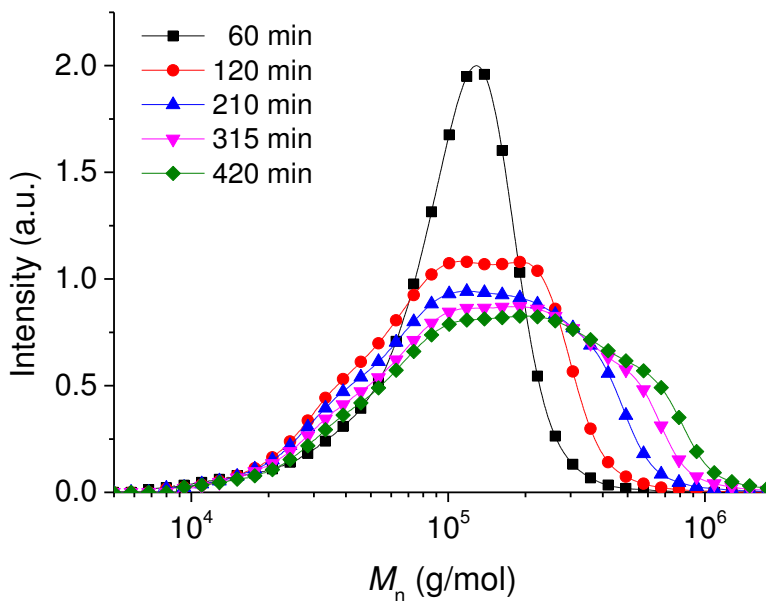


Fig. 80: Molecular weight (M_n) of free, sacrificial PMMA obtained from GPC measurements of aliquots taken after a prescribed amount of reaction time.

5. Surface Hydrophobization of AgNPs through SI-ATRP

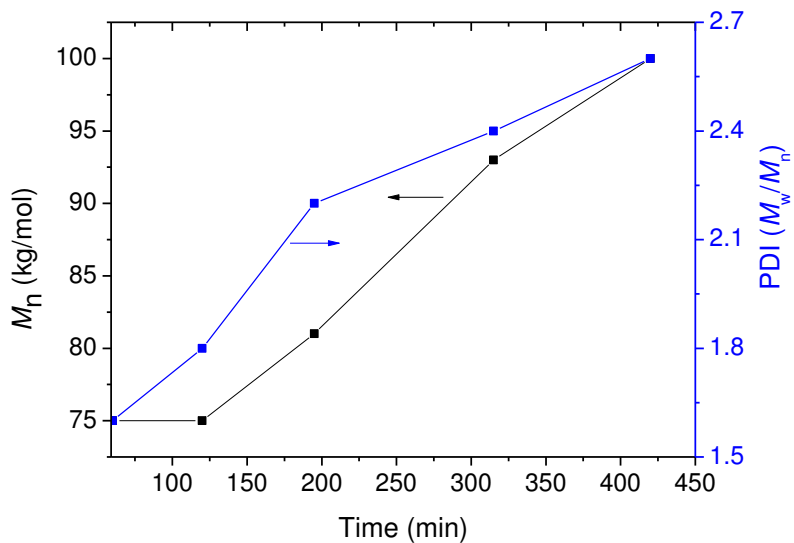


Fig. 81: The development of the molecular weight M_n and the polymer dispersity index (PDI) with time.

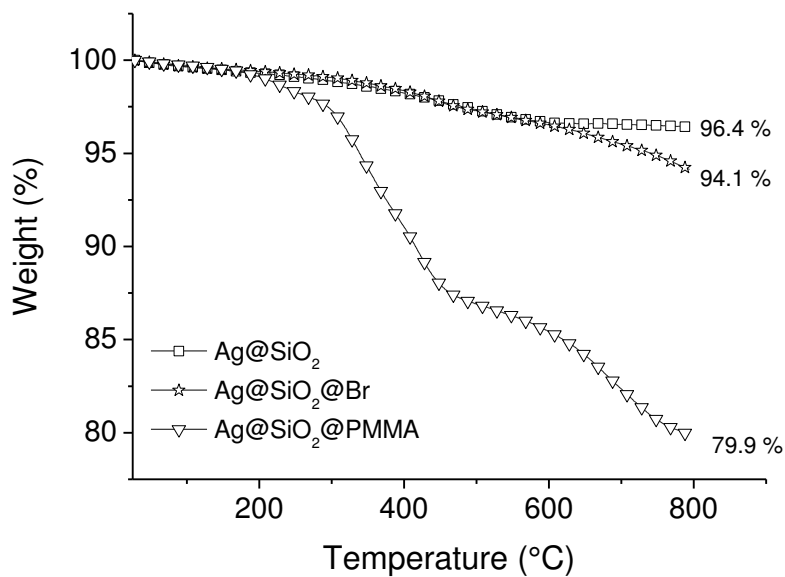


Fig. 82: TGA curves of Ag@SiO₂, APTES-Br and PMMA-coated Ag@SiO₂ core-shell particles.

5.4 Conclusion and Outlook

In summary, PMMA-coated Ag@SiO₂ core-shell particles which exhibit enhanced solubility in organic, non-polar solvents have been prepared in gram scale. They can serve as an alternative set of core-shell particles to be used for the preparation of nanocomposites with a hydrophobic polymer matrix. The enhanced dispersibility of the particles can lead to a homogenous dispersion of the particles into the polymer matrix and avoid the formation of micron-sized agglomerates which are likely to occur when the particles are dispersed into an incompatible matrix. Further work on the improvement of the PDI of the resulting polymers will be on the agenda. The dielectric properties of the filler as well as those of their resulting nanocomposites will be examined in the near future.

5.5 Acknowledgements

Our special thanks go out to S. Dünki and B. Fischer for conducting the GPC and TGA measurements, respectively. We also gratefully acknowledge Swiss National Science Foundation (SNF132101), (SNFS 150638) and Swiss Federal Laboratories for Materials Science and Technology (Empa, Dübendorf) for financial support.

5.6 References

- (1) Reszczyńska, J.; Jurek, A.; Łacka, I.; Skwarek, E.; Zaleska, A. Preparation of Silver Nanoparticles in Reverse Micelles and Antibacterial Activity of Silver Modified-Paints. *Adv. Mater. Sci.* **2010**, *10*, 12–20.
- (2) Goyal, A.; Kumar, A.; Patra, P. K.; Mahendra, S.; Tabatabaei, S.; Alvarez, P. J. J.; John, G.; Ajayan, P. M. In Situ Synthesis of Metal Nanoparticle Embedded Free Standing Multifunctional PDMS Films. *Macromol. Rapid Commun.* **2009**, *30*, 1116–1122.
- (3) Sharma, V. K.; Yngard, R. A.; Lin, Y. Silver Nanoparticles: Green Synthesis and Their Antimicrobial Activities. *Adv. Colloid Interface Sci.* **2009**, *145*, 83–96.
- (4) Wiley, B. J.; Chen, Y.; McLellan, J. M.; Xiong, Y.; Li, Z.-Y.; Ginger, D.; Xia, Y. Synthesis and Optical Properties of Silver Nanobars and Nanorice. *Nano Lett.* **2007**, *7*, 1032–1036.
- (5) Evanoff, D. D.; Chumanov, G. Synthesis and Optical Properties of Silver Nanoparticles and Arrays. *Chemphyschem* **2005**, *6*, 1221–1231.
- (6) Adam D. McFarland, R. P. V. D. Single Silver Nanoparticles As Real Time Optical Sensors With Zeptomole Sensitivity. *Nano Lett.* **2003**, *3*, 1057–1062.
- (7) Xu, R.; Wang, D.; Zhang, J.; Li, Y. Shape-Dependent Catalytic Activity of Silver Nanoparticles for the Oxidation of Styrene. *Chem. - An Asian J.* **2006**, *1*, 888–893.
- (8) Jiang, Z.-J.; Liu, C.-Y.; Sun, L.-W. Catalytic Properties of Silver Nanoparticles Supported on Silica Spheres. *J. Phys. Chem. B* **2005**, *109*, 1730–1735.
- (9) Lu, J.; Moon, K.-S.; Wong, C. P. Silver/polymer Nanocomposite as a High-K Polymer Matrix for Dielectric Composites with Improved Dielectric Performance. *J. Mater. Chem.* **2008**, *18*, 4821–4826.
- (10) Qi, L.; Lee, B. I.; Chen, S.; Samuels, W. D.; Exarhos, G. J. High-Dielectric-Constant Silver-Epoxy Composites as Embedded Dielectrics. *Adv. Mater.* **2005**, *17*, 1777–1781.
- (11) Lu, J.; Moon, K.-S.; Xu, J.; Wong, C. P. Synthesis and Dielectric Properties of Novel High-K Polymer Composites Containing in-Situ Formed Silver Nanoparticles for Embedded Capacitor Applications. *J. Mater. Chem.* **2006**, *16*, 1543–1548.
- (12) Atwater, H. A.; Polman, A. Plasmonics for Improved Photovoltaic Devices. *Nat. Mater.* **2010**, *9*, 205–213.

5. Surface Hydrophobization of AgNPs through SI-ATRP

- (13) Quinsaat, J. E. Q.; Testino, A.; Pin, S.; Huthwelker, T.; Bowen, P.; Hofmann, H.; Ludwig, C.; Opris, D. M. Continuous Production of Tailored Silver Nanoparticles by Polyol Synthesis and Reaction Yield Measured by X-Ray Absorption Spectroscopy: Towards a Growth. *J. Phys. Chem. C* **2014**, *118*, 11093–11103.
- (14) Nishioka, M.; Miyakawa, M.; Kataoka, H.; Koda, H.; Sato, K.; Suzuki, T. M. Continuous Synthesis of Monodispersed Silver Nanoparticles Using a Homogeneous Heating Microwave Reactor System. *Nanoscale* **2011**, *3*, 2621–2626.
- (15) Mehenni, H.; Sinatra, L.; Mahfouz, R.; Katsiev, K.; Bakr, O. M. Rapid Continuous Flow Synthesis of High-Quality Silver Nanocubes and Nanospheres. *RSC Adv.* **2013**, *3*, 22397–22403.
- (16) Huang, J.; Lin, L.; Li, Q.; Sun, D.; Wang, Y.; Lu, Y.; He, N.; Yang, K.; Yang, X.; Wang, H.; et al. Continuous-Flow Biosynthesis of Silver Nanoparticles by Lixivium of Sundried Cinnamomum Camphora Leaf in Tubular Microreactors. *Ind. Eng. Chem. Res.* **2008**, *47*, 6081–6090.
- (17) Wiley, B.; Sun, Y.; Xia, Y. Synthesis of Silver Nanostructures with Controlled Shapes and Properties. *Acc. Chem. Res.* **2007**, *40*, 1067–1076.
- (18) Dong, Q.; Yu, H.; Jiao, Z.; Lu, G.; Bi, Y. New Facile Synthesis of One-Dimensional Ag@TiO₂ Anatase Core-shell Nanowires for Enhanced Photocatalytic Properties. *RSC Adv.* **2014**, *4*, 59114–59117.
- (19) Zhang, X.; Zhu, Y.; Yang, X.; Wang, S.; Shen, J.; Lin, B.; Li, C. Enhanced Visible Light Photocatalytic Activity of Interlayer-Isolated Triplex Ag@SiO₂@TiO₂ Core-Shell Nanoparticles. *Nanoscale* **2013**, *5*, 3359–3366.
- (20) Qi, J.; Dang, X.; Hammond, P. T. ; Belcher, A. M. . Highly Efficient Plasmon-Enhanced Dye-Sensitized Solar Cells through Metal@Oxide Core-Shell Nanostructure. *ACS Nano* **2011**, *5*, 7108–7116.
- (21) Baida, H.; Billaud, P.; Marhaba, S.; Christofilos, D.; Cottancin, E.; Crut, A.; Lermé, J.; Maioli, P.; Pellarin, M.; Broyer, M.; et al. Quantitative Determination of the Size Dependence of Surface Plasmon Resonance Damping in Single Ag@SiO₂ Nanoparticles. *Nano Lett.* **2009**, *9*, 3463–3469.
- (22) Rainville, L.; Dorais, M.-C.; Boudreau, D. Controlled Synthesis of Low Polydispersity Ag@SiO₂ Core-shell Nanoparticles for Use in Plasmonic Applications. *RSC Adv.* **2013**, *3*, 13953-13960.

5. Surface Hydrophobization of AgNPs through SI-ATRP

- (23) Wang, W.; Zhipeng, L.; Baohua, G.; Zhenyu, Z.; Hongxin, X. Ag@SiO₂ Core-Shell Nanoparticles for Probing Spatial Distribution of Electromagnetic Field Enhancement via Surface-Enhanced Raman Scattering. *ACS Nano* **2009**, *3*, 3493–3496.
- (24) Zhou, Y.; Wang, L.; Zhang, H.; Bai, Y.; Niu, Y.; Wang, H. Enhanced High Thermal Conductivity and Low Permittivity of Polyimide Based Composites by Core-Shell Ag@SiO₂ Nanoparticle Fillers. *Appl. Phys. Lett.* **2012**, *101*, 012903.
- (25) Liang, X.; Yu, S.; Sun, R.; Luo, S.; Wan, J.; Yu, S.; Sun, R.; Luo, S.; Liang, X.; Wan, J.; et al. Microstructure and Dielectric Behavior of the Three-Phase Ag@SiO₂/BaTiO₃/PVDF Composites with High Permittivity. *J. Mater. Res.* **2012**, *27*, 991–998.
- (26) Quinsaat, J. E. Q.; Nüesch, F. A.; Hofmann, H.; Opris, D. M. Dielectric Properties of Silver Nanoparticles Coated with Silica Shells of Different Thicknesses. *RSC Adv.* **2013**, *3*, 6964–6971.
- (27) Balazs, A. C.; Emrick, T.; Russell, T. P. Nanoparticle Polymer Composites: Where Two Small Worlds Meet. *Science* **2006**, *314*, 1107–1110.
- (28) Cho, H. K.; Cho, H.-J.; Lone, S.; Kim, D.-D.; Yeum, J. H.; Cheong, I. W. Preparation and Characterization of MRI-Active Gadolinium Nanocomposite Particles for Neutron Capture Therapy. *J. Mater. Chem.* **2011**, *21*, 15486–15493.
- (29) Suratwala, T. I.; Hanna, M. L.; Miller, E. L.; Whitman, P. K.; Thomas, I. M.; Ehrmann, P. R.; Maxwell, R. S.; Burnham, A. K. Surface Chemistry and Trimethylsilyl Functionalization of Stöber Silica Sols. *J. Non. Cryst. Solids* **2003**, *316*, 349–363.
- (30) Gun'ko, V.; Vedamuthu, M.; Henderson, G.; Blitz, J. Mechanism and Kinetics of Hexamethyldisilazane Reaction with a Fumed Silica Surface. *J. Colloid Interface Sci.* **2000**, *228*, 157–170.
- (31) Lee, C. H.; Park, S. H.; Chung, W.; Kim, J. Y.; Kim, S. H. Preparation and Characterization of Surface Modified Silica Nanoparticles with Organo-Silane Compounds. *Colloids Surfaces A Physicochem. Eng. Asp.* **2011**, *384*, 318–322.
- (32) Kaas, R. L.; Kardos, J. L. The Interaction of Alkoxy Silane Coupling Agents with Silica Surfaces. *Polym. Eng. Sci.* **1971**, *11*, 11–18.
- (33) Huang, Z. F.; Qu, X. Y.; Chen, Z. Nano-SiO₂/PMMA-PU Composite Particles with Core-Shell Structure via Emulsion Polymerization and Their Application in Epoxy Resin. *J. Appl. Polym. Sci.* **2015**, *132*, n/a – n/a.

5. Surface Hydrophobization of AgNPs through SI-ATRP

- (34) Matyjaszewski, K.; Xia, J. Atom Transfer Radical Polymerization. *Chem. Rev.* **2001**, *101*, 2921–2990.
- (35) Hui, C. M.; Pietrasik, J.; Schmitt, M.; Mahoney, C.; Choi, J.; Bockstaller, M. R.; Matyjaszewski, K. Surface-Initiated Polymerization as an Enabling Tool for Multifunctional (Nano-)Engineered Hybrid Materials. *Chem. Mater.* **2014**, *26*, 745–762.
- (36) Mora-Barrantes, I.; Valentín, J. Poly (styrene)/silica Hybrid Nanoparticles Prepared via ATRP as High-Quality Fillers in Elastomeric Composites. *J. Mater. Chem.* **2012**, *22*, 1403–1410.
- (37) Von Werne, T.; Patten, T. E. Atom Transfer Radical Polymerization from Nanoparticles: A Tool for the Preparation of Well-Defined Hybrid Nanostructures and for Understanding the Chemistry of Controlled/“living” Radical Polymerizations from Surfaces. *J. Am. Chem. Soc.* **2001**, *123*, 7497–7505.
- (38) Patten, T. E.; Matyjaszewski, K. Atom Transfer Radical Polymerization and the Synthesis of Polymeric Materials. *Adv. Mater.* **1998**, *10*, 901–915.
- (39) Mandal, T. K.; Fleming, M. S.; Walt, D. R. Preparation of Polymer Coated Gold Nanoparticles by Surface-Confined Living Radical Polymerization at Ambient Temperature. *Nano Lett.* **2002**, *2*, 3–7.
- (40) Dong, H.; Zhu, M.; Yoon, J. A.; Gao, H.; Jin, R.; Matyjaszewski, K. One-Pot Synthesis of Robust Core/shell Gold Nanoparticles. *J. Am. Chem. Soc.* **2008**, *130*, 12852–12853.
- (41) Nuss, S.; Böttcher, H. Gold Nanoparticles with Covalently Attached Polymer Chains. *Angew. Chemie (International ed. English)* **2001**, *40*, 4016–4018.
- (42) Li, D.; Jang, Y. J.; Lee, J. J.-E.; Kochuveedu, S. T.; Kim, D. H. Grafting poly(4-Vinylpyridine) onto Gold Nanorods toward Functional Plasmonic Core-shell Nanostructures. *J. Mater. Chem.* **2011**, *21*, 16453–16460.
- (43) Chakraborty, S.; Bishnoi, S. W.; Pe, H. Gold Nanoparticles with Poly (N-Isopropylacrylamide) Formed via Surface Initiated Atom Transfer Free Radical Polymerization Exhibit Unusually Slow Aggregation Kinetics. *J. Phys. Chem. C* **2010**, *114*, 5947–5955.
- (44) Ohno, K.; Koh, K.; Tsujii, Y.; Fukuda, T. Synthesis of Gold Nanoparticles Coated with Well-Defined, High-Density Polymer Brushes by Surface-Initiated Living Radical Polymerization. *Macromolecules* **2002**, *35*, 8989–8993.

5. Surface Hydrophobization of AgNPs through SI-ATRP

- (45) Zhang, J.; Jiang, L.; Pan, K.; Yi, Z.; Dan, Y. Controlled Polymerization of Methylmethacrylate from Fumed SiO₂ Nanoparticles through Atom Transfer Radical Polymerization. *Polym. Int.* **2014**, *63*, 413–419.
- (46) Sun, Y.; Ding, X.; Zheng, Z.; Cheng, X.; Hu, X.; Peng, Y. Surface Initiated ATRP in the Synthesis of Iron Oxide/polystyrene Core/shell Nanoparticles. *Eur. Polym. J.* **2007**, *43*, 762–772.
- (47) Luo, Y.-R. *Comprehensive Handbook of Chemical Bond Energies*; CRC Press: Boca Raton, FL, USA 2007.
- (48) Matsui, J.; Parvin, S.; Sato, E.; Miyashita, T. Preparation of Organic–ceramic–metal Multihybrid Particles and Their Organized Assembly. *Polym. J.* **2010**, *42*, 142–147.
- (49) Li, G. L.; Xu, L. Q.; Neoh, K. G.; Kang, E. T. Hairy Hybrid Microrattles of Metal Nanocore with Functional Polymer Shell and Brushes. *Macromolecules* **2011**, *44*, 2365–2370.
- (50) Ohno, K.; Akashi, T.; Huang, Y.; Tsujii, Y. Surface-Initiated Living Radical Polymerization from Narrowly Size-Distributed Silica Nanoparticles of Diameters Less Than 100 Nm. *Macromolecules* **2010**, *43*, 8805–8812.
- (51) Husseman, M.; Malmström, E. Controlled Synthesis of Polymer Brushes by “living” Free Radical Polymerization Techniques. *Macromolecules* **1999**, *32*, 1424–1431.
- (52) Carrot, G.; Diamanti, S.; Manuszak, M.; Charleux, B.; Vairon, J. P. Atom Transfer Radical Polymerization of N-Butyl Acrylate from Silica Nanoparticles. *J. Polym. Sci. Part A Polym. Chem.* **2001**, *39*, 4294–4301.
- (53) Matsuura, K.; Ohno, K.; Kagaya, S.; Kitano, H. Carboxybetaine Polymer-Protected Gold Nanoparticles: High Dispersion Stability and Resistance against Non-Specific Adsorption of Proteins. *Macromol. Chem. Phys.* **2007**, *208*, 862–873.
- (54) Fernandes, N. J.; Akbarzadeh, J.; Peterlik, H.; Giannelis, E. P. Terms of Use Synthesis and Properties of Highly Dispersed Ionic Silica À Poly (Ethylene Oxide) Nanohybrids. *ACS Nano* **2013**, *7*, 1265–1271.
- (55) Naik, V. V; Crobu, M.; Venkataraman, N. V; Spencer, N. D. Multiple Transmission-Reflection IR Spectroscopy Shows That Surface Hydroxyls Play Only a Minor Role in Alkylsilane Monolayer Formation. *J. Phys. Chem. Lett.* **2013**, *4*, 2745–2751.
- (56) Sun, Y.; Mayers, B.; Herricks, T.; Xia, Y. Polyol Synthesis of Uniform Silver Nanowires: A Plausible Growth Mechanism and the Supporting Evidence. *Nano Lett.* **2003**, *3*, 955–960.

5. Surface Hydrophobization of AgNPs through SI-ATRP

- (57) Louis Chakkalakal, G.; Alexandre, M.; Abetz, C.; Boschetti-de-Fierro, A.; Abetz, V. Surface-Initiated Controlled Radical Polymerization from Silica Nanoparticles with High Initiator Density. *Macromol. Chem. Phys.* **2012**, *213*, 513–528.
- (58) Edmondson, S.; Huck, W. T. S. Controlled Growth and Subsequent Chemical Modification of Poly(glycidyl Methacrylate) Brushes on Silicon Wafers. *J. Mater. Chem.* **2004**, *14*, 730–734.
- (59) Chatterjee, U.; Jewrajka, S. K.; Mandal, B. M. The Beneficial Effect of Small Amount of Water in the Ambient Temperature Atom Transfer Radical Homo and Block Co-Polymerization of Methacrylates. *Polymer (Guildf)*. **2005**, *46*, 1575–1582.
- (60) Su, K. H.; Wei, Q. H.; Zhang, X.; Mock, J. J.; Smith, D. R.; Schultz, S. Interparticle Coupling Effects on Plasmon Resonances of Nanogold Particles. *Nano Lett.* **2003**, *3*, 1087–1090.
- (61) Ohno, K.; Morinaga, T.; Koh, K.; Tsujii, Y.; Fukuda, T. Synthesis of Monodisperse Silica Particles Coated with Well-Defined, High-Density Polymer Brushes by Surface-Initiated Atom Transfer Radical Polymerization. *Macromolecules* **2005**, *38*, 2137–2142.
- (62) Kashiwagi, T.; Inaba, A.; Brown, J. E.; Hatada, K.; Kitayama, T.; Masuda, E. Effects of Weak Linkages on the Thermal and Oxidative Degradation of Poly(methyl Methacrylates). *Macromolecules* **1986**, *19*, 2160–2168.
- (63) Inaba, A.; Kashiwagi, T.; Brown, J. E. Effects of Initial Molecular Weight on Thermal Degradation of Poly(methyl Methacrylate): Part 1—Model 1. *Polym. Degrad. Stab.* **1988**, *21*, 1–20.
- (64) Kashiwagi, T.; Inabi, A. Behavior of Primary Radicals during Thermal Degradation of Poly (Methyl Methacrylate. *Polym. Degrad. Stab.* **1989**, *26*, 161–184.
- (65) Manring, L. E. Thermal Degradation of Poly(methyl Methacrylate). 4. Random Side-Group Scission. *Macromolecules* **1991**, *24*, 3304–3309.
- (66) Rajesh, S.; Sonoda, K.; Uusimäki, A.; Yang, K. H.; Lu, H. Y.; Jantunen, H. Effective Dielectric Response of Polymer Composites with Ceramic Coated Silver Flakes. *J. Mater. Sci. Mater. Electron.* **2012**, *24*, 191–195.

6. Conclusions

The polyol synthesis enabled the preparation of AgNPs in large quantities which was essential for the preparation of nanocomposites with PDMS. Although the preparation of AgNPs in gram scale could be achieved with traditional batch reactions, the SFTR provided the possibility of preparing large amounts of the AgNPs with an enhanced control over the particle size and distribution at a production rate of around 2 g/h at a conversion of almost 100 %. The tests with the SFTR showed that it was possible to prepare AgNPs with sizes ranging from 7-104 nm by tuning the reaction parameters. The synthesis of AgNPs with the SFTR, which was applied and accomplished in the course of this project, will replace the conventional batch synthesis of AgNPs in the future stages of this work. The encapsulation of the AgNPs with a SiO₂ shell was possible by performing a modified Stöber method at silver concentrations of ~ 50 mM. The dielectric properties of the Ag@SiO₂ core-shell particles depended heavily on the thickness of the insulating shell. While a SiO₂ shell thickness of ~ 3 nm (Ag core ~ 38 nm) was too thin to prevent the AgNPs from forming a percolation pathway, the growth of the SiO₂ shell to 20 nm led to dielectric properties similar to pure SiO₂ ($\epsilon' \sim 3.9$). Between those two thickness values, the permittivity of the core-shell particles increased with decreasing SiO₂ shell thickness and reached a maximum permittivity $\epsilon' \sim 41$. Therefore, a very thin SiO₂ is essential to obtain a maximum enhancement in the resulting permittivity of the core-shell particles although the insulation should still be ensured. Therefore, the SiO₂ shell was kept at 4 nm for the other projects of this work.

The preparation of Ag@SiO₂ core-shell particles allowed further surface functionalization due to the presence of the hydroxyl-groups on the particle surface. Since the particles will be dispersed into hydrophobic PDMS, the core-shell particles were rendered hydrophobic through the grafting of alkyl silanes or by growing polymers on the surface through the SI-ATRP. The hydrophobicity of the functionalized core-shell particles was observed through their enhanced dispersion in non-polar solvents. The surface treatment is also essential in

6. Conclusions

order to reduce the possibility of water adsorption on the surface which can influence the dielectric measurements.

The resulting set of nanocomposites of the functionalized Ag@SiO₂ core-shell particles with PDMS ($M_w \sim 139'000$ g/mol) denoted as series A in Chapter 4 featured enhanced dielectric properties with increasing filler content, with a maximum of permittivity of 7.8 at 18 vol% Ag. However, an increase in the Young's modulus Y as well as a decrease in the strain-at-break values were observed with the increase in the Ag content in the nanocomposites, and therefore further modifications were applied by (i) using an ultrasonicator tip for the dispersion of the filler and (ii) by using PDMS with a higher molecular weight ($M_w \sim 692'000$ g/mol). The nanocomposites with the high molecular weight PDMS featured high elasticity, but the permittivities exhibited by this new series of nanocomposites (series B) were lower than the nanocomposites of the series A at Ag contents exceeding 15 vol%. This can be explained by the better dispersion of the particles in series B which leads to larger interparticle distances, while the nanocomposites of series A feature the presence of large agglomerates (tens of microns) which give larger permittivities as a result of the closer proximity of the particles to each other. This effect is particularly pronounced with increasing filler contents as the nanocomposite A₁₈ (18 vol% Ag) has a larger permittivity than the nanocomposite B₂₀ (20 vol% Ag). However, the nanocomposites of series B featured lower values for $\tan \delta$ as well as higher breakdown strengths E_B in comparison to the nanocomposites of series A. The sample B₂₀ was subjected to actuator tests, but did not reveal any strain in thickness direction which can be attributed to the relatively high Young's modulus Y of the nanocomposites compared to conventional actuator membranes. In summary, functionalized Ag@SiO₂ core-shell particles have been used as high permittivity filler in nanocomposites. The nanocomposites show a modest increase in permittivity, but rather low $\tan \delta$ values and low electric conductivities attributed to both the PDMS matrix and the effective insulation of the AgNPs. The surrounding SiO₂ serves both as an insulating material that prevents the Ag particles from percolating and as an effective interface to enhance the compatibility of the Ag with the PDMS matrix upon undergoing surface treatment.

7. Outlook

Despite the remarkable elastic properties observed for the nanocomposites, there is still room for further improvement. The permittivities of the nanocomposites are still relatively low despite the high filler content. A potential increase in the permittivity can be expected from the use of anisotropic structures, for example silver nanowires (AgNWs) or silver nanorods (AgNRs). Preliminary experiments using AgNWs coated with thin SiO₂ shells as filler were performed by a co-worker, and the nanocomposites featured slightly higher permittivities compared to the values observed for the nanocomposites using the AgNPs at the corresponding volume fraction of Ag. However, a further increase in the content of AgNWs led to the formation of conductive pathways, and the resulting nanocomposites exhibited electrical conductivity. Perhaps, the use of AgNRs can lead to higher enhancements in the composite permittivity in comparison to the use of AgNPs, but the preparation of this particular nanostructure still remains a challenge. Further increase in the permittivity can be achieved by replacing the silica insulator shell with a material that has a higher permittivity (e.g. TiO₂). The high strains that were achieved with the nanocomposites using functionalized AgNPs emphasizes their potential for energy harvesting, but the low breakdown strength is still a limiting factor for their potential application. The optimization of this parameter is essential and would enhance their ability to store energy thus eventually paving the way for their effective use as a novel dielectric elastomer generator (DEG).

7. Outlook

8. Appendix

A1. Preparation of Silver Nanoparticles by Inverse Miniemulsions (Water-in-Oil System)

An alternative route for the preparation of AgNPs is the synthesis via inverse miniemulsions. In this scenario, water droplets are dispersed in an oil phase.^{1,2} The resulting particles would be hydrophobic in nature and could be readily dispersed in hydrophobic media. The variation of the water/surfactant molar ratio (ω), which is the critical parameter in this system, can lead to the variation of the average particle size due to the control of the size of the water droplets where the particles are effectively formed.³ In general terms, this synthesis method yields AgNPs with a narrow size distribution. In this study, ω , the reactant concentrations, and the type of continuous phase was varied and the formed particles were characterized. The hydrophobic phase consisted of hexadecane (Entries 1-6, Tab. 16) or octamethylcyclotetrasiloxane (D₄, Entries 7-8, Tab. 16), Span 85 (Fig. 83) was used as a surfactant, while formaldehyde (CH₂O, 37 wt%) was the reducing agent in this reaction.

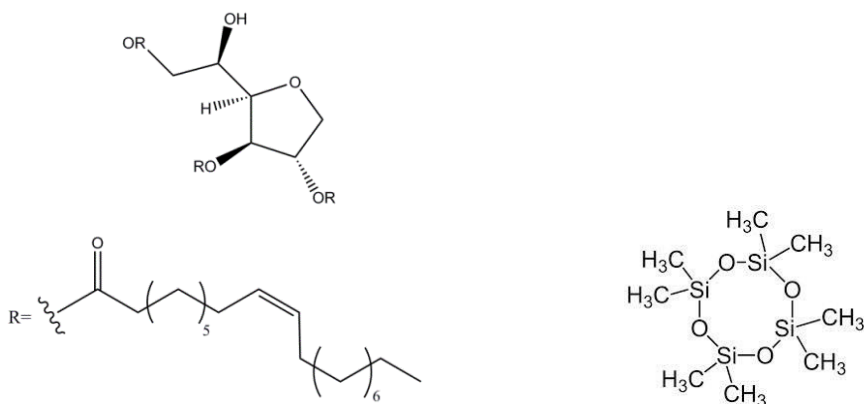


Fig. 83: Structure of Span 85 (left) and D₄ (right).

8. Appendix

Briefly, the surfactant was dissolved in the organic phase and the aqueous AgNO_3 and formaldehyde solutions were added consecutively followed by the treatment of the resulting mixture with the tip sonicator (Sonics VCX-500 Model CV33) for around 10 min. The mixture was stirred overnight at 25 °C in order to observe an increase in the intensity of the color of the mixture as a result of the surface plasmons which are indicative for the formation of AgNPs. TEM, DLS and UV-vis spectra (Fig. 84, Fig. 85, Fig. 86 and Fig. 87) show that the formed particles are quite small in size and do not vary significantly with the variation of reaction parameters (Tab. 16). An interesting feature observed with this preparation method is the periodic arrangement of the AgNPs with constant interparticle distance as a result of the steric stabilization offered by the surfactant. When the amount of Span 85 was decreased, the control over the interparticle distance deteriorated and the periodic arrangement of the nanoparticles is perturbed as a result of the increase in the particle size distribution. However, no clear trend in the average particle size was established through the variation of the reactand concentration while keeping the AgNO_3 /Span 85 mass ratio constant. The decrease AgNO_3 /Span 85 mass ratio led to the slight decrease in the average particle size (Entries 1 and 2 in Tab. 16) as a result of the formation of more stabilized water droplets due to the larger availability of the surfactant in the mixture.³ At the other hand, an increase in ω subsequently led to an increase in the particle size (Entries 4 and 6 in Tab. 16) along with an increase in the particle size distribution. This was also observed in the case where D_4 was used as the continuous phase. The use of D_4 was motivated by the possibility of polymerizing D_4 in order to yield PDMS with the AgNPs blended *in situ*. However, the AgNPs were not stable at elevated temperatures and agglomerated at the polymerization temperature of 110 °C. A further decrease in the surfactant concentration led to the destabilization of the miniemulsions system followed by the phase separation. Overall, due to the limited particle sizes feasible, the low reaction yield (< 5-10 %) as well as the difficulty of isolating the particles from hexadecane or D_4 , this preparation method was found unsuitable for the preparation of AgNPs for our purposes, and therefore no further optimization of this reaction was pursued. Eventually, the focus shifted to the polyol synthesis of the silver nanostructures due to the advantages associated with this reaction as mentioned in Chapter 1.

8. Appendix

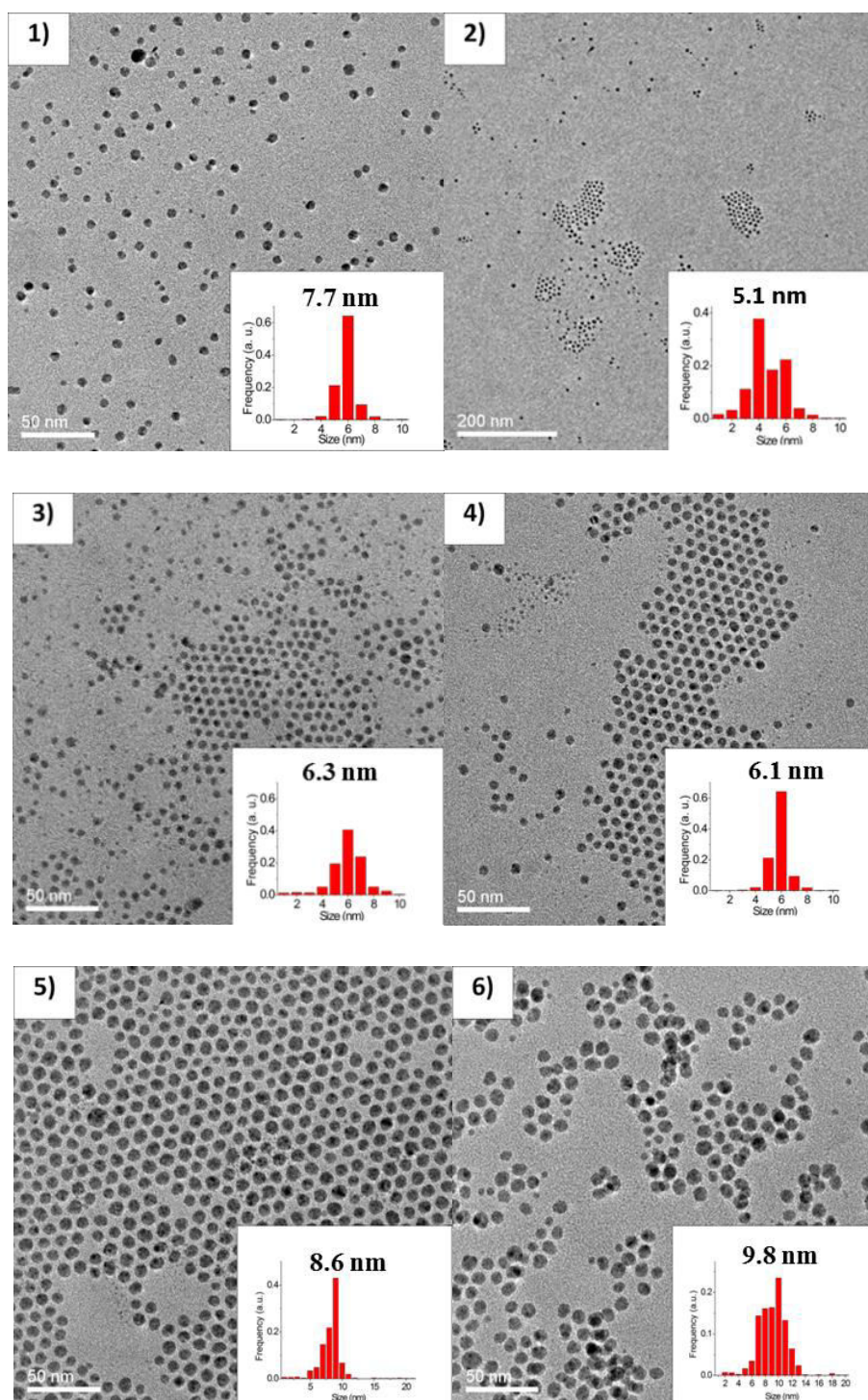


Fig. 84: TEM Micrographs of the samples 1-6 and the particle size distribution inserted in the images.

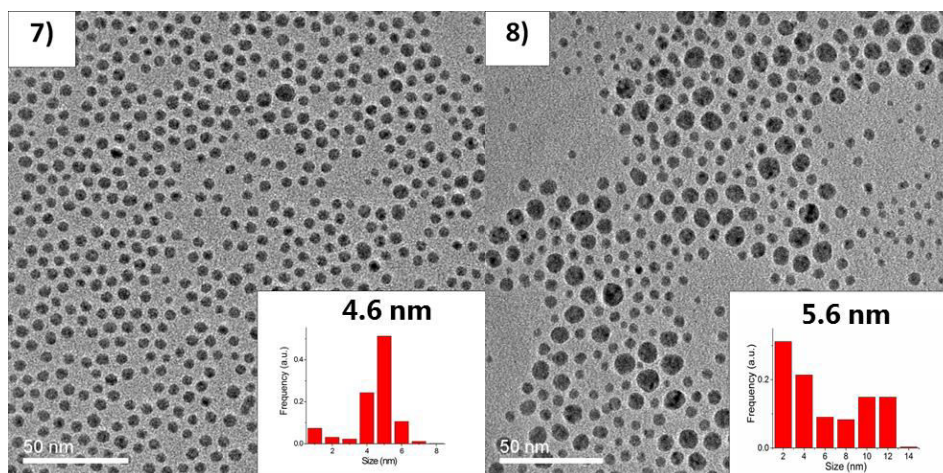


Fig. 85: TEM Micrographs of the samples 7 and 8 and the particle size distribution inserted in the images.

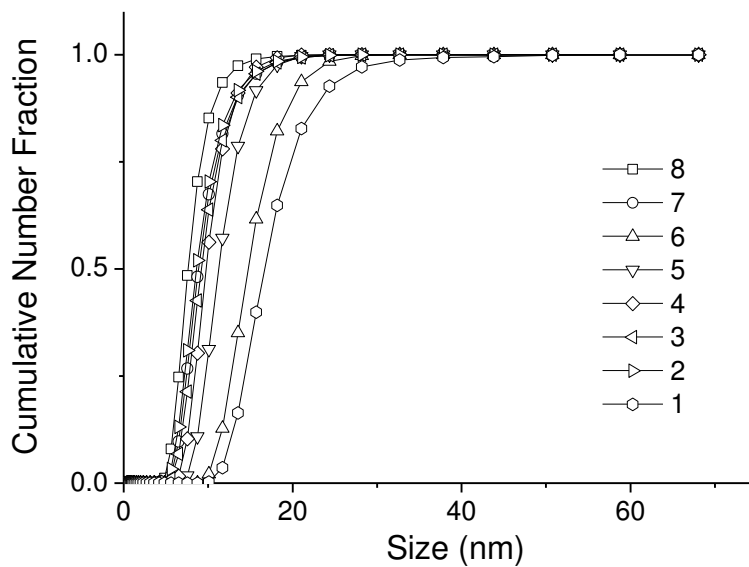


Fig. 86: DLS spectra of AgNPs (Tab. 16, samples 1-8) which were prepared by reverse miniemulsions measured in toluene.

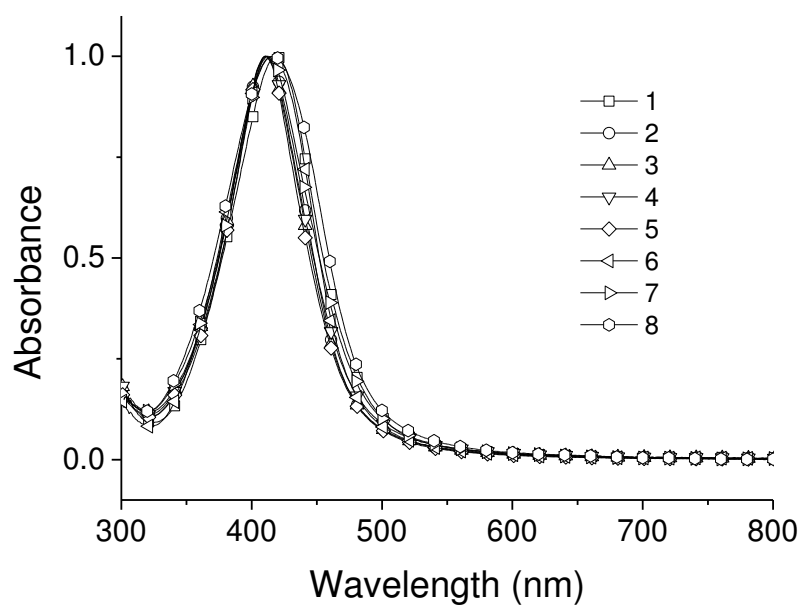


Fig. 87: UV-vis spectra of AgNPs (Tab. 16, samples 1-8) which were prepared by the inverse miniemulsions technique measured in hexadecane.

Tab. 16: List of experiments conducted for the preparation of AgNPs via inverse miniemulsions.^a

No.	m (AgNO ₃)/g	m (Span85)/g	ω	λ_{\max} (nm)	Size (TEM, nm)	Size ^b (DLS, nm)
1	0.1	0.1	1000	419	7.7(3.4)	17(4.8)
2	0.1	0.2	500	411	5.1(1.4)	8.5(2.5)
3	0.1	0.4	250	410	6.3(1.4)	9.0(2.4)
4	0.3	0.3	333	412	6.1(0.8)	9.6(2.1)
5	0.6	0.6	167	410	8.6(2.0)	11(2.4)
6	0.3	0.03	3330	416	9.8(2.5)	15(3.0)
7	0.3	0.3	333	412	4.6(1.4)	8.8 (2.5)
8	0.3	0.1	1000	417	5.6(3.1)	7.5 (2.0)

^a The reaction conditions were: hexadecane (6 mL), formaldehyde (37 wt%, 2 mL) and water (0.5 mL) (Entries 1-6); D₄ (6 mL), formaldehyde (37 %, 2 mL) and water (0.5 mL) (Entries 7-8). ^b Mean numerical diameter (standard deviation in parenthesis);

ω = H₂O/Span 85 molar ratio.

A2. The Preparation of Ag/PDMS Nanocomposites with Varying Particle Size and their Resulting Dielectric Properties

The effect of the particle size on the resulting composite permittivity has also been investigated in this work. For this purpose, different sets of AgNPs with average particle diameters ranging from 25 to 76 nm were prepared (Fig. 88) and subjected to the surface functionalization with SiO_2 and HMDS as illustrated in Chapters 3 and 4. As the designated preparation method, the polyol synthesis was used in order to prepare the AgNPs intended to be used as high permittivity filler. While the AgNPs stabilized by PVP10 ($M_w \sim 10'000$ g/mol) were prepared in a continuous fashion with the SFTR, the AgNPs with the average diameter of 76 nm stabilized by PVP40 ($M_w \sim 40'000$ g/mol) were prepared by performing multiple batch reactions. The reason for the deviation of the preparation method is the high viscosity of the mixture of PVP40 in EG which prevented a smooth introduction of the stabilizer into the SFTR (not the same as in Chapter 2). However, the particle sizes feasible with the SFTR through the use of PVP10 as stabilizer were limited to below 50 nm (even at a reaction temperature of 160 °C). Therefore, the polyol synthesis involving the use of PVP40 was conducted in traditional batch reactions in order to obtain AgNPs larger than 50 nm (similar reaction conditions as in Chapter 4, reaction temperature was 150 °C) while the particles below 50 nm were prepared with the SFTR at a reactor temperature 140, 150 and 160 °C, respectively. The reaction conditions are similar to those reported in Chapter 2, although another SFTR was used for this series of experiments which explains the deviation in the obtained particle sizes compared to the ones reported in Chapter 2. The AgNPs were characterized by DLS, TEM and UV-vis spectroscopy and the measurements show a clear trend with the varying particle size (Fig. 88, Fig. 89 and Fig. 90). The purified AgNPs were then subjected to the modified Stöber method in order to insulate them with a thin SiO_2 shell (~ 4 nm, Fig. 91).⁴ However, the UV-vis spectra show the presence of shoulders at larger wavelengths for the particles with sizes below 50 nm. These could indicate the presence of either agglomerates or the

8. Appendix

presence of particles which deviate from the spherical shape. The latter effect is more pronounced for particles with small diameters, but disappears for larger particles as a result of the larger particle size distribution.⁵ The agglomerates could have been formed through the high reaction temperatures as a result of the low steric repulsions offered by the PVP10 compared to PVP40 where the longer polymer chains can perhaps offer a better steric stabilization of the particles towards agglomeration. The preparation of the particles with the SFTR was conducted for a couple of hours in order to generate sufficient particles, and initially the reaction mixture was collected in a vessel cooled in an ice bath. Possibly, the ice water was insufficient for the quenching/cooling of the incoming reaction mixture and therefore, there might have been some agglomeration ongoing in the vessel where the products are both collected and cooled simultaneously. Further modifications of this set-up are still ongoing and will be on the future agenda which will consist of the continuous cooling of the collecting vessel with a cooling medium. The silica-coating was performed with a modified Stöber method and led to the successful coating of the AgNPs with a SiO₂ shell thickness of ~ 4 nm. However, the surface passivation with SiO₂ also led to the formation of multiple silver cores within a SiO₂ carpet. This effect is present in the silica-coating of AgNPs with a diameter of 25 nm and manifests itself in the appearance of a broad shoulder at larger wavelengths as well as the large particle size obtained from the DLS measurement (Fig. 92 and Fig. 93). It has been claimed elsewhere that particles below 50 nm are unstable during the Stöber process and are thus susceptible to undergo agglomeration.⁶

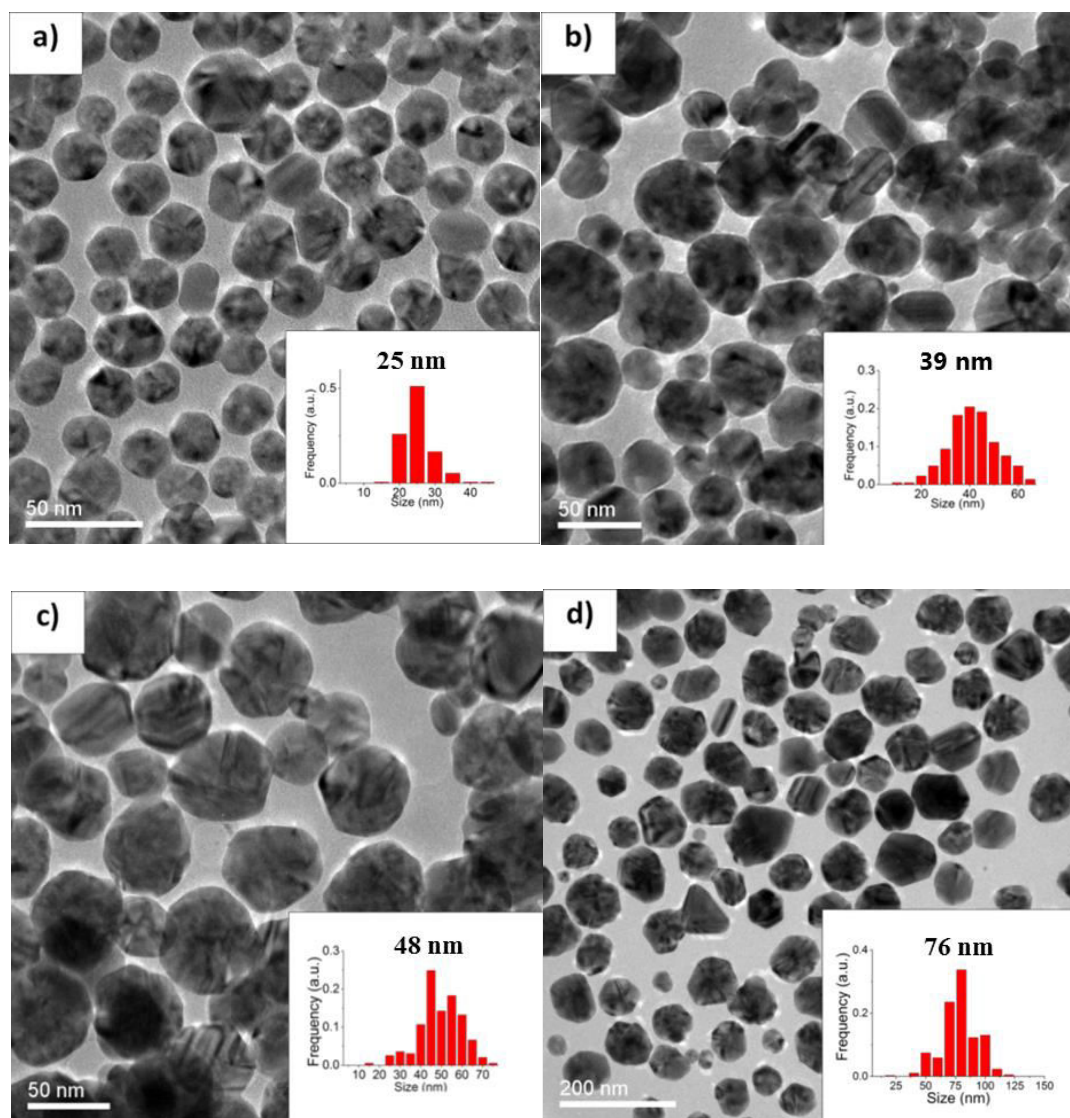


Fig. 88a-d: TEM micrographs and size distribution (inserted) of the different AgNPs.

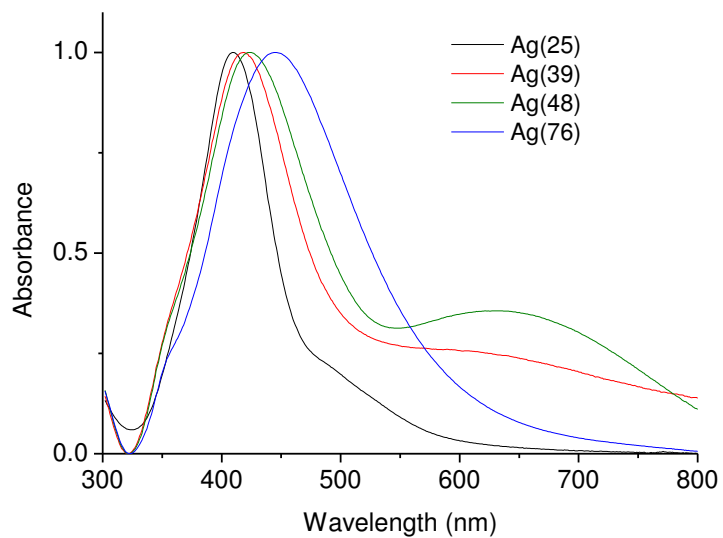


Fig. 89: UV-vis spectra of AgNPs of different sizes recorded in EtOH.

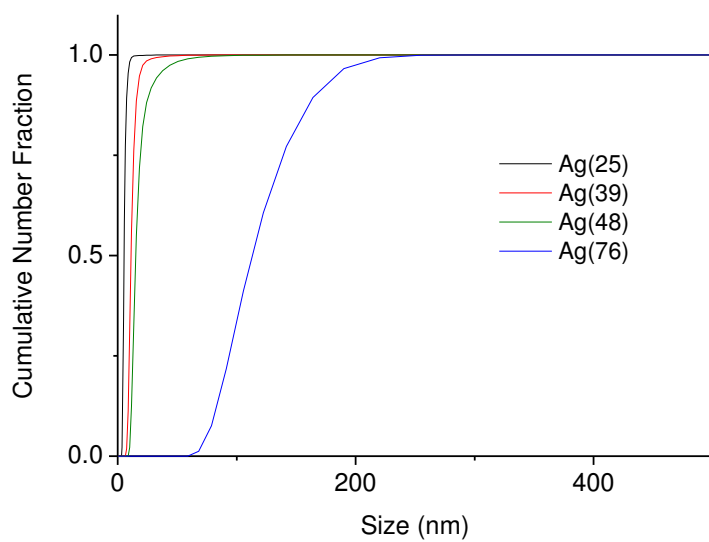


Fig. 90: DLS spectra of AgNPs of different sizes recorded in EtOH.

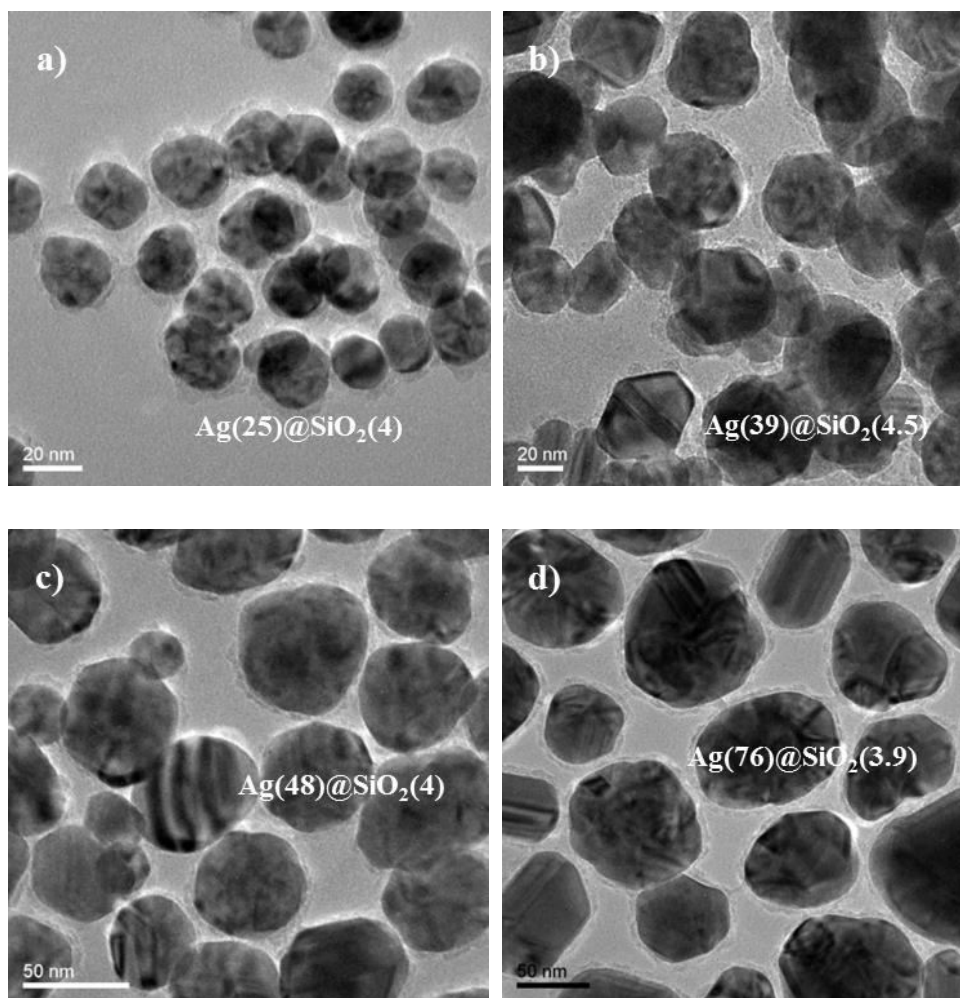


Fig. 91a-d: TEM micrographs of the different Ag@SiO₂ core-shell particles. The diameter of the AgNPs as well as the thickness of the SiO₂ shell is mentioned in parenthesis.

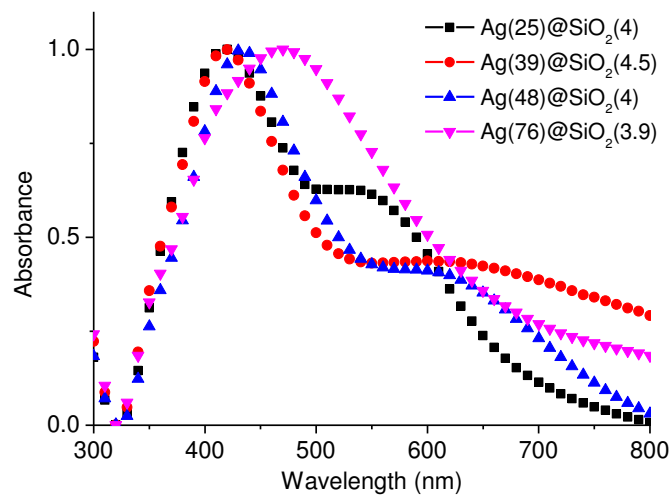


Fig. 92: UV-vis spectra of Ag@SiO₂ core-shell particles (~ 4 nm thick SiO₂ shell) of different core sizes recorded in EtOH.

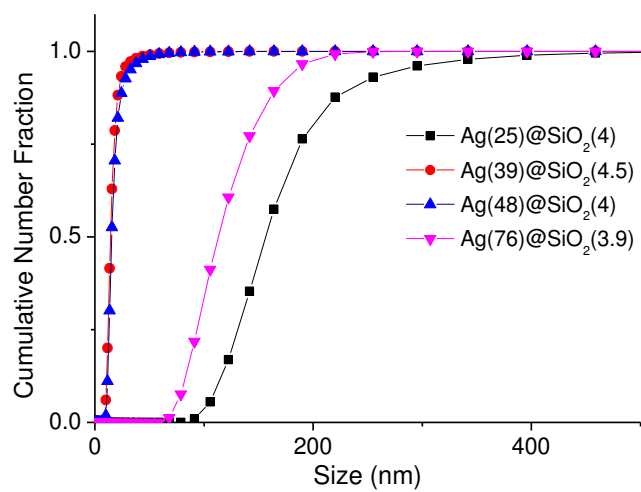


Fig. 93: DLS spectra of Ag@SiO₂ core-shell particles (~ 4 nm thick SiO₂ shell) of different core sizes recorded in EtOH.

Tab. 17: Summary of the size parameters of the different AgNPs and Ag@SiO₂ core-shell particles.

No.	Size AgNPs (TEM, nm)	Thickness SiO ₂ shell (nm)	λ_{max} (AgNPs) (nm)	λ_{max} (Ag@SiO ₂) (nm)	^a Size AgNPs (DLS, nm)	^a Size Ag@SiO ₂ (DLS, nm)
S1	76(15)	3.9 (0.8)	445	470	100 (31)	108(32)
S2	48(10)	4.0 (0.7)	423	433	16 (6)	16(7)
S3	39(10)	4.5 (1.2)	418	420	11 (4)	13(4)
S4	25(5)	4.0 (0.6)	410	420	4.9(1.4)	175(51)

^a Mean numerical diameter. The standard deviation is shown in parenthesis.

8. Appendix

After the surface hydrophobization of the Ag@SiO₂ core-shell particles through the reaction with HMDS, the core-shell particles were used as filler for the preparation of nanocomposites with high molecular weight PDMS. The nanocomposites were prepared and characterized according to the procedure reported in Chapter 4. The essential components for the preparation of the nanocomposites using functionalized Ag@SiO₂ core-shell particles are listed in Tab. 18.

Tab. 18: Composition of the nanocomposites using functionalized Ag@SiO₂@Si(CH₃)₃ core-shell particles as high permittivity filler. The particles used for the composites were: S1 (C-series), S2 (D-series), S3 (E-series) and S4 (F-series).

No.	Ag content (vol%)	$m(\text{PDMS})/\text{g}^{\text{a}}$	$V(\text{CL})/\mu\text{L}^{\text{b}}$	$V(\text{cat})/\mu\text{L}^{\text{c}}$
C1	27	0.15	16	4
C2	23	0.15	16	4
C3	7.2	0.15	16	4
C4	3.1	0.15	16	4
D1 ^d	19	0.15	16	4
D2	11	0.15	16	4
D3	10	0.15	16	4
E1 ^d	21	0.15	16	4
E2	15	0.15	16	4
F ^d	15	0.15	16	4

^a $M_{\text{w}} \sim 692\,000$ g/mol; ^b (25-35 % methylhydrosiloxane)-dimethylsiloxane-copolymer

^c 50 wt% dibutyltin dilaurate in toluene; ^d Cross-linking was inhibited.

8. Appendix

The dielectric properties of the nanocomposites are featured in Tab. 19, Fig. 94 and Fig. 95. It has to be mentioned that the nanocomposites were measured in the absence of sputtered Au electrodes, which therefore may have led to relatively low permittivity values due to the presence of air voids which affect the measurements. However, the results of the measurements can still give information on the potential effects of the Ag core dimensions on the dielectric properties of the resulting nanocomposites. The rise in the permittivity with increasing filler content is observed for all fillers used in this work. However, the size of the AgNPs has a profound effect on the feasible composite permittivity (Fig. 94). It becomes evident that the decrease in the size of the AgNPs leads to larger permittivities compared to the nanocomposites using filler with large AgNPs at the same corresponding Ag content. A similar observation has been reported for BaTiO₃/PVDF composites where the permittivity decreased with increasing particle diameter. A plausible explanation for this observation could be the facilitated dipole orientation for smaller BaTiO₃ as well as the great deal of phase interphases between the matrix and the small BaTiO₃ particles i.e. a larger interfacial volume to which the amount of polarization is proportional to.⁷ This eventually leads to a large contribution in the resulting permittivity from the interfacial polarization, and thus to higher composite permittivities. However, this effect is more pronounced at low frequencies (0-100 Hz) and the size effect fades away with increasing frequency.⁸ Another report states that the surface to volume ratio of the particles increases with decreasing particle size at unaltered volume fraction of particles in the composite system. This leads to higher multipole interactions between the neighboring particles and causes polarization enhancement.⁹

The drawback of using small AgNPs (< 50 nm) is the inhibition of the cross-linking reaction at Ag contents ≥ 15 vol%. It is possible that the mobility of the polymer chains or the cross-linker is reduced by the presence of large amounts of core-shell particles, and this inhibition of the cross-linking reaction is more pronounced for smaller particles due to their ability of optimizing the occupation of a given volume which eventually serves as an obstacle towards the cross-linking in the nanocomposite. For a given vol% of Ag, there are quantitatively more particles in the nanocomposite when using smaller particles compared

8. Appendix

to the scenario where larger particles are used. The heating of these nanocomposites in an oven was an alternative method to obtain cross-linking. However, this treatment did not lead to the formation of cross-linked elastomers. The addition of further cross-linker or catalyst could perhaps lead to a cross-linking of the films, but this step is associated with an increase in the cross-linker density or a subsequent decrease in the flexibility of the materials as well as the increase in the tin content, respectively. The effect of the latter has yet been investigated. The mentioned changes would render it difficult to compare the mechanical properties of the elastomers with each other. Therefore it was essential to remain consistent with the procedure of preparing the nanocomposites. In direct contrast, the inhibited cross-linking at high filler content does not occur in the nanocomposites using AgNPs with a core size of 76 nm, and even the nanocomposites with Ag contents exceeding 20 vol% still exhibit elastomeric properties, although the mechanical properties deteriorate as a result of the increase in the Young's modulus Y (Tab. 19). Presently, the Y values of the nanocomposites depicted in this Chapter are already 2-10 times higher than the Y of the pure PDMS elastomer prepared with the same reaction conditions (Chapter 4, sample B₀), and the potential application of such nanocomposites as membrane materials for DEAs requires low values for Y in order to achieve high actuated strains in thickness direction. The values for $\tan \delta$ as well as the composite conductivities remained low for all nanocomposites. Surprisingly, the former decreases with increasing filler. However, $\tan \delta$ is expected to increase with increasing filler content. There is no apparent size dependency of $\tan \delta$ on the particle size as shown in Fig. 95, which is also supported by literature results.^{10,11}

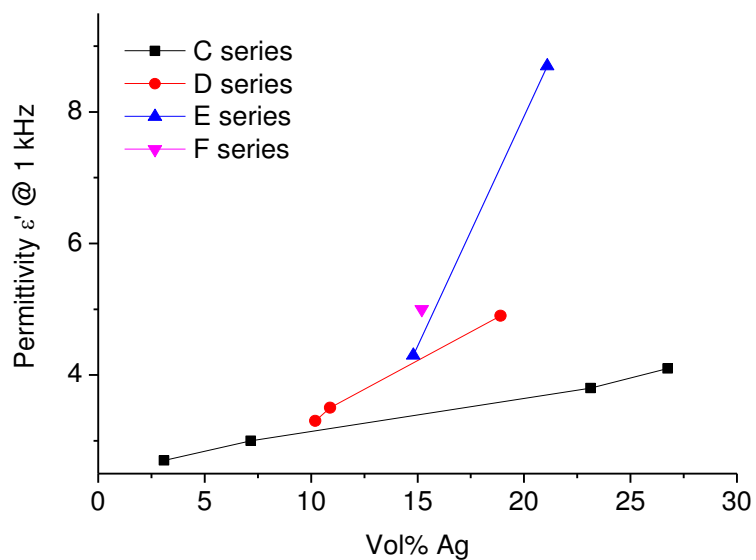


Fig. 94: The permittivity of the Ag@SiO₂/PDMS nanocomposites with varying Ag core and filler content.

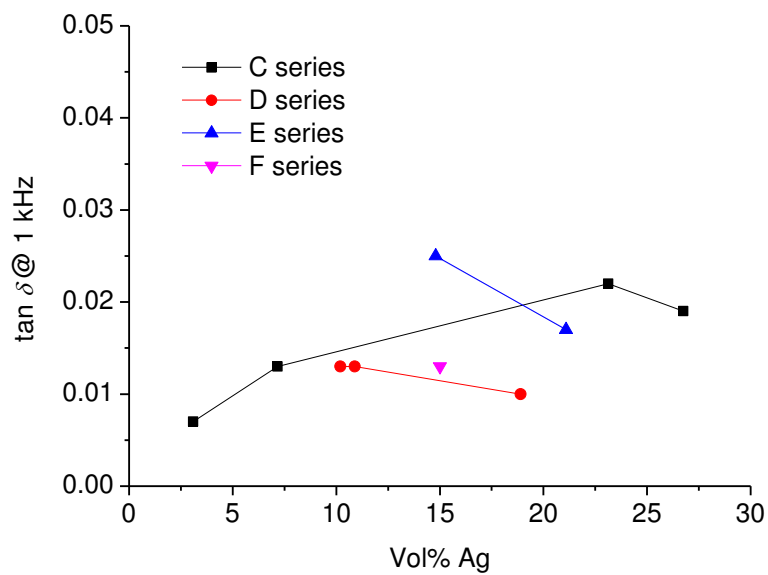


Fig. 95: The tan δ values of the Ag@SiO₂/PDMS nanocomposites with varying Ag core and filler content.

Tab. 19: Summary of the mechanical and dielectric properties (at 1 kHz) of the different nanocomposites using different filler.

No.	Vol% Ag	Young's modulus Y @ 10 % (MPa)	Strain @ break (%)	Permittivity ϵ'	Conductivity σ (S·cm ⁻¹)	tan δ
C1	27	2.1	371	4.1	$4.3 \cdot 10^{-11}$	0.019
C2	23	2.1	422	3.8	$4.7 \cdot 10^{-11}$	0.022
C3	7.2	0.9	585	3	$1.2 \cdot 10^{-11}$	0.013
C4	3.1	0.7	740	2.7	$1.0 \cdot 10^{-11}$	0.007
D1	19	-	-	4.9	$2.7 \cdot 10^{-11}$	0.010
D2	11	0.5	787	3.5	$2.5 \cdot 10^{-11}$	0.013
D3	10	0.7	815	3.3	$2.4 \cdot 10^{-11}$	0.013
E1	21	-	-	8.7	$8.0 \cdot 10^{-11}$	0.017
E2	15	0.7	341	4.3	$5.9 \cdot 10^{-11}$	0.025
F	15	-	-	5	$3.9 \cdot 10^{-11}$	0.013

In conclusion, the permittivity shows a degree of dependency on the size of the Ag core, and the rise in the permittivity is more pronounced with decreasing core diameter. However, the preparation of flexible nanocomposites is limited to Ag contents ≤ 15 vol% (core diameter < 50 nm) as the film formation is inhibited by the introduction of large amounts of particles. Particles with Ag core > 50 nm enable the film formation even at large Ag contents, but the increase in the permittivity is relatively low.

A3. References

- (1) Barnickel, P., Wokaun, A., Sager, W., Eicke, H.-F. Size Tailoring of Silver Colloids by Reduction in W / O Microemulsions. *J. Colloid Interface Sci.* **1992**, *148*, 80–90.
- (2) Capek, I. Preparation of Metal Nanoparticles in Water-in-Oil (w/o) Microemulsions. *Adv. Colloid Interface Sci.* **2004**, *110*, 49–74.
- (3) Solanki, J. N.; Murthy, Z. V. P. Controlled Size Silver Nanoparticles Synthesis with Water-in-Oil Microemulsion Method: A Topical Review. *Ind. Eng. Chem. Res.* **2011**, *50*, 12311–12323.
- (4) Quinsaat, J. E. Q.; Nüesch, F. A.; Hofmann, H.; Opris, D. M. Dielectric Properties of Silver Nanoparticles Coated with Silica Shells of Different Thicknesses. *RSC Adv.* **2013**, *3*, 6964–6971.
- (5) Lance Kelly, K.; Coronado, E.; Zhao, L. L.; Schatz, G. C. The Optical Properties of Metal Nanoparticles: The Influence of Size, Shape, and Dielectric Environment. *J. Phys. Chem. B* **1992**, *107*, 7178–7186.
- (6) Bastakoti, B. P.; Guragain, S.; Yusa, S.; Nakashima, K. Novel Synthesis Route for Ag@SiO₂ Core-shell Nanoparticles via Micelle Template of Double Hydrophilic Block Copolymer. *RSC Adv.* **2012**, *2*, 5938–5940.
- (7) Kochetov, R.; Andritsch, T.; Morshuis, P. H. F.; Smit, J. J. Effect of Filler Size on Complex Permittivity and Thermal Conductivity of Epoxy-Based Composites Filled with BN Particles. *Annu. Rep. - Conf. Electr. Insul. Dielectr. Phenomena, CEIDP* **2010**, 3–6.

8. Appendix

- (8) Dang, Z.-M.; Xu, H.-P.; Wang, H.-Y. Significantly Enhanced Low-Frequency Dielectric Permittivity in the BaTiO₃/poly(vinylidene Fluoride) Nanocomposite. *Appl. Phys. Lett.* **2007**, *90*, 012901.
- (9) Xu, L.; Liu, C.; Cao, Z.; Li, X. Particle Size Influence on Effective Permittivity of Particle-Gas Mixture with Particle Clusters. *Particuology* **2013**, *11*, 216–224.
- (10) Qi, L.; Lee, B. I.; Chen, S.; Samuels, W. D.; Exarhos, G. J. High-Dielectric-Constant Silver-Epoxy Composites as Embedded Dielectrics. *Adv. Mater.* **2005**, *17*, 1777–1781.
- (11) Lu, J.; Moon, K.-S.; Xu, J.; Wong, C. P. Synthesis and Dielectric Properties of Novel High-K Polymer Composites Containing in-Situ Formed Silver Nanoparticles for Embedded Capacitor Applications. *J. Mater. Chem.* **2006**, *16*, 1543–1548.

9. Curriculum Vitae

Personal Information



- Name: Quinsaats
- First Name(s): Jose Enrico Quijano
- Date of Birth: 10th December 1986
- Nationality: Filipino
- Religion: Christian (Roman Catholic)
- Occupation: Chemist/Materials Scientist
- Languages: Filipino (fluent), German (fluent), English (fluent), French (basic knowledge)
- Current Address: Georg-Kempfer-Strasse 27, 8046 Zürich, Switzerland
- Permanent Address: Lot 29, Block 4, Yokohama St. Legacy Homes, BF Las Pinas, Metro Manila, Philippines
- Telephone No.: +41(0)765717056 (Switzerland) and +63(0)9989934935 (PH)
- Email: jose-enrico.quinsaats@empa.ch (work); jozeli86@gmail.com (private)

Academic/Professional Career

- **1991-2002:** Attendance of the German School in Lagos, Nigeria.
- **2002-2005:** Attendance of the boarding school “Schule Schloss Salem” in Salem, Germany. Graduated from High School (“*Abitur*”) in 2005 (Average grade: 1.5).
- **2005-2009:** Bachelor Studies in Chemistry at ETH Zurich, Switzerland (Swiss Federal Institute of Technology).
- **2009-2011:** Master Studies in Chemistry at ETH Zurich, Switzerland (Swiss Federal Institute of Technology).
- **2011-2015:** PhD Studies as a Research Assistant at the Functional Polymers Group at Empa (Swiss Federal Laboratories for Material Science and Technology) in Dübendorf, Switzerland and as member of the Powder Technology Laboratory (LTP) in the Department of Materials Science and Technology (EDMX) at the Swiss Federal Institute of Technology (EPFL) in Lausanne, Switzerland. Thesis Title: “Synthesis and Functionalization of Silver Nanoparticles for the Preparation of High Permittivity Nanocomposites”. Conclusion in August 2015. Thesis is co-supervised by Prof. Dr. H. Hofmann (EPFL) and Dr. D.M. Opris (Empa).

Master Studies

Specialization in the field of Organic Chemistry

- *Core Subjects:* Advanced Physical Chemistry: Statistical Thermodynamics; Advanced Methods and Strategies in Organic Synthesis; Functional Inorganics.
- *Elective Courses:* Organic Synthesis: Methods and Strategies; Reactive Intermediates in Organic Chemistry; Inorganic and Organometallic Polymers; Introduction to Macromolecular Chemistry; Advanced Polymer Chemistry.

Laboratory/Research Experiences

- Research Project under the supervision of Prof. Dr. Ryan Gilmour at ETH Zurich, spring semester 2009 (“Synthesis of Organofluorine Catalysts based on L-Proline and Cinchona Alkaloids”).
- Research Project under the supervision of Prof. Dr. Nicolai Cramer at ETH Zurich, spring semester 2010 (“Synthesis of 1,3-Diketones as Precursors for Grob-type Fragmentation Reactions”).
- Master Thesis under the supervision of Prof. Dr. François Diederich at ETH Zurich, spring semester 2011 (“Novel Synthesis of Inhibitors of Parasitic Cysteine Proteases”).
- PhD Thesis on “Synthesis and Functionalization of Silver Nanoparticles for the Preparation of High Permittivity Nanocomposites” (Conclusion by August 2015).

Teaching Experience

- Teaching Assistant of the lecture “Organic Chemistry I” (held by Prof. Dr. F. Diederich at ETH Zurich during autumn semester 2008). Workload: 4 hours/week.

9. Curriculum Vitae

- Teaching Assistant for the lecture “Organic Chemistry for Pharmacists” (held by Prof. Dr. B. Jaun at ETH Zurich during autumn semester 2010). Workload: 8 hours/week.

Characterization/Analytical Skills

- Trained in characterization of the properties of organic compounds (LC-MS, NMR, IR), nanoparticles and composite materials (UV-vis spectroscopy, Dynamic Light Scattering (DLS), Transmission- and Scanning Electron Microscopy (TEM and SEM), Impedance spectroscopy and mechanical tensile testing).

Computer/IT Skills

- High knowledge in the use of Microsoft Office (Microsoft Word, Microsoft Excel, Microsoft Powerpoint), OriginLab, ChemDraw and Digital Micrograph. Basic knowledge in the use of MNova NMR and TopSpin NMR.

Publications

- Dascalu, M.; Quinsaat, J.E.Q.; Ko, Y.S.; Dünki, S.J.; Nüesch, F.A.; Opris, D.M. Silicone Elastomers Containing Trifluoropropyl Groups: From Synthesis to Application. *Manuscript in preparation* (Submission to *RSC Adv.*)
- Testino, A.; Pilger, F.; Lucchini, M.A.; Quinsaat, J.E.Q.; Stähli, C.; Bowen, P. Continuous Polyol Synthesis of Metal and Metal Oxide Nanoparticles Using the Segmented Flow Tubular Reactor, *Molecules* **2015**, 20(6), 10566.
- Quinsaat, J.E.Q.; Alexandru, M.; Nüesch, F.A.; Hofmann H.; Borgschulte, A.; Opris, D. M. Highly Stretchable Dielectric Elastomer Composites Containing High

- Volume Fraction of Silver Nanoparticles, *J. Mater. Chem. A* **2015**, 3, 14675.
- Opris, D.M.; Quinsaat, J.E.Q.; Dünki, S.; Ko, Y.S.; Alexandru, M.; Racles, C.; Nüesch, F. A. Dielectric Materials, Design and Realization. *Proc. SPIE Electroact. Polym. Actuators Devices (EAPAD)* **2015**, 9430, 9430-9 (Invited Paper).
 - Quinsaat, J.E.Q.; Testino, A.; Pin, S.; Huthwelker, T.; Nüesch, F. A.; Bowen, P.; Hofmann, H.; Ludwig, C.; Opris, D. M. Continuous Production of Tailored Silver Nanoparticles by Polyol Synthesis and Reaction Yield Measured by X-Ray Absorption Spectroscopy: Towards a Growth Mechanism. *J. Phys. Chem. C* **2014**, 118, 11093.
 - Quinsaat, J.E.Q.; Nüesch, F.A.; Hofmann, H.; Opris, D.M. Dielectric Properties of Silver Nanoparticles Coated with Silica Shells of Different Thicknesses. *RSC Adv.* **2013**, 3, 6964.
 - Ehmke, V.; Quinsaat, J.E.Q.; Rivera-Fuentes, P.; Heindl, C.; Freymond, C.; Rottmann, M.; Brun, R.; Schirmeister, T.; Diederich, F. Tuning and Predicting Biological Affinity: Aryl Nitriles as Cysteine Protease Inhibitors. *Org. Biomol. Chem.* **2012**, 10, 5764.

Participations in Conferences/Workshops

2011

- Swiss Chemical Society (SCS) Meeting 2012 in Lausanne (EPFL), Switzerland, on the 9th of September, 2011.

2012

- Swiss Chemical Society (SCS) Meeting 2012 in Zurich (ETH), Switzerland, on the 13th of September, 2013.
- European Scientific Network for Artificial Muscles (ESNAM) Workshop in Neuchâtel, Switzerland, on the 16th-18th of October, 2012.
- OMICS Group, International Conference and Expo on Material Science and Engineering in Chicago, USA, on the 22nd-24th of October, 2012.

2013

- Makromolekulares Kolloquium in Freiburg, Germany, on the 21st-23rd of February, 2013.
- Swiss Nano Convention 2013 in Basle, Switzerland, on the 23rd-24th of May, 2013.
- International Conference on Electromechanically Active Polymers (EAP), transducers and artificial muscles, in Dübendorf, Switzerland, on the 25th-26th of June, 2013.
- Swiss Chemical Society Meeting 2013 in Lausanne (EPFL), Switzerland, on the 6th September, 2013.
- Empa PhD Student's Symposium 2014 at Empa in Dübendorf on 23rd October, 2013.

9. Curriculum Vitae

- 6th EDMX Research Day in Lausanne (EPFL), Switzerland, on the 6th September, 2013.
- Workshop on Nanocrystals in Optoelectronics in Zurich (ETH), Switzerland, on the 11th of September, 2013.

2014

- Polycoll 2014, Annual Meeting of the Division of Polymers, Colloids and Interfaces, in Dübendorf, Switzerland, on the 20th June, 2014.
- Swiss Chemical Society Meeting 2014 in Zurich (University of Zurich), Switzerland, on the 11th September, 2014.
- PhD Student's Symposium 2014 at Empa in St. Gallen on 21st October, 2014.
- NANOCON 2014, 6th International Conference on Nanomaterials – Research and Application in Brno, Czech Republic, on the 5th-7th of November, 2014.

Scientific Awards/Prizes

- 2nd Place Oral Presentation Award at the Empa PhD Symposium 2014 in St. Gallen, Switzerland, on October 21, 2014.

